



## AVERTISSEMENT

Ce document est le fruit d'un long travail approuvé par le jury de soutenance et mis à disposition de l'ensemble de la communauté universitaire élargie.

Il est soumis à la propriété intellectuelle de l'auteur. Ceci implique une obligation de citation et de référencement lors de l'utilisation de ce document.

D'autre part, toute contrefaçon, plagiat, reproduction illicite encourt une poursuite pénale.

Contact : [ddoc-theses-contact@univ-lorraine.fr](mailto:ddoc-theses-contact@univ-lorraine.fr)

## LIENS

Code de la Propriété Intellectuelle. articles L 122. 4

Code de la Propriété Intellectuelle. articles L 335.2- L 335.10

[http://www.cfcopies.com/V2/leg/leg\\_droi.php](http://www.cfcopies.com/V2/leg/leg_droi.php)

<http://www.culture.gouv.fr/culture/infos-pratiques/droits/protection.htm>



UNIVERSITÉ  
DE LORRAINE



Institut Jean Lamour



Ecole doctorale EMMA

# THÈSE

Pour l'obtention du titre de :

DOCTEUR de L'UNIVERSITÉ DE LORRAINE

Spécialité : Chimie

Présentée par :

**FLAVIA LEGA BRAGHIROLI**

---

## **Polyphénols végétaux traités par voie humide: synthèse de carbones biosourcés hautement poreux et applications**

---

Thèse soutenue publiquement le 1 décembre 2014 à Epinal devant le jury composé de :

M. Dominique BEGIN	Chargé de Recherches au CNRS, Institut de Chimie et Procédés pour l'Energie, l'Environnement et la Santé (ICPEES), Université de Strasbourg	Rapporteur
M. Jesús SANTAMARIA	Professeur, Instituto de Nanociencia de Aragón (INA), Espagne	Rapporteur
M. Alain CELZARD	Professeur, Institut Jean Lamour, Université de Lorraine	Examineur
M. Jean Michel LEBAN	Directeur de Recherche à l'INRA, Laboratoire LERFOB UMR 1092 INRA-AgroParisTech	Examineur
Mme Vanessa FIERRO	Directrice de Recherches au CNRS, Institut Jean Lamour	Directrice de thèse
M. Julien PARMENTIER	Maître de Conférences à l'Institut de Sciences des Matériaux de Mulhouse (IS2M)	Co-directeur de thèse
Mme María Teresa IZQUIERDO	Chargée de Recherches à l'Instituto de Carboquímica (ICB), Espagne	Invitée

*Institut Jean Lamour – UMR 7198- Département N2EV – Equipe 402  
ENSTIB - CS 60036- 88026 EPINAL Cedex  
Université de Lorraine – Pôle M4 - Collegium Sciences et Technologie*



## Remerciements

En premier, je voudrais remercier tous les membres du jury :

Les rapporteurs qui ont accepté l'invitation à venir à l'ENSTIB et qui ont consacré du temps à lire, relever des erreurs ou omissions et à proposer des explications de certaines parties : M. Jesús SANTAMARIA, professeur à l'Instituto de Nanociencia de Aragón (INA) en Espagne et M. Dominique BEGIN, chargé de recherches au CNRS à l'Institut de Chimie et Procédés pour l'Energie, l'Environnement et la Santé (ICPEES) à l'université de Strasbourg ;

Les examinateurs : M. Jean-Michel LEBAN, président du jury et directeur de recherche à l'Institut National de la Recherche Agronomique (INRA) et le Prof. Alain CELZARD dont la compétence et la rigueur scientifique m'ont beaucoup appris pendant ces trois ans.

Et l'invité: Mme María Teresa IZQUIERDO, chargée de recherches à l'Instituto de Carboquímica (ICB) en Espagne.

J'exprime tous mes remerciements à Mme Vanessa FIERRO, directrice de thèse, pour sa disponibilité, son attention et la confiance qu'elle m'a accordée en me proposant une place dans son groupe de recherche à l'Institut Jean Lamour (IJL) à Epinal et M. Julien PARMENTIER qui a accepté d'être le co-directeur de thèse et dont l'attention et le savoir m'ont été précieux pendant trois ans.

Je remercie aussi Prof. Antonio PIZZI pour ses conseils et suggestions à propos des synthèses avec le tanin, et pour avoir bien voulu partager ses précieuses connaissances.

Je remercie également pour leur collaboration importante :

Mme María Teresa IZQUIERDO de l'Instituto de Carboquímica (ICB) à Zaragoza en Espagne; M. Julien PARMENTIER de l'Institut de Science des Matériaux de Mulhouse (IS2M); Prof. Antonio PIZZI du Laboratoire d'Etudes et de Recherches sur le Matériau Bois (LERMAB); M. Nicolas STEIN de l'Institut Jean Lamour (IJL) à Metz et à Mme Andreea PASC du NANO Group de l'Université de Lorraine à Nancy.

Ma gratitude va aussi à tous mes collègues : Andrzej, Prasanta, Maxime, Sébastien, Philippe, Clara, Asma, César, Thouraya, Van Dang, Ismael. Egalement pour ceux qui sont déjà partis : Ummi, Gisèle, Li, Zhou, Sabrina, Luda, Iman, Ludo.

Un grand merci au personnel de l'atelier, spécialement à Jean-Jacques BALLAND et à John THOMAS pour leur disponibilité et leur sens de l'humour. Merci aussi à Amira, Corinne et Najete pour les quelques petits moments de discussions et d'encouragements.

Je voudrais remercier aussi les copains avec qui j'ai mangé tous les jours à la cuisine de l'ENSTIB. Nous avons eu des moments de détente en discutant de sujets variés.... des



voyages jusqu'à la politique française ! Merci aussi pour les petites sorties avec Clément, Marion et Marie-Christine. C'était un plaisir de vous connaître et de passer de très agréables moments avec vous.

Un grand merci à Elisabeth et Véronique, mes professeurs de français pour toutes les règles de français apprises avec les amusantes dictées, toujours accompagnées de bonne humeur.

Je voudrais remercier Gisèle, ma copine de toujours, pour m'avoir aidé à obtenir un stage dans le laboratoire IJL. Sans elle, je n'aurais pas eu cette opportunité. Merci beaucoup encore une fois. Et aussi à Rodrigo pour toute l'aide, la gentillesse et le sens de l'humour depuis mon arrivée en France.

Je voudrais aussi remercier mes amies "sœurs de cœur" Ana Paula, Ana Cristina, Ésoly, Heide, Gisele pour tous les moments de détente pendant et après l'université à Lorena et même éloignées nous avons eu une très forte connexion et amitié. Merci, vous êtes formidable !

Mes chers copains de Londres : Adri, Maisa, Michele, Saadia, Naoki, Audrey et Vagner qui ont eu toujours quelques petits mots de motivation pendant ce chemin et qui sont aussi très aimables.

Je remercie mon frère Francisco, ma sœur Fernanda et ma nièce Melissinha pour leur tendresse et leurs encouragements.

Je voudrais également remercier Jacqueline et Gérard pour tout l'aide pendant ce chemin et aussi leur gentillesse.

Merci à mon défunt grand-père qui a soutenu sa nationalité italienne et qui indirectement m'a apporté une facilité à connaître le monde de l'autre côté de l'Atlantique.

Je voudrais également remercier mon père et ma mère qui ont passé des moments heureux et moins heureux sans ma présence physique pendant ces trois années. Ma mère pour le soutien moral au téléphone et qui m'a toujours encouragée à aller jusqu'au bout. Merci beaucoup, je vous aime énormément.

Je voudrais m'excuser auprès de tous ceux que j'ai oublié dans ces remerciements... Ces années à l'ENSTIB resteront toujours dans ma mémoire. Merci beaucoup !

Enfin, je remercie Arnaud qui a parcouru ce chemin avec moi, pour sa gentillesse, la patience, son affection, son amabilité,... c'était beaucoup moins difficile de passer ces trois années de travail et dévouement à ton côté. Je t'aime et je te remercie encore une fois.

*“It is by doubting that we come to investigate, and by  
investigating that we recognize the truth”*

[Pierre Abélard]



## Table of Contents

<b>Résumé</b> .....	1
<b>Introduction</b> .....	16
<b>Chapter 1: State of the art</b> .....	18
1.1 Biomass as raw material for fuel and chemicals.....	19
1.2 Tannins.....	22
1.2.1 Tannins structure and reactivity.....	22
1.2.2 Tannin extraction and economic aspects .....	25
1.3 Carbon materials .....	27
1.3.1 Crystalline carbons .....	28
1.3.2 Amorphous carbon .....	29
1.3.2.1 Amorphous carbons production .....	30
1.3.2.2 Determination of textural properties.....	32
1.4 Hydrothermal carbonization (HTC).....	34
1.4.1 Mechanism of hydrochars formation.....	36
1.4.2 Increase of HTC yield.....	39
1.4.3 Synthesis of N-doped carbon materials .....	42
1.4.4 Synthesis of N-doped carbon gels .....	43
1.4.5 Applications of HTC-derived carbon materials.....	45
1.5 Synthesis of ordered mesoporous carbons .....	50
<b>Chapter 2: Mechanism and kinetics of hydrochar synthesis from Mimosa tannin</b> .....	53
2.1 Hydrochar synthesis and yield determination.....	53
2.2 Chemical composition .....	57
2.3 Materials' morphology and particle size.....	60
2.4 Effect of the reaction time.....	63
2.5 Effect of the tannin concentration.....	64
2.6 Effect of the temperature .....	65
2.7 Proposed mechanism for particle formation .....	66
2.8 Kinetics study.....	69
2.9 Conclusions.....	74
<b>Chapter 3: Carbons produced from tannin by alteration of the HTC reactional medium: addition of H<sup>+</sup>, sucrose and Ag<sup>+</sup></b> .....	75
3.1 HTC synthesis.....	75
3.2 Effect of H <sup>+</sup> addition.....	76
3.2.1 Textural and chemical properties of 100T materials at different pHs .....	78
3.3 Effect of sucrose addition .....	80

3.3.1 Textural and chemical properties of 50S50T materials at different pHs .....	80
3.3.2 Textural and chemical properties of 50S50T materials prepared at various temperatures and pHs .....	82
3.3.3 Textural and chemical properties of tannin/sucrose materials at different proportions and pHs .....	84
3.3.4 Van Krevelen diagram, TPD (Temperature Programmed Desorption) and XPS analysis.....	90
3.4 Effect of silver nitrate addition into HTC of tannin.....	92
3.5 Conclusions.....	97

## **Chapter 4: N-doped carbon materials and their use as electrodes for supercapacitors .....**

4.1 Preparation of N-doped materials by HTC .....	99
4.2 Chemical structure of hydrothermally treated tannin .....	101
4.2.1 <sup>13</sup> C NMR studies.....	101
4.2.2 MALDI-ToF studies .....	105
4.2.3 Elemental analysis .....	109
4.2.4 XPS technique .....	112
4.3 Materials' morphology and porous texture.....	116
4.3.1 Morphological characteristics: TEM and SEM photos.....	116
4.3.2 Textural properties.....	120
4.4 Comparison of NCM's made from tannin and other precursors.....	124
4.5 Electrochemical performances of N-doped, tannin-based, hydrothermal carbons .....	127
4.5.1 Electrochemical experiments.....	127
4.5.2 Effect of oxygen and nitrogen-containing functional groups .....	131
4.5.3 Comparison with previous studies.....	133
4.6 Conclusions.....	135

## **Chapter 5: Synthesis of N-doped carbon gels and their use as electrodes for supercapacitors .....**

5.1 Introduction to gel drying .....	137
5.1.1 Subcritical Drying or xerogels synthesis .....	138
5.1.2 Freeze-drying or Cryogels synthesis .....	139
5.1.3 Supercritical Drying or Aerogel synthesis.....	139
5.2 N-doped carbon gel synthesis by HTC .....	140
5.3 Morphology of carbon gels.....	142
5.4 Porous texture of organic and carbon gels.....	144
5.5 Elemental composition of organic and carbon gels .....	147
5.6 Electrochemical performances of carbon gels .....	150
5.7 Conclusions.....	156

<b>Chapter 6: Synthesis of mesoporous carbons by a soft-templating route using tannin as a carbon precursor</b> .....	157
6.1 F-127 Pluronic <sup>®</sup> and OMC synthesis .....	158
6.2 Synthesis of OMC's from tannin and F127 .....	160
6.2.1 Effect of the pH .....	161
6.2.2 Effect of the carbonization temperature.....	164
6.3 Conclusions.....	168
<b>Conclusions and Perspectives</b> .....	169
<b>Annexes</b> .....	172
<b>Annex 1: Techniques of characterisation</b> .....	172
A1. Chemical characterisation .....	172
A1.1 Elemental Analysis (EA) .....	172
A1.2 Mass Spectrometry - MALDI ToF .....	173
A1.3 Nuclear Magnetic Resonance Spectroscopy (NMR) <sup>13</sup> C.....	174
A1.4 Temperature Programmed Desorption (TPD) .....	175
A1.5 Thermogravimetric Analysis (TGA) .....	176
A1.6 X-ray photoelectron spectroscopy (XPS) .....	176
A2. Physical characterisation.....	176
A2.1 Adsorption - desorption of gases .....	176
A2.2 Scanning and Transmission Electron Microscopy (SEM and TEM).....	178
A2.3 Small Angle X-rays Scattering (SAXS) .....	179
A2.4 Determination of the skeletal density and the particle size.....	180
A3. Electrochemical characterization .....	181
A3.1 Electrical Double-Layer Capacitors (EDLC).....	181
<b>Annex 2: Published materials</b> .....	182
A2.1 List of Publications in scientific journals:.....	182
A2.2 Articles in Conference .....	183
A2.3 Oral Communications .....	183
A2.4 Communications by Poster .....	183
<b>Bibliography</b> .....	185
<b>Résumé/Summary</b> .....	206



## List of Figures

Fig. 1: Scheme of possible applications for wood biomass [Balat et al. 2009].	19
Fig. 2: The main extractives obtained from trees [Patten et al. 2010].	21
Fig. 3: Scheme of extraction of tannins from Acacia in the barks [Feng et al. 2013].	22
Fig. 4: Classification of tannins [Khanbabaee and Ree 2001].	23
Fig. 5: Flavan structure - the main model molecule present in tannins [Aron and Kennedy 2007].	24
Fig. 6: The four main polyflavonoids present in condensed tannins: a) prorobinetinidin; b) prodelfphinidin; c) profisetinidin and d) procyanidin [Pizzi 2008].	24
Fig. 7: Autocondensation reaction of Mimosa tannin [Pizzi 1994].	25
Fig. 8: Scheme of extraction of tannins from Acacia barks [Pizzi 1994].	26
Fig. 9: Crystalline and amorphous structures of carbon [Ebbesen 1997].	28
Fig. 10: The allotropic forms of carbon: diamond and graphite [Oganov et al. 2013].	29
Fig. 11: The new carbon structures discovered in the last 25 years: graphene, fullerene and SWCNT [Oganov et al. 2013].	29
Fig. 12: Schematic representation of the structure of activated carbon [Oberlin 1984].	32
Fig. 13: Representation of the textural properties of a porous material and all techniques which are used to measure its porosity [Celzard et al. 2007; Achaw 2012; Falco et al. 2013].	33
Fig. 14: Physisorption isotherms according to IUPAC [Gregg and Sing 1982].	34
Fig. 15: Possible reactions occurring during hydrochar formation [Sevilla and Fuertes 2009a].	37
Fig. 16: The main reactions described after HTC at 180°C of hexoses and pentoses in water [Titirici et al. 2008].	37
Fig. 17: The microspheres core-shell structure of hydrochars [Sevilla and Fuertes 2009a].	38
Fig. 18: Tannin degradation in hot and acid conditions to form of catechin and anthocyanidins [Pizzi 1983].	40
Fig. 19: Tannin autocondensation by acid hydrolysis of heterocyclic rings [Pizzi 1983].	41
Fig. 20: Schematic synthesis of HTC of glycine and glucose with their possible hydrocarbons as final material [Baccile et al. 2011].	43
Fig. 21: Schematic preparation and structure of gels [Jung et al. 2012].	44
Fig. 22: The main applications of porous hydrothermal carbon materials (adapted from Titirici (2013)).	46
Fig. 23: Schematic representation of a supercapacitor [Frackowiak and Béguin 2001].	49
Fig. 24: Synthesis of ordered mesoporous carbon materials using mesoporous silica hard templates and block copolymer soft templates (adapted from Ma et al. (2013)).	51
Fig. 25: Scheme for the synthesis of mesoporous carbon from tannin and the surfactant F127 as precursors and the method EISA (adapted from Schlienger et al. (2012)).	52
Fig. 26: Graphical procedure for the synthesis of hydrochars made from tannin.	53
Fig. 27: Hydrochars obtained at different experimental conditions.	54
Fig. 28: TEM images of the particles that could not be recovered by centrifugation, thus remaining in the filtrate after HTC of 0.5 g tannin in 16 mL of water for: (a) and (b) 24 h at 130°C; (c) and (d) 1 h 20' at 200°C.	55
Fig. 29: Hydrothermal carbon yield (a) at different HTC temperatures, as a function of reaction time (initial amount of tannin: 0.5 g in 16 mL of water); (b) as a function of HTC time at 180°C for different initial amounts of tannin. The data points are here connected by a dot line to guide the eye.	56
Fig. 30: Chemical composition of all tannin-derived hydrothermal carbons as a function of carbon yield: (a) from elemental analysis (EA); (b) from XPS.	59
Fig. 31: Surface area, $S_{\text{BET}}$ , of hydrothermal carbons derived from tannin and plotted as a function of yield: (a) at different HTC temperatures and constant initial amount of tannin of 0.5 g; (b) at the same HTC temperature of 180°C and different initial amounts of tannin.	61
Fig. 32: Skeletal density of hydrothermal carbons as a function of yield for all different HTC temperatures and different amounts of tannin used in this work.	62
Fig. 33: TEM images of the hydrothermal carbons produced at 200°C using 0.5g of tannin in 16 mL of water during different HTC times: (a) and (b) 6h; (c) and (d) 12 h; (e) and (f) 24h.	63



Fig. 34: TEM images of the hydrothermal carbons produced at 180°C during 24h, using different initial amounts of tannin: (a) 0.5g; (b) 1.0g; (c) 1.5g, (d) 2.0g.....	64
Fig. 35: TEM images of the hydrothermal carbons produced at different HTC temperatures, using constant initial amount of tannin, 0.5g, and reaction time, 24 h: (a) and (b) 160°C; (c) and (d) 180°C; (e) and (f) 200°C.....	66
Fig. 36: TEM images of the hydrothermal carbons produced at 130°C with 0.5 g of tannin in 16 mL of water for different HTC times: (a) and (b) 48 h; (c) and (d) 120 h.....	67
Fig. 37: TEM images of hydrothermal carbons showing: (iii) aggregation of primary carbon particles onto secondary particles produced at a) 180°C for 24 h with 1.5 g of tannin and b) 180°C for 24 h with 2.0 g of tannin; (iv) aggregation of primary carbon particles with precipitation of hydrothermally treated tannin produced at c) 160°C for 5 h with 0.5 g of tannin and d) 200°C for 6 h with 0.5 g of tannin.....	68
Fig. 38: Amount of elemental carbon, <i>C</i> , remaining in the solution after HTC: (a) Experimental results after HTC at 180°C of different amounts of tannin in 16 mL of water; (b) Method for determining the reaction rate. ....	71
Fig. 39: Elucidation of HTC kinetics of tannin: (a) Determination of reaction order by application of Eq. (8) to the initial reaction rates at 180°C; (b) Determination of kinetic constants at different HTC temperatures by application of Eq. (11).....	72
Fig. 40: Arrhenius plot for the determination of HTC activation energy of tannin by application of Eq. (9).....	73
Fig. 41: Three main modifications applied to the system of HTC of tannin.....	75
Fig. 42: Monolith obtained at pH 1 on the left and compacted solid material obtained at unmodified pH on the right side.....	78
Fig. 43: SEM images of CH100T submitted to HTC at 180°C with, a) unmodified pH and b) pH=2, and further pyrolysis at 900°C.....	79
Fig. 44: a) Nitrogen adsorption-desorption isotherms (full and open symbols, respectively) at -196°C after carbonization at 900°C of pristine tannin (C100T) and of two hydrochars obtained at 180°C at pH 1 (CT100T180_1) and unchanged (pH=4.2, CT100T180_u ); and b) their corresponding pore size distribution obtained by DFT (slit-like pore geometry).....	79
Fig. 45: HTC yield of H100T and H50S50T at different pHs and $S_{BET}$ ( $m^2 g^{-1}$ ) of the carbon materials after posterior pyrolysis at 900°C (discontinuous lines are guides for the eyes). ....	82
Fig. 46: SEM images of 50S50T submitted to HTC at a) unmodified pH and b) at pH=2. ....	82
Fig. 47: Total carbon yield and surface area BET ( $m^2 g^{-1}$ ) for the carbonized (900°C) carbon samples CH50S50T prepared with different HTC temperatures and pH values. ....	83
Fig. 48: SEM images of 50S50T submitted to HTC at pH 2 a) 160°C and b) 200°C.....	83
Fig. 49: SEM images of carbon materials derived from sucrose submitted at HTC at 180°C with a) unchanged pH (pH=8) and b) pH = 2 and further carbonized at 900°C. ....	85
Fig. 50: SEM images of carbon materials derived made from sucrose and tannin at proportion of 25 and 75% submitted at HTC at unmodified pH (a, c) and pH = 2 (b, d) and further carbonised (900°C). ....	87
Fig. 51: a) HTC yield of all materials at different proportions of T / S; b) Surface areas $S_{BET}$ ( $m^2 g^{-1}$ ) for the same materials after HTC and posterior carbonization at 900°C.....	88
Fig. 52: Surface areas $S_{BET}$ ( $m^2 g^{-1}$ ) (open symbols) and the product Total carbon Yield x $S_{BET}$ (full symbols) as function of the total carbon yield for all materials at different proportions of T / S after HTC and posterior pyrolysis at 900°C. ....	89
Fig. 53: a) Nitrogen adsorption-desorption isotherms (full and open symbols, respectively) at 77K; and b) their pore size distribution determined by the DFT method (slit-like geometry) for CH50S50T_2 and CH50S50T_u samples. ....	89
Fig. 54: a) van Krevelen diagram for all materials before (100S and 100T) and after HTC (H100S and H100T) and at unmodified pH (HsStT_u) and at pH 2 (HsStT_2) and posterior pyrolysis at 900°C (HTC_900°C); and b) the total amount of CO and CO <sub>2</sub> gases produced during TPD analysis for T / S materials at different proportions.....	91
Fig. 55: TEM images of three filtrates obtained after HTC of tannin at 180°C in presence of AgNO <sub>3</sub> solution during 1, 2 and 4h respectively.....	94

Fig. 56: TEM images of three filtrates obtained after HTC of tannin with 1, 2 or 6 mL of 0.1M AgNO <sub>3</sub> solution at 180°C for 24h and posterior carbonization at 900°C. ....	94
Fig. 57: HTC yield and surface area (BET) of all samples made with tannin and AgNO <sub>3</sub> solution. ....	95
Fig. 58: a) Nitrogen adsorption-desorption isotherms (full and open symbols, respectively) at -196°C for pristin two materials made after HTC at 180°C having 4 and 8g of an aqueous solution of AgNO <sub>3</sub> after posterior pyrolysis at 900°C; and b) their correspondent pore size distribution obtained by PSD. ....	97
Fig. 59: Graphical procedure for the synthesis of hydrochars made from N-modified tannin. ....	99
Fig. 60: The methods used for preparing N-doped carbon materials and their respective final products. ....	100
Fig. 61: The spectrum of RMN of C <sup>13</sup> of tannin Mimosa in a solid state [Pizzi 1994]. ....	102
Fig. 62: Solid-state CP-MAS <sup>13</sup> C NMR spectra of all materials after HTC at 180°C: (a) H-T; (b) H-EAT, and (c) H-AT. ....	104
Fig. 63: MALDI-TOF spectra of all materials after HTC at 180°C: (a) H-EAT; (b) H-AT, and (c) H-T. ....	106
Fig. 64: MALDI mass spectrum of natural Mimosa tannin extract [Pasch et al. 2001]. ....	107
Fig. 65: Chemical species suggested from the analysis of MALDI-ToF spectra of hydrothermal aminated carbon gel before pyrolysis, H-EAT: (a) 554 Da; (b) 555 Da; (c) 843 Da (the sodium of weight 23 was implicitly taken into account). ....	108
Fig. 66: Nitrogen content of N-doped materials prepared by HTC at different temperatures, before and after pyrolysis. ....	112
Fig. 67: Chemical species suggested from the analysis of MALDI-ToF spectra of catechin treated with an aqueous ammonia solution. ....	115
Fig. 68: TEM images of the samples after HTC at 180°C and subsequent pyrolysis at 900°C: CH-T (a and d), CH-EAT (b and e) and CH-AT (c and f). ....	117
Fig. 69: SEM images of tannin-based materials after HTC and posterior pyrolysis at 900°C: (a, b) CH-T prepared at 190°C; (c, d) prepared at 210°C; (e,f) CH-AT prepared at 190°C; (g,h) CH-AT prepared at 210°C; (i,j) CH-EAT 190°C; (k,l) and 210°C. ....	119
Fig. 70: Surface areas, $S_{BET}$ , of all materials obtained after HTC at different temperatures: (a) before, and (b) after pyrolysis at 900°C. ....	121
Fig. 71: Nitrogen adsorption-desorption isotherms (full and open symbols, respectively) at 77K of tannin-based carbon materials, i.e. after HTC at 190 and 210°C followed by pyrolysis at 900°C; and their respective DFT. ....	123
Fig. 72: Surface areas, $S_{BET}$ , and nitrogen content of our materials: (a) before pyrolysis (H-T $\diamond$ , H-AT $\square$ and H-EAT $\triangle$ ); (b) after pyrolysis (CH-T $\blacklozenge$ , CH-AT $\blacksquare$ and CH-EAT $\blacktriangle$ ) compared to results reported in literature. ....	126
Fig. 73: Three – electrode cell for measuring electrochemical properties of carbon materials. ....	127
Fig. 74: a) Cyclic voltammograms of CH-T1, CH-AT1 and CH-EAT1 samples, at a scan rate of 2 mV s <sup>-1</sup> ; b) Specific capacitance of samples CH-T1, CH-AT1 and CH-AT1 as a function of scan rate. ....	129
Fig. 75: The relationship between oxygen a) and nitrogen b) content and specific capacitance. ....	132
Fig. 76: a) Comparison, at a constant scan rate of at 2 mV s <sup>-1</sup> , of a) specific capacitances and b) normalized EDLC capacitance of our materials with those of other carbonaceous materials as a function of their BET surface area (AC: Activated carbons, CG: Carbon gels, OMC: Ordered mesoporous carbons, HTC: Hydrothermal carbons). ....	134
Fig. 77: Principle of a sol-gel reaction: i) starting solution with precursor, ii) sol system and iii) gel. ....	137
Fig. 78: Phase diagram of the solvent present in the gel and the corresponding drying pathways used for the formation of xerogel (grey), aerogel (green) and cryogel (red) and their corresponding drying nodular structure of the resulting porous materials. ....	138
Fig. 79: The three dried gels made from tannin and formaldehyde resin and dried in supercritical CO <sub>2</sub> conditions (aerogel) on the left; freeze-drying conditions (cryogel) on the centre and subcritical conditions (xerogel) on the right. ....	140
Fig. 80: The three gels made from evaporate aminated tannin (EAT) and water after HTC at 180°C and 24h a) in and b) outside of a glass vial at different initial concentrations of 11, 18 and 27%. ....	142
Fig. 81: SEM images of all samples after HTC and posterior pyrolysis at 900°C for all carbon gels: CA, CC and CX at 27%. ....	143

Fig. 82: BET surface area of all gels: a) before pyrolysis (A, C and X), and b) after pyrolysis (CA, CC and CX). .....	145
Fig. 83: (a), (b) and (c) Nitrogen adsorption-desorption isotherms at -196 °C of CA, CC and CX carbon gels at different percentages 11, 18 and 27%, and (d), (e) and (f) their corresponding pore size distributions. ....	146
Fig. 84: a) Van Krevelen diagram for all materials including the pristine tannin, and b) relationship between the nitrogen content and the BET surface area for all materials. ....	148
Fig. 85: a) Cyclic voltammograms of CA, CC and CX carbon gels at different percentages of tannin: 11, 18 and 27% at a scan rate of 2 mV s <sup>-1</sup> , and b) their corresponding specific capacitance at different scan rates (the dotted lines are just guides for the eye). ....	152
Fig. 86: Specific capacitance of all prepared, HTC-derived, carbon gels plotted as a function of: a) BET surface area, and b) pore volumes classified according to pore widths: below 0.7 nm ( $V_{0.7}$ , ultramicropores), below 2 nm ( $V_2$ , micropores), below 10 nm ( $V_{10}$ , micropores and narrow mesopores) and total ( $V_t$ ). ....	153
Fig. 87: Normalised capacitance of all prepared, HTC-derived (TM), carbon gels plotted as a function of: a) nitrogen, and b) oxygen functional groups. ....	153
Fig. 88: a) Specific capacitance, and b) normalised capacitance, both plotted as a function of BET surface area for all carbon gels and other materials from the literature (CG: other carbon gels; HTC: HTC-derived materials; TM: HTC-derived tannin-based materials; AC: activated carbons). ....	155
Fig. 89: Schematic approach for the production of OMC's using tannin Mimosa (adapted from Schlienger et al. (2012)). ....	157
Fig. 90: Schematic representation of the four main types of surfactants a) neutral, b) anionic, c) cationic and d) amphoteric on the left and the phase diagram of Pluronic F127 in aqueous medium on the right [Wanka et al. 1994]. ....	158
Fig. 91: Schematic approach of OMC's synthesis using tannin and F127. ....	160
Fig. 92: TEM images of some PTW samples synthesized after agitation at pH 1 (on the left) and pH 5 (on the right), drying at 80°C and posterior pyrolysis at 400°C. ....	161
Fig. 93: a) to d) Nitrogen adsorption-desorption isotherms (full and open symbols, respectively) at -196°C for different pHs; e) CO <sub>2</sub> adsorption isotherms at 0°C for PTW carbon materials at different pHs after pyrolysis at 400°C; and f) pore size distribution calculated by DFT model for all samples prepared at different pHs and calcined at 400°C. ....	163
Fig. 94: TEM images of PTW samples at pH<1 synthesized after agitation, drying at 80°C and posterior pyrolysis at 400, 700 and 900°C. ....	164
Fig. 95: a) to c) Nitrogen adsorption-desorption isotherms (full and open symbols, respectively) at -196°C; d) CO <sub>2</sub> adsorption isotherms at 0°C for PTW carbon materials at different pHs after pyrolysis; e) pore size distribution calculated by DFT model for the samples prepared at different pHs and calcined at 900°C; f) SAXS patterns for the same samples in d) and e). ....	165
Fig. 96: a) Nitrogen adsorption-desorption isotherms (full and open symbols, respectively) at -196°C; b) pore size distribution calculated by DFT model for the samples prepared at different pHs and calcined at 900°C; c) SAXS patterns for the same samples in a) and b); d) to g) TEM photos of all PTW samples after pyrolysis at 900°C. ....	167
Fig. 97: Metal oxide nanoparticles made from HTC of tannin together with metal salts and oxidized in air at 550°C. ....	171

## List of Tables

Table 1: Summary of the main characteristics of Mimosa, Quebracho and Maritime pine tannins.....	27
Table 2: Ultimate analysis of hydrothermal carbons, and C/O and C/H weight ratios. ....	58
Table 3: Elemental analysis (wt.%) of tannin before and after HTC.....	60
Table 4: Textural properties and elemental analysis obtained for pristine tannin (100T), HTC materials and carbon materials made at different pHs.....	77
Table 5: Textural properties and elemental analysis obtained for materials 50S50T, HTC and carbon materials made at different pHs. ....	81
Table 6: Textural properties and elemental analysis obtained for materials 50S50T after HTC and carbonization at different temperatures and pHs.....	84
Table 7: Textural properties and elemental analysis obtained for pristine tannin (100T), HTC materials and carbon materials. ....	86
Table 8: Contributions to the C1s O1s bands in XPS patterns. ....	92
Table 9: Textural properties of all silver nanoparticles samples prepared after HTC and posterior pyrolysis.....	96
Table 10: <sup>13</sup> C NMR peaks in ppm of the numbered carbons and gallic acid residues present in Mimosa tannin.....	102
Table 11: MALDI-ToF peaks of H-T, i.e. tannin submitted to HTC at 180°C. ....	107
Table 12: MALDI-ToF peaks of H-AT, i.e. tannin aminated by direct HTC in ammonia at 180°C.....	109
Table 13: Elemental analyses of all samples after HTC at different temperatures, before (H-T, H-EAT and H-AT) and after pyrolysis at 900°C (CH-T, CH-EAT and CH-AT). ....	110
Table 14: Contributions to the N1s bands in XPS patterns of HTC-derived materials. ....	113
Table 15: Contributions to the N1s bands in XPS patterns of carbonised HTC samples.....	113
Table 16: Surface areas and pore volumes of all materials pyrolysed at 900°C, determined by N <sub>2</sub> adsorption at -196°C.....	124
Table 17: Main characteristics of the six carbon materials tested.....	130
Table 18: Main characteristics of all organic and carbon gels synthesized.....	147
Table 19: Contributions to N1s and O1s bands in XPS patterns of X11 and CX11 materials. ....	149
Table 20: Textural properties and elemental analysis of all carbon materials synthesized.....	162



## Résumé

L'utilisation intensive des ressources fossiles pour la préparation de nombreux matériaux et pour la production d'énergie va probablement conduire à leur épuisement dans un avenir proche. De plus, les ressources fossiles contribuent au réchauffement climatique en générant des gaz à effet de serre avec des conséquences dramatiques pour le climat et l'environnement. D'intenses efforts ont donc été fournis par la communauté scientifique pour fournir des matériaux ayant les mêmes caractéristiques (voire améliorés) par des voies respectueuses de l'environnement en développant des procédés verts qui utilisent la biomasse d'une manière durable. La biomasse est constituée de matières organiques issues d'organismes vivants, plus généralement de l'agriculture ou de la forêt. Elle est utilisée à l'échelle industrielle pour produire des matériaux ou des polymères à partir de cellulose ou de caoutchouc par exemple. Cependant, son utilisation comme précurseur pour la préparation de nouveaux matériaux nécessite encore des nombreux efforts.

Dans ce travail, nous avons étudié la conversion de la biomasse en carbone pour la préparation de matériaux à propriétés contrôlées. Nous nous sommes intéressés plus spécifiquement à la carbonisation en condition hydrothermale d'un précurseur bio-sourcé appelé tanin. Les carbones poreux peuvent être utilisés dans de nombreux domaines dû à leurs propriétés physicochimiques comme une grande capacité d'adsorption, une stabilité thermique et chimique élevée, une bonne conductivité électrique et thermique et une faible densité. Pour ces raisons, ils sont largement utilisés en catalyse, en séparation et stockage de gaz, pour la dépollution de l'eau ou dans les électrodes des batteries Li-ion ou les supercondensateurs. Il existe de nombreuses méthodes pour préparer un carbone poreux selon l'application recherchée et le coût du matériau. Les carbones activés sont parmi les carbones les plus utilisés à l'échelle industrielle. Ils sont habituellement préparés à partir de matière végétale et sont de relativement bas coût. D'autres matériaux comme les carbones mésoporeux présentent aussi des potentialités intéressantes. Cependant l'optimisation de ces matériaux carbonés pour des applications spécifiques requiert un contrôle de plus en plus pointu de la distribution de taille de pores ainsi que des fonctionnalités de surface tout en conservant un coût modique pour permettre leur développement à l'échelle industrielle.

Le principal objectif de ce travail a été de développer de nouveaux matériaux carbonés poreux par un procédé économiquement viable et respectueux de l'environnement. Ces matériaux ont ensuite été caractérisés et leurs potentialités dans le cadre d'applications ont été

évaluées. Le précurseur utilisé ici est le tanin, extrait de l'écorce de nombreux arbres. Le tanin est un composé naturel, non toxique et constitué d'unités flavonoïdes contenant des groupements phénoliques essentiels aux réactions d'autocondensation ou de polymérisation (Fig. 1). Pour ces raisons, le tanin est un bio-précurseur très intéressants pour la préparation de résines de mousses, de gels et de matériaux carbonés.

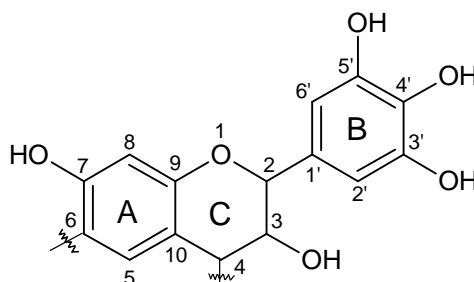


Fig. 1: Le principal polyflavonoïde présent dans tanins condensés, Mimosa: prorobinetinidin composé de résorcinol anneau-A et pyrogallol anneau-B.

La conversion du tanin en carbone a ici été réalisée par voie hydrothermale. Cette technologie a des nombreux avantages: simplicité, faible coût, utilisation d'un solvant vert (l'eau), facilité de scale-up, bon rendement de carbonisation et surtout absence de génération de CO<sub>2</sub>. Le produit solide récupéré après HTC est appelé carbone hydrothermale ou hydrochar et il est produit en soumettant un précurseur carboné dans un système aqueux à des températures et pressions modérés. Le précurseur est mis dans un récipient avec le volume souhaité d'eau et introduit dans l'autoclave, qui est fermé et placé dans une étuve à température inférieure à 250°C. Au cours du traitement HTC, la pression est générée automatiquement par le système à la température fixée; des pressions allant jusqu'à 20 bars (2 MPa) peuvent être atteintes et très peu de gaz est libéré.

Dans ce conditions, il y a plusieurs réactions qui se produisent: des réactions de polymérisation mais également des réactions de condensation, qui pourraient survenir par plusieurs chemins: déshydratation intermoléculaire et intramoléculaire, condensation aldol, céto-énol et déshydratation intermoléculaire des matières aromatisées<sup>1</sup>. Après les réactions, la formation de hydrochars est due à un mécanisme de nucléation et de croissance qui suit le modèle de LaMer<sup>2</sup>. Lorsque la concentration de carbone aromatique soluble atteint le point de saturation, un processus de nucléation est initié. En résumé, les processus de nucléation et de

<sup>1</sup> Sevilla M, Fuertes AB. Chemical and structural properties of carbonaceous products obtained by hydrothermal carbonization of saccharides. Chem Eur J 2009;15(16):4195-4203.

<sup>2</sup> La Mer VK. Nucleation in phase transitions. Ind Eng Chem 1952;44(6):1270-1277.

croissance ont lieu après les réactions d'hydrolyse, condensation, la déshydratation, aromatisation et de polymérisation dans les conditions de HTC. Puis, il y a deux produits:

(i) une particule insoluble carbonée, souvent sphérique, ayant une structure contenant une partie hydrophobe (noyau aromatique) et une partie hydrophile ou coquille. Le noyau présente des atomes d'oxygène stable sous forme d'éther, quinone, etc, tandis que les coquilles présentent des groupes fonctionnels oxygénés (hydroxyle phénolique, carbonyle, acide carboxylique, ester, etc)<sup>1,3,4</sup>. Ces deux parties sont illustrées à la Fig. 2;

(ii) une solution aqueuse ayant des composés organiques tels que du furfural, ou des acides, dans le cas de HTC de saccharose.

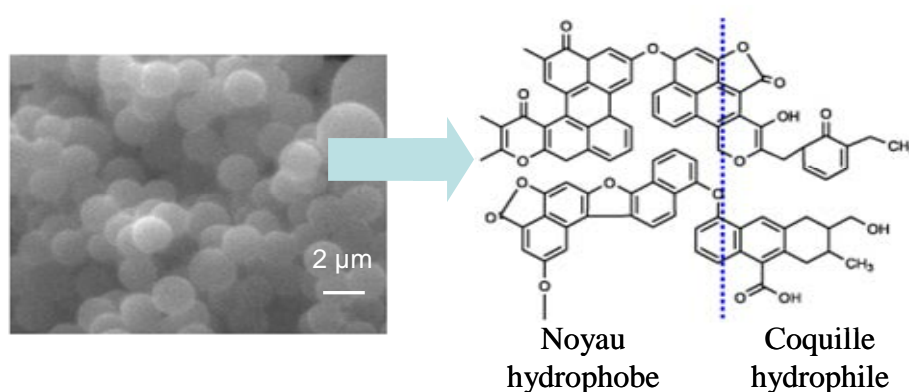


Fig. 2: La structure des microsphères noyau-enveloppe de hydrochars<sup>1</sup>.

Après un second traitement thermique, les hydrochars peuvent présenter une porosité très élevée et donc une grande capacité d'adsorption, une stabilité thermique et chimique élevées, et des augmentations de conductivité électrique et thermique. Les matériaux carbonés poreux peuvent présenter différentes tailles de pores: macro, méso et / ou micro pores, selon la classification effectuée par l'IUPAC. Les pores ayant une taille supérieure à 50 nm sont appelés macropores, des pores dont la taille est comprise entre 2 et 50 nm sont nommés comme des mésopores et ils sont appelés micropores lorsque la taille est inférieure à 2 nm. Nous nous sommes intéressés à la carbonisation des hydrochars pour développer cette porosité et étendre le domaine d'applications de ces matériaux.

Ce travail a été réalisé à l'Institut Jean Lamour (1) (IJL – UMR CNRS 7198) localisé à l'Ecole Nationale Supérieure des Techniques et Industries du Bois (ENSTIB), de l'Université de Lorraine (UL). Il a été rendu possible grâce à des collaborations fructueuses avec d'autres

<sup>3</sup> Tang MM, Bacon R. Carbonization of cellulose fibers—I. Low temperature pyrolysis. Carbon 1964;2(3):211-214.

<sup>4</sup> Asghari FS, Yoshida H. Acid-catalyzed production of 5-hydroxymethyl furfural from d-fructose in subcritical water. Ind Eng Chem Res 2006;45(7):2163-2173.



instituts de recherche que sont: (2) Instituto de Carboquímica à Zaragoza en Espagne; (3) Institut de Science des Matériaux de Mulhouse (LRC CNRS 7228); (4) Laboratoire d'Etudes et de Recherches sur le Matériau Bois (LERMAB – EA 4370); (5) Institut Jean Lamour (IJL – UMR CNRS 7198) à Metz et (6) NANO Group (UMR CNRS 7565 SRSM) de l'Université de Lorraine à Nancy. Pour la préparation, la caractérisation et l'évaluation des applications potentielles des matériaux, nous nous sommes appuyés sur l'expertise des laboratoires (1) à (3) pour les matériaux désordonnés, les laboratoires (3) et (6) pour les carbones mésoporeux organisés, le laboratoire (4) pour leurs connaissances en biochimie et le laboratoire (5) pour les applications dans le domaine de l'électrochimie.

Le premier chapitre comprend trois parties: 1) description de la biomasse et en particulier des procédés d'extraction du tanin à partir de l'écorce des arbres; 2) généralités sur les carbones et leurs méthodes de préparation traditionnelles; 3) les voies de synthèse de matériaux carbonés à partir de la biomasse telle que la carbonisation par voie hydrothermal et les applications potentielles de ces matériaux. Le résumé des chapitres 2 à 6 est présenté ci-dessous en incluant les résultats obtenus par le procédé de carbonisation hydrothermale de tanin et de tanin modifié par l'ammoniaque de manière à introduire de l'azote dans le matériau final. Un simple procédé, à pression atmosphérique sera également décrit pour la synthèse d'un carbone mésoporeux organisé obtenu à partir de tanin de mimosa.

## Chapitre 2: Mécanisme et cinétique du traitement hydrothermal de tanin

Dans ce chapitre, le tanin a été soumis à un traitement de carbonisation hydrothermal (HT) en faisant varier plusieurs paramètres de manière à réaliser des études cinétiques, comprendre les mécanisme de formation de ces carbones HT et évaluer leurs propriétés physico-chimiques. Pour cela, nous avons fait varier les paramètres suivants: la quantité de tanin dans l'autoclave, la température et la durée du traitement HT (Fig. 3). A partir de toutes ces expériences, nous avons pu tracer le rendement de carbonisation en condition HT en fonction du temps pour chaque température.

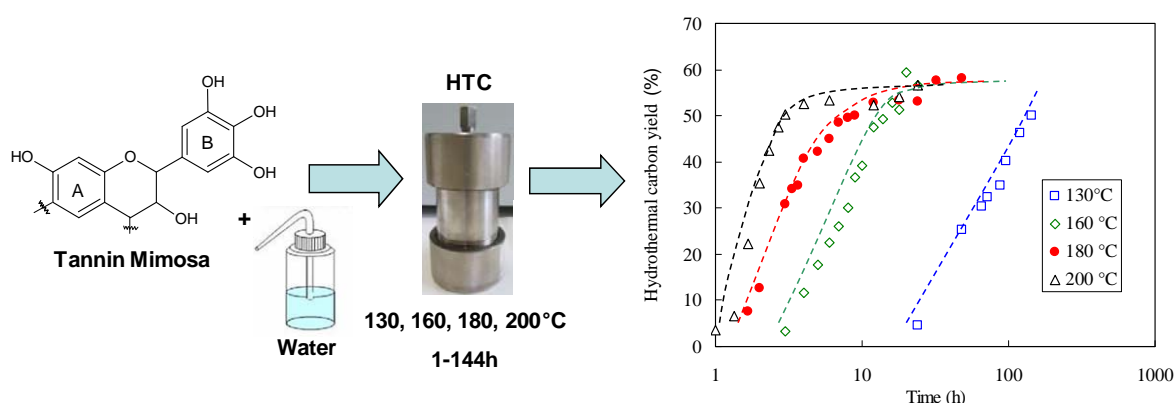


Fig. 3: Approche schématique pour la production de hydrochars de tanin.

Grâce à l'utilisation des techniques appropriées (MET, adsorption de krypton à  $-196^{\circ}\text{C}$  pycnométrie à hélium), nous avons pu comparer et expliquer les différences morphologiques des particules micrométriques obtenues par traitement HT. Ces particules sont structurées sous forme d'agrégats de microsphères plus ou moins étendus selon les conditions de synthèse. Pour les températures basses ( $130, 160^{\circ}\text{C}$ ) et les traitements courts (6h), des particules de petite taille, de forme mal définie, faiblement agrégées et présentant les surfaces les plus élevées sont alors obtenues (environ  $8\text{ m}^2\text{ g}^{-1}$ ). Pour des synthèses plus longues (24h) à plus haute température ( $200^{\circ}\text{C}$ ), la morphologie sphérique est mieux définie et la taille des particules est plus importante ( $\sim 5\text{ }\mu\text{m}$ ) en accord avec la surface spécifique la plus faible observée (env.  $1\text{ m}^2\text{ g}^{-1}$ ) (voir Fig. 4).

Dans les deux cas, les carbones HT sont non poreux et leur surface spécifique correspond donc à leur surface externe. Différents phénomènes, se produisant simultanément ou de manière décalée selon les conditions de traitement HT, ont été proposés pour expliquer ces évolutions: a) nucléation et formation de particules primaires de carbone HT, b) croissance

par coalescence de particules (entre particules primaires et/ou entre particules primaires et secondaires), et c) croissance par précipitation/greffage des fractions solubles de tanin polymérisé sur la surface des particules. Le premier et second processus (a et b) interviennent principalement pour les matériaux formés à basse température et pour des temps de réaction courts. Les processus b) et c) se produisent quant à eux pour des températures plus élevées et des temps longs.

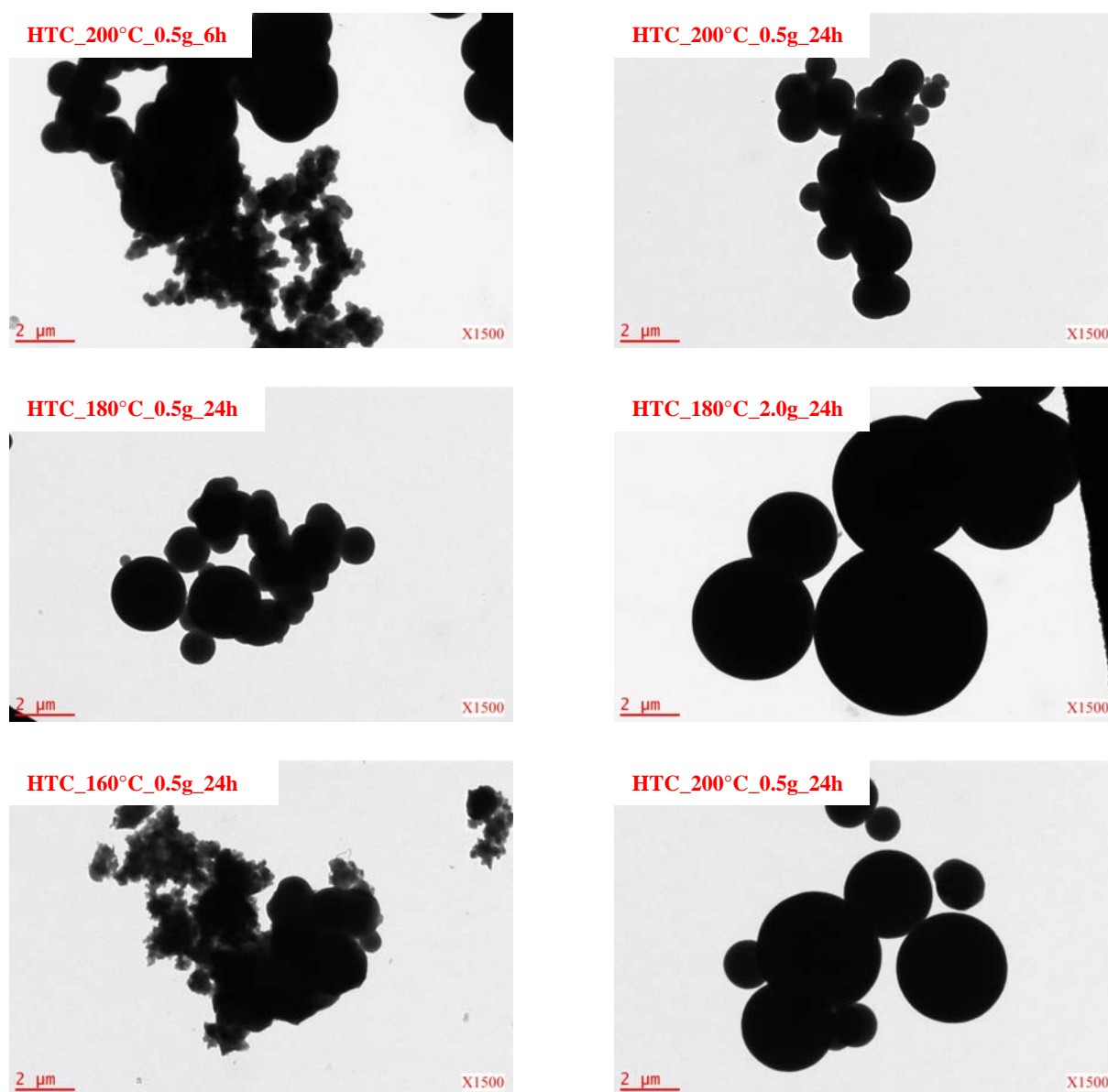


Fig. 4: Images MET de quelques échantillons à différentes conditions de HT telles que la température, le temps de réaction et la masse initiale de tanin.

Par analyse chimique des particules solides isolées par filtration après traitement HT, nous avons pu montrer que le pourcentage de carbone ne varie pas de façon significative avec la température (de 130 à 200°C), la durée du traitement (1 à 720 h) et le rendement de

carbonisation HT (de 4 à 64%). La concentration massique en carbone dans la solution durant le traitement HT ( $C(t)$ ) a donc pu être calculé par différence entre la quantité de carbone présente initialement dans la solution de tanin solubilisé et la quantité de carbone solide isolée par filtration après le traitement HT. Des synthèses réalisées à différentes températures et pour différents temps ont permis de tracer les courbes de  $C(t)$  en fonction du temps (h). Il apparaît que le processus de carbonisation hydrothermal peut être décrit par une cinétique de 1<sup>er</sup> ordre avec une énergie d'activation de  $91 \text{ kJ mol}^{-1}$ .

### **Chapitre 3: Matériaux carbonés produits à partir de tanin par modification de l'environnement réactionnel HT: addition de $\text{H}^+$ , saccharose et $\text{Ag}^+$**

Grâce aux connaissances acquises dans le chapitre précédent sur les mécanismes de formation des matériaux carbonés par traitement HT du tanin, nous avons cherché à nous écarter de cette voie de synthèse de manière à jouer sur les caractéristiques finales du matériau, telles que son rendement de carbonisation, sa composition chimique et sa texture finale après à une carbonisation secondaire à  $900^\circ\text{C}$  sous atmosphère inerte.

Le milieu réactionnel a été modifié en explorant trois nouvelles voies de synthèse en condition HT: 1) un abaissement du pH du milieu réactionnel de manière à favoriser la réticulation du tanin par des réactions de polymérisation catalysées en milieu acide. Ceci conduit à un gel de carbone (monolithe) sans l'utilisation des agents de réticulation classiques et cancérigènes que sont les aldéhydes; 2) l'utilisation d'un hydrate de carbone à bas coût ajouté au milieu de synthèse: le saccharose. Lorsqu'il est associé au tanin, sa différence de cinétique de carbonisation en condition HT (à différents températures et en milieu acide) permet d'obtenir des microsphères de carbone; 3) l'addition de nitrate d'argent au milieu de synthèse de manière à accélérer la cinétique de nucléation et produire ainsi des nanoparticules de carbone avec une structure particulière (Fig. 5).

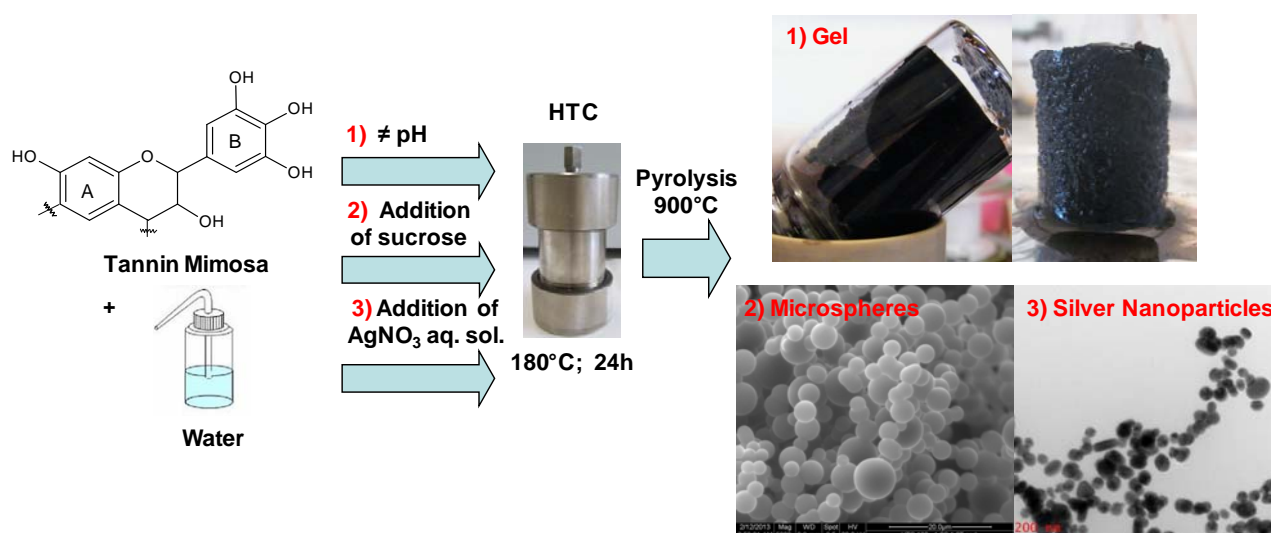


Fig. 5: Modifications appliquées dans le système tanin soumis à HTC.

Les principales conclusions sont les suivantes:

- 1) La réduction du pH, a augmenté le rendement de hydrochar mais réduit le rendement de carbone résultant finalement en un impact positive sur le rendement total. La réduction du pH produit aussi la diminution du diamètre des microsphères, qui pourrait être due à une nucléation promue à un pH inférieur (voir figure 6 a) et b)). Cependant, les matériaux carbonés produits à un faible pH ont des surfaces supérieures avec la même distribution de taille microporeuse. Le produit: rendement total en carbone x  $S_{BET}$  était beaucoup plus élevé pour les matériaux carbonés préparés par réduction du pH à 1, il a augmenté de  $220 \text{ m}^2 \text{ g}^{-1}$  (pH inchangé) à  $319 \text{ m}^2 \text{ g}^{-1}$ . En appliquant l'étape de traitement hydrothermal et en diminuant le pH à 1, la surface est passée de 476 (pour tanin carbonisé directement à  $900^\circ\text{C}$ ) à  $791 \text{ m}^2 \text{ g}^{-1}$  (tanin après HT et pyrolyse à  $900^\circ\text{C}$ ).
- 2) L'addition de sucre produit des microsphères de granulométrie inférieure à cause de l'augmentation de germes produits par hydrolyse du saccharose (voir figure 6 c) et d)). Le rendement de carbone augmente seulement au pH inchangé et reste constant à pH = 2 par rapport à tanin pur soumis à HT. L'addition de saccharose a également produit une légère augmentation de la surface BET. Après carbonisation, la chimie de surface de matériaux carbonés préparés à pH = 2 est semblable à celle de ces matériaux préparés à pH inchangé.

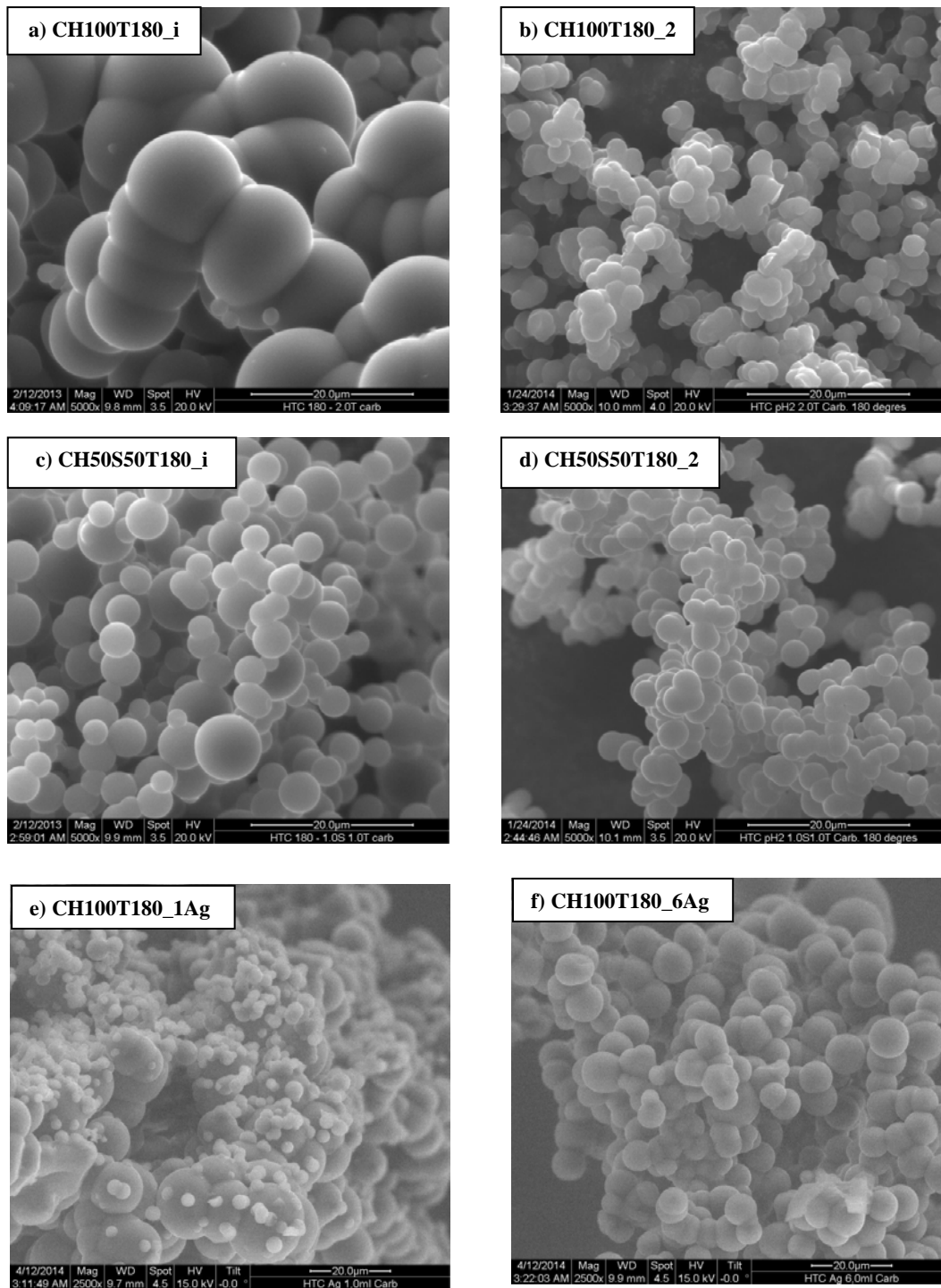


Fig. 6: Matériaux carbonés produits avec 100% tanin et 50% tanin / sucre préparé à pH inchangé (i) (a et c) et à pH 2 (b et d) respectivement; HTC de tanin avec 1 mL (e) et 6 mL (f) de solution de  $\text{AgNO}_3$  à  $180^\circ\text{C}$  et 24h (Tous carbonisés à  $900^\circ\text{C}$ ).

- 3) La présence de nitrate d'argent dans la solution aqueuse de tanin produit une réduction et une homogénéisation de la taille de particule des microsphères (voir figure 6 e) et f)). Avec l'augmentation de nitrate d'argent, le rendement à hydrochar augmente, mais

la surface diminue due à la présence de nanoparticules d'Ag bloquant la microporosité. De tels matériaux contenant des nanoparticules d'argent présentent de nombreuses applications potentielles dans la biochimie et également dans des capteurs électroniques.

#### **Chapitre 4: Synthèse de carbones dopés à l'azote et leur utilisation comme électrodes de supercondensateurs**

Dans ce chapitre, des matériaux carbonés dopés à l'azote ont été préparés par amination du tanin avant ou pendant le traitement HT. Ces matériaux possèdent de bonnes propriétés électriques et un comportement pseudo-capacitif important dans le domaine du stockage d'énergie électrochimique dans les supercondensateurs. Dans une première étape, nous avons cherché à comprendre la structure du tanin modifié par traitement à l'ammoniaque concentrée à température ambiante. Pour cela et pour simplifier l'étude, nous avons choisi la catéchine, unité structurale de base du tanin, qui a été traitée dans les mêmes conditions que le tanin avant d'être caractérisée par RMN du solide, Maldi-Tof et XPS. D'après la littérature, l'amination du tanin était supposée être régio-sélective et ne se produire que sur un seul site hydroxyle du cycle B. Nous avons pu montrer qu'en réalité, une multi-amination se produit dans des proportions significatives sur les groupements hydroxyles des cycles A et B de la structure flavonoïde (voir Fig. 1). Des réactions secondaires d'oligomérisation se produisent avec l'ouverture d'hétérocycles et la formation de ponts  $-N=$  entre les unités flavonoïdes.

Dans une deuxième étape et pour optimiser l'incorporation d'azote dans les carbones obtenus par traitement HT, deux voies HT ont été étudiées: i) amination du tanin par sa dissolution dans une solution d'ammoniaque concentrée et séchage à température ambiante avant traitement HT dans l'eau (voie EAT), ii) traitement HT du tanin directement en solution ammoniacale (voie AT). Pour la voie EAT, un gel a été obtenu sans l'utilisation d'agent de réticulation comme le formaldéhyde (voir Fig. 7).

Pour la voie AT, une poudre composée de microsphères a été formée. L'analyse XPS suggère qu'après traitement HT, la plupart de l'azote est sous forme d'amine avec une présence possible de groupement pyridiniques. Ces tanins hydrotraités présentent des surfaces relativement faibles et une quantité importante d'azote qui peut atteindre 14 % en masse par la voie AT.

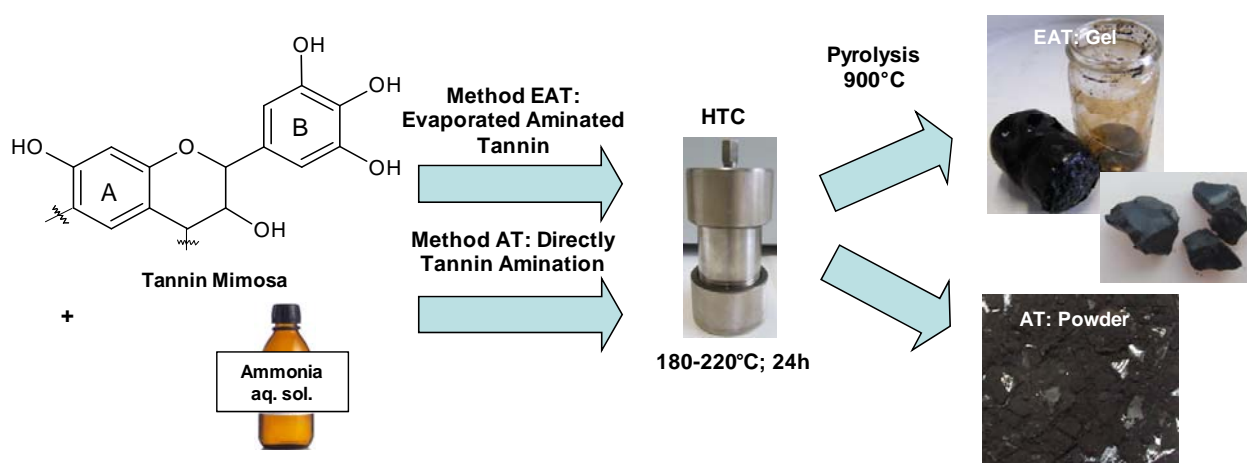


Fig. 7: Approche schématique pour la production des matériaux carbonés dopé à l'azote par deux méthodes: AT (tanin directement aminé) et EAT (tanin aminé à température ambiante pendant l'évaporation d'ammoniaque).

Ces composés intermédiaires ont ensuite été carbonisés à 900°C sous atmosphère inerte et leurs caractéristiques texturales et chimiques ont été analysées. Comme attendu, la quantité d'azote diminue avec la température de carbonisation et s'accompagne d'un développement significatif de la porosité. Ces carbones présentent des surfaces spécifiques modérées (442 – 684 m<sup>2</sup> g<sup>-1</sup>) et une quantité d'azote comprise entre 0.7 to 8.0 % en masse; cette dernière valeur est importante pour une température de carbonisation aussi élevée. D'après nos connaissances, il n'existe pas d'autres carbones dopés à l'azote issus de précurseurs naturels modifiés par de l'azote qui présentent une quantité d'azote aussi importante ainsi qu'une surface spécifique aussi élevée pour des températures de carbonisation aussi élevée. Ces résultats sont donc tout à fait intéressants. Nous avons donc réussi à développer un procédé bon marché, respectueux de l'environnement et qui permet de préparer des carbones dopés à l'azote avec des propriétés remarquables et des applications potentielles dans le domaine de la purification de l'eau ou la production/stockage d'énergie par voie électrochimique.

Ces carbones ont donc été testés comme matériau d'électrode de supercondensateur dans un système à trois électrodes (Fig. 8). Des capacitances spécifiques élevées ont été obtenues (320 F g<sup>-1</sup> (solvant : eau)) avec des capacitances normalisées de 58 μF cm<sup>-2</sup> (à 2 mV s<sup>-1</sup>). Elles figurent parmi les valeurs les plus élevées jamais reportées pour des matériaux carbonés avec des valeurs du même ordre que celles des meilleurs carbones activés. Ces bonnes propriétés électrochimiques ont été attribuées à: 1) la surface spécifique élevée associé à la présence de



micropores; 2) l'existence de mésopores dans le domaine 3-13 nm qui améliorent les performances aux vitesses de variation de potentiel élevées; et 3) l'association bénéfique de l'oxygène et de l'azote avec des compositions optimales de respectivement 10 - 16 % et 3 - 6 % massiques.

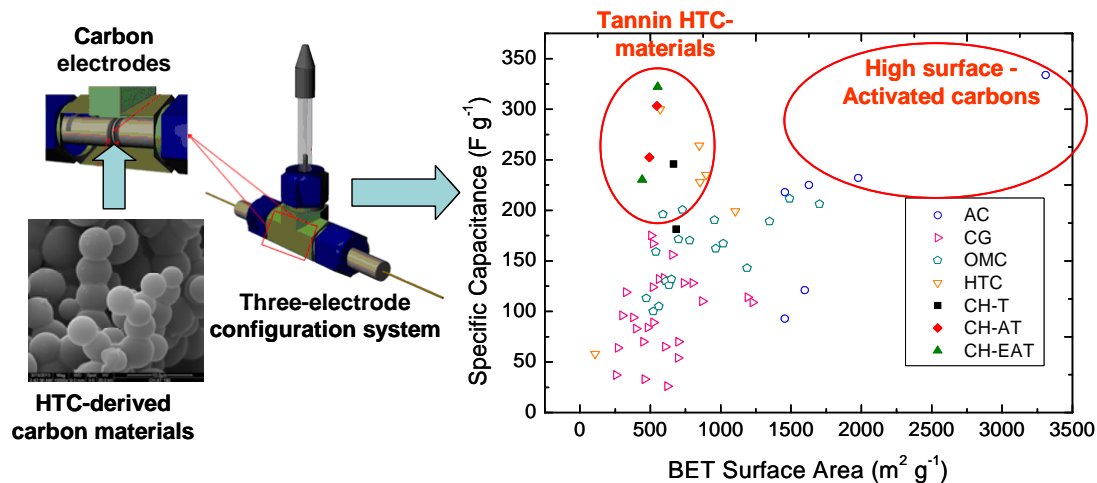


Fig. 8: Configuration à trois électrodes en utilisant une cellule en Téflon Swagelok<sup>®</sup>. A droite, la capacité de nos matériaux est comparable à celles de charbons actifs avec une haute surface.

## Chapitre 5: Synthèse des gels de carbone dopés à l'azote et leur utilisation comme électrodes de supercondensateurs

Comme nous l'avons vu dans le chapitre 4, les tanins aminés soumis à un traitement HT conduisent à des hydrogels carbonés dopés à l'azote en l'absence d'agents réticulants (voie EAT). Ici, nous avons utilisé cette particularité pour préparer des gels qui ont été séchés dans différentes conditions de manière à moduler, les caractéristiques texturales des carbones finaux carbonisés à 900°C, leurs teneurs en azote et leurs performances comme matériaux d'électrode de supercondensateur.

Par la voie EAT nous avons préparé différents types de gels avec des quantités variables de tanin modifiés qui ont été séchés selon les procédés décrits ci-dessous. Trois procédés de séchage des gels ont été utilisés: 1) séchage en conditions subcritiques avec un retrait important du gel; 2) séchage supercritique après échange du solvant par le CO<sub>2</sub>; et 3) lyophilisation après échange du solvant par le ter-butanol. Les deux derniers procédés conduisent à un retrait limité du gel sec du fait de l'absence d'interface liquide/vapeur et des forces capillaires associées qui s'exercent sur le réseau solide du gel pendant le séchage. Les

gels secs obtenus sont respectivement appelés xérogels, aérogels et cryogels (voir le graphique en Fig. 9). Les trois types de gels secs sont homogènes à l'œil et ils présentent des fissurations. Le plus dense est le xérogel, les deux autres ayant des densités comparables. Du fait de la formation de cristaux durant la lyophilisation, le cryogel a des pores plus gros et plus largement distribués en taille. A l'échelle microscopique, tous les gels secs sont constitués de la même structure nodulaire.

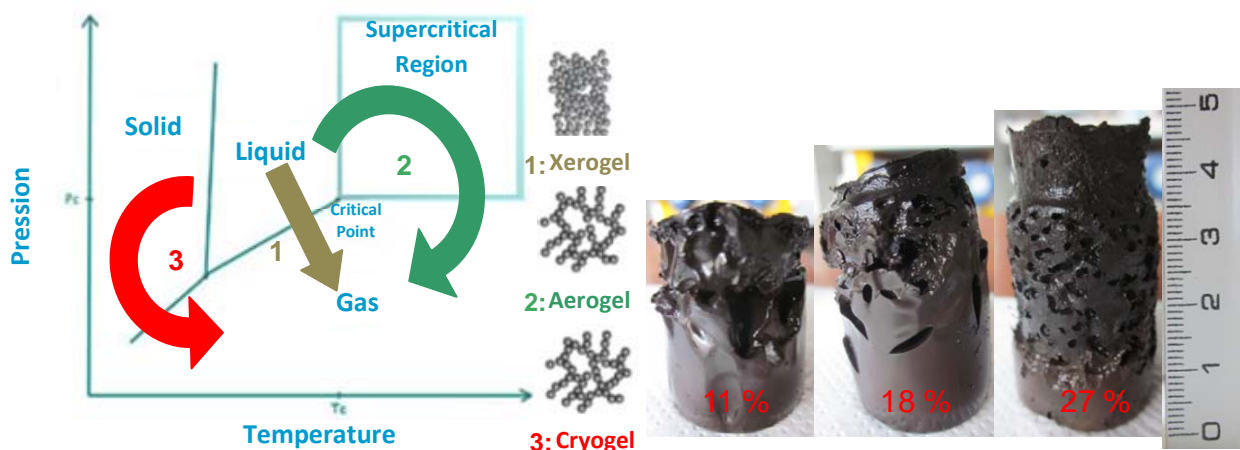


Fig. 9: Représentation des trois types de séchage de gel utilisées dans ce travail (à gauche): évaporation, supercritique et lyophilisation. A droite, les gels faits à 11, 18 et 27% de la concentration initiale d'EAT après HT à 180°C.

Ces gels secs ont été carbonisés à 900°C et caractérisés par analyse élémentaire, physisorption d'azote à -196°C avant d'être évalué comme matériau d'électrode pour supercondensateur. La quantité d'azote varie de 1.9 à 3.0 % en masse et les surfaces spécifiques sont respectivement de 860, 754 and 585  $\text{m}^2\text{g}^{-1}$  pour les carbones issus des aérogels (CA), des cryogels (CC) et des xérogels (CX), respectivement. Ils présentent tous des micropores associés à des mésopores de taille et quantité variables selon le mode de séchage et la concentration initiale en EAT dans le gel. Il apparait que la stabilité de l'azote dans la structure carbonée diminue avec la surface spécifique du matériau carboné.

Ces gels de carbone ont été testés dans des électrodes de supercondensateur. Ils présentent des capacités spécifiques et normalisées exceptionnelles de 409.5  $\text{F.g}^{-1}$  et 72.3  $\mu\text{F.cm}^{-2}$  (vitesse de balayage 2  $\text{mV s}^{-1}$  dans 4  $\text{mol L}^{-1}$   $\text{H}_2\text{SO}_4$ ) respectivement qui sont parmi les plus élevées jamais reportées parmi les carbones activés. Ces performances excellentes ont été attribuées aux trois paramètres décrits dans le chapitre précédent.

## Chapitre 6: Synthèse des atomes de carbone mésoporeux en utilisant un tensio-actif

Comme nous l'avons vu dans les chapitres précédents, la mésostructuration est un paramètre important à contrôler pour optimiser les performances des matériaux dans des applications spécifiques. De ce fait, nous nous sommes intéressés à la préparation d'un carbone poreux présentant des mésopores parfaitement définies en taille et dans leur organisation. Pour cela, nous avons associé le tanin (précurseur de carbone) à un tensio-actif structurant de la porosité (le copolymère triblocs Pluronic F127). Ce dernier présente la particularité de former des phases de type cristal liquide et d'interagir fortement avec les composés phénoliques *via* des liaisons hydrogène. L'utilisation d'un tel structurant a permis d'obtenir des matériaux carbonés avec des mésopores ordonnées, ce qui n'est pas réalisable par les procédés conventionnels de carbonisation de la biomasse.

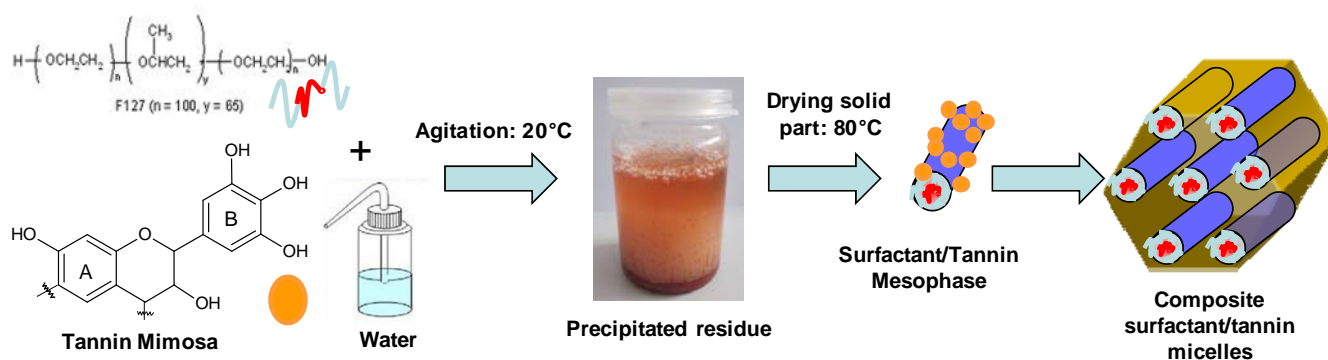


Fig. 10: Approche schématique pour la production de carbones mésoporeux ordonnés (d'après Schlienger et al. 2012<sup>5</sup>).

Ces matériaux ont de nombreuses applications potentielles dans les domaines comme la catalyse, l'électrochimie, les capteurs, les isolants thermiques et dans la libération contrôlée de biomolécules. Pour la préparation de telles structures, nous avons choisi le procédé le plus "vert" possible en évitant l'emploi d'agent de réticulation toxique comme le formaldéhyde, en diminuant le coût énergétique en travaillant sous simple agitation mécanique à température et pression ambiante, et en l'absence de solvant organique. En mélangeant la solution aqueuse de F127 à celle du tanin (Fig. 10), au pH approprié, une séparation de phase se produit instantanément avec la formation d'une phase solide. Cette dernière est ensuite isolée, séchée et carbonisée à 400°C (libération de la porosité par pyrolyse du tensio-actif) et 900°C.

<sup>5</sup> Schlienger S, Graff AL, Celzard A, Parmentier J. Direct synthesis of ordered mesoporous polymer and carbon materials by a biosourced precursor. *Green Chem* 2012;14:313-316.

Les matériaux carbonés obtenus par ce procédé très économique présentent des micropores ainsi que des mésopores ayant une organisation de type nid d'abeilles. La surface spécifique est élevée, jusqu'à  $700 \text{ m}^2 \text{ g}^{-1}$ , malgré l'absence de traitement d'activation du carbone. Les photos MET montrent leur organisation entre leur pores (Fig. 11).

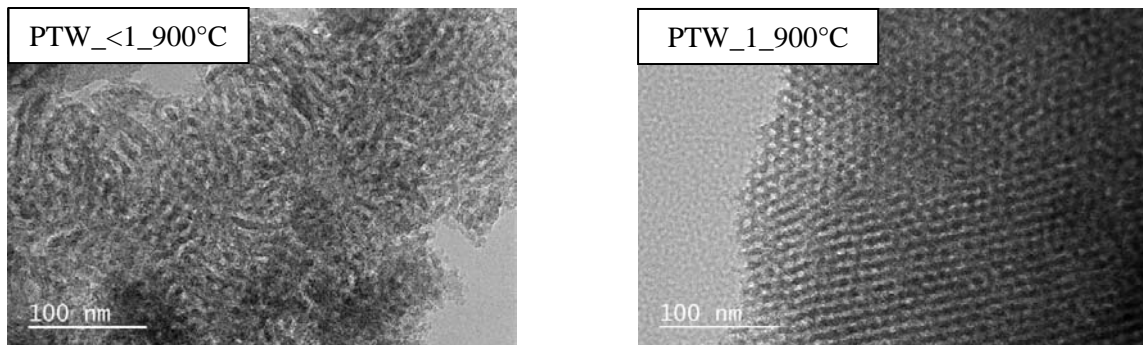


Fig. 11: Photos MET des carbones mésoporeux ordonnés préparés à partir de tanin soumis à HTC à pH très acide ( $< 1$  ; gauche) et 1 (droite) et pyrolyse postérieure à  $900^\circ\text{C}$ .

Une conclusion et la liste des références bibliographiques viennent enfin clore le mémoire. La description des équipements et des techniques d'analyse utilisées sont données en annexe. Les résultats présentés dans ce mémoire sont donc tout à la fois nombreux et originaux, et d'intérêt pour la communauté des matériaux carbonés, de l'adsorption, et en particulier de l'électrochimie. Ils ont déjà donné lieu à six articles publiés dans des revues scientifiques à haut facteur d'impact : Carbon (IF : 6.6), Bioresource Technology (IF : 5.6) et Industrial Crops and Products (3.6). Deux autres manuscrits sont actuellement soumis et sont en cours d'évaluation, et trois autres encore sont en préparation.



## Introduction

Renewable resources are foreseen as sustainable, and sometimes cheaper, alternatives to substitute raw materials of petrochemical origin. The challenge is to have products with the same or better characteristics than those prepared from non-renewable resources, which are commercialised and applied in our daily life. In this study, we used tannin coming from the barks of *Acacia mearsii* tree or Mimosa, as it is called. Tannin is a quite attractive precursor to synthesize new organic porous materials due to the presence of highly reactive phenolic molecules. These organic materials, after carbonization, are converted into porous carbon materials with a broad range of important applications. The synthesis of these new carbon materials comprises a two step process. The first step is a hydrothermal carbonization (HTC) at moderate temperatures, 180-200°C, which allows carbon enrichment as well as fixing heteroatoms and produces different morphologies: i.e. microspheres, gels. The second step is a carbonization at higher temperature, i.e. 900°C, which allows increasing surface area and porosity as well as improving conductivity.

Porous carbon materials are applied in very different fields because of their varied physico-chemical properties such as high adsorption capacity, high thermal and chemical stability, good electrical and thermal conductivity and low density. For this reason, they are widely used in catalysis, separation and gas storage, water and air depollution or as electrodes for lithium batteries or supercapacitors. There are several methods to produce carbon materials depending on the application and also on the cost of the final product. On the one hand, activated carbons are easily prepared in large scale and at low cost to be applied especially in wastewater treatment and water purification. On the other hand, mesoporous carbons are costly to be produced but they have a great potential as electrodes or in biosciences for cellular or drug delivery.

The main objective of this PhD work is, to get an insight on the production of porous carbon materials using more economically viable and eco-friendly precursors and methods, to characterize these carbon materials and to evaluate their potential applications. It is divided into six chapters as follows:

The **Chapter 1** reviews the state of the art on biomass conversion, especially tannin. The methods to produce carbon materials and their textural properties are presented with an overview of the HTC technique and the potential applications of HTC derived carbons.

The **Chapter 2** illustrates the mechanism of the hydrochars formation from tannin together with its kinetics. The main purpose was to study the morphology and composition of hydrochars at different temperatures, reaction times or initial tannin concentrations.

The **Chapter 3** shows the effect of pH, addition of sucrose or silver nitrate aqueous solution on the HTC process. Changes on the carbon yield, chemical and textural properties of the final carbon materials are pointed out.

The **Chapter 4** examines the possibility to synthesise N-doped carbon materials (NCM's) by HTC and pyrolysis at 900°C. Different materials and structures were obtained depending on the amination method. Their morphology, chemical structure and textural properties are illustrated. NCM's were also tested as carbon electrodes for supercapacitors showing great results.

The **Chapter 5** is centred on the synthesis of carbon gels, aero-, cryo- and carbon xerogels and their use also in electrochemistry is presented. Such kinds of materials containing nitrogen connected into the carbon structure are promising materials in a large variety of electronic applications such as supercapacitors.

Finally, **Chapter 6** presents the synthesis of mesoporous carbons by using a soft template. This procedure was chosen to be the greenest as possible, without any presence of toxic and expensive reactants such as formaldehyde and also by an attempt to eliminate any organic solvent.

Conclusions and perspectives of the whole work are also presented at the end.

# **Chapter 1: State of the art**





The intense use of fossil fuels to produce energy and a wide range of materials will come to inevitable exhaustion in the near future. According to recent information, the world oil production will still increase from the actual value of 84 million barrels a day to 116 million a day in 2030 to start diminishing afterwards [Cherubini 2010]. This trend is also confirmed by several major oil companies [O'Connor 2013]. Fossil fuels also produce a negative effect on the planet, especially in very industrialized areas, due to CO<sub>2</sub> emissions that has been directly related to global warming. It has been confirmed the world percentage of CO<sub>2</sub> of 400 parts per million (ppm) - amount considerably enough to increase a warming of 2°C in the atmosphere [REN 21 2013a]. Many countries have agreed in reducing CO<sub>2</sub> emissions and so research on potential renewable resources to produce fuels and materials has enormously risen. An energy source can be considered renewable if it regenerates naturally or if it regenerates at the same rate as it is consumed. Fossil fuels are obviously not renewable; wind and solar energy are completely renewable; and biomass and geothermal are partially renewable as the condition of reasonable exploitation [Tiwari and Mishra 2011]. Nowadays, it is estimated that about 17-18% of world energy comes from renewables: 9% from "traditional biomass" and 8% from "modern renewables" including wind and solar energy [REN 21 2013b]. Therefore, more than 80% of the energy supplied in the world is still based on fossil fuels.

Petrochemicals have been used to manufacture thousands of products such as petrol, paraffin, kerosene, diesel oil, etc applied in today's life over 150 years. They are derived from ethane, propane, butane and other hydrocarbons extracted from crude oil and natural gas liquids. Hydrocarbons chemical bonds are broken down into simpler molecules and separated through the process of cracking through high temperatures. The first use was invented by Robert Chesebrough (1872), a chemist that used a balm from an oil well to produce vaseline [Chesebrough 1872]. Afterwards, it was seen the introduction of carbon black into rubber during tyre production by the B.F. Goodrich Company in 1910 for obtaining longer life tyres [Donnet 1993]. Combustible is another by-product of fossil fuels with enormous applications in motor vehicles. The petrochemical industry supports millions of jobs however the emission of greenhouse gases during this procedure is very high and most of these chemical materials synthesized are possibly carcinogenic to humans [Höök and Tang 2013]. Therefore, renewable alternatives to obtain similar materials having the same characteristics are a subject of intense research nowadays.

## 1.1 Biomass as raw material for fuel and chemicals

Biomass refers to wood and agricultural residues, energy crops and other kind of waste such as solid municipal waste, landfill, sewage gas and farming waste. In terms of energy, woody biomass presented 9% of world primary energy consumption and 65% of world renewable primary energy consumption in 2010. For 2050, it has been foreseen that if all the resources (including unproductive land) were used for energy production, they could cover 10–40% of the world's primary energy consumption [Lauri et al. 2013]. The most important processes to valorise biomass are: gasification, liquefaction, saccharification, defibration, combustion and carbonization. They are illustrated in Fig. 1 [Deglise and Donnot 2004; US DOE 2004].

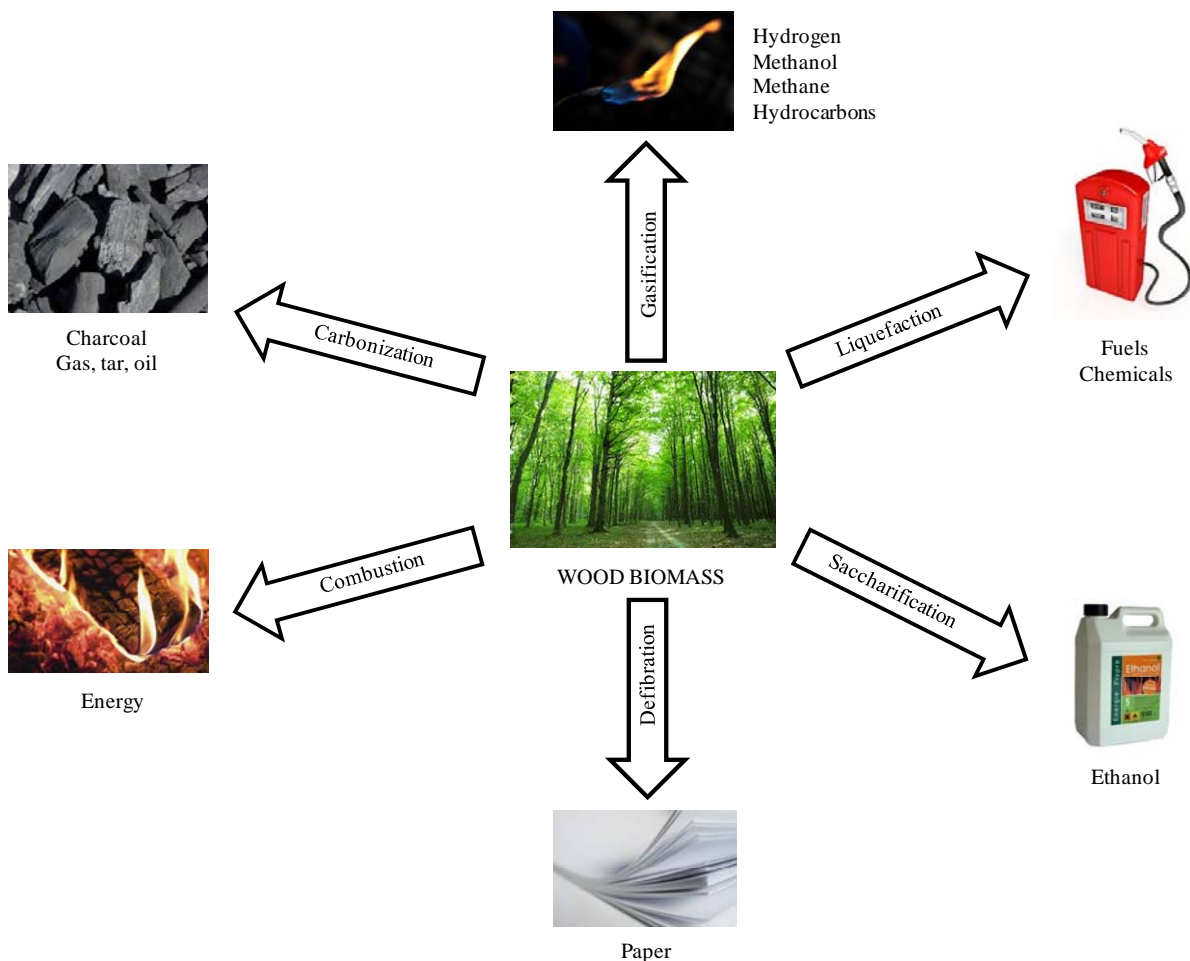


Fig. 1: Scheme of possible applications for wood biomass [Balat et al. 2009].

- *Gasification* involves conversion of organic carbonaceous materials into gases, methanol and hydrocarbons at controlled oxygen source and high temperature. Hydrogen and methanol can be also fabricated and used to produce ammonia and formaldehyde;

- *Liquefaction* decomposes biomass into small molecules quite reactive and unstable. The reaction takes place in water or in a solvent and the products are raw materials for fuel and chemicals;
- *Saccharification* is a biochemical process in which lignocellulosic materials are transformed into ethanol, which can be used as biocombustible;
- *Defibration* allows obtaining fibres for the paper manufacture;
- *Combustion* is the reaction of biomass with oxygen to produce energy as well as carbon dioxide and water;
- *Carbonization* is the thermal decomposition of organic carbonaceous materials (e.g. wood) in the absence of oxygen for carbon production.

The main and most well-known biomass, having a large range of applications, is wood. Basically, plants derivatives are divided into five groups: carbohydrates, such as cellulose (38-50%) and hemicellulose (23-32%), lignins (15-25%), tannins, unsaturated oils and proteins [Cotê 1968], the three later accounting for extractives (~5%). Some of these derivatives are already used in industry but some others remain unused because research and optimization are still needed although they have a great potential. Dry wood chemical composition varies according to the species but a typical composition is: 52.0% of carbon, 40.5% of oxygen, 6.3% of hydrogen and 0.4% of nitrogen. In average, ashes represent 0.8% in mass [Demirbaş 2001].

The main components of the tree: wood, bark and foliage together with the possible extractives depending on the methods used for extraction are shown in Fig. 2. Leaves are used for the production of leaf protein by mechanical extraction, essential oils by distillation, chlorophylls and carotenoids by solvent extraction or animal fodder by drying. Barks are referred to all tissues external and they can be divided in two parts: inner bark and outer bark. The inner part is closer to wood and it is also called as active bark; the outer is the dead part and it is also called the external part. Although the chemical composition of both parts is quite different, their separation is expensive so they are commonly processed together [Feng et al. 2013].

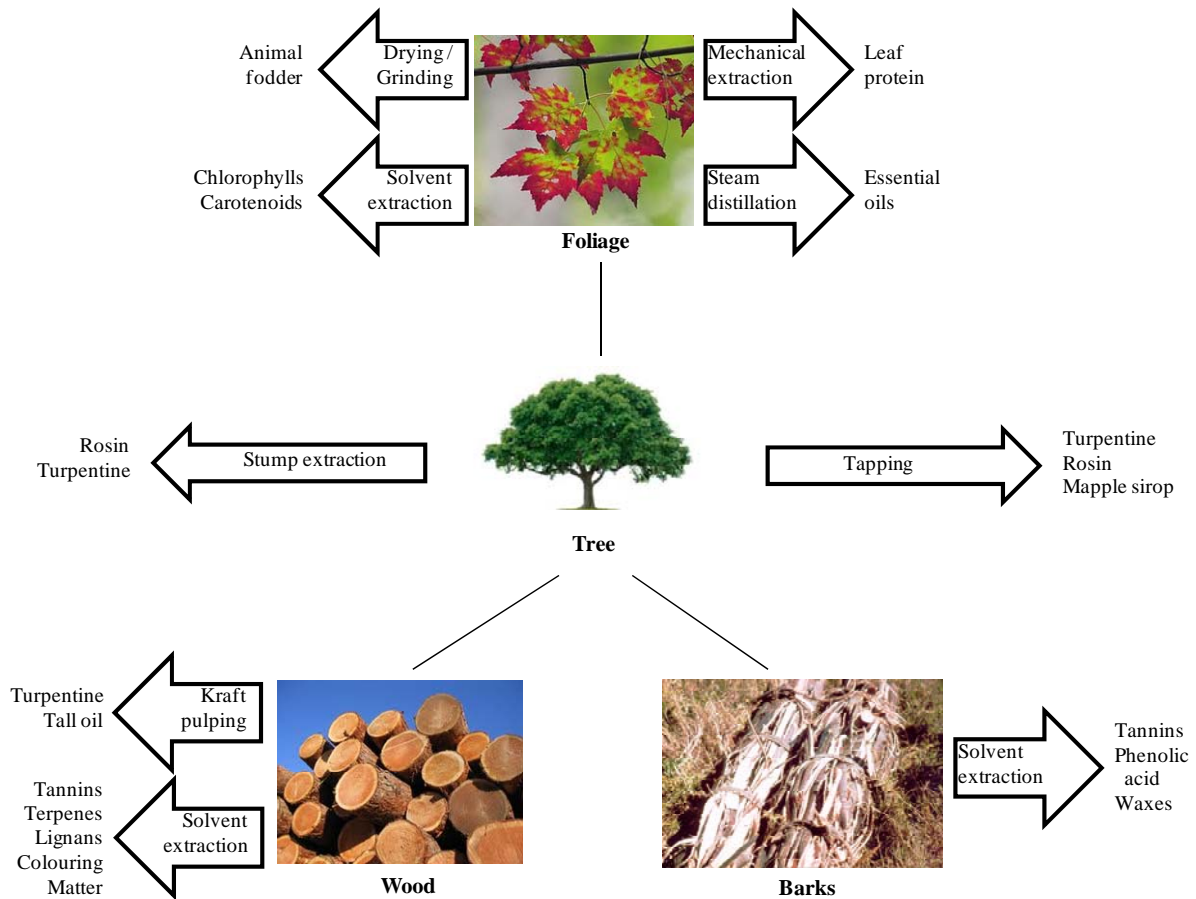


Fig. 2: The main extractives obtained from trees [Patten et al. 2010].

What to do with barks is a major question facing the wood conversion industries. Great utilization of bark residues demands comprehension of their complexity, mostly their chemical and physical properties from different wood species. Fig. 3 shows a range of fields in which barks can be used [Pizzi 2008; Feng et al. 2013]. They can be incinerated or kept in a landfill as waste material; they can be used in horticulture as mulching, mostly in gardens and barks can be also burnt to generate energy. However, the caloric value of burning barks is lower than fossil fuels and, the high level of ash content can damage combustors. Valorisation of barks is still a challenge mostly because of its heterogeneous structure, varied chemical composition, low resistance and dark colour [Feng et al. 2013]. However, barks contain a large amount of phenolic polymers including tannins, which are reactive materials used to produce adhesives, foams or bioresourced carbon materials, among others.

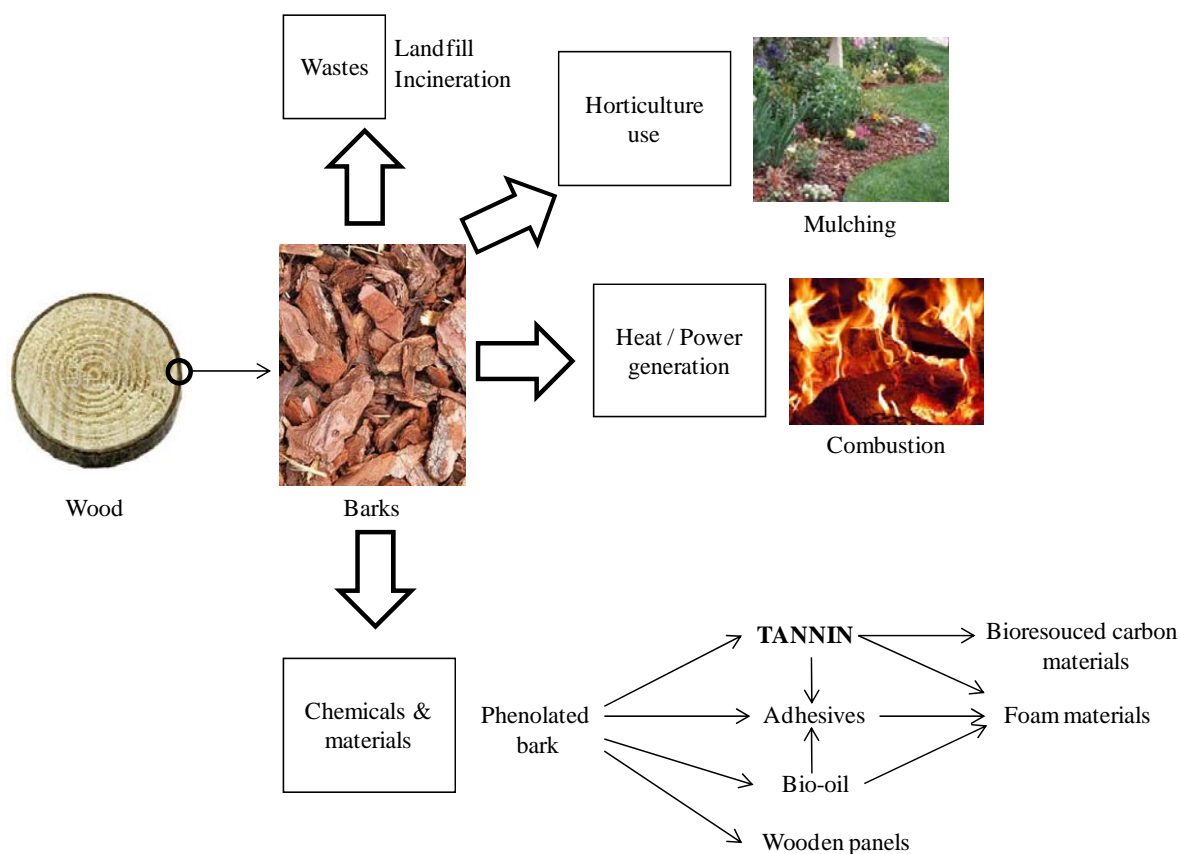


Fig. 3: Scheme of extraction of tannins from Acacia in the barks [Feng et al. 2013].

## 1.2 Tannins

### 1.2.1 Tannins structure and reactivity

Tannins are natural materials present in several types of plants but mostly present in dicotyledons ones [Barbehenn and Constabel 2011]. Tannin is distributed in different parts of the tree such as: in the roots, trunk, barks, seeds, fruits and leaves at diverse concentrations [Feng et al. 2013]. It is also essential for the plant physiology and development as it contributes to nitrogen fixation and attracts pollinating insects [Sagan et al.1995; Debeaujon et al. 2003]. Tannins were classified depending on their chemical structures by Freudenberg in 1920 [Gross 1999] and divided in four major groups: gallotannins, ellagitannins, complex tannins and condensed tannins [Khanbabaee and Ree 2001].

Gallotannins are all tannins in which galloyl units are connected to diverse polyol-, catechin-, or triterpenoid units. They can be also classified as hydrolysable tannins which have been used as partial substitutes of phenol in the preparation of phenol-formaldehyde resins but the lack of macromolecular structure and the low level of phenol substitution limit their commercialization and economical potential [Pizzi 1983]. Because of its low reactivity,

similar to simple phenols of low reactivity, and also limited production, hydrolysable tannins are less used than the condensed ones.

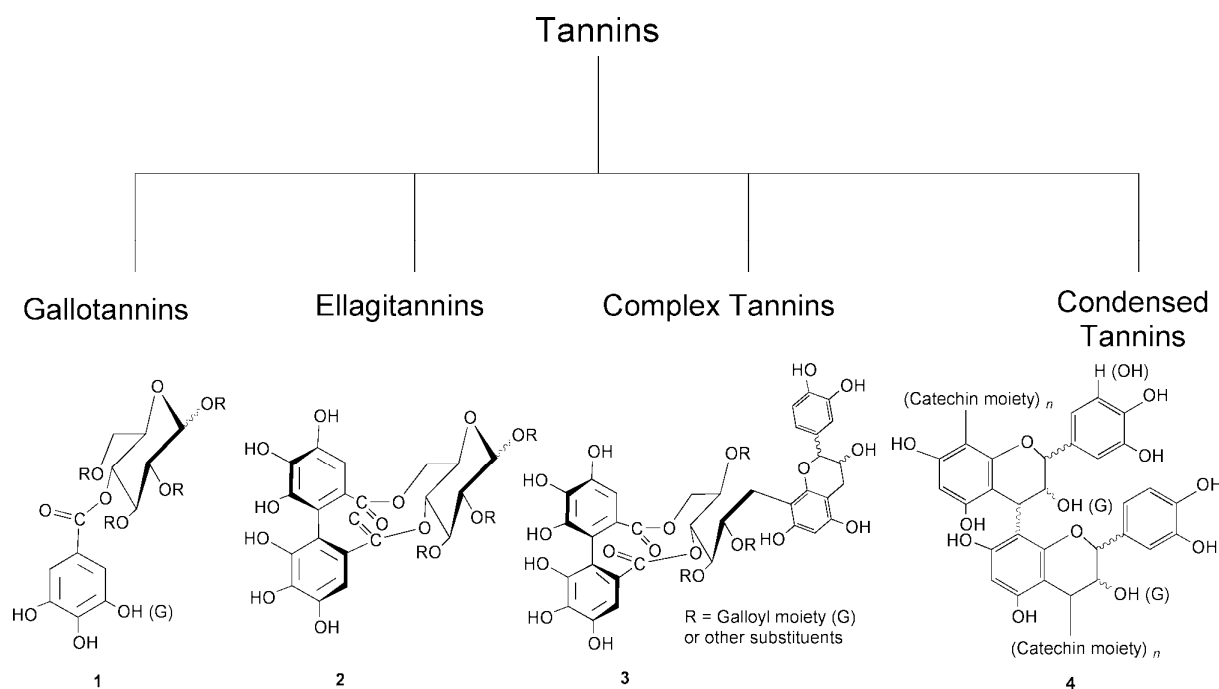


Fig. 4: Classification of tannins [Khanbabaee and Ree 2001].

Ellagitannins are those tannins in which at least two galloyl units are C–C coupled to each other, and do not contain a glycosidically linked to catechin unit. Complex tannins are tannins in which a catechin unit is connected glycosidically to a gallotannin or an ellagitannin unit and finally, condensed tannins are all oligomeric and polymeric proanthocyanidins formed by linkage of C<sub>4</sub> of one catechin with C<sub>8</sub> or C<sub>6</sub> of the next monomeric catechin (Fig. 5) [Khanbabaee and Ree 2001]. The main structure of condensed tannin - the flavonoid molecule is numbered to distinguish the carbon positions and the three rings referred as A, B for phenolic ring and C for pyrane ring are shown in Fig. 5. Flavonoids are classified according to their chemical structure and they are named as: flavonols, flavones, flavanones, catechins (or flavanols), anthocyanidins, isoflavones, dihydroflavonols and chalcones [Aron and Kennedy 2007].

There are four types of polyflavonoids composing condensed tannins: a) prorobinetinidin, b) prodelfphinidin, c) profisetinidin, and d) procyanidin as shown in Fig. 6. Procyanidin is the most reactive polyflavonoid. The reactivity of tannins is an important characteristic to take into account because it is directly connected to their potential applications. Condensed flavonoid tannins are divided into two classes according to their reactivity towards an aldehyde used as a crosslinking agent: the most and the least reactive. Usually the method

consists in measuring the gelling time, or time to reach high viscosity, as a function of pH once the formaldehyde has been added. Another technique used to measure the reactivity of those final materials is by Nuclear Magnetic Resonance (NMR), which will be described in Annex 1. This technique is useful to identify all the numbered carbons present in phloroglucinol or resorcinol A-rings and catechol or pyrogallol B-rings of the tannin. The free sites at C<sub>6</sub> and/or C<sub>8</sub> on the A-ring react with formaldehyde due to their strong nucleophilicity and their characteristic shifts can be determined by NMR. If their characteristic shifts show peaks of lower intensity, as in the case of Mimosa tannin, this indicates that such tannin is in the least reactive group [Pizzi 1994].

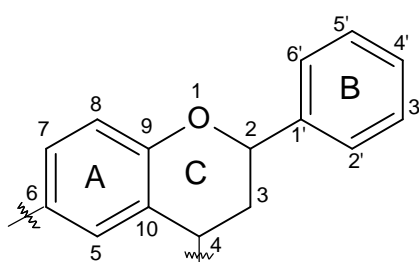


Fig. 5: Flavan structure - the main model molecule present in tannins [Aron and Kennedy 2007].

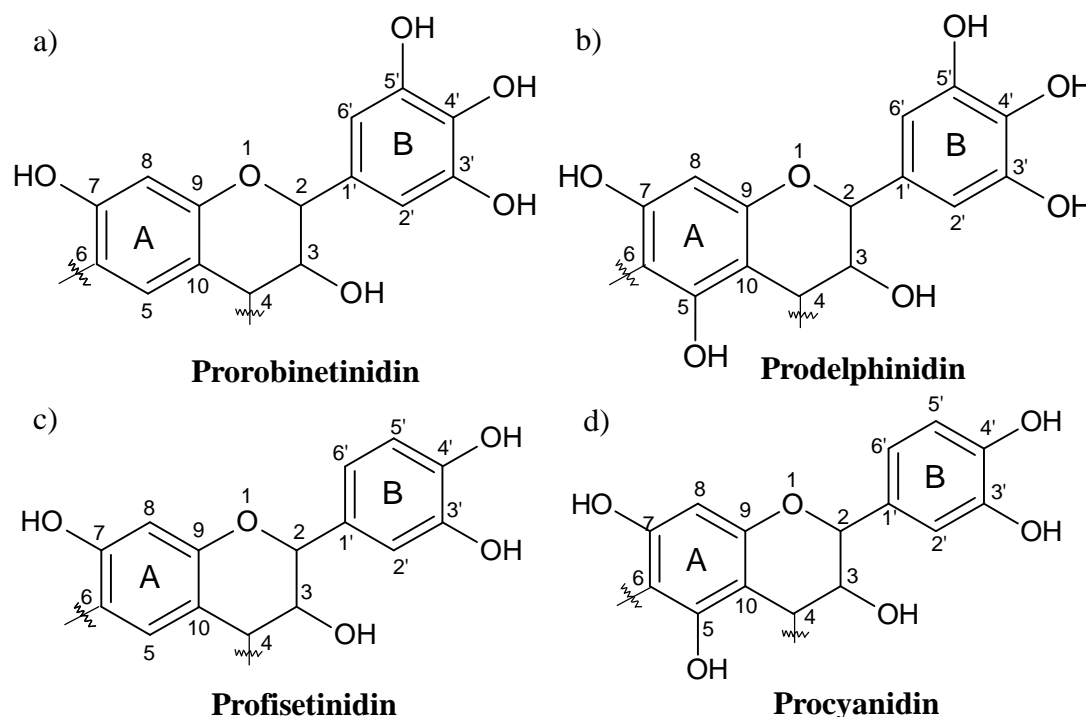


Fig. 6: The four main polyflavonoids present in condensed tannins: a) prorobinetinidin; b) prodelphinidin; c) profisetinidin and d) procyanidin [Pizzi 2008].



The interflavonoid linkage can be either C<sub>4</sub>-C<sub>8</sub> or C<sub>4</sub>-C<sub>6</sub>. In the case of fisetinidin (resorcinol A-ring, catechol B-ring) and robinetinidin (resorcinol A-ring, pyrogallol B-ring) the linkage is primarily C<sub>4</sub>-C<sub>6</sub>. In the case of catechin and cyanidin (phloroglucinol A-ring, catechol B-ring) and delphinidin (phloroglucinol A-ring, pyrogallol B-ring) the linkage is mostly C<sub>4</sub>-C<sub>8</sub>. In this work, we used Mimosa tannin (*Acacia mearnsii* formerly *mollissima*, De wildt), which is a mixture of 70% of prorobinetinidin (having a total of five hydroxyl groups) and 25% of prorofisetinidin and is generally composed of two up to ten monomers flavonoid units to produce tannin of a number-average degree of polymerization of 4-5 [Pizzi 2008]. The frequency of some molecules present in flavonoid structure can also define the reactivity of tannin. Therefore, Mimosa tannin extract presents a lower degree of polymerisation comparing to other types of tannin. For Mimosa tannin barks, the reactivity of the flavonoid A-rings is comparable, although slightly lower, to that of resorcinol. Tannins can be hardened by reaction with formaldehyde or by induced autocondensation. Fig. 7 shows the main flavonoid present in Mimosa tannin, being robinetinidin, and its autocondensation reaction. The C<sub>4</sub> and C<sub>6</sub> sites are involved in the interflavonoid linkage during the conventional polymerization reaction of Mimosa tannin, as discussed beforehand.

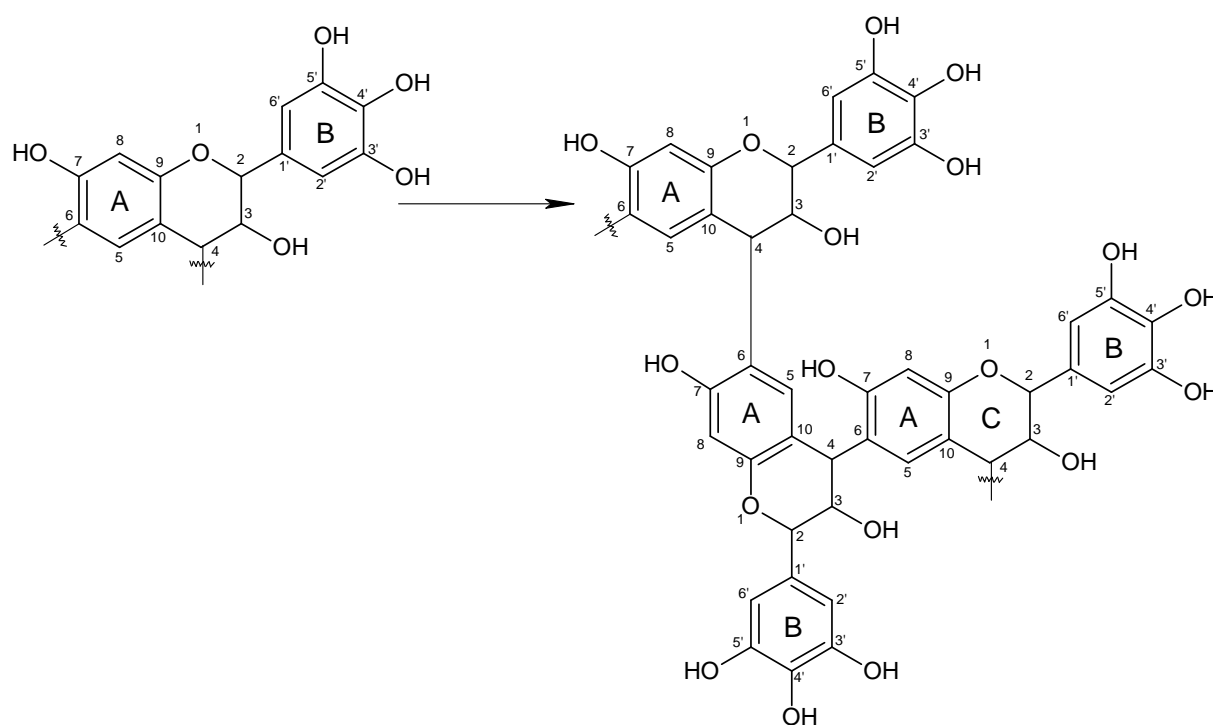


Fig. 7: Autocondensation reaction of Mimosa tannin [Pizzi 1994].

### 1.2.2 Tannin extraction and economic aspects

Mimosa tannin is extracted from the barks of *Acacia mearnsii* trees, which are grown mainly in Brazil and Africa (South Africa and Tanzania). In this work, tannin was extracted in

Tanzania and the extraction procedure is showed in Fig. 8. The process starts with the plantation of the Acacia trees that grow up first before being ready for cutting down [Molan et al. 2009]. After cutting down, barks are separated from wood and they are cut into smaller pieces for tanning extraction. In parallel, wood is used for pellets manufacturing and energy production. Tannin extraction/stripping takes place in autoclaves in series, with hot water, at around 70°C, having a very small percentage of sodium bisulphite. The late additive reduces tannin autocondensation and improves tannin solubility [Sealy-Fisher and Pizzi 1992]. After stripping, the solution contains 50% of extractives that are concentrated by spray-drying. The light-brown powder obtained generally contains 80 – 82% of polyphenolic flavonoid materials, 4 – 6% of water, 1% of amino and imino acids, the remainder being monomeric and oligomeric carbohydrates, in general broken pieces of hemicelluloses. The polyphenolic molecules have low molecular weight ranging from 500 to 3500 g mol<sup>-1</sup> [Pizzi 1983]. The older is the bark, the darker is the colour of tannin. Its colour also changes because of the facility of hydroxyl groups present in tannin oxidize to form quinones [Feng et al. 2013].

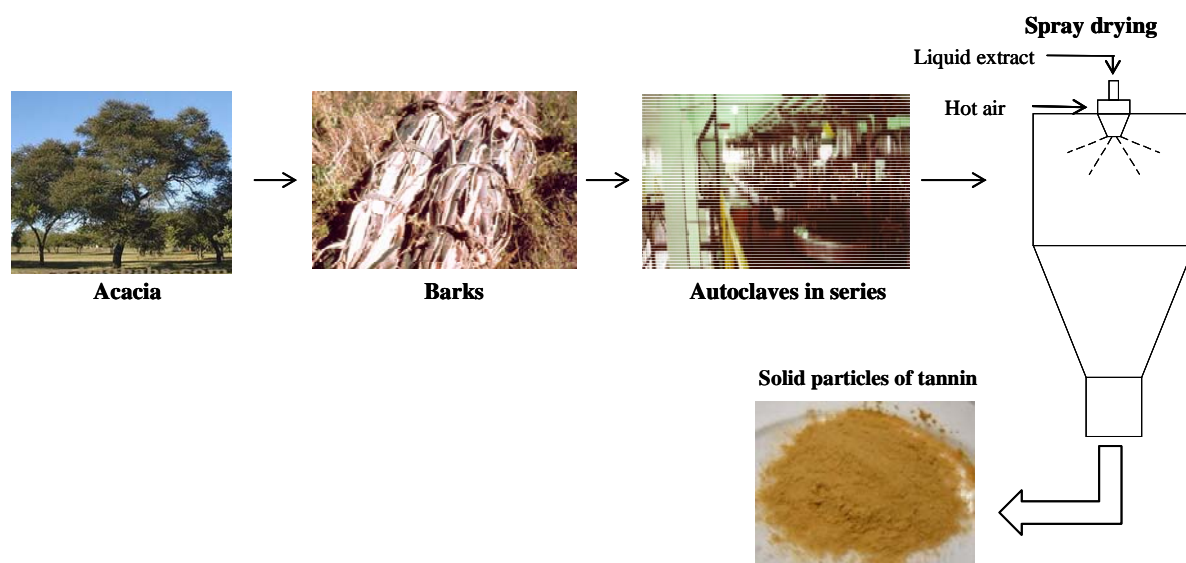


Fig. 8: Scheme of extraction of tannins from Acacia barks [Pizzi 1994].

Table 1 gathers some information on three different types of condensed tannins from Mimosa (*Acacia mearnsii*), Quebracho (*Schinopsis balansae* and *lorentzii*) and Maritime pine (*Pinus pinaster*). Maritime pine tannin is more reactive than Quebracho and Mimosa tannins, these latter presenting similar reactivities. The condensed tannins are the most abundant and represent more than 90% of the world production [Stokke et al. 2014]. Other condensed tannins are those extracted from chestnut, tara or galls which represent together 27 300 tons/year\*. The production of Mimosa tannin is of 60 000 tons/year and its price is

remarkably low, estimated from 1500 to 2300 €/ton (1.5 to 2.3 €/kg). Maritime pine tannin from France has a much higher price, 29 000 €/ton, and it is not yet commercially available. Therefore, we used Mimosa tannin as materials precursor due to its availability in the market and low price.

Table 1: Summary of the main characteristics of Mimosa, Quebracho and Maritime pine tannins.

<b>Tannins</b>	<b>Species of dominant flavonoid</b>	<b>Reactivity</b>	<b>Annual Production (tons/year)</b>	<b>Price (€/ton)</b>
Mimosa	Prorobinetinidine	low	60 000*	1 500 à 2 300€/ton*
Quebracho	Profisetinidine	low	60 000*	1 500€/ton*
Maritime Pine	Procyanidine	high	300*	29 000€/ton**

\* Indicative figures of tannin's market today provided by Silva Team (2014)

\*\* Value obtained by DRT Company (2013)

Tannins were extracted and commercialised for being applied in leather tanning industry for long time. However, after the end of the Second World War, their commercialisation declined with the emergence of synthetic phenolic materials. Several scientific showed other possible uses of tannins due to the fact that these materials are quite reactive and have a great economical potential. The commercialisation of condensed tannin-formaldehyde adhesives started in 1970. These adhesives were successfully applied together with wood for producing particleboard, plywood, glulam (horizontal wood pieces glued together), among others to fabricate furniture and buildings [Pizzi 1983]. Apart from the classical application of tannin as leather conditioner [Sreeram and Ramasami 2003] other minor application coexist as: wine additives [Harbertson et al. 2012], dying agents [Sánchez-Martín et al. 2010], pollutant adsorbents [Chow 1972; Vazquez et al. 2007; Dalahmeh et al. 2012] or antioxidants in health supplements [Ku et al. 2007; Shahat and Marzouk 2013], among others. Indeed, tannin contains quite reactive polyphenols, which are useful to produce high added value materials as gels [Amaral-Labat et al. 2012a], foams [Szcurek et al. 2013] or carbons [Szcurek et al. 2011a; 2011b], etc. The latter materials can be then applied in separation/storage of gas, depollution or as electrodes for lithium batteries or supercapacitors.

### 1.3 Carbon materials

Carbon is one of the most abundant elements in the Earth. From the Latin, *carbo* means coal and charcoal. It has the unique ability to form bonds with other carbon atoms, as well as

with other elements, leading to an infinite number of chemical compounds, which are the basis of organic chemistry and so the basis of life on Earth [Burchell 1999]. Carbon is the most versatile and functional element in nature and it can be found in nature as ordered or crystalline, and as amorphous phases. Fig. 9 shows a crystalline structure on the left and an amorphous structure on the right having no atomic ordering.

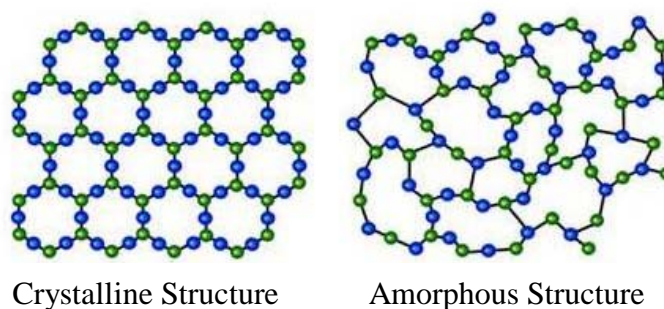


Fig. 9: Crystalline and amorphous structures of carbon [Ebbesen 1997].

### 1.3.1 Crystalline carbons

Fig. 10 shows the two most common ordered allotropic forms of carbon: diamond and graphite [Legendre 1992]. These two allotropic forms contain the same element, carbon (C), but they present different crystallographic ordering. Diamond presents a face centred-cubic structure and their atoms display a tetrahedral arrangement [Richter et al. 2000; Roy 2012]. Because of the covalent bonds between atoms of carbons, diamond presents several specific characteristics such as: hardness, high density and high melting point. Graphite is a layered material having strong covalent bonds in the plane and weak Van der Waals' interaction between layers. Therefore it is considered as one of the softest material known [Cowlard and Lewis 1967]. Graphite has the most thermodynamically stable form at normal conditions.

New other structures of carbons were discovered in the last 25 years which have been awarded with Nobel and Kavli Prizes as recognition: the 1991 Nobel Prize in Chemistry and the 2008 Kavli Prize in Nanoscience for carbon nanotubes (CNTs), the 1996 Nobel Prize in Chemistry for spherical fullerenes and the 2010 Nobel prize in Physics for graphene. Fig. 11 shows those new materials: fullerenes, carbon nanotubes and graphene. Those carbon materials present high electron affinity, chemical reactivity and good mechanical properties [Lue 2007]. Spherical fullerenes, also called buckyballs, are spheres made of carbon rings having five and six carbon atoms. Carbon nanotubes, single-walled or multi-walled, are graphene layers rolled in form of tubes [Roy 2012]. Graphene is a monolayer of graphite

having atoms of carbon arranged in a regular hexagonal pattern. The recent discovery of those new materials opened the development of new technologies.

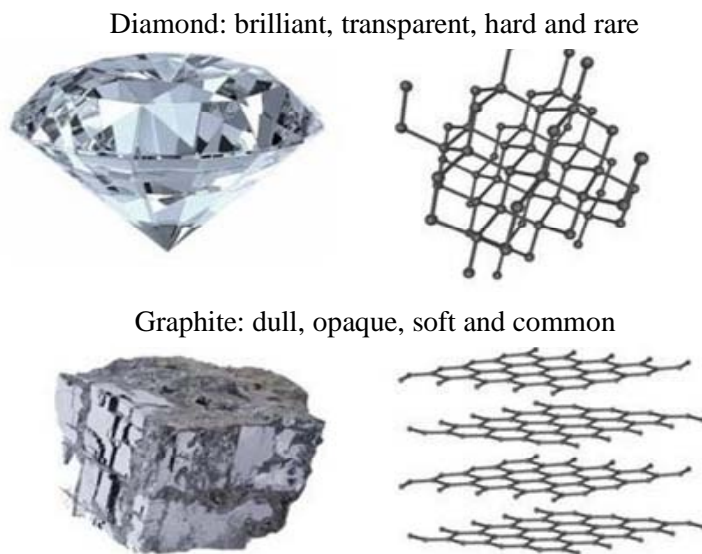


Fig. 10: The allotropic forms of carbon: diamond and graphite [Oganov et al. 2013].

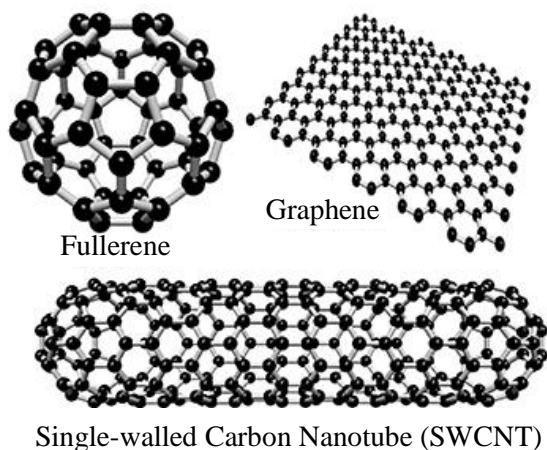


Fig. 11: The new carbon structures discovered in the last 25 years: graphene, fullerene and SWCNT [Oganov et al. 2013].

### 1.3.2 Amorphous carbon

Amorphous carbon is a very important class of carbon material and it has enormous industrial applications. Similar to graphite, it is composed of parallel layer planes. However, the stacked layers planes are limited in size (nm) and are found to be randomly oriented in amorphous carbons whereas the layer planes have a fixed “three dimensional” order in graphite. Carbons show a degree of “three-dimensional” ordering usually by heating an

amorphous carbon at high temperatures [Walker et al. 1955]. A terminology exists depending of carbons ability to be graphitized or not: soft and hard carbons respectively.

- Soft carbons are carbons that form graphitized materials. Precursors such as carbon blacks, cokes and pitches are submitted to a thermal treatment at quite high temperature ( $> 2000^{\circ}\text{C}$ );
- Hard carbons are nongraphitized materials. Because of the strong crosslinking bonds existent in these materials, there is no movement or reorientation of atoms to form an ordered structure of graphite. They are obtained by heat treatment of precursors such as: phenol-formaldehyde resins, furfuryl alcohol, cellulose, charcoal or coconut shells, among others [Kinoshita 1999].

### 1.3.2.1 Amorphous carbons production

The amorphous carbons produced in this work from tannin are hard carbons. There are two methods to produce them:

*Carbonization or dry pyrolysis* is the transformation of an organic material into a carbon matrix by heating in a flow of inert gas, i.e. nitrogen, in the absence of oxygen. Pyrolysis removes volatile species [Basu 2010]. If pyrolysis is carried out in an autoclave with a liquid at moderate temperature and pressure, is called as wet pyrolysis or hydrothermal carbonization (HTC) [Libra et al. 2011]. HTC will be explained in detail afterwards.

The precursor has an enormous influence on the resultant carbon yield. Materials containing large amounts of carbon or even aromatic structures will present a high carbon yield, calculated as the ratio of the final mass of the carbon residue and the organic material. While precursors containing a lower amount of carbon such as sugars, will present a lower carbon yield [Junpirom 2006; Marsh and Rodriguez-Reinoso 2006; Abdullah et al. 2011].

Pyrolysis conditions have an important effect not only on carbon yield but also on porosity. The way that gases evolve during pyrolysis controls the materials' characteristics. Pyrolysis involves several reactions such as dehydrogenation, condensation, transfer and isomerisation. During these reactions, volatiles are released and new radicals are produced, which react with other molecules producing the rearrangement of stable molecules [Marsh and Rodriguez-Reinoso 2006; Abdullah et al. 2011]. Two competing phenomena could occur during the pyrolysis: i) a shrinkage of

the materials and of its porosity may be observed by rearrangement of atoms in a more compact structure [Fischer et al. 1997]; ii) creation of porosity owing to the formation of volatiles species. Indeed, materials continue losing mass up to 1000°C and a concomitant creation of mesopores and micropores volume and an increase of the surface area (for example at 900°C) [Al-Muhtaseb and Ritter 2003; Matos et al. 2006; Job et al. 2008; Bruno et al. 2010]. Particles may also expand producing mainly macropores and therefore, the applications range for such materials would be reduced [Manocha 2003].

The heating rate is also a parameter that must be controlled to obtain high carbon yield [Saddawi et al. 2010]. At higher heating rate, the thermal degradation tend to be delayed, promoting gases released and reducing the carbon yield [Damartzis et al. 2011 and refs therein]. This effect has been seen in the pyrolysis of cherry stones [Gonzalez et al. 2003], rapeseed [Haykiri-Acma et al. 2006] or olive residue and sugar cane bagasse [Ounas et al. 2011]. The same trend has been seen for the pyrolysis of coal. Moreover, surface areas and total pore volume are decreased with the increase of heating rate such as 20-30 °C min<sup>-1</sup> [Seo et al. 2011 and refs. therein]. Thus, the effect of heating rate must be taken into account and should remain slow enough to preserve high porosity.

Activation is a process that develops surface and porosity in carbon and it can be either physical or chemical. Physical activation consists in partial carbon gasification by reaction with steam, CO<sub>2</sub>, or air at temperatures up to 1000°C [Hernández-Montoya et al. 2012] and most reactive amorphous components are burned off. Chemical activation consists of heat treatment in the presence of alkali (NaOH, KOH), inorganic acids (H<sub>2</sub>SO<sub>4</sub>, H<sub>3</sub>PO<sub>4</sub>), or salts (ZnCl<sub>2</sub>) in an inert atmosphere at typical temperatures from 400 to 800°C. The advantage of the chemical activation is a more uniform pore structure of the resultant activated carbon. Chemical activation is also a one step process while physical activation requires a previous pyrolysis [Marsh and Rodriguez-Reinoso 2006].

Activated carbon (AC) is one type of amorphous or disordered carbon having been processed to make it extremely porous, and thus to have a very large surface area available for adsorption or chemical reactions. The term active or activated carbon refers to carbon materials manufactured by high temperature (500 to 1000°C) pyrolysis of various vegetable residues (i.e., wood chips, peat, nutshells, pits, etc) as well as pitch, coal or polymers, followed by activation to create desirable porous structure of the target materials. AC's structure is formed by imperfect stacking of carbon layers, which are



bonded together to build a three-dimensional structure, as shown in Fig. 12 [Oberlin 1984]. The basic structural unit of activated carbon may be approximated by that of graphite with, however, a higher interlayer spacing and the possibility of having some carbon layers domains rotated with respect to each other. Activated carbon may thus be considered as a carbon form allied to graphite, but highly disorganised due to impurities and to the method of preparation (activation process). ACs can be classified on the basis of their application (e.g. gas vs liquid phase), precursor (e.g. wood, coal, etc.), and final shapes (e.g. powder, grains, pellets, etc) [Marsh and Rodriguez-Reinoso 2006].

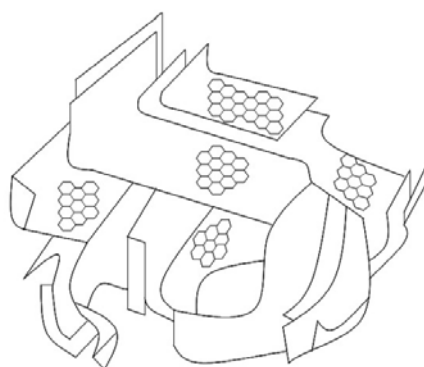


Fig. 12: Schematic representation of the structure of activated carbon [Oberlin 1984].

### 1.3.2.2 Determination of textural properties

Porous carbon materials may present different size of pores: macro-, meso and / or micropores, according to the classification performed by the IUPAC (International Union of Pure and Applied Chemistry) [Sing 1985]. The pores having a size greater than 50 nm are called macropores, pores with size between 2 and 50 nm are appointed as mesopores and micropores are those with the size narrower than 2 nm. This nomination is related to the behaviour during nitrogen adsorption at  $-196^{\circ}\text{C}$  [Sing 1989; Celzard et al. 2007; Inagaki 2009]. The physical adsorption of gases and vapours in solids is one of most used techniques for studying the porous texture of all types of solids. Adsorption is due to physical interactions without altering the molecular structure. The characterization of the porous solid material is determined by the textural parameters such as the specific surface area ( $S_{\text{BET}}$ ), pore volume and pore size distribution (PSD). For the determination of these parameters, the adsorption isotherms are obtained through the adsorption of a gas ( $\text{N}_2$ , Kr,  $\text{CO}_2$ , etc) at constant temperature [Garrido et al. 1987; Rodriguez-Reinoso and Linares-Solano 1989; Lozano-Castello et al. 2002].



Fig. 13 shows the different types of pores and a symbolic representation of their size together with the main techniques used for determining them. According to each technique, it is possible to size the pores distributed in the samples. For example, transmission electron microscope (TEM) can visually determine the size of the three types of pores (micro, meso and macro) and the gas adsorption, using  $N_2$  or  $CO_2$ , can determine the volume of micropores and mesopores. Both techniques were used in this study and will be described in techniques of characterisation (see Annex 1) [Inagaki 2009].

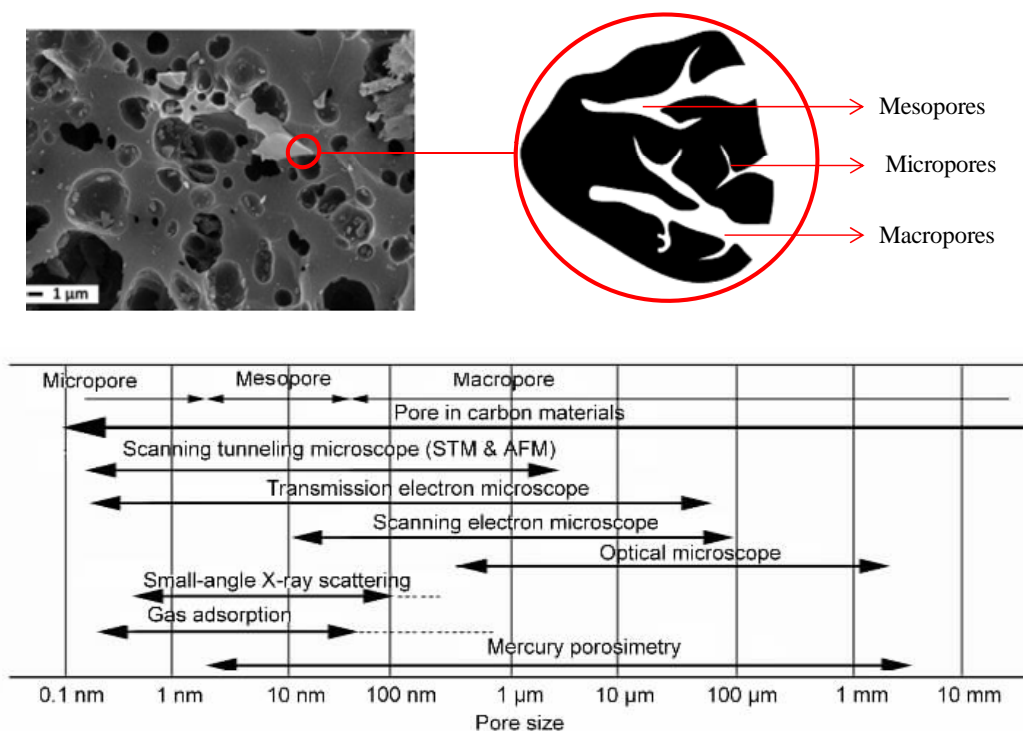


Fig. 13: Representation of the textural properties of a porous material and all techniques which are used to measure its porosity [Celzard et al. 2007; Achaw 2012; Falco et al. 2013].

There are several forms of adsorption-desorption isotherms, that describe the interaction between the gas (usually  $N_2$ ) and the solid surface. The adsorption isotherms are generally represented as the amount of gas adsorbed ( $cm^3 g^{-1}$ ) versus the equilibrium relative pressure ( $p/p^0$ ).  $p^0$  is the saturation pressure of the pure adsorptive (at the temperature of measurement) and  $p$  is the adsorbable gas pressure. Fig. 14 shows the six possible adsorption isotherms according to the IUPAC [Gregg and Sing 1982]:

- Type I has a concave form and it is characteristic of microporous materials;
- Type II represents the isotherm obtained on macroporous or nonporous materials;

- Type III has a convex form and it is characteristic of non-porous or macroporous materials with small adsorbent-adsorbate interactions;
- Type IV is characteristic of mesoporous materials presenting a hysteresis loop, which is due to capillary condensation in mesopores;
- Type V is an uncommon, linked to the type III;
- Type VI presents some steps and each step corresponds to an adsorption layer.

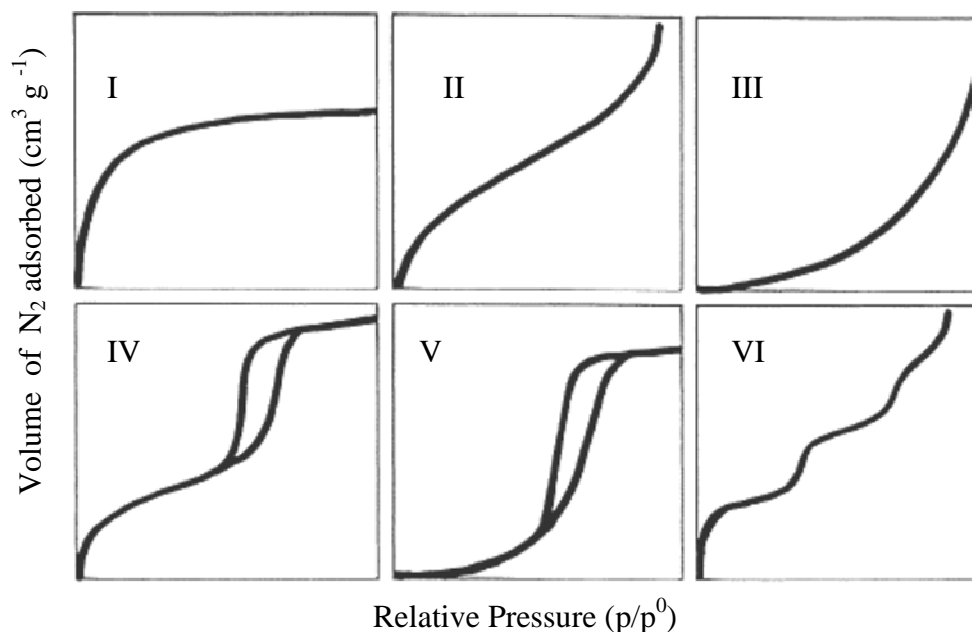


Fig. 14: Physisorption isotherms according to IUPAC [Gregg and Sing 1982].

#### 1.4 Hydrothermal carbonization (HTC)

Hydrothermal carbonization (HTC) or wet pyrolysis, as it is called, was first studied by Friedrich Bergius in 1911, when he submitted peat to hydrothermal treatment at 600°C and 200 bars [Bergius 1915]. The aim was to obtain an alternative of bio-sourced fuels and hydrogen production, limiting the formation of CO<sub>2</sub> but it was not successful. Some years later, he submitted cellulose to hydrothermal treatment at milder conditions: temperature of 200-330°C and pressure up to 200 bars obtaining a residue enriched in carbon [Bergius 1928]. Bergius received a Nobel Prize of Chemistry for the development of high pressure chemistry in 1931. Through the subject on the production of liquid and soluble compounds from coal, Bergius studies encouraged other scientists. Berl and Schmidt submitted different types of biomass to hydrothermal carbonization at different temperatures between 150-350°C [Berl and Schmidt 1928]. Schumacher et al. (1956) studied the influence of the pH, Berl et al. (1932) got insight on the elemental composition of HTC materials and Haenel (1992)

reviewed the coal structure of these materials. Many researchers used HTC to get different products but the first carbon spheres through the use of HTC of glucose were first reported by Wang et al. (2001).

The solid product recovered after HTC is called hydrothermal carbon or hydrochar and it is produced by submitting a carbonaceous precursor in aqueous system at moderate conditions of pressure and temperature. The precursor is put in a recipient with the desired volume of water and the whole is introduced in the autoclave, which is closed and placed into an oven at temperature lower than 250°C. During HTC, the pressure is auto-generated by the system at the fixed temperature; pressures up to 20 bars (2 MPa) can be reached and very little gas is released. At increasing temperatures, two other hydrothermal processes are carried out: hydrothermal liquefaction and gasification. In the first one, biomass is submitted to the follow conditions: 300-350°C and 15-20 MPa. The main products obtained are: biocrude (mainly phenols), an aqueous solution having dissolved organics and a gas phase consisting of carbon dioxide. Alkali hydroxides and carbonates are used as catalysts [Libra et al. 2011; Kruse et al. 2013].

During hydrothermal gasification however, there are three main conditions of reactions carried out in the presence of heterogeneous catalysts: 1) degradation of carbohydrates: in which the temperature is between 215 and 265°C producing hydrogen and carbon dioxide; 2) gasification of carbohydrates: temperatures at 350-400°C producing gases mainly methane and carbon dioxide; 3) supercritical water gasification: the degradation of carbohydrates are carried out at 600-700°C producing hydrogen and carbon dioxide and this can be performed without the presence of catalysts [Kruse et al. 2013]. The production of such gases by hydrothermal gasification cannot be performed by dry thermochemical conversion.

After the study made by Wang et al. (2001), other precursors were submitted to HTC such as xylose, maltose, sucrose, amylopectin, starch and also biomass derivatives, 5-hydroxymethyl-furfural-1-aldehyde (HMF) and furfural. Other precursors such as beet root chips [Riling et al. 2010], starch and rice grains [Cui et al. 2006], maize silage [Mumme et al. 2011] and even polymer wastes: polyethylene and sulphur-containing rubber [Zheng et al. 2011] have been also submitted to HTC. Recently, several other scientific studies have published results on HTC of faecal biomass [Danso-Boateng et al. 2013], sewage sludge [Parshetti et al. 2013; Zhao et al. 2014] and agricultural residues [Oliveira et al. 2013]. When biomass precursors are submitted to HTC, the resultant materials are in the form of spherical particles due to the broken fibrous lignocellulosic chain at some places [Barin et al. 2014],

with diameters from 700 nm and not exceeding 10  $\mu\text{m}$  depending on the precursor [Deshmukh et al. 2010].

HTC is used as a first step of carbonization to convert high oxygen content carbohydrates or lignocellulosic biomass into surface-functional carbonaceous materials. HTC-process conserves a significant part of oxygen content and most of their surface functionalities contrary to dry pyrolysis in which the amount of oxygen in the final materials is drastically reduced. In average, when sugars are submitted to HTC, carbon content increases from 25-30% and oxygen content is reduced from 53% to 27-30%, which is still very high oxygen content [Titirici et al. 2008]. During that HTC process, biomass precursors (rich in aromatic molecules and hydroxyl anions) have been transformed into hydrophilic and thermo-chemically more stable hydrochar materials at moderate conditions of temperature and pressure. The obtained hydrochars do not present porosity. To increase and develop it, a second thermal treatment and sometimes physical or chemical activation are required [Antonietti and Titirici 2010].

#### 1.4.1 Mechanism of hydrochars formation

Sugar molecules, as sucrose, have been used as model systems to study the mechanism of hydrochar formation. Fig. 15 shows the different reactions occurring when sucrose is submitted to HTC. Sucrose undergoes hydrolysis producing glucose and fructose; hydrolysis reactions are possible because of the high amount of  $\text{H}^+$  and  $\text{OH}^-$  present at hydrothermal conditions under water at moderate temperatures and pressures. Afterwards, glucose and fructose decompose into organic acids (acetic, formic, levulinic acids, etc) as confirmed by the rapidly change of the pH, from 8 to 3 [Antal and Mok 1990; Lujkx et al. 1995; Kabyemela et al. 1997; Sasaki et al. 1998; Sevilla and Fuertes 2009a].

Glucose and fructose can also undergo polymerization and condensation reactions, which could occur by several paths as: intermolecular and intramolecular dehydration, aldol condensation, keto-enol tautomerism and intermolecular dehydration of aromatized materials (Fig. 15). Other sugars as hexoses and pentoses have been also used to study the HTC reaction mechanism. Fig. 16 shows the first hydrolysis products of hexose and pentose when submitted to HTC at 180°C. Hexoses are converted into hydroxymethylfurfural (HMF) and pentoses dehydrate into furfural. Those intermediates decompose to levulinic and formic acid and also produce polymeric carbonaceous materials [Titirici et al. 2008].

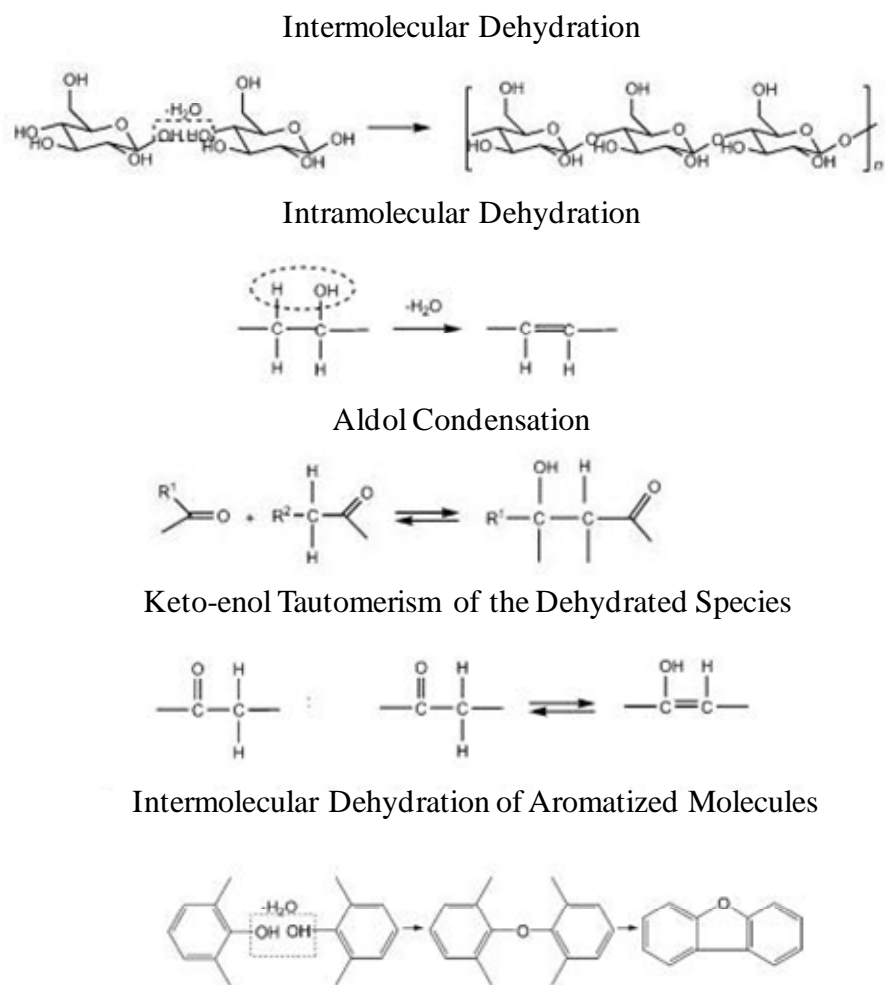


Fig. 15: Possible reactions occurring during hydrochar formation [Sevilla and Fuertes 2009a].

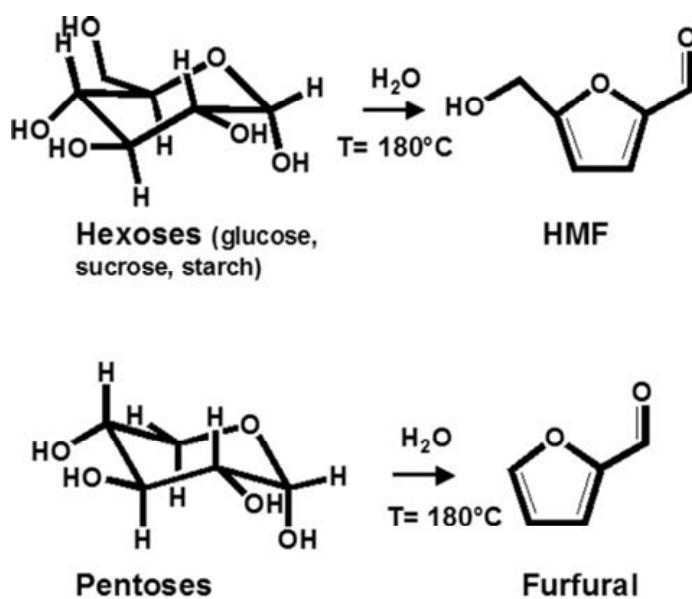


Fig. 16: The main reactions described after HTC at 180°C of hexoses and pentoses in water [Titirici et al. 2008].

After HTC reactions, the formation of hydrochars is due to a mechanism of nucleation and growth that follows LaMer model. When the concentration of carbon/aromatic chain in aqueous conditions reaches the supersaturation point, a nucleation process initiates [La Mer 1952]. In summary, nucleation and growth processes take place after hydrolysis, condensation, dehydration, aromatisation and polymerisation reactions at HTC conditions [Titirici et al. 2012]. Then, there are two products:

- (i) an insoluble carbonaceous particle, frequently spherical, having a structure containing a hydrophobic part (aromatic core) and a hydrophilic part or shell. The core presents stable oxygen atoms in form of ether, quinone, etc, while the shell presents oxygenated functional groups (hydroxyl, phenolic, carbonyl, carboxylic, ester, etc) [Tang and Bacon 1964; Asghari and Yoshida 2006; Sevilla and Fuertes 2009a]. These two parts are illustrated in Fig. 17.
- (ii) an aqueous solution having organic compounds such as furfural compounds, acids in the case of HTC of sucrose.

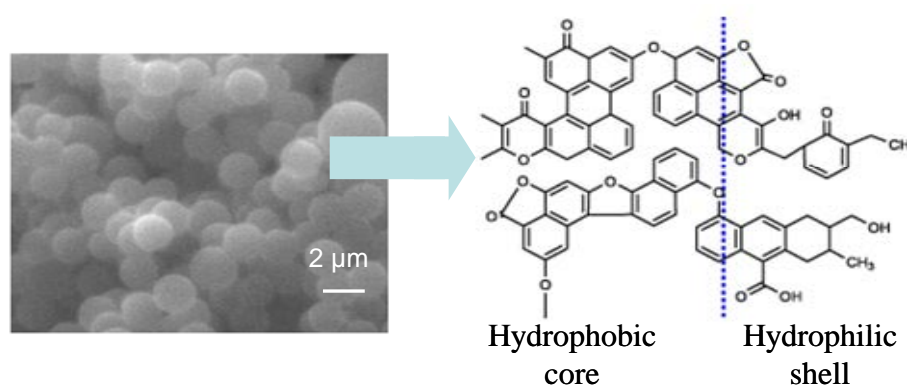


Fig. 17: The microspheres core-shell structure of hydrochars [Sevilla and Fuertes 2009a].

Carbonaceous materials having different sizes, shapes and surface functional groups have been synthesized by HTC. In general, carbon precursors are treated in HTC conditions at mostly 180°C for different residence times: 10h [Zheng et al. 2011], 12h [Cui et al. 2006], 18h [Riling et al. 2010], 20h [Tang et al. 2012], 24h [Titirici et al. 2006; Titirici et al. 2008; Yu et al. 2012]. However, the effect of HTC conditions has not yet been fully explored and research on this subject is fundamental. In this PhD work, aqueous solutions of condensed tannins were submitted to HTC in a stainless steel autoclave, and the kinetics of hydrothermal carbon formation was investigated by changing several parameters: amount of tannin (0.5; 1.0; 1.5; 2.0 g in 16 mL of water), HTC temperature (130, 160, 180 and 200°C) and reaction times (from 1 to 720h). Thus, a complete investigation of the hydrochars mechanism

formation together with a kinetics study will be presented in **Chapter 2** to cover the first objective of this work: understanding and discussing the morphology, mechanism and the kinetics studies of HTC of tannin.

### 1.4.2 Increase of HTC yield

Biomass materials submitted to HTC under acidic conditions and temperatures below 200°C produce hydrochars in which most of the original carbon stays bound to the final carbon matrix [Titirici et al. 2007a]. Differences of the thermal decomposition of carbohydrates due to variations of pHs were already verified by Schuhmacher et al. (1960) and moreover it was observed differences in their elemental composition (C/H/O). It has been seen that the HTC kinetics and the carbon yield content are modified at acidic pHs when compared to basic or neutral pHs [Schumacher et al. 1956; Titirici et al. 2007b]. During the hydrolysis of starch for example, the pH reduction has a catalytic effect. At pH 3, the maximum conversion of starch to simple sugars was reached [Bej et al. 2008]. Therefore, those sugars undergo several reactions during HTC producing hydrochars which are the most favourable at lower pHs.

The pH is fundamental during the hydrolysis of carbohydrates into sugars and their decomposition into humic acids and formic acids. It has been reported that hydroxymethylfurfural (HMF) and furfural are the main reaction products in acidic and HTC conditions but are not produced in alkaline conditions. Glucose is the most abundant sugar existent in biomass and therefore, it is the main product of biomass hydrolysis in acidic medium [Bobleter and Bonn 1983; Bonn and Bobleter 1983]. In addition, many studies on HTC of carbohydrates observed a reduction of the pH due to the formation of several acids i.e. acetic, formic, levulinic, therefore, a neutral to acidic environmental appears to be necessary modifying also the reaction rate and the products characteristics at the final system [Schwalbe and Neumann 1933; Leibnitz et al. 1958; Schuhmacher et al. 1960; Titirici et al. 2007; Funke and Ziegler 2010]. Arrhenius acids, for example, catalyse dehydration reactions as well [Peterson et al. 2008].

Regarding tannin, it has an acidity constant pKa equal to 8. To a pH greater than pKa + 1 or above pH 9, tannin is negatively charged due to the presence of phenoxide-type anions. At a pH near to pKa (pH = 8), the proportion of the phenol groups becomes comparable to the phenolate type groups. The pH between 3 and 7, tannin self-condensed slowly, especially at pH 4.5. In this case, tannins polymerize slowly but a high degree of crosslinking is normally achieved and thus a sufficiently connected three-dimensional network is obtained. At pH

extremely acid (below 1.5), the reaction of polymerization of tannin is the most favourable. Therefore, the pH could play an important role in tannin reactivity.

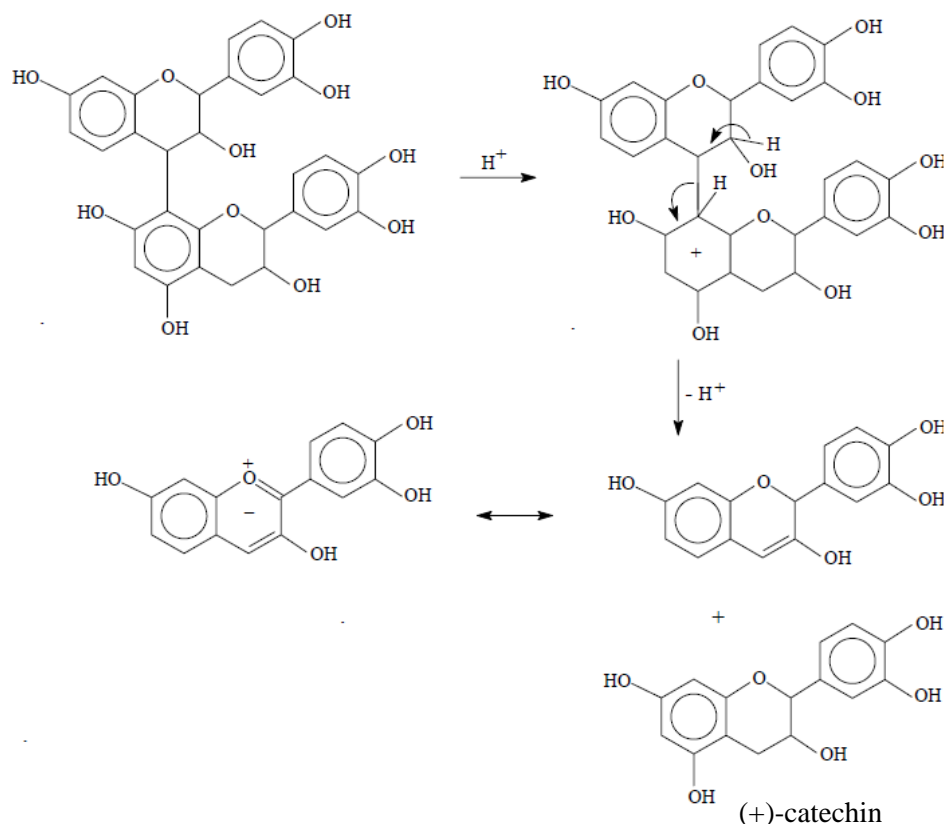


Fig. 18: Tannin degradation in hot and acid conditions to form of catechin and anthocyanidins [Pizzi 1983].

In hot conditions and in the presence of strong mineral acids, tannins are capable of reacting by two different manners; the first one is the tannin degradation which leads to the formation of catechin and anthocyanidins (Fig 18) and the second reaction is the condensation of the resulting heterocyclic rings (p-hydroxybenzyl ether) by hydrolysis [Roux et al. 1975]. The p-hydroxybenzylcarbonium ions (Fig. 19) created can then condense with the nucleophilic centres on other tannin units to form the “phlobaphenes” or “tanner reds” which are insoluble materials having high molecular weight. Condensation may also proceed by free radical coupling of B-ring catechol units in the presence of atmospheric oxygen [Pizzi 1983].

In order to increase the HTC yield, the first strategy will be modifying the pH for the HTC of tannin. A second strategy will be studying the addition of another carbohydrate i.e. sucrose at low pH in the system of HTC. Indeed, it has been shown that the addition of glucose to microalgae organisms submitted to HTC allowed the incorporation of nitrogen into the final carbon matrix but also the increase of carbon yield [Falco et al. 2012]. The reason for that is



that additional crosslinking reaction occurred with the degradation of glucose to monosaccharides that will further react with the amino acids from the microalgae organisms. Therefore, we are going to investigate the hydrothermal tannin-sugar system.

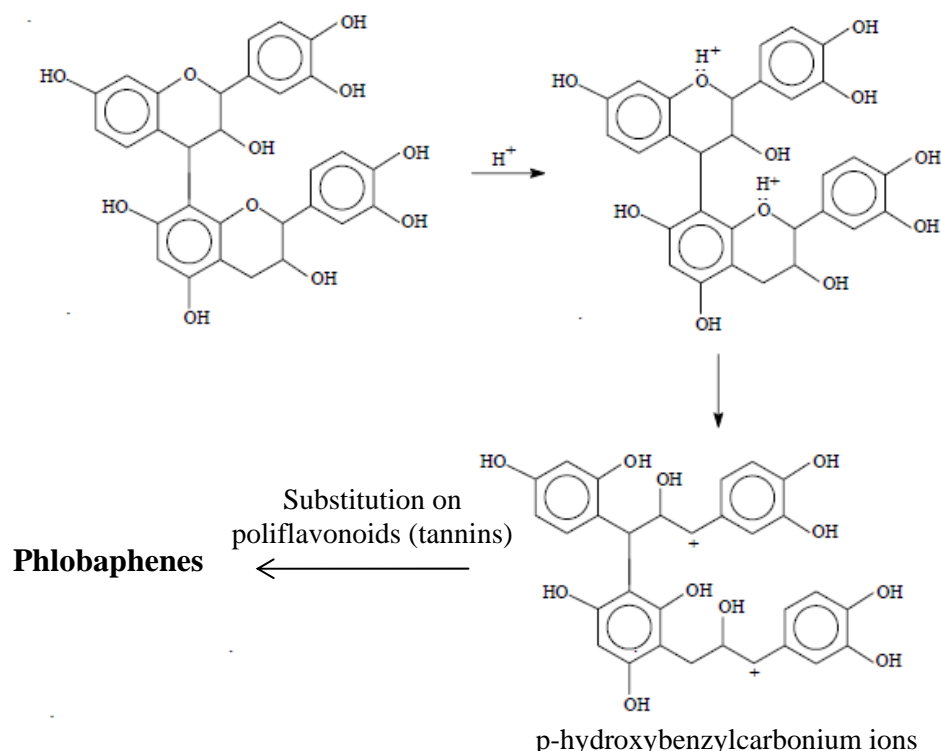


Fig. 19: Tannin autocondensation by acid hydrolysis of heterocyclic rings [Pizzi 1983].

Finally, the third strategy used in literature is the addition of silver nanoparticles. Sun and Li (2005) demonstrated the encapsulation of silver nanoparticles into shells made from glucose submitted to HTC. Silver nanomaterials have shown to be promising materials in several fields specifically in optical instruments and in biochemistry as drug delivery [El-Ansary and Faddah 2010; Sivasankar and Kumar 2010; Sironmani and Daniel 2011]. Tannin, with its large amount of hydroxyl groups present, has been applied as a reducing agent of  $\text{Ag}^+$  to  $\text{Ag}^0$  at soft conditions such as agitation at room temperature conditions [Tian et al. 2009] or at 70-80°C [Bulut and Özacar 2009]. Therefore, silver nanoparticles could be produced here using tannin in HTC conditions and these silver nanoparticles could act as nucleating agent, increasing hydrochar nucleation and leading silver nanoparticles embedded into a carbonaceous shell.

In this PhD work, we have studied the effect of  $\text{H}^+$ , sucrose and  $\text{AgNO}_3$  addition, on the carbon yield and on the evolution of textural properties and elemental composition of the carbon materials after carbonization at 900°C. The results are thoroughly discussed in **Chapter 3**.

### 1.4.3 Synthesis of N-doped carbon materials

The incorporation of heteroatoms such as nitrogen into aromatic/graphitic carbon materials contributes to enhance electrical conductivity [Terrones et al. 2002], alter and improve the surface functionality of those materials with consequences on their adsorption and catalytic performances [Bimer et al. 1998; Li et al. 2001; Przepiórski 2006]. Increasing the electronic conductivity of those materials is directly related to increasing their use mostly in electrochemical applications for example in supercapacitors. There are several procedures used to synthesize N-doped carbon materials (NCM's), which generally involves very high temperature pyrolysis, chemical vapor deposition (CVD) or arc-discharge techniques. In the high temperature pyrolysis process, high energy generation is needed; during the CVD process, the formation of a non-volatile final solid material is made through vapour phase chemical reactants and several parameters must be controlled such as gases, pressure and temperature and the arc-discharge process presents also the same inconvenient [Rafique and Iqbal 2011; Shen and Fan 2013].

HTC is a simple and easy synthesis route for producing carbon materials and it has gained an increasing interest in the last decade. N-doped hydrochar can be produced by using ammonia, amines or urea or using directly carbon precursors containing nitrogen such as acetonitrile, pyrrole, polyacetonitrile, among others, or through non-toxic and natural carbohydrate precursors from biomass naturally rich in nitrogen [Titirici 2013]. Systems using sustainable or natural precursors will be focused on this work, for instance, carbon particles were prepared from, a mixture of glucose and ovalbumin [Baccile et al. 2010], chitosan and glucosamine [Zhao et al. 2010a], or from prawn shells biomass [White et al. 2009]. In Fig. 20, the mechanism of nitrogen-doped hydrothermal carbon from the mixture of glucose and glycine is presented. The scheme shows also the possible structures of the hydrocarbon obtained with the incorporation of nitrogen into their carbon structure. The elemental composition of that final material contains about 8.4 wt.% of nitrogen. The introduction of nitrogen induces a systematic aromatization of the carbonaceous network [Baccile et al. 2011].

**Chapter 4** focus on the amination of tannin through HTC. NCM's presented different morphologies being as: (i) powders by HTC of tannin in a concentrated aqueous ammonia solution; (ii) gels without using any crosslinker agent by HTC in distilled water of tannin first modified by reaction with concentrated ammonia and then evaporated. Whatever the method, (i) or (ii), HTC was carried out at different temperatures: 180, 190, 200, 210 or 220°C, with

further pyrolysis at 900°C under nitrogen. The morphology and chemical composition of the resultant materials are discussed and compared. It will be included also the potential of NCM's as carbon electrodes for supercapacitors (Section 1.4.5).

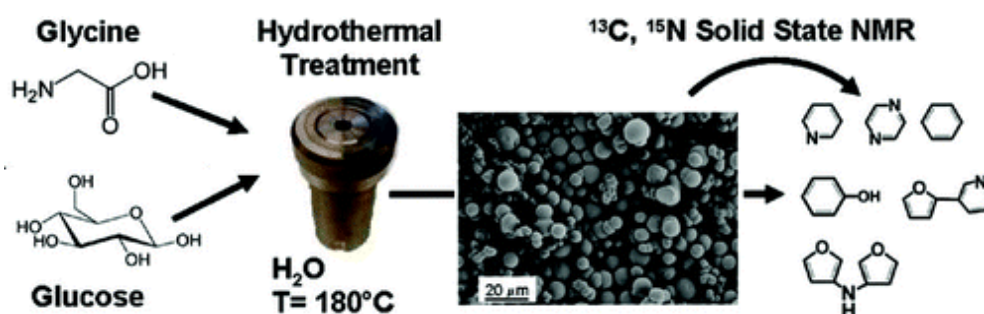


Fig. 20: Schematic synthesis of HTC of glycine and glucose with their possible hydrocarbons as final material [Baccile et al. 2011].

#### 1.4.4 Synthesis of N-doped carbon gels

Gels are usually obtained from a sol-gel system, a colloidal suspension of solid particles in a liquid initially from soluble precursors as seen in Fig. 21 [Jung et al. 2012]. Following the pioneer investigation of Ebelmen in 1845 on polymerisation of silicic acid and leading to a “glass-like material”, the sol-gel process was first limited due to the extremely long drying time (one or more than one year) to avoid cracking of the gel into a fine powder [Ebelmen 1846]. An alternative drying process of a silica gel, preserving the structural integrity of the gel using supercritical solvent extraction, was first developed by Kistler in 1932 and gave a dried gel called aerogel [Kistler 1932]. Gels are interesting materials because they have high surface areas, high porosity (up to 95% of their volume, or even more, is air) and low density [Aegeter et al. 2011].

Phenolic gels, mainly prepared from resorcinol or phenol, and using formaldehyde as crosslinker, have been widely studied [Job et al. 2004]. However, toxicity and cost of these molecules encouraged the research for greener alternatives. Thus, the possibility of using natural and reactive precursors such as cellulose [Heath and Thielemans 2010], starch (Starbon gel) [Budarin et al. 2006], soy flour [Amaral-Labat et al. 2012a] and lignin [Grishechko et al. 2013], among others, has been reported. Tannins also appeared to be new and sustainable substitutes. Tannin-formaldehyde (TF) gels indeed have physicochemical properties comparable to those of resorcinol-formaldehyde (RF) gels [Nakano et al. 2001; Ogata and Nakano 2005; Kraiwattanawong et al. 2007; Szczurek et al. 2011a, 2011b; Celzard et al. 2012]. In a typical synthesis, TF gels were prepared by mixing tannin dissolved in a water/organic solvent (ethanol or methanol) mixed solution with formaldehyde (crosslinker),

and then this solution was put in a glass tube which was sealed and placed in an oven at 85°C for gelation and ageing for 5 days [Szcurek et al. 2011a]. The main drawbacks of this method are the long gelling time and the use of formaldehyde.

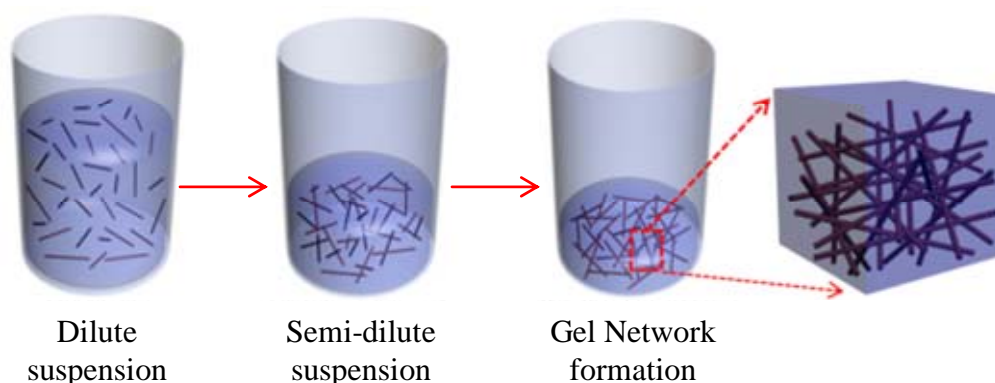


Fig. 21: Schematic preparation and structure of gels [Jung et al. 2012].

Hydrothermal carbonization (HTC) allows decreasing both formaldehyde amount and reaction time, and thereby allows producing ‘greener’ gels. Various precursors were already successfully submitted to HTC to produce gels: S-(2-thienyl)-L-cysteine and 2-thienyl carboxaldehyde [Wohlgemuth et al. 2012b], borax and glucose [Fellinger et al. 2012] and phloroglucinol with some carbohydrates (glucose, fructose or xylose) [Brun et al. 2013a]. The physicochemical properties of these materials were similar to those of phenolic aerogels such as RF [Job et al. 2005] and TF [Szcurek et al. 2011a, 2011b] gels, though some of them were doped with nitrogen or/and with sulphur.

Apart from the synthesis method and the chemical nature of precursors, the drying process is also an important parameter that determines gels porosity. Depending on the drying method, three kinds of gels can be obtained: (i) xerogels, using subcritical conditions, i.e. at moderate temperatures and normal or reduced pressure in a conventional oven or at room temperature. The shrinkage is most of times fast and abrupt, and the resultant porosity is generally low; (ii) cryogels, using freeze-drying. The shrinkage is low but the resultant porosity is generally coarser than that of aerogels; (iii) aerogels, using supercritical conditions, and leading to well-developed and narrow porosity in general.

**Chapter 5** is focused on the synthesis and characterisation of N-doped carbon xero-, cryo- and aerogels produced from different solid fractions of tannin in ammonia and submitted to HTC (180°C; 24h). It will be included also the potential of carbon gels as carbon electrodes for supercapacitors (Section 1.4.5).

### 1.4.5 Applications of HTC-derived carbon materials

The main application for hydrochars obtained by submitting biomass into HTC is as CO<sub>2</sub> geo-sequestrator. The bio-coal or charcoal produced can be used as precursor for producing porous materials but it can be also stored as soil amendment. It is said that biomass materials after being submitted into HTC conditions create carbon-negative energy systems to immediately clean up the CO<sub>2</sub> emissions from the past. Therefore, HTC has great potential to be applied at a large scale and several companies in Europe such as *AVA CO<sub>2</sub>* (Germany), *SunCoal* (Germany), *Carbon Solutions* (Germany) and *Ingelia* (Spain) have been working on this field. HTC applied at large scale has a great economical potential and it is essentially sustainable, having no emissions of CO<sub>2</sub> (CO<sub>2</sub>-neutral) during this process. Moreover, not just woody biomass but also municipal solid waste, wastewater sludge and animal waste can be recycled to produce hydrochars and then, reused in the environment as soil amendment in agriculture sites and also to sequester atmospheric CO<sub>2</sub> [Titirici 2013]. Hydrochars can be also used to generate energy or to produce solid fuels, which have been described by few authors: Ramke et al. (2009), Berge et al. (2011) and Hwang et al. (2012). Biomass is the biggest CO<sub>2</sub> binder existent and therefore, HTC should be a good investment not only for industries but also for cities reusing and recycling urban waste.

The price for the transformation of biomass into hydrochars after HTC can be quite competitive compared to conventional procedures already existent. Pulp and paper industry sludge (PPS) and anaerobically digested municipal sewage sludge (ADS) can be treated by HTC for less than 13 and 33 € per ton of sludge, respectively, comparing to traditional treatment options (incineration or disposal in landfills) which are more expensive ranging from 30 - 80 € per ton of wet sludge, respectively [Child 2014]. Some researchers in Germany have studied the possibility of converting sewage sludge into coal through the HTC process at large scale. Studies showed that such waste after four hours at HTC conditions is transformed into a carbonaceous material that can be removed from the bottom of the reactor. This material was subsequently dewatered to obtain a product with a dry matter content of 60% that was transformed into pellets. They also found that the calorific value of this material is 4-5 MW/ton, which is a bit lower than the calorific value of lignite (5-6 MW/ton), a carbon material composed of 65-75% of C and largely used for heating to produce electricity in Germany. The pressure in the reactor during this process is auto-generated (from 14 to 20-24 bars) and they have found that if 9000 tons of dry sewage sludge are produced by a population of 30000 people, 800 tons of coal can be produced and therefore, this procedure

was considered as eco-friendly and also as economically viable [Cleaner Production Germany 2014].

After a second thermal treatment, hydrochars may present high adsorption capacity, high thermal and chemical stability, and high electrical and thermal conductivity. The physicochemical characteristics of these materials make them great candidates to be applied in catalysis, gas storage and separation, pollutant removal from aqueous phase, drinking water and wastewater treatment systems and in energy sector as electrodes for batteries, supercapacitors or fuel cells (see Fig. 22).

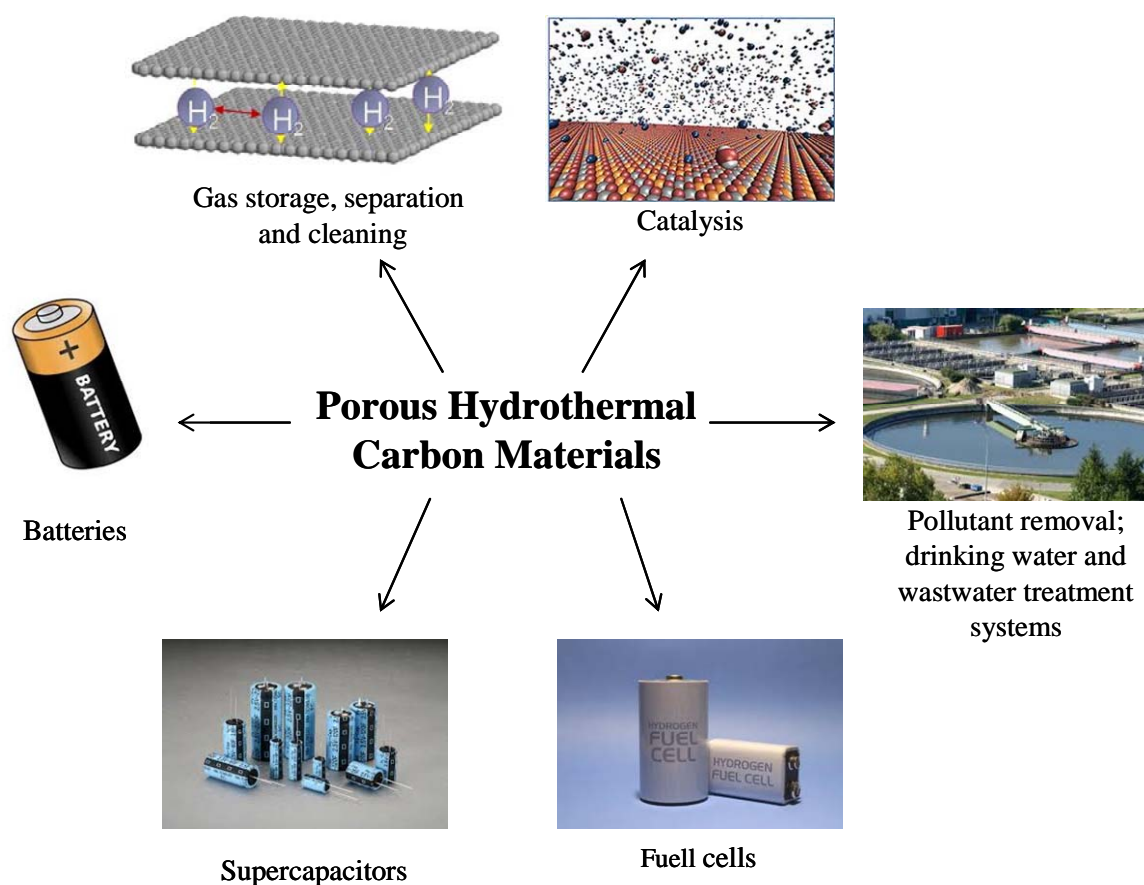


Fig. 22: The main applications of porous hydrothermal carbon materials (adapted from Tititrici (2013)).

HTC-derived materials have showed to be a great option as a catalyst support. There are several factors that influence their performance such as higher surface area, large pore volumes, controlled pore size and structures. The presence of oxygenated functional groups on their surface producing a core/shell structure makes such materials even better candidates as catalysts supports. HTC of furfural in presence of Pd acetylacetonate was applied as a support of catalyst for the reaction of hydrogenation of phenol to produce cyclohexanone - the

intermediate which participates in the synthesis of nylon-6 and nylon-6,6. The performance of the hydrophilic HTC material was compared with two other hydrophobic materials: a commercial charcoal and an alumina. Phenol was converted to cyclohexanol using the commercial materials and 95% of cyclohexanone was synthesised after 20h of reaction using the hydrophilic HTC material. The main explanation for the outstanding reactivity of HTC material was the presence of oxygenated groups and homogeneous active sites proving that the hydrophilic HTC-supports are quite selective in chemical reaction processes [Makowski et al. 2008]. Other studies have been also proposed as low-cost and efficient catalyst supports: HTC-derived material made from glucose, silver nitrate and imidazolium ionic liquid [Wu et al. 2008] and, from lobster shell in presence of  $Pt^{+2}$  [Soorholtz et al. 2013].

In fuel cell applications, NCM's based on ordered mesoporous graphitic arrays [Liu et al. 2010a], graphene [Qu et al. 2010], mesoporous carbons [Yang et al. 2011], SWCNTs [Yu et al. 2010], nanotube cups [Tang et al. 2009] and hybrid carbon materials [Yu and Dai 2010] have been developed as potential alternatives for metal-free oxygen reduction reaction (ORR) catalysts. Nitrogen-doped carbon spheres have also been tested and found to exhibit high catalytic activity, long-term stability, and excellent methanol tolerance for ORR in alkaline medium [Zhou et al. 2011]. HTC-derived materials have been also proposed for fuel cells to convert chemical into electrical energy. Recently, N-doped materials made by HTC have shown to present active sites on their surface able to binding with transition metal complexes. Between the electrocatalytic processes in which transition metals could participate are  $CO_2$  reduction reactions, electrocatalytic reactions such as oxygen reduction reaction (ORR) and oxygen evolution reaction (OER). Brun et al. (2013b) described a great procedure applying NCM's made by HTC of glucose and phloroglucinol as metal-free oxygen reduction catalyst. This is a great step forwards to the green approaches through the use of biomass and natural and non-toxic carbohydrates precursors in electrocatalysis without catalysts.

As porous carbon materials, one of the most common applications is adsorption of organic pollutants and heavy metals in water media. Adsorption is widely used to remove such materials in wastewater or drinking water systems because of its low-cost and high surface area and porosity. The use of carbons made from HTC of glucose and acrylic acid provided carbon's functionality such as carboxylic groups. The final material was then applied for the removal of heavy metals:  $Pb^{+2}$  and  $Cd^{+2}$  proving to reach an adsorption capacity of 351.4 and 88  $mg\ g^{-1}$  respectively which are relatively high comparing to other types of adsorbent materials [Demir-Cakan et al. 2009]. Other studies also proposed the adsorption of  $Pb^{+2}$  and



Cd<sup>+2</sup> metals by HTC-derived material from glucose [Chen et al. 2011]; the removal of uranium by carbons prepared after HTC of lignocellulosic biomass [Kumar et al. 2011] and finally, materials prepared after HTC of pinewood for removing Cu<sup>+2</sup> [Liu et al. 2010]. The HTC-derived materials were also activated to increase their textural properties to be applied for the adsorption of CrO<sub>4</sub><sup>-2</sup> and Fe<sup>+3</sup> [Xu et al. 2008] and Ag<sup>+</sup> [Hu et al. 2008]. Organic pollutants such as bisphenol A, 17  $\alpha$ -ethinyl estradiol and phenanthrene, the global environmental pollutants were also removed from water using a HTC-carbon material presenting great adsorption performance and made from poultry litter and wheat straw [Sun et al. 2011b].

There is a great interest on using porous carbon materials for the adsorption of gases such as CO<sub>2</sub> which are the main responsible for the climate change. Of course these materials must have great capacity for CO<sub>2</sub> uptake and must be made from low-cost technique and precursors. HTC-derived materials have been studied as an option to storage CO<sub>2</sub> [Zhang et al. 2012b]. They were prepared from biomass: starch, cellulose and eucalyptus sawdust and submitted to activation to obtain high surface areas and pore volumes mostly micropores. Great CO<sub>2</sub> uptake was observed, from 5.2 to 6.6 mmol g<sup>-1</sup> CO<sub>2</sub> at 0°C [Sevilla and Fuertes 2011a]. Nitrogen-derived materials from *Enteromorpha prolifera* (an ocean contaminant) was submitted to HTC and KOH activation and gave also great results. Sevilla et al. (2012) prepared NCM's from mixtures of algae and glucose. These materials were activated obtaining CO<sub>2</sub> storage capacities of up to 7.4 mmol g<sup>-1</sup> at 0°C, 1 atm. Hydrogen storage was also studied by Sevilla et al. (2011b) activating HTC-derived materials from glucose, starch, furfural, cellulose and sawdust. It was observed a great porosity for those materials and a high H<sub>2</sub> uptake up to 4.8 mmol g<sup>-1</sup> at 25°C, 1 atm. These studies proved that HTC-derived materials after activation obtained higher H<sub>2</sub> uptakes than other ACs.

NCM's and N-doped carbon gels can be largely used in electrochemical applications with the increasing of their electronic conductivity of their carbon structure. In this work, these materials were tested as supercapacitors which are electrochemical energy devices having a capacity of energy storage moderate but with high power. In supercapacitors, there are two ways to store energy that occur simultaneously and contribute to the total capacitance : a) an electrostatic storage contributing to the electrical-double-layer capacitance (EDLC's) where electrical energy is stored through the system electrode/electrolyte by a charge separation in the double layer at the interface between an electrolyte (a solution which can be a salt, an acid, a base or even a non-aqueous organic mixture) and an electrode (the surface of the



porous material used) as demonstrated in Fig. 23; and b) a Faradaic electrochemical storage contributing to the pseudocapacitance where energy is stored by redox reactions through an electrode/electrolyte system [Pandolfo and Hollenkamp 2006; Shukla et al. 2012; Du et al. 2013].

Supercapacitors have an ideal behaviour when the cyclic voltammetry curves are rectangular in shape (see Fig. 23). If the electrode materials have redox properties, i.e. pseudocapacitance, corresponding to faradaic reactions, there is a deviation from the rectangular shape of the cycle and it is possible to visualise redox peaks. In this case, the charge accumulated in the capacitor is highly dependent on the potential of the electrode [Frackowiak and Béguin 2001]. In addition, having nitrogen atoms in the carbon matrix of those materials, it has been proved to be an effective way to improve the wettability in EDLC's and contribute to an additional capacitance through pseudofaradaic reactions [Hulicova et al. 2006; Frackowiak et al. 2006; Hulicova-Jurcakova et al. 2009].

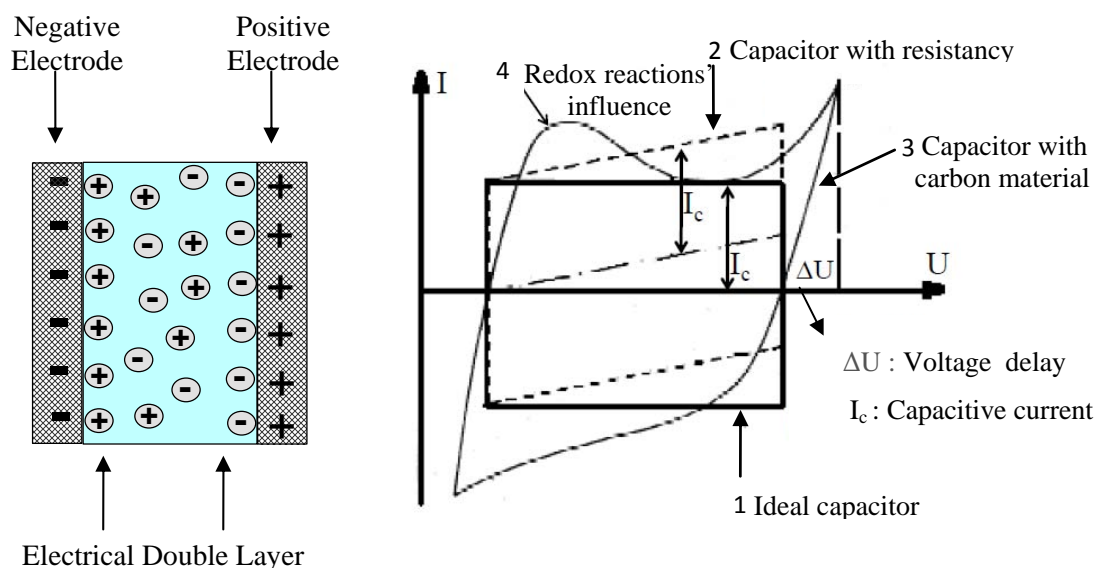


Fig. 23: Schematic representation of a supercapacitor [Frackowiak and Béguin 2001].

Several hydrochars after activation or pyrolysis presented excellent performance in supercapacitors. Wood submitted to HTC and activation using potassium hydroxide (KOH) produced supermicroporous materials having surface areas as high as  $3000 \text{ m}^2 \text{ g}^{-1}$  and capacitance values of  $236 \text{ F g}^{-1}$  at  $1 \text{ mV s}^{-1}$  [Wei et al. 2011]. D-glucosamine was also activated after HTC with KOH obtaining microporous materials presenting surface area of around  $600 \text{ m}^2 \text{ g}^{-1}$  and capacitance values of  $300 \text{ F g}^{-1}$  at  $0.1 \text{ A g}^{-1}$  in an acid electrolyte [Zhao et al. 2010b] and rice husk impregnated with phosphoric acid obtained micro/mesoporous with values of  $2530 \text{ m}^2 \text{ g}^{-1}$  and capacitance of  $130 \text{ F g}^{-1}$  [Wang et al. 2011]. Other materials

were made by submitting human hair with glucose to HTC at 180°C of overnight. The level of nitrogen content increased due to the presence of hair. The hydrochar was then activated using KOH and surface areas and capacitance were around 600 m<sup>2</sup> g<sup>-1</sup> and 264 F g<sup>-1</sup>, respectively [Si et al. 2013].

In **Chapters 4** and **5**, we are going to demonstrate that HTC-derived materials (NCM's and gels) can be used as carbon electrodes for supercapacitors.

## 1.5 Synthesis of ordered mesoporous carbons

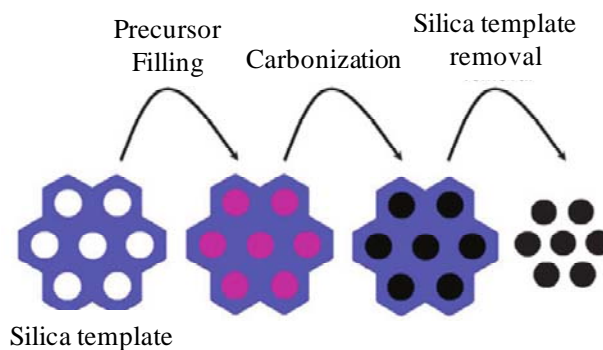
The use of templates or scaffolds is a powerful method for producing carbon materials with ordered structures or porosity. It has attracted considerable research effort over the past decades [Ryoo et al. 1999]. These materials present regular and controlled pore size distribution and pore structural stability, which cannot be obtained by conventional carbonization. Ordered structures can be prepared by the introduction of hard and soft templates, which will create available and ordered spaces. After template removal by carbonization (soft-template route) or by chemical etching (hard-template route), the carbon has a regular pore network. Ordered mesoporous carbons (OMC's) are applied in several fields such as catalysis [Freire et al. 2009], electrochemistry [Chang et al. 2007; Liu et al. 2009; Dai et al. 2011, Léonard et al. 2014], many high technology applications such as sensors [Kanungo et al. 2002], thermal insulators [de Boer et al. 2000], bioreactors [Peters et al. 1999] and also in biomedicine as drug delivery [Lu et al. 2007].

Fig. 24 shows the two strategies to produce OMC's: hard and soft templating [Ma et al. 2013]. On the one hand, hard templates are normally inorganic materials such as zeolite [Kyotani et al. 1997; Garsuch and Klepel 2005] and silica [Wang et al. 2006] but this procedure is costly and unsafe. Zeolites are expensive and they are destroyed using harmful substances such as concentrated fluoridric acid that is used for the template's removal. On the other hand, soft templates are organic materials having amphiphilic properties such as the non ionic triblock copolymers PF127 that forms spherical or tubular micelles that assemble together to give liquid crystal phases also called mesophases. The commercial material known under the name of Pluronic F-127 (PF-127) was used in this work to produce OMC's.

These surfactants have a hydrophilic part, which is at the outer part and in direct interaction with the aqueous solution, and a hydrophobic part, which is directed to the centre of the micelle. The carbon precursor, usually a polymeric network material, interacts with the hydrophilic part of the surfactant through hydrogen bonding and covers the micelles. Phenolic

materials containing a large amount of hydroxyl groups (-OH) such as phenol [Zhang et al. 2007; Huang et al. 2008; Fang et al. 2010], resorcinol [Wang et al. 2008] or phloroglucinol [Liang and Sheng 2006] together with formaldehyde as crosslinkers have been used. The final stage is the carbonization to remove the template giving place to the regular nanostructures.

Hard templating:



Soft templating:

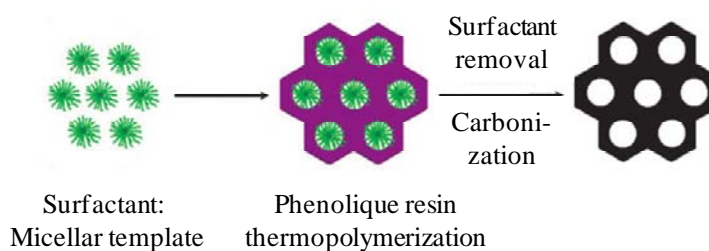


Fig. 24: Synthesis of ordered mesoporous carbon materials using mesoporous silica hard templates and block copolymer soft templates (adapted from Ma et al. (2013)).

The maximum temperature applied for their synthesis is 130°C because PF127 decomposes at higher temperatures [Huang et al. 2008; Liu et al. 2011]. Not too many natural materials have been applied to produce OMC's. D-fructose together with PF127 in water were submitted to HTC and after carbonization around 400°C, the surfactant was removed but limited pore volume and surface area were obtained [Kubo et al. 2011]. Tannin has been also used to produce ordered materials due to its great amount of hydroxyl anions that can interact with the hydrophilic part of the surfactant such as PF127 for the production of ordered mesoporous carbon materials though the method of EISA (Evaporation Induced Self-Assembly). A very acidic medium was applied to promote tannin polymerization eliminating the crosslinker agent formaldehyde as seen in Fig. 25 [Schlienger et al. 2012].

Taking advantage of the high level of autocondensation of tannin at acidic conditions avoiding any kind of crosslinker agent, mesostructured carbon materials using the soft-templating route were synthesized in this PhD work. Therefore, **Chapter 6** focuses on the

synthesis of OMC's using tannin, PF127 and agitation at room temperature (20°C) in acidic medium eliminating any kind of aldehyde (i.e. formaldehyde) and organic solvents (i.e. ethanol). All of these materials were dried and pyrolysed at 400 and/or 900°C for the template removal and all the textural properties and results obtained will be discussed.

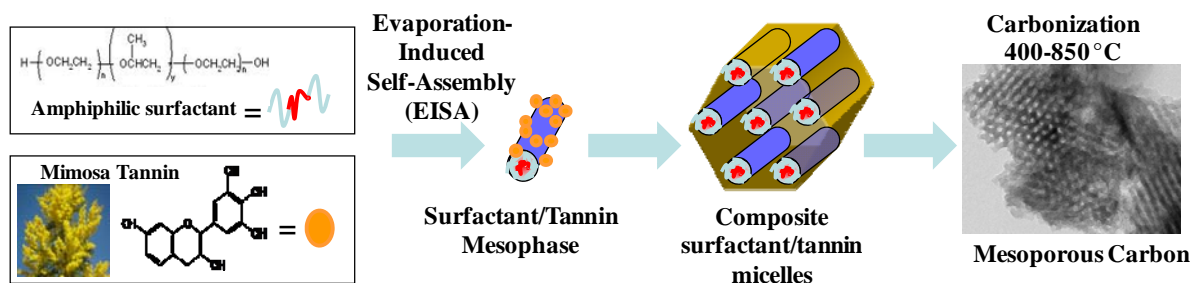


Fig. 25: Scheme for the synthesis of mesoporous carbon from tannin and the surfactant F127 as precursors and the method EISA (adapted from Schlienger et al. (2012)).



## **Chapter 2: Mechanism and kinetics of hydrochar synthesis from Mimosa tannin**



Since the HTC of tannin was barely explored, a systematic study of this process was performed in this chapter using basic conditions: pure water, different tannin concentrations and reaction times (Fig. 26). The hydrochars recovered by centrifugation were characterized by a large panel of techniques (described in Annex 1) such as TEM, krypton adsorption at  $-196^{\circ}\text{C}$  and helium pycnometer, elemental analysis and X-ray photoelectron spectroscopy (XPS) bringing knowledge about particles (size, morphology, surface area) and chemical composition. Thanks to those data, it appeared that HTC can be described by a classical nucleation – growth process like for the sol-gel process. The measurement of the carbon yield for each synthesis condition also allowed determining for the first time the kinetic law of tannin's HTC.

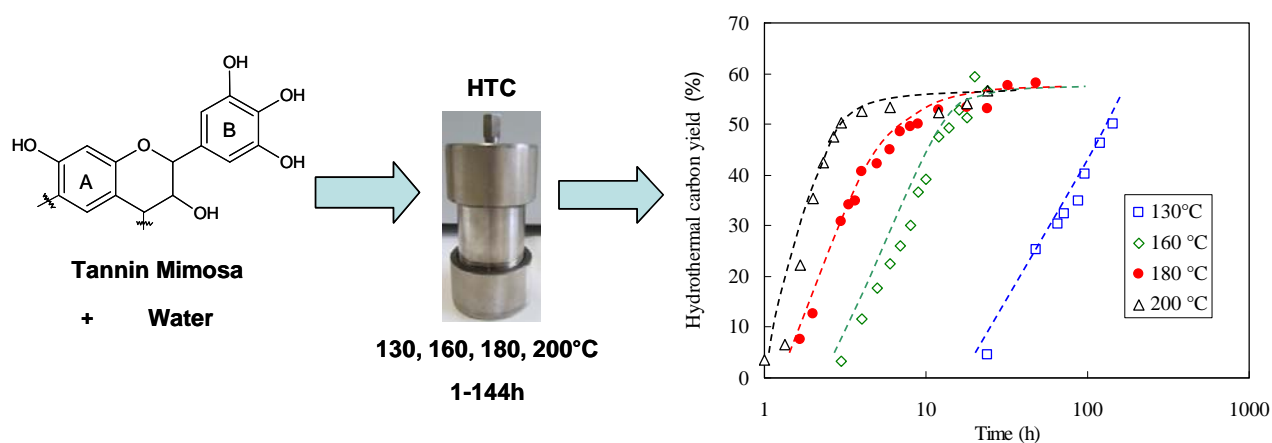


Fig. 26: Graphical procedure for the synthesis of hydrochars made from tannin.

## 2.1 Hydrochar synthesis and yield determination

In a typical synthesis, 0.5g of tannin were dissolved in 16g of water and introduced in an open glass vial in order to prevent autoclave contamination. The vial was then placed in a Teflon®-lined stainless steel autoclave for HTC. The inner volume of the autoclave was 50  $\text{cm}^3$ , so that the volume of liquid placed inside was exactly 1/3 of its capacity, taking the volume of the glass vial into account. The autoclave was directly installed in a ventilated oven pre-heated at different temperatures: 130, 160, 180 or 200°C. After different reaction times depending on the temperature, ranging from 1 to 144h, the autoclave was left to cool down at room temperature. The obtained solids were then separated from the remaining aqueous solution by centrifugation (6800 rpm for 20 min) and placed inside a vacuum oven at 80°C for drying before characterisation. Wattle tannin, which is a light-brown powder before



hydrothermal treatment, progressively turned to reddish brown and black when increasing the severity of HTC conditions, i.e., reaction time and temperature (see Fig. 27).

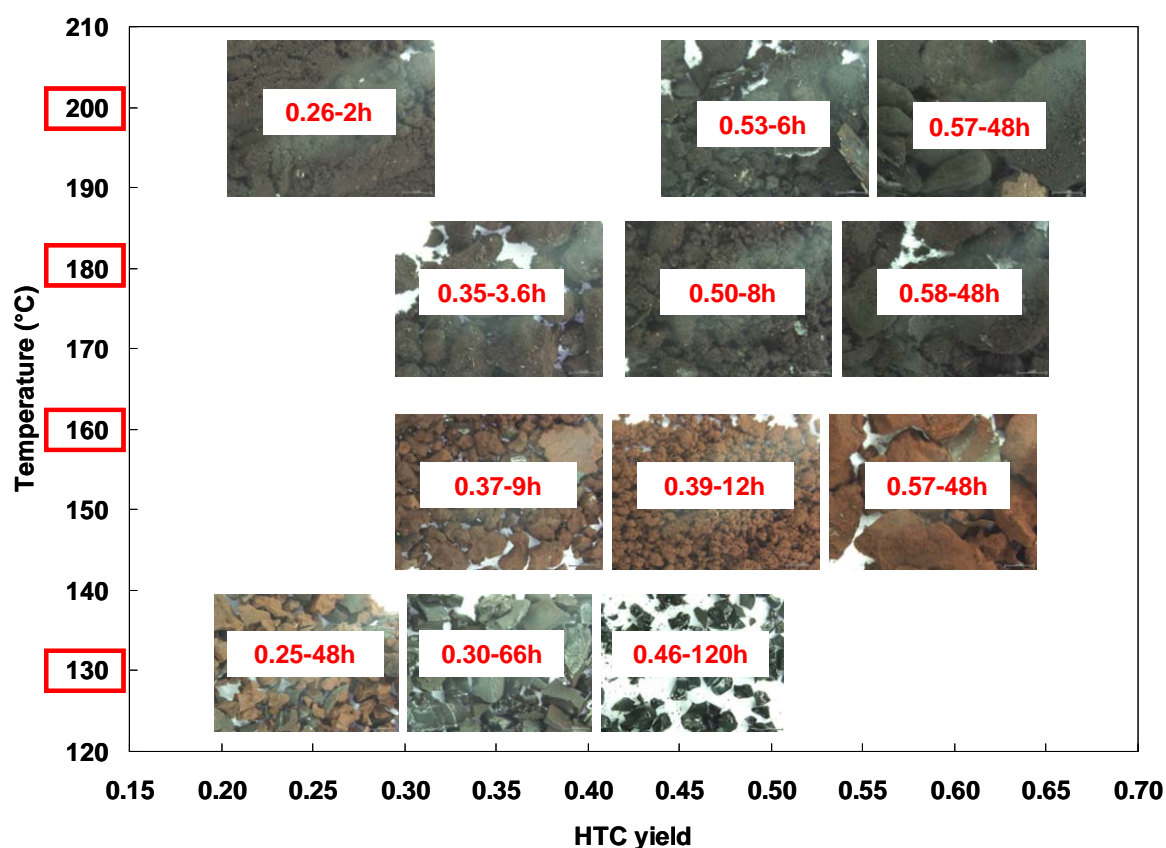
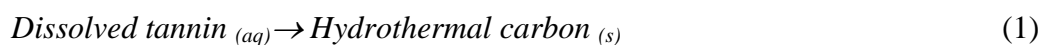


Fig. 27: Hydrochars obtained at different experimental conditions.

In the present case, the reactant was tannin initially dissolved in water, which was gradually converted into solid according to the following, deliberately simplified, HTC reaction:



No gaseous products were formed, as proved by the absence of pressure when opening the autoclave once cooled after the experiment. In Eq. (1), the subscripts *aq* and *s* mean aqueous and solid, respectively. In our experiments, for a given known, initial mass of tannin in the solution,  $m_T$ , only the mass of resultant hydrothermal carbon,  $m_{HTC(t)}$ , was measured after a HTC time  $t$ . Few particles were suspected to remain in the filtrate and could not be recovered by centrifugation, so they were not considered for calculating the yield. This mass takes into account only the solid part that could be recovered by centrifugation; the solid part that was still present in the filtrate was not considered in the  $m_{HTC}$  determination according to our definition. The filtrate has been observed by TEM (Fig. 28) for HTC experiments leading to

low carbon yields (< 10%). It is composed of spherical particles with a diameter ranging from 100 to 200 nm and a rather hollow core surrounded by dense and rough shell. These particles might correspond to the primary particles of hydrothermal carbon as discussed later.

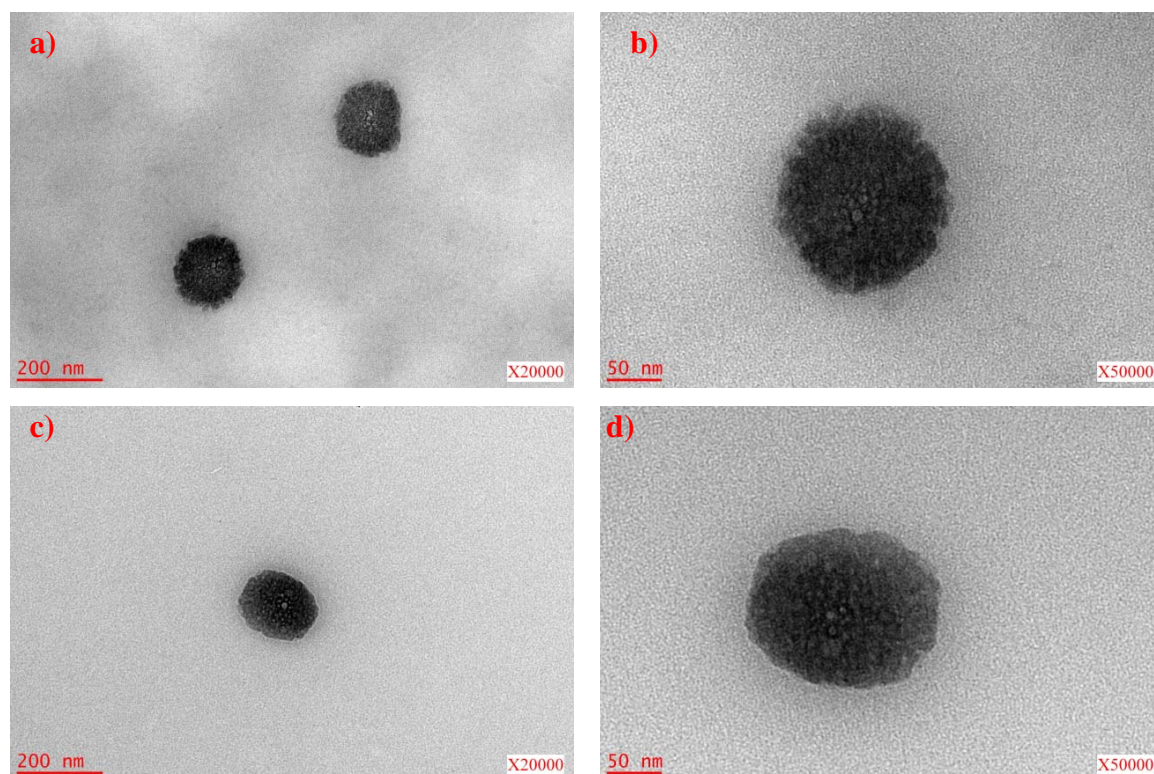


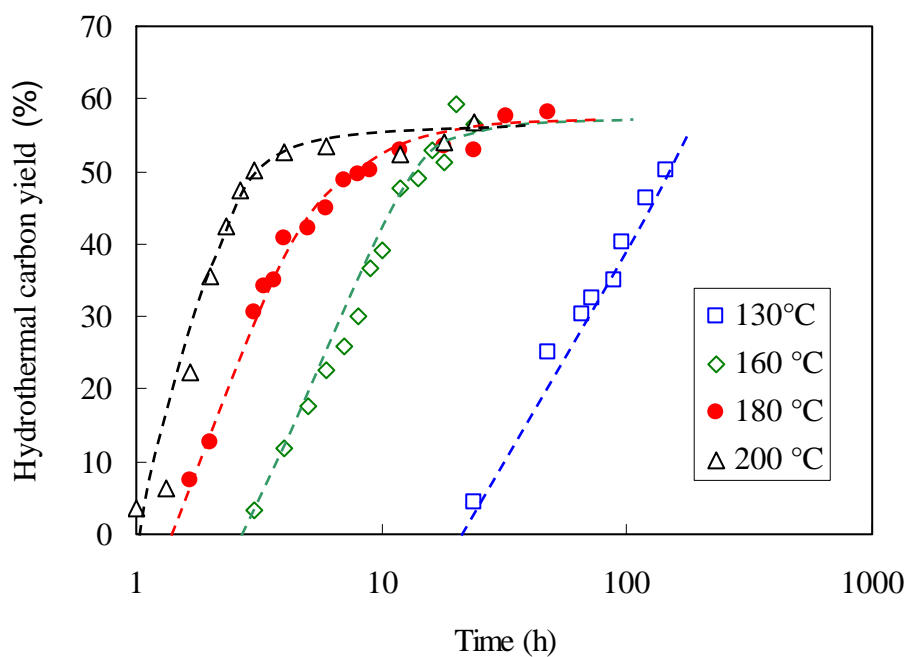
Fig. 28: TEM images of the particles that could not be recovered by centrifugation, thus remaining in the filtrate after HTC of 0.5 g tannin in 16 mL of water for: (a) and (b) 24 h at 130°C; (c) and (d) 1 h 20' at 200°C.

Soluble species possibly adsorbed at the surface of the HTC material were also neglected, considering the very low surface area of the materials. Then the hydrothermal carbon yield,  $Y(t)$ , was calculated as a function of time for all the different experimental conditions which were tested, according to:

$$Y(t) = \frac{m_{HTC}(t)}{m_T} \times 100 \quad (2)$$

Fig. 29(a) presents the measured carbon yields as a function of time and temperature of hydrothermal treatment, using an initial amount of tannin of 0.5g. The maximum yield remained constant around  $58 \pm 1\%$ , whatever the temperature. As temperature increased, such final carbon yield was reached at lower reaction times. Before the maximum was reached, at a fixed reaction time, the yield increased with HTC temperature. The colour of hydrothermally treated materials also changed when the temperature increased (see Fig. 27).

a)



b)

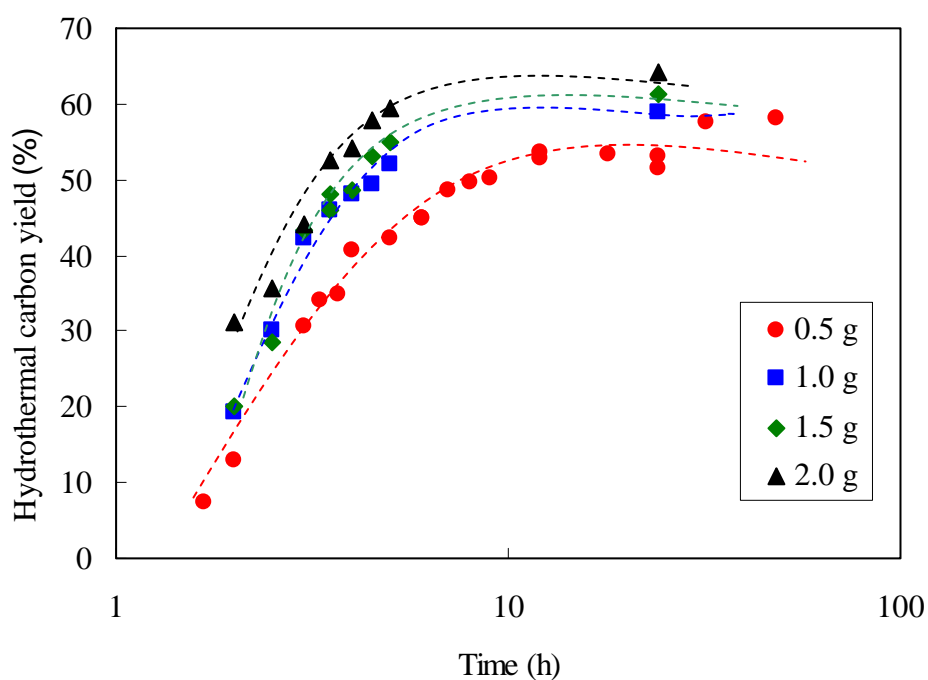


Fig. 29: Hydrothermal carbon yield (a) at different HTC temperatures, as a function of reaction time (initial amount of tannin: 0.5 g in 16 mL of water); (b) as a function of HTC time at 180°C for different initial amounts of tannin. The data points are here connected by a dot line to guide the eye.

The increase of yield with HTC temperature was also reported by Ryu et al. (2010) when increasing the HTC temperature of fructose and xylose from 130 to 170°C. The same trend was found by Sevilla and Fuertes (2009b) who submitted to HTC cellulose and a microalgae at 230 and 250°C, and at 180 and 220°C, respectively [Sevilla and Fuertes 2009b; Falco et al. 2012]. Falco et al. (2011) reported a more complex temperature dependence of yield, studying the HTC of other precursors such as glucose, cellulose, lignin and rye straw. The case of glucose was the most similar to that of tannin, with the same increase of the yield up to a maximum when the temperature increased up to 200°C. Likewise, almost no solid residue was obtained at low temperature, i.e. below 160°C and below 130°C for glucose and tannin, respectively. Such small difference is related to a difference of solubility [Falco et al. 2011], glucose being more soluble in water than tannin, thus requiring a slightly higher HTC temperature for nucleating solid particles from the solution. The effect on carbon yield of the amount of tannin dissolved in the solution submitted to HTC was also investigated at a fixed temperature of 180°C. As seen in Fig. 29(b), the HTC yield increased with the amount of tannin at a given reaction time and reached a plateau. Such plateau corresponded to HTC yields of 58, 59, 61 and 64 wt.% using 0.5, 1.0, 1.5 and 2.0 g of tannin in 16mL of water, respectively.

## 2.2 Chemical composition

The results of EA and XPS of some samples obtained at different yields by a combination of various reaction times and temperatures are shown in Table 2. Part of the data of this table was used to plot the Fig. 30, and no significant change in the weight percent of carbon in the solids obtained after HTC could be seen. Likewise, no clear trend was observed when the yield increased, and the same was found when oxygen was considered. Therefore, it can be assumed that the composition of hydrothermal carbons derived from tannin in the experimental conditions reported in this work was constant, and that higher temperatures or reaction times only led to higher amounts of solid. The average of all data of C (%) measured by EA was 59.7 wt.%. This value was used for kinetics studies.

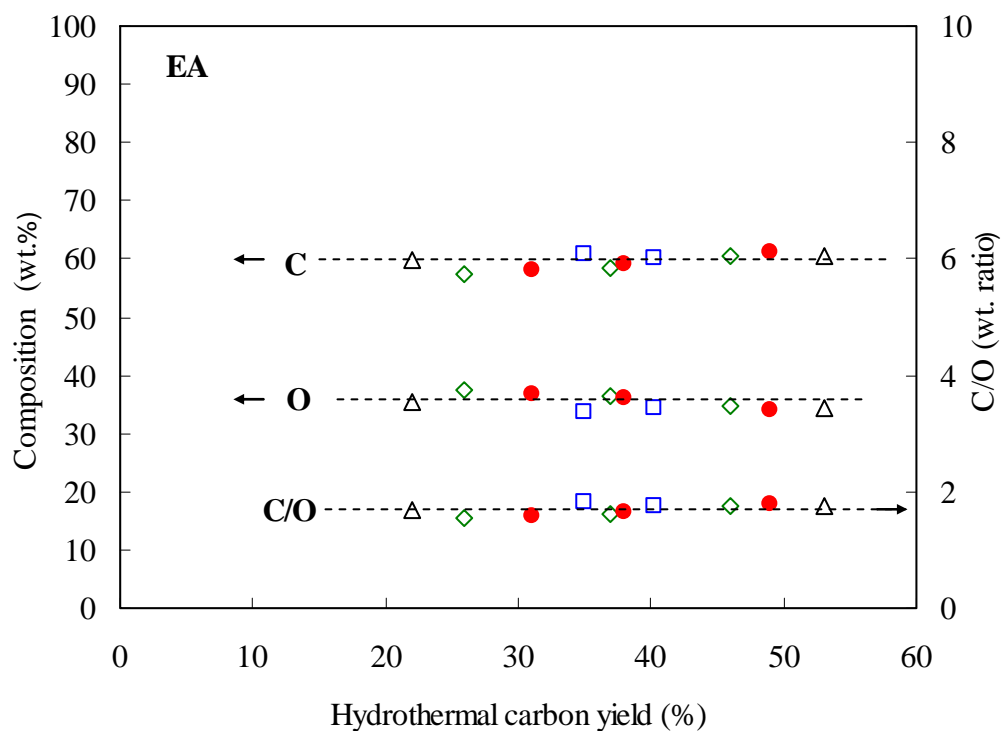
Table 2: Ultimate analysis of hydrothermal carbons, and C/O and C/H weight ratios.

HTC yield (%)	t (h)	T (°C)	<i>EA</i>							<i>XPS</i>		
			C (wt.%)	H (wt.%)	N (wt.%)	S (wt.%)	O* (wt.%)	C/O	C/H	C (wt.%)	O (wt.%)	C/O
22	1.7	200	59.9	4.1	0.6	0.0	35.4	1.7	14.6	81.2	18.8	4.3
26	7	160	57.5	4.5	0.4	0.0	37.6	1.5	12.7	80.9	19.1	4.2
31	3	180	58.2	4.4	0.7	0.0	36.7	1.6	13.2	82.1	17.9	4.6
35	88	130	60.9	4.9	0.4	0.0	33.8	1.8	12.4	81.1	18.9	4.3
37	9	160	58.6	4.5	0.4	0.0	36.5	1.6	13.0	79.6	20.4	3.9
38	4	180	59.1	4.3	0.5	0.0	36.1	1.6	13.7	82.2	17.8	4.6
40	96	130	60.3	4.8	0.5	0.0	34.4	1.8	12.6	80.8	19.2	4.2
46	14	160	60.5	4.3	0.5	0.0	34.7	1.7	14.0	80.0	20.2	4.0
49	7	180	61.3	4.2	0.5	0.0	34.0	1.8	14.6	80.9	19.1	4.2
53	12	200	60.5	4.6	0.5	0.0	34.4	1.8	13.2	82.1	17.9	4.6

\* measured by difference

Steadiness of C and O contents whatever the HTC conditions was also observed from XPS analysis. However, the carbon content was always higher when measured by XPS (e.g. the weight ratio C/O was  $\sim 2$  by EA compared to  $\sim 3$  by XPS). This finding clearly indicates that the surface of hydrothermal carbons derived from tannin was less oxidised than the interior. O content measured by EA was indeed 35.7 wt.% on average, a value somewhat higher than that determined by XPS, 23.7 wt.% on average. Such values are in agreement with measurements from other authors: 27.3 and 31.1 wt.% for xylose and sucrose submitted to HTC at 180°C for 24 h [Titirici et al. 2008], and between 31.6 and 40.9 wt.% in carbon spheres derived from HTC of xylose and fructose in the presence of phenolic compounds at 130 or 170°C for 12 h [Ryu et al. 2010]. In Ryu et al. (2010), just like in this case, the O amount determined by XPS at the surface of the microspheres, ranging from 22.4 to 25.3 wt.%, was lower than what was measured by EA, 33.7 to 37.5 wt.%. Table 3 compares the elemental analyses of pristine tannin on one hand, and the average of the data of all resultant hydrothermal carbons on the other hand. As expected, the weight fraction of carbon increased after HTC, but it was only around 6 % higher as pristine tannin contains 53.8% of carbon.

a)



b)

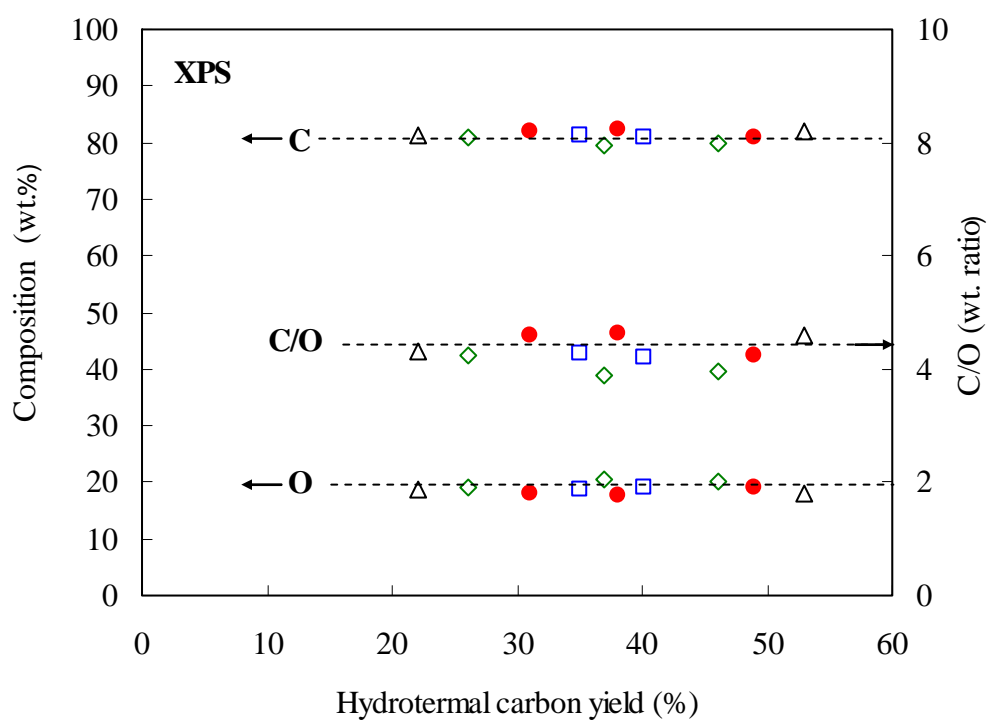


Fig. 30: Chemical composition of all tannin-derived hydrothermal carbons as a function of carbon yield: (a) from elemental analysis (EA); (b) from XPS.

Table 3: Elemental analysis (wt.%) of tannin before and after HTC.

	C	H	N	S	O*
Raw tannin	53.8	5.4	0.6	0.1	40.1
Average of all hydrothermal carbons	59.7	4.5	0.5	0	35.7

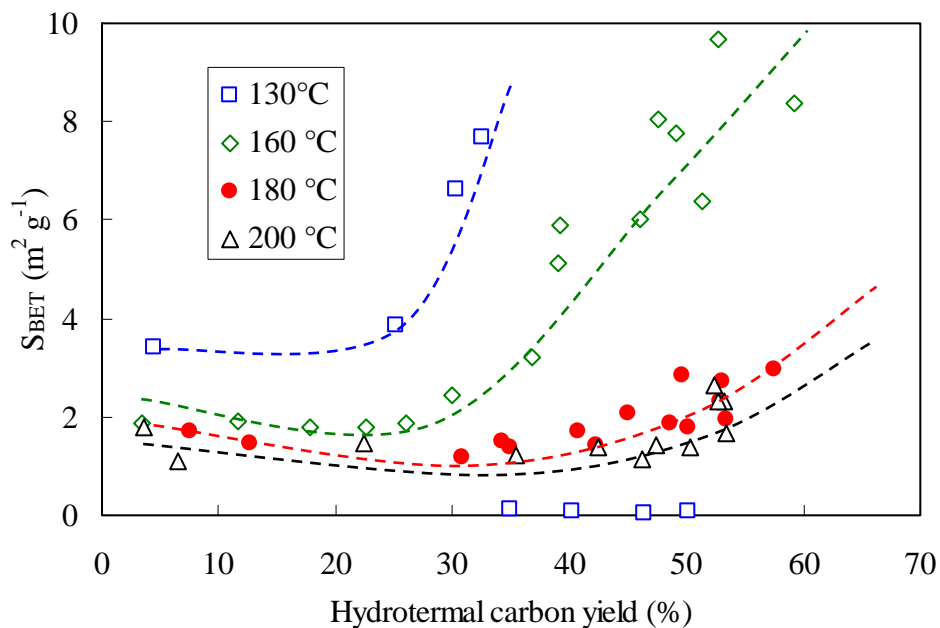
\* measured by difference

### 2.3 Materials' morphology and particle size

Fig. 31 gathers the data of specific surface areas,  $S_{\text{BET}}$ , determined by Kr adsorption at -196°C. The typical error for this kind of measurements is less than 5%. Two cases were considered: (a) different HTC temperatures at constant initial amount of tannin, and (b) different amounts of tannin at the same HTC temperature. For both cases,  $S_{\text{BET}}$  of hydrothermal carbons were all below  $10 \text{ m}^2 \text{ g}^{-1}$ , suggesting the absence of porosity, and exhibited a complex behaviour. At a given hydrothermal carbon yield, i.e., at a given reaction time,  $S_{\text{BET}}$  decreased when the HTC temperature increased. Such a finding should be related to the growth of hydrothermal particles, leading to a lower surface area, and will be confirmed below by TEM observations in Fig. 35.

For temperatures higher than 130°C, a shallow minimum of  $S_{\text{BET}}$  was observed at values of carbon yield around 30 – 40%, see again Fig. 31(a). However, the main trend was an increase of  $S_{\text{BET}}$  with the yield, and hence with the HTC time. Such findings may be interpreted as follows. When HTC goes on, carbon particles are continuously nucleated from the solution, hence the resultant, broad, distribution of sizes seen by TEM pictures in Figs. 31-33. At the moment at which they appear, these particles are very small and hence present a rather high surface area. During HTC, an antagonistic effect also occurs, consisting in the growth and coalescence of hydrothermal carbon particles, and leading to a decrease of  $S_{\text{BET}}$ . If the nucleation of carbon particles is faster than their growth and coalescence, then the surface area is expected to increase with time, on average, with a possible minimum when both effects compensate, as shown in Fig. 31. Finally, and according to Fig. 31(b), the behaviour remained qualitatively the same when the amount of tannin increased at the same HTC temperature, but  $S_{\text{BET}}$  decreased. It can be indeed expected that a higher concentration of precursor leads to bigger carbon particles, thus exhibiting lower surface areas. All these assumptions agree well with TEM images (Figs. 31-33).

a)



b)

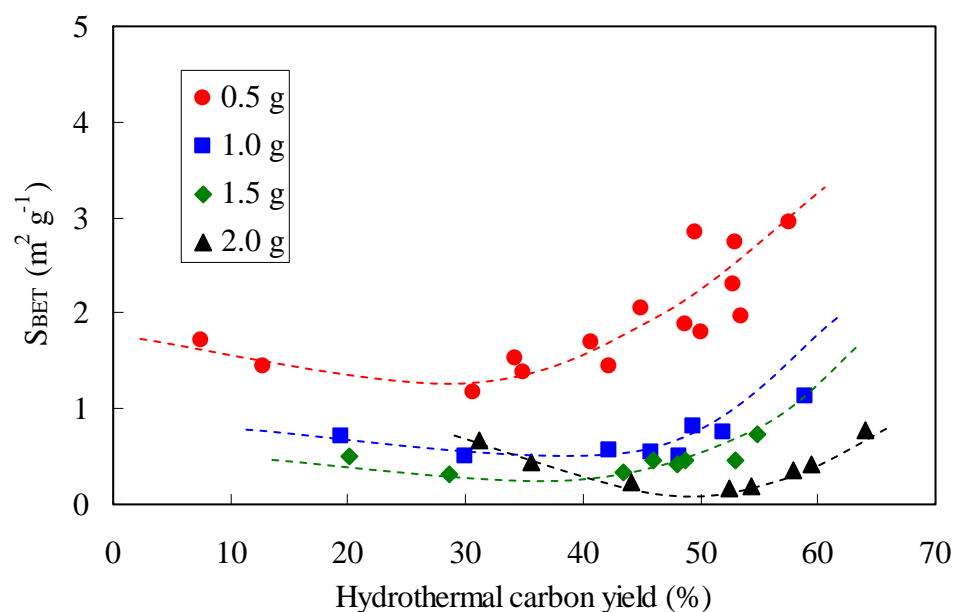


Fig. 31: Surface area,  $S_{BET}$ , of hydrothermal carbons derived from tannin and plotted as a function of yield: (a) at different HTC temperatures and constant initial amount of tannin of 0.5 g; (b) at the same HTC temperature of 180°C and different initial amounts of tannin.



Different values of  $S_{\text{BET}}$ , depending on the material and on the conditions of HTC, have been reported in the literature. Titirici et al. (2007b) reported  $S_{\text{BET}}$  of  $15.5 \text{ m}^2 \text{ g}^{-1}$  after HTC of oak leaves at  $200^\circ\text{C}$ . The hydrothermal carbon derived from a mixture of glucose and an amino-acid, L-cysteine, presented no porosity after HTC at  $180^\circ\text{C}$ , but the porosity could be developed by pyrolysis, making the value of  $S_{\text{BET}}$  increase up to  $730 \text{ m}^2 \text{ g}^{-1}$  [Wohlgemuth et al. 2012b]. In contrast, the  $S_{\text{BET}}$  of pinewood submitted to HTC was found to be 21 and  $29 \text{ m}^2 \text{ g}^{-1}$  before and after carbonization, respectively [Liu et al. 2010b].  $S_{\text{BET}}$  after HTC thus seems to depend on the reactivity of the precursor with respect to dehydration and subsequent condensation [Mumme et al. 2011]. In our case, slower reaction kinetics observed at lower temperatures, and lower initial masses of tannin, promoted higher surfaces areas.

Fig. 32 shows the skeletal density of all the materials prepared in this work by HTC of tannin. Whatever the yield, and in agreement with the previous elemental analyses, the skeletal density was found to have a constant value close to  $1.50 \text{ g cm}^{-3}$ . The scattering of the data was much higher at low yield, with values sometimes as high as  $1.95 \text{ g cm}^{-3}$ . In our opinion, these discrepancies are related to the very low amounts of hydrothermal carbon which were recovered at low yield, and which were not enough to fill the chamber of the pycnometer. Therefore, the experimental error in the determination of skeletal density was much higher.

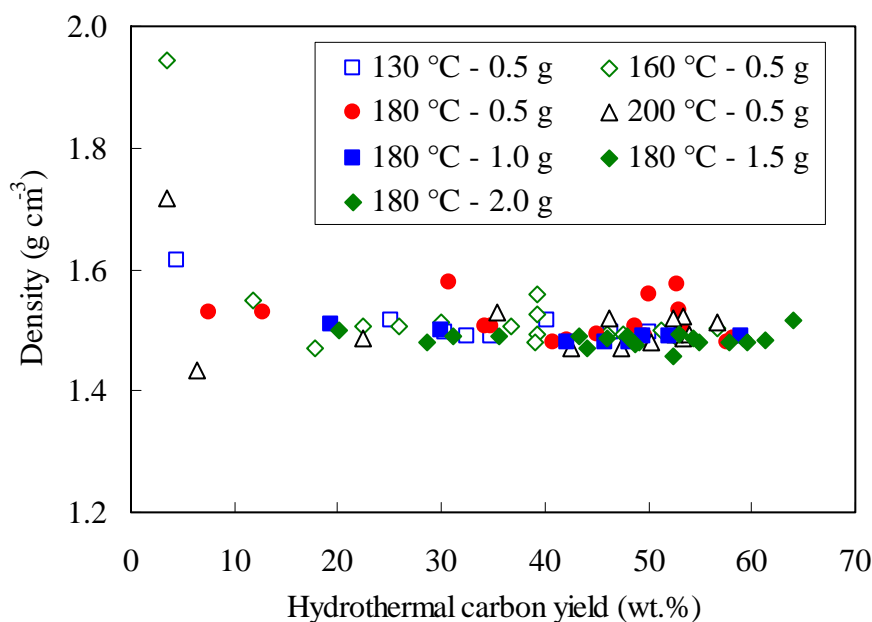


Fig. 32: Skeletal density of hydrothermal carbons as a function of yield for all different HTC temperatures and different amounts of tannin used in this work.

## 2.4 Effect of the reaction time

Fig. 33 shows materials produced at 200°C with an initial tannin mass of 0.5g and different reaction times: 6, 12 and 24 h. As the reaction time increased, the spherical forms were better defined but they were perfectly formed and rounded at 24h, i.e. at the end of the reaction, as suggested by the data at 200°C shown in Fig. 29(a). However, these spherical particles were very heterogeneous in diameter, which varied from 200 nm to 5  $\mu\text{m}$ , in good agreement with the nanostructures formed after HTC process [Hu et al. 2010 and ref. therein].

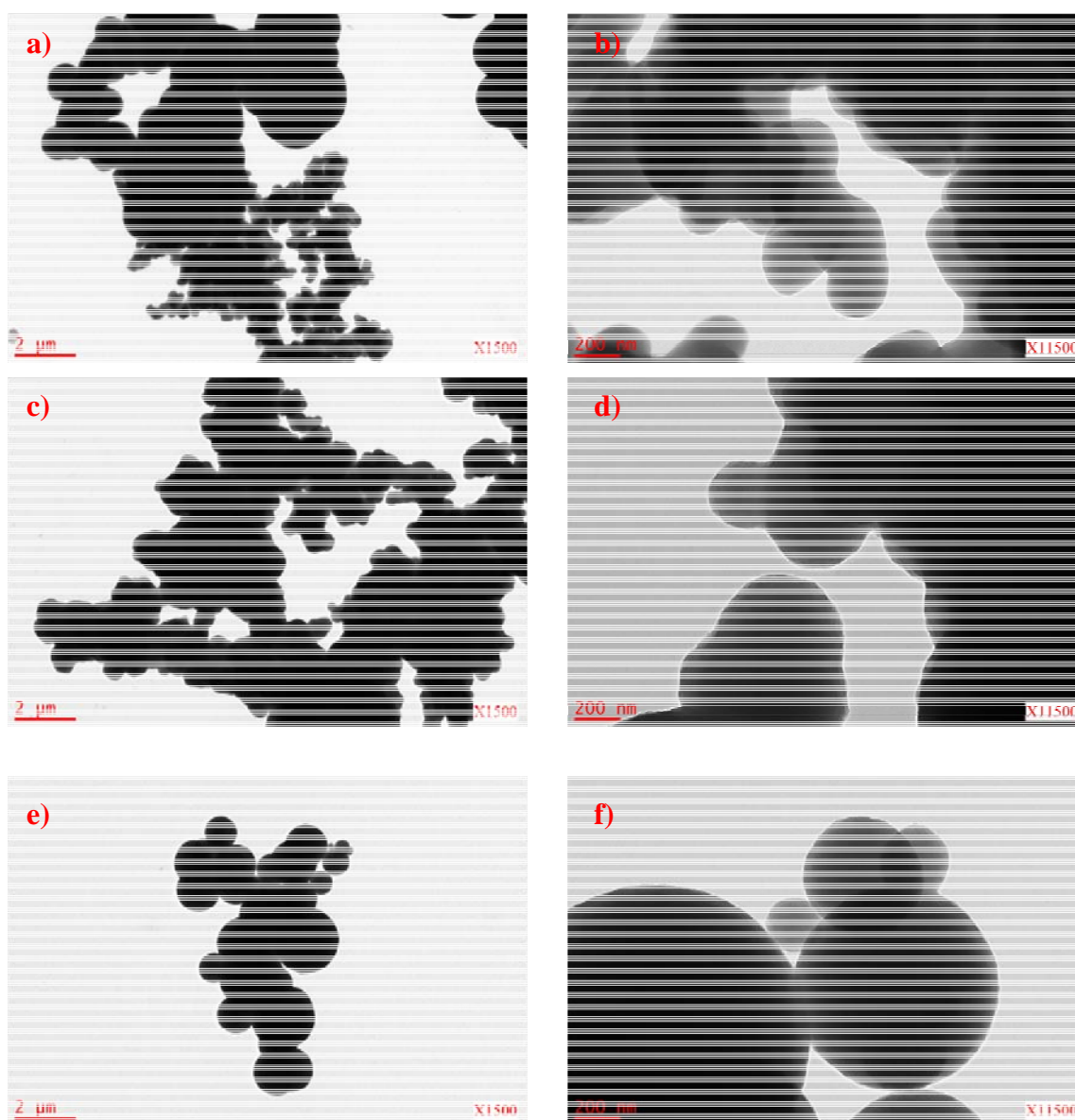


Fig. 33: TEM images of the hydrothermal carbons produced at 200°C using 0.5g of tannin in 16 mL of water during different HTC times: (a) and (b) 6h; (c) and (d) 12 h; (e) and (f) 24h.

Based on Eq. (3), equivalent particle diameters were estimated, using the data shown in Fig. 31 and 32. The equivalent average diameters,  $d$  ( $\mu\text{m}$ ), of hydrothermal carbon particles, assumed to be non-porous were estimated according to Rouquerol et al. (1999).

$$d = \frac{6}{\rho_s S_{BET}} \quad (3)$$

The results were 0.97, 1.72 and 1.74  $\mu\text{m}$  for materials produced by HTC of 0.5 g of tannin at 200°C during 6, 12 and 24 h, respectively. Such values can be compared to what can be seen in Fig. 33(a), 33(b) and 33(c), respectively. Although the comparison is not obvious because of the heterogeneity of the particle sizes, the trend and the order of magnitude were both correct, suggesting that the assumption of non porous particles was realistic.

### 2.5 Effect of the tannin concentration

TEM pictures of hydrothermal carbons obtained at 180°C and after 24h of HTC, using different initial amounts of tannin: 0.5, 1, 1.5 and 2.0g are shown in Fig. 34. The particles had a spherical shape and a heterogeneous distribution of sizes at lower reaction time seen in the previous discussion, but the average diameters clearly increased with the initial mass of tannin.

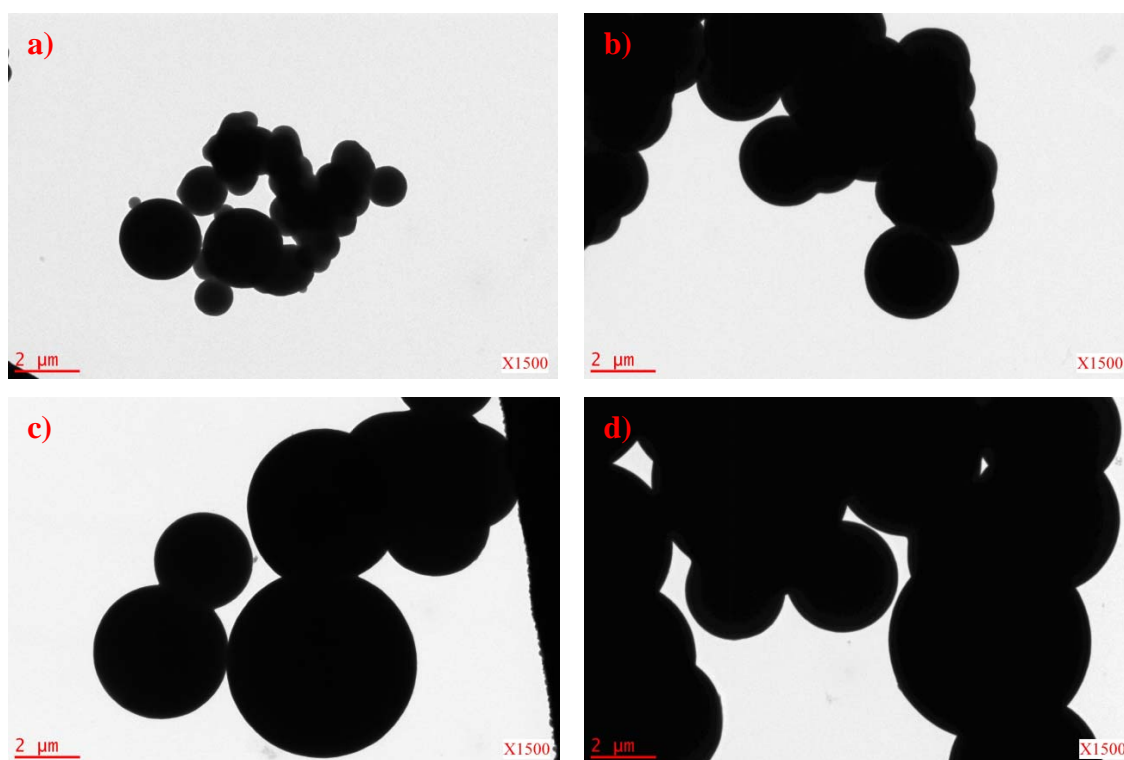


Fig. 34: TEM images of the hydrothermal carbons produced at 180°C during 24h, using different initial amounts of tannin: (a) 0.5g; (b) 1.0g; (c) 1.5g, (d) 2.0g.

Using the software Image Pro-Plus 6.0 and assuming particles having a perfect spherical shape, the average particle diameter was calculated and found to have the following values:  $1.6 \mu\text{m}$  (0.5 g) <  $2.4 \mu\text{m}$  (1.0 g) <  $3.7 \mu\text{m}$  (1.5 g) <  $4.4 \mu\text{m}$  (2.0 g). Application of Eq. (3) led to rather similar results:  $1.8 \mu\text{m}$  (0.5 g) <  $3.5 \mu\text{m}$  (1.0 g) <  $5.5 \mu\text{m}$  (1.5 g)  $\approx$   $5.1 \mu\text{m}$  (2.0 g). It has also been suggested elsewhere that the final size of the particles after HTC are indeed affected by the precursor concentration [Titirici and Antonietti 2010]. Such findings explain and confirm the decrease of surface area when the amount of precursor increased, which was observed in Fig. 31(b).

## 2.6 Effect of the temperature

Finally, the materials obtained at different HTC temperatures but at constant initial amount of tannin, 0.5 g, and constant reaction time of 24 h, are shown in Fig. 35. As temperature increased, the particles got more and more spherical shapes and presented increasingly high diameters. Fig. 35(a) indeed shows irregular contours, suggesting that HTC reaction was not finished at  $160^\circ\text{C}$  after 24 h as also shown by Fig. 29(a), whereas the contours were very clear and circular in Fig. 35(c). Application of Eq. (3) led to the following results:  $0.6 \mu\text{m}$  ( $160^\circ\text{C}$ ) <  $1.8 \mu\text{m}$  ( $180^\circ\text{C}$ ) <  $2.2 \mu\text{m}$  ( $200^\circ\text{C}$ ), in reasonable agreement with Fig. 35.

Falco et al. (2011) reported the same trends. Increasing the temperature indeed led to larger and more spherical particles in the case of glucose at  $260^\circ\text{C}$ . These results confirm and explain the decrease of  $S_{\text{BET}}$  which was observed in Fig. 31(a) when the HTC temperature increased, all other things being equal. It is suggested that coalescence of particles and coarsening by precipitation of soluble tannin occur, successively at  $130^\circ\text{C}$  and simultaneously at  $200^\circ\text{C}$ , with an intermediary regime between  $130$  and  $200^\circ\text{C}$  as seen in Fig. 35. Therefore, for a similar HTC yield, aggregated small particles are rather observed at  $130^\circ\text{C}$  whereas bigger spherical particles are present at  $200^\circ\text{C}$ . An Ostwald ripening mechanism, a phenomenon seen during the HTC reaction in which small solid particles are constantly produced in aqueous solution and are then deposited onto larger sol particles already formed might also occur.

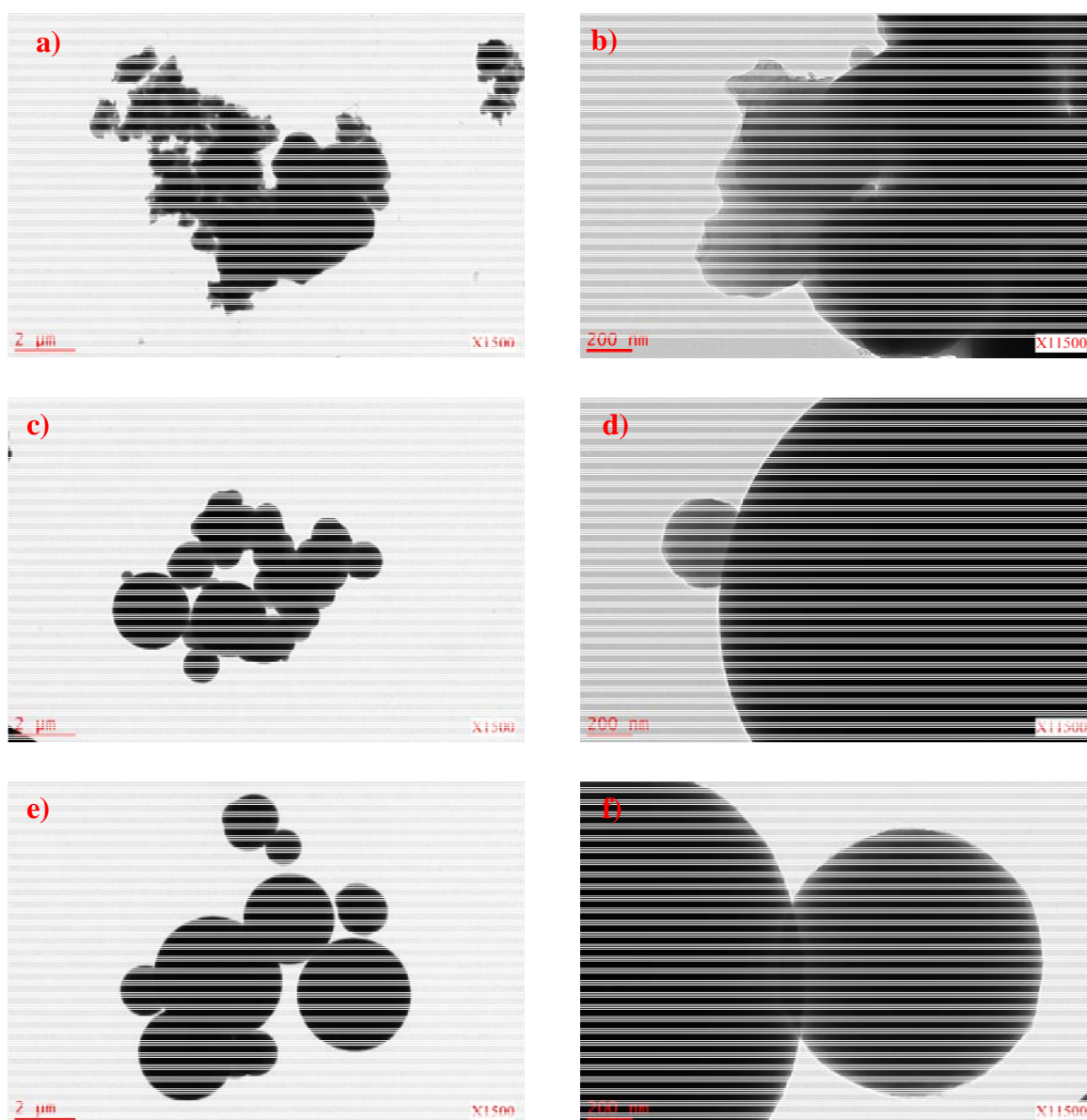


Fig. 35: TEM images of the hydrothermal carbons produced at different HTC temperatures, using constant initial amount of tannin, 0.5g, and reaction time, 24 h: (a) and (b) 160°C; (c) and (d) 180°C; (e) and (f) 200°C.

## 2.7 Proposed mechanism for particle formation

Some experiments carried out at 130°C (see Fig. 31(a)), showed unusual behaviour with a surface area that abruptly decreased from around  $10 \text{ m}^2 \text{ g}^{-1}$  to  $0.1 \text{ m}^2 \text{ g}^{-1}$  as the carbon yield exceeded 35%, i.e. for reaction times higher than 66 h. Fig. 36 shows TEM photos of such materials prepared at 130°C and for different HTC times: 48h (a and b) and 120h (c and d). Clear morphologic differences could be observed between those two samples: small particles (200-400 nm) highly agglomerated into micrometric particles for the short reaction time and a

a glassy morphology composed of dense and homogenous distributed matter for long reaction time.

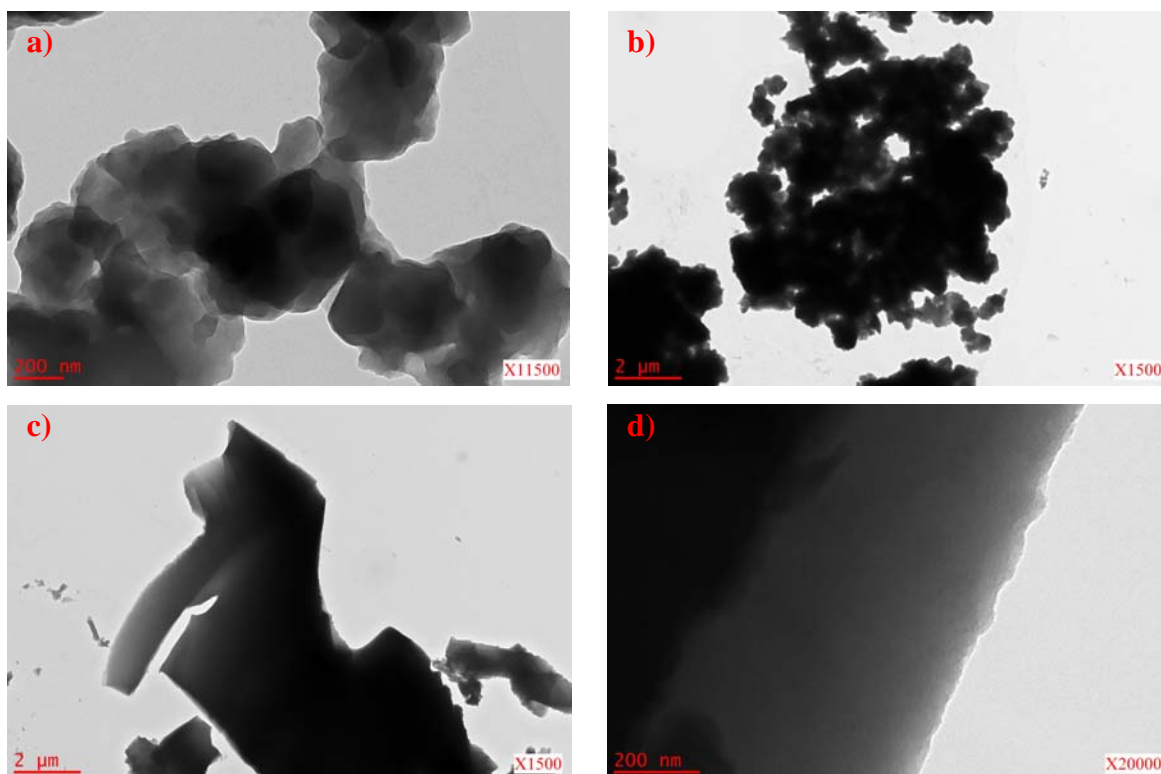


Fig. 36: TEM images of the hydrothermal carbons produced at 130°C with 0.5 g of tannin in 16 mL of water for different HTC times: (a) and (b) 48 h; (c) and (d) 120 h.

A tentative explanation for such structural evolution, not observed for materials prepared in other conditions, might explain the observed vanishing of surface area. During the hydrothermal treatment, different processes occur more or less simultaneously:

- i) Formation of soluble and modified tannin molecules of high molecular weight by different reactions such as dehydration and condensation reactions,
- ii) Formation of primary particles (size around 100 - 200 nm) as observed for instance by TEM for low carbon yields (Fig. 28) at can be separated by centrifugation.
- iii) Coalescence of particles (by primary – primary particle aggregation (a) and/or primary – secondary particles aggregation (b)) (see Fig. 37);
- iv) Precipitation of the soluble fraction of polymerized hydrothermally-modified tannin onto those particles. It leads (a) to an increase of the particle's roughness in a first step with an increase of the surface area and (b) when the growth is pushed forward, to a

significant increase of the particle size with a decrease of their surface area (see Fig. 37).

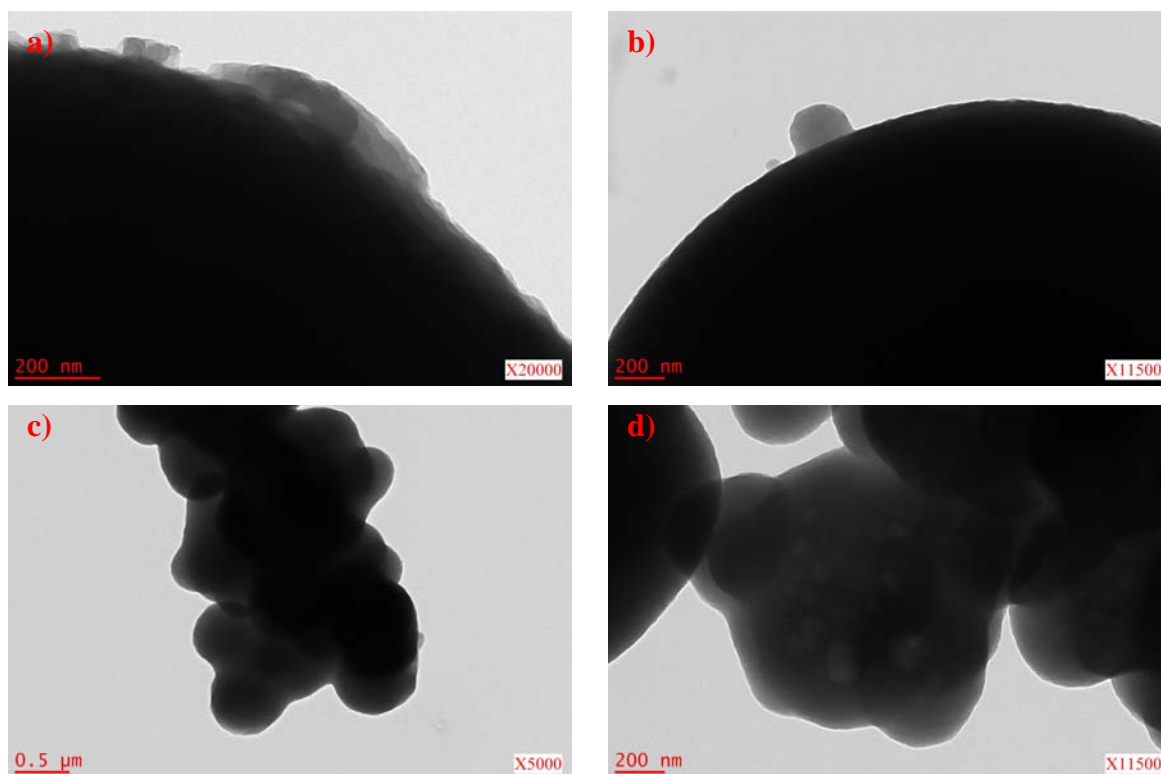


Fig. 37: TEM images of hydrothermal carbons showing: (iii) aggregation of primary carbon particles onto secondary particles produced at a) 180°C for 24 h with 1.5 g of tannin and b) 180°C for 24 h with 2.0 g of tannin; (iv) aggregation of primary carbon particles with precipitation of hydrothermally treated tannin produced at c) 160°C for 5 h with 0.5 g of tannin and d) 200°C for 6 h with 0.5 g of tannin

Those different phenomena appear to be more decoupled at 130°C compared to higher temperatures ( $T \geq 160^\circ\text{C}$ ) where they occur rather simultaneously and lead to different morphologies. At 130°C, for reaction times below 66 h, newly formed primary particles (process ii) and their subsequent aggregation (process iii) associated to polymers precipitation onto their surface (process iv.a)) increase respectively the HTC yield and their surface roughness with an increase of the surface area up to  $10 \text{ m}^2 \text{ g}^{-1}$  (see Fig. 31(a)). It seems here that the growth of the primary particles by precipitation of soluble polymeric hydrothermally-modified tannin units onto those particles (process iv.b)) does not occur at this step. After 66 h and a sufficient maturation of the solution, the process iv.b) appears to mainly happen with a significant fraction of condensed tannin present in the supernatant that precipitates onto those aggregates and acts as glue, closing the porosity. This phenomenon results in dense, shapeless and glassy big particles (see Fig. 37(b)). The surface area drops then suddenly to a



value close to zero. For higher temperature, the process iv.b) is associated with the others and allows the growth of large spherical particles with a diameter up to 5 $\mu$ m.

## 2.8 Kinetics study

Kinetics laws express the way the concentration of a reactant decreases with time. Since the volume of solution was always constant, the decrease of reactant concentration, i.e. of tannin in the solution, was followed as a function of HTC time by calculating the amount of elemental carbon,  $C(t)$ , remaining in the solution. Such amount reads:

$$C(t) = C \text{ in the initial solution} - C \text{ in the resultant solid} \quad (4)$$

Carbon fractions in pristine tannin,  $F_{C(T)}$ , and in hydrothermal carbons,  $F_{C(HTC)}$ , being both determined by elemental analysis (see above), Eq. (4) can be rewritten as:

$$C(t) = m_T \times F_{C(T)} - m_{HTC} \times F_{C(HTC)} \quad (5)$$

Combining Eqs. (4) and (5), one finally gets:

$$C(t) = m_T \times [F_{C(T)} - Y(t) \times F_{C(HTC)}] \quad (6)$$

The curves  $C(t)$  were then plotted for different initial conditions corresponding to HTC experiments carried out at 180°C with four initial masses of tannin: 0.5, 1.0, 1.5 and 2.0g in order to determine the kinetic law. For that purpose, the simple, following, equation was assumed and tested:

$$r = k [C]^n \quad (7)$$

wherein  $r$  is the reaction rate,  $k$  is the kinetic constant and  $n$  is the order with respect to elemental carbon in the solution, hence with respect to tannin since both are strictly proportional. If Eq. (7) applies, then the initial reaction rate  $r_0$ , i.e. near  $t = 0$ , obeys:

$$\log r_0 = \log k + n \log C_0 \quad (8)$$

in which  $C_0$  is the initial amount of elemental carbon dissolved in the solution, i.e. before HTC started. In other words, plotting  $\log r_0$  versus  $\log C_0$  should be a straight line whose intercept and slope are  $\log k$  and  $n$ , respectively.

Such reaction order should not depend on the temperature, except if a change of reaction mechanism occurs, which is very unlikely within the experimental temperature range 130 – 200°C. Moreover, all the resultant materials were found to have constant composition and density, excluding some changes in their formation mechanisms. Thus, by using a constant initial amount of tannin of 0.5g in 16mL of water submitted to HTC at different temperatures,



the changes of the kinetic constant  $k$  can be determined. Doing so, the activation energy of the HTC process of tannin in water can be obtained by application of Arrhenius equation:

$$k = A \exp\left(-\frac{E_a}{RT}\right) \quad (9)$$

in which  $A$  is the pre-exponential factor,  $R$  is the universal gas constant and  $T$  is the HTC temperature.

The decrease of carbon content in the solution submitted to hydrothermal treatment, corresponding to the conversion of soluble tannin into solid carbonaceous particles according to Eq. (2), has been calculated by application of Eq. (6). For that purpose, the weight fractions of carbon in tannin and in hydrothermal carbon measured were used,  $F_{C(T)} = 53.8\%$  and  $F_{C(HTC)} = 59.7\%$ , respectively. Fig. 38(a) shows the corresponding curves  $C(t)$  which were plotted for HTC experiments carried out at  $180^\circ\text{C}$  with four initial masses of tannin: 0.5, 1.0, 1.5 and 2.0 g. The initial reaction rates,  $r_0$ , were thus determined as the slopes of the linear parts of the curves at low values of  $t$ , as explained in Fig. 38(b).

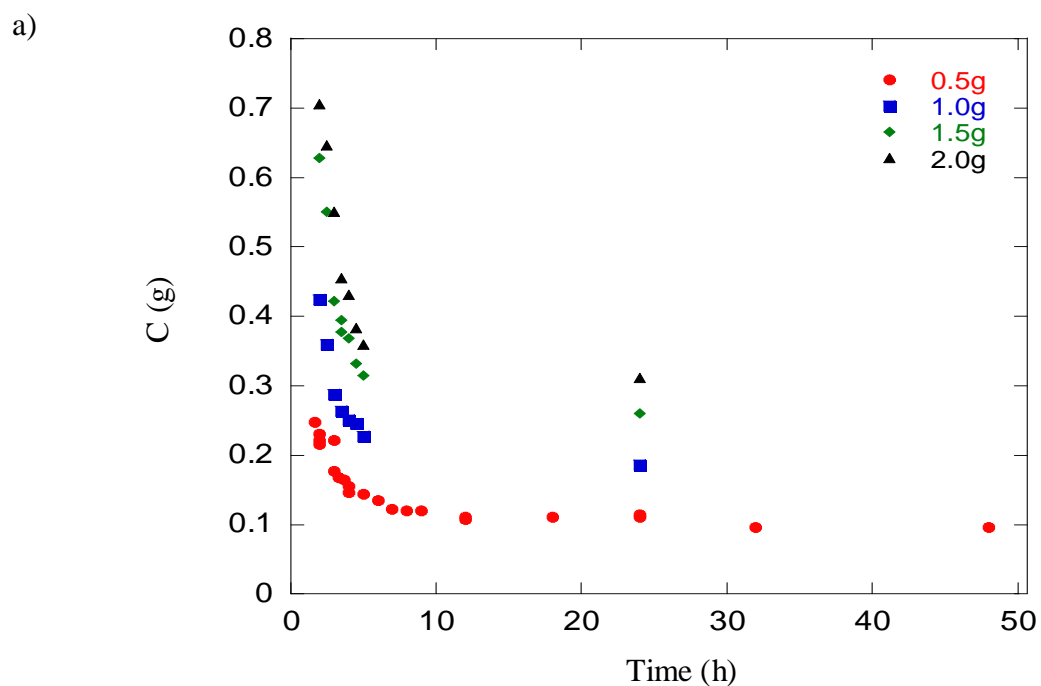
The initial reaction rates,  $r_0$ , determined from Fig. 38(a) were 0.038, 0.111, 0.165 and  $0.170 \text{ g h}^{-1}$  for initial amounts of tannin of 0.5, 1.0, 1.5 and 2.0 g, respectively. Eq. (8) was found to apply, and to fit the data very satisfactorily ( $R^2 = 0.94$ ). The value of the slope, 1.13, suggests a first-order reaction, as seen in Fig. 39. If  $n = 1$ , then Eq. (7) reads:

$$r = -\frac{dC(t)}{dt} = k C(t) \quad (10)$$

and therefore, after integration:

$$\ln C = \ln C_0 - k t \quad (11)$$

Eq. (11) was thus applied to the data obtained at 130, 160, 180 and  $200^\circ\text{C}$ , using a constant amount of tannin of 0.5 g in 16 mL of water. Each temperature gave a linear region, as shown in Fig. 39, whose slope,  $k$ , was determined. The kinetic constants were found to be 0.00679, 0.0671, 0.197 and  $0.356 \text{ h}^{-1}$  at 130, 160, 180 and  $200^\circ\text{C}$ , respectively. Finally, from the aforementioned values of kinetic constants, Eq. (9) was applied for determining the activation energy of the HTC process of tannin. Plotting  $\ln k$  versus  $1/T$  led to a straight line with a good correlation coefficient ( $R^2 = 0.98$ ). The slope was  $-E_a/R = -10997$ . Using  $R = 8.31 \text{ J mol}^{-1} \text{ K}^{-1}$ , the activation energy was found to be equal to  $91 \text{ kJ mol}^{-1}$  in Fig. 40.



b)

Amount of elemental carbon in the solution (calculated by Eq. (6))

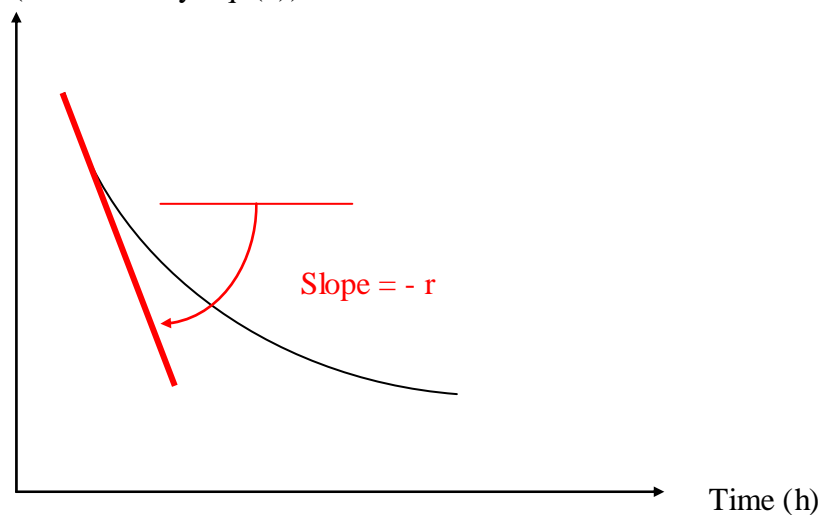
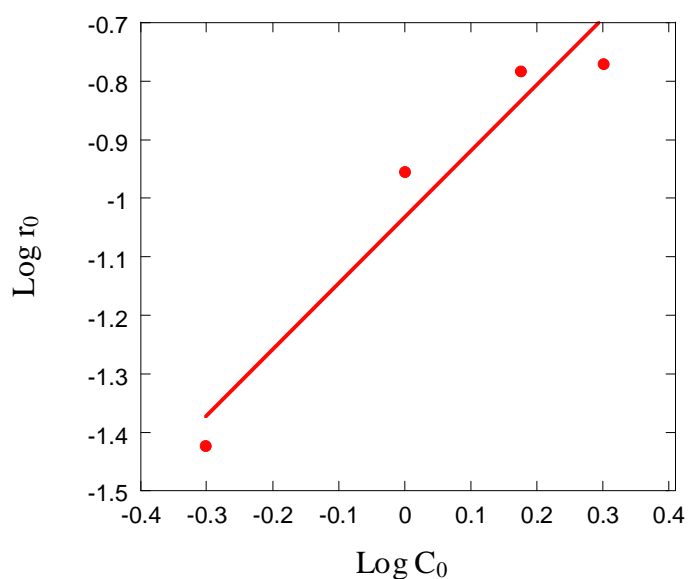


Fig. 38: Amount of elemental carbon,  $C$ , remaining in the solution after HTC: (a) Experimental results after HTC at  $180^{\circ}\text{C}$  of different amounts of tannin in 16 mL of water; (b) Method for determining the reaction rate.

a)



b)

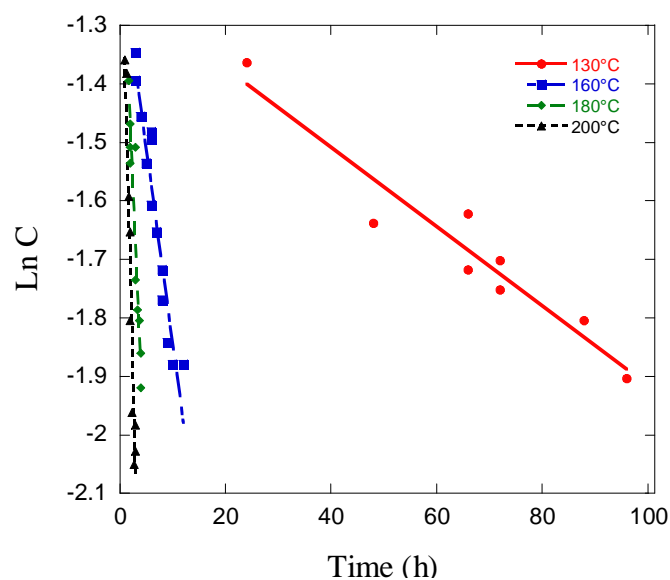


Fig. 39: Elucidation of HTC kinetics of tannin: (a) Determination of reaction order by application of Eq. (8) to the initial reaction rates at 180°C; (b) Determination of kinetic constants at different HTC temperatures by application of Eq. (11).

Most of kinetics studies of biomass conversion in pressurized hot water have been carried out to obtain certain chemicals, e.g. sugars and furfural. These studies were performed at higher pressures, between 10 and 40 MPa; higher temperatures, 200-400°C; and lower reaction times, 0.06s-1.6 min [Yu et al. 2008 and ref. therein] than those used in the present work. Then, kinetic studies of the decomposition of hemicellulose and cellulose led to activation energies of 85-150 and 130-220 kJ mol<sup>-1</sup>, respectively [Yu et al. 2008 and ref.

therein]. Mochidzuki et al. (2003) studied the hydrothermal reaction of cellulose, rice husk, old newspaper and spent malt over a temperature range up to 300°C and 10 MPa. Biomass decomposition took place in two temperature ranges, below around 200°C and above 250°C. Pure cellulose sample, however, showed a simple rapid mass loss at a temperature range of 250-280°C. Activation energies in the first temperature range, corresponding to our experimental temperature range, were 79, 96 and 100 kJ mol<sup>-1</sup> for old newspaper, spent malt and rice husk, respectively. Considering the aforementioned results, it is clear that the activation energy found in our work is in the range of values reported in the literature.

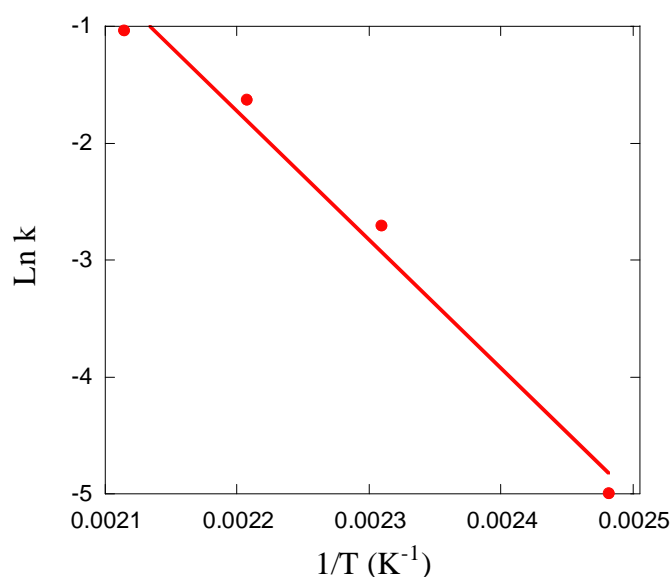


Fig. 40: Arrhenius plot for the determination of HTC activation energy of tannin by application of Eq. (9).

Detailed kinetics studies of HTC of tannin or polyphenols in general have never been carried out as far as the authors of this manuscript know. When tannin is submitted to HTC, different reactions are foreseen, such as hydrolysis, dehydration, and polymerization and/or polycondensation, leading to the final aromatic network. Lu et al. (2008) were the only authors who determined the apparent activation energies for the hydrolysis of tannins. They found  $63.9 \pm 6.2$  and  $96.0 \pm 7.5$  kJ mol<sup>-1</sup> for gallotannin and tara tannin, respectively. These reactions were carried out at high pressure, 5 MPa, and at temperatures ranging from 140 to 180°C. Dehydration of 1-phenylethanol to styrene, which might be similar to the conversion of a phenolic molecule into an aromatic compound, was found to range from 56.7 to 95.2 kJ mol<sup>-1</sup>, depending on the catalyst used [Hasan et al. 2012 and ref. therein]. Activation energies for various polycondensation reactions also led to similar values: 29 – 48 kJ mol<sup>-1</sup> for the polycondensation of the system hemoglobin – glutaric aldehyde, depending on the

experimental conditions [Akperov et al. 1974], and 73.5 and 135.38 kJ mol<sup>-1</sup> for the transesterification and esterification reactions, respectively, leading to the polycondensation of polyethylene terephthalate [Zhao et al. 2005 and ref. therein]. All these values, even if not obtained in HTC conditions, are also of the same order of magnitude as what was found for tannin submitted to HTC. As a conclusion, the activation energy determined here for the dehydration / polycondensation / aromatisation of tannin is realistic with respect to many other values reported for various chemical systems.

## 2.9 Conclusions

Hydrothermal treatment of tannin produced carbonaceous microspheres of a constant composition, whatever the experimental conditions such as tannin amount, from 0.5 to 2 g in 16 mL of water, HTC temperature, from 130 to 220°C, and reaction times from 1 to 144 h were applied. These microspheres were agglomerated and had a diameter lower than 5 µm and a surface area lower than 10 m<sup>2</sup> g<sup>-1</sup>, suggesting non-porous particles. Surface area exhibited a complex behaviour, related to mechanisms expected to occur simultaneously: nucleation, growth and coalescence. Whereas nucleation led to a high number of small particles, making surface area increase, growth and coalescence led to bigger particles of lower surface. A first-order kinetic law and activation energy of 91 kJ mol<sup>-1</sup> were evidenced to control carbonaceous microsphere production.

**Chapter 3: Carbons produced from tannin  
by alteration of the HTC reactional  
medium: addition of  $H^+$ , sucrose and  $Ag^+$**



This study proposes modifications to the system tannin in aqueous solution submitted to hydrothermal carbonization (HTC) in order to increase the hydrochar yield but also to change the physicochemical properties of the resultant carbon materials. HTC was carried out at 180°C for 24h and the three modifications are presented therein: 1) acid addition (pH reduction) as catalyst of tannin autocondensation; 2) sucrose addition as a nucleating- growth modifier agent and; 3) silver nitrate addition as nucleating agent as well (Fig. 41). It was observed that the three modifications produced an increase of the hydrochar yield. Carbon materials derived from hydrochars gel produced at low pH had higher surfaces area with almost the same microporous size distribution. The addition of sugar produced microspheres of lower particle size due to the increase of germs created by sucrose hydrolysis. The presence of silver nitrate in the tannin aqueous solution produced a significant reduction of the spherical particle size to the nanometer range with a narrow distribution of their size. Hydrochar yield increased but surface area decreased possibly due to the presence of Ag nanoparticles blocking the carbon microporosity.

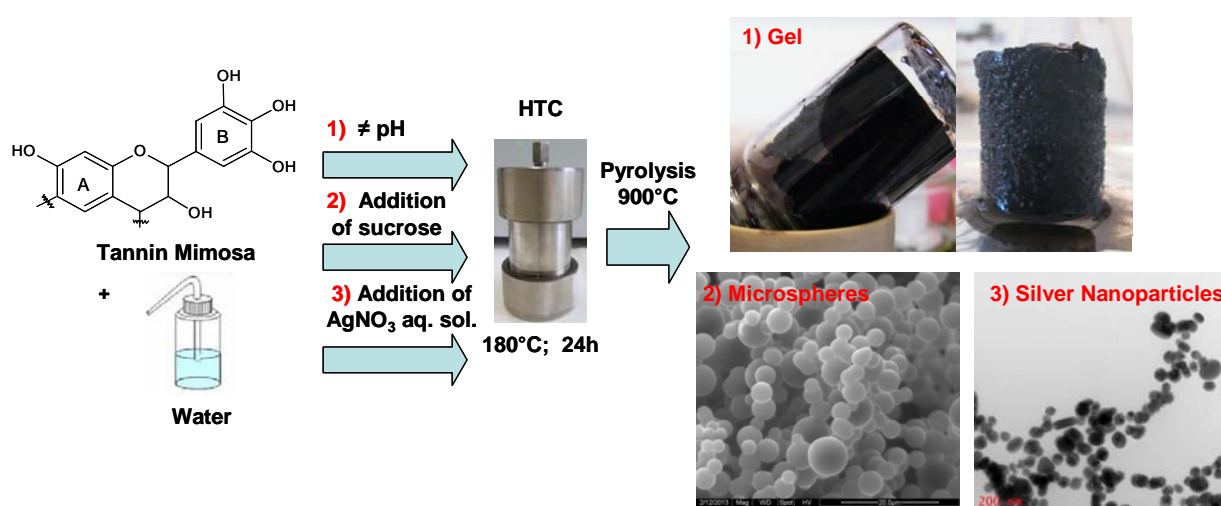


Fig. 41: Three main modifications applied to the system of HTC of tannin.

### 3.1 HTC synthesis

In a typical synthesis, 2.0 g of tannin were mixed with 16.0 g of water and put inside of a glass vial and then into a Teflon-lined autoclave for 24h in a oven at 180°C. This system however, was modified by three means:

- 1) pH modification: tannin solution has an initial pH of approximately 4.2. Para-toluenesulfonic acid (pTSA) was added in order to vary the initial pH down to 3, 2 or 1. The pH of synthesis was indicated in the label by adding 'u', for unmodified pH, or the



pH value for an adjusted initial pH; i.e. H100T180\_u or H100T180\_2 for a sample prepared by submitting 2 g of tannin (100%) to HTC at 180°C with unmodified pH or pH=2 respectively.

- 2) sucrose addition: tannin (T) and sucrose (S) were submitted separately or together to HTC at different conditions and proportions but not exceeding 2.0g in total. The proportions of S to T were: 0, 25, 50, 75 and 100 wt. %. The addition of sugar changed the pH from 4.2 (100% T) till 8 (100% S) and these materials were called as HsStT180\_u, s and t being the percentage of sucrose and tannin respectively. We did a second series of experiments fixing pH at 2, with pTSA, and materials were labelled as HsStT180\_2. HTC temperatures were also varied, 160 or 200°C, and samples were labelled as HsStT160\_u or HsStT200\_u for unmodified pH experiments.
- 3) silver nitrate (AgNO<sub>3</sub>) addition: two series of experiments were carried out; in the first one, 2.0 g of tannin were dissolved into 15.5 g of water and 0.5 mL of an aqueous solution of 0.1M of AgNO<sub>3</sub> was vigorously stirred for 10 min. Three identical solutions were prepared and introduced into an autoclave at 180°C for 1, 2 or 4h. The filtrates were recovered and labelled as i.e. H100T180\_0.5Ag\_t, where t stands for 1, 2, or 4 h.

In the second series of experiments, five solutions were prepared using 2.0 g of tannin with 8, 10, 12, 14 or 15 mL of water together with 8, 6, 4, 2 or 1 mL, respectively, of an aqueous solution of 0.1M of AgNO<sub>3</sub>. The resultant solution was vigorously stirred for 10 min and introduced into an autoclave at 180°C for 24h. The filtrates were recovered and labelled as i.e. H100T180\_vAg, where 'v' stands for 8, 6, 4, 2 or 1 mL, respectively, of an aqueous solution of 0.1M of AgNO<sub>3</sub>.

In all the cases, the recovered filtrates were washed with water and dried in a vacuum oven at 80°C. Carbonization was carried out under nitrogen flow in a tubular furnace heated at 1°C min<sup>-1</sup> up to 900 °C and this temperature was hold for 3h. Pristine tannin (100T) was also carbonized at the same conditions and labelled as C100T. In order to distinguish hydrochar from carbon samples, we added a 'C' at the beginning of the label; i.e. samples H100T180\_vAg became CH100T180\_vAg after carbonization at 900°C.

### 3.2 Effect of H<sup>+</sup> addition

The pH of tannin water solution is usually around 4.2 and it was reduced to 3, 2 or 1. Table 4 shows the main characteristics of materials after HTC at different pHs and further carbonization at 900°C. Pristine tannin (100T) and carbonised at 900°C (C100T) are also

included in this table as a reference. HTC yield brutally increased from 64.6 % at pH=4.2 to 86.7 % at pH=1. At pH extremely acid (below 1.5), the reaction of polymerization of tannin is the most favourable [Pizzi 1999; Meikleham and Pizzi 2003; Lu et al. 2008 and refs. therein; Tondi 2009; Schlienger et al. 2012]. Mimoso tannin when subjected to heating in acidic conditions is subject to two competing reactions: tannin degradation to form anthocyanidin and catechin; and tannin condensation as a result of hydrolysis of heterocyclic rings with nucleophilic centres to form “phlobaphenes” or “tanner reds” which are insoluble and have high molecular weight [Pizzi 1983]. Hydrochars produced by HTC of tannin at acidic pHs (3, 2 and 1) were monolithic and cylindrical in shape (Fig. 42 on the left side), while a more solid compacted material was obtained at pH equal to 4.2 (Fig. 42 on the right).

Table 4: Textural properties and elemental analysis obtained for pristine tannin (100T), HTC materials and carbon materials made at different pHs.

	Yield (wt. %)			Textural Properties					Elemental Analysis (wt %)					
	HTC	Carbon	Total	S <sub>DFT</sub> (m <sup>2</sup> g <sup>-1</sup> )	S <sub>BET</sub> (m <sup>2</sup> g <sup>-1</sup> )	V <sub>0.97</sub> (m <sup>3</sup> g <sup>-1</sup> )	V <sub>μ</sub> (cm <sup>3</sup> g <sup>-1</sup> )	V <sub>CO2</sub> (cm <sup>3</sup> g <sup>-1</sup> )	C	H	N	S	O	C/O
<b>100T</b>					0.27				53.8	5.4	0.6	0.1	40.1	1.3
<b>After HTC</b>														
<b>H100T180_1</b>	86.7				1.34				60.8	4.5	0.2	0.7	33.8	1.8
<b>H100T180_2</b>	77.3				1.25				62.3	4.3	0.5	0.2	32.7	1.9
<b>H100T180_3</b>	73.1				0.84				62.4	4.7	0.3	0.1	32.5	1.9
<b>H100T180_u</b>	64.6				0.78				60.9	4.4	0.8	0.1	33.8	1.8
<b>After carbonization at 900°C</b>														
<b>C100T</b>		44.5	44.5	508	471	0.20	0.19	0.38	90.3	0.8	0.6	0.0	8.3	10.9
<b>CH100T180_1</b>		46.3	40.1	954	796	0.33	0.30	0.35	93.0	1.4	0.4	0.0	5.2	17.9
<b>CH100T180_2</b>		47.9	37.1	826	689	0.28	0.26	0.32	94.7	0.8	0.5	0.0	4.0	23.7
<b>CH100T180_3</b>		49.1	35.9	876	734	0.29	0.28	0.33	93.0	0.8	0.6	0.0	5.6	16.6
<b>CH100T180_u</b>		51.6	33.4	743	601	0.24	0.23	0.28	88.4	0.9	0.6	0.0	10.1	8.8

Tannin has a phenolic structure with a high oxygen content (40.1 wt.%) mainly due to the hydroxyl groups. After HTC, carbon content increased from 53.8 to 60.8-62.4 wt.% and oxygen content decreases in almost the same extent, down to 32.5-33.8 wt.%. Differences of the thermal decomposition of carbohydrates due to variations of pHs identified by their

elemental composition (C/H/O) were first mentioned by Schumacher et al. (1960) through HTC reactions. It was known that a neutral to weak acidic medium was required for the natural coalification reaction [Shah 2014 and refs. therein]. HTC of stillage, a residual carbohydrate obtained after grain fermentation, produced a carbon material having high carbon yield at 180-250°C and using citric acid as catalyst [Bauer 2013]. Moreover, many studies on HTC of biomass carbohydrates observed a reduction of the pH due to the formation of several acids i.e. acetic, formic, levulinic which could act as a catalyst of the hydrolysis reaction at moderate conditions of temperature and pressure [Antal and Mok 1990; Luijkx et al. 1995; Kabyemela et al. 1997; Sasaki et al. 1998; Sevilla and Fuertes 2009a].



Fig. 42: Monolith obtained at pH 1 on the left and compacted solid material obtained at unmodified pH on the right side.

### 3.2.1 Textural and chemical properties of 100T materials at different pHs

HTC produced hydrochar microspheres with a surface area around  $1.25 \text{ m}^2 \text{ g}^{-1}$  at pH=2 and  $0.78 \text{ m}^2 \text{ g}^{-1}$  at pH=4.2 (at unmodified pH). Taking into account the real density of hydrochars produced,  $1.63 \text{ g cm}^{-3}$  at pH 2 and  $1.65 \text{ g cm}^{-3}$  at pH 4.2, we can calculate equivalent diameter equal to:  $2.9 \text{ }\mu\text{m}$  at pH=2 and  $4.7 \text{ }\mu\text{m}$  at pH 4.2. The decrease of particle diameter was confirmed by SEM observations, as shown in Fig. 43, carbon materials derived from 100T submitted to HTC at pH=2 and at unmodified pH (pH=4.2). pH reduction produced the decrease of the microspheres diameter, that could be due to a promoted nucleation at lower pH. The microspheres are then smaller and more numerous due to higher HTC yield at low pHs.

Carbonization of the hydrochars at 900°C produced also a decrease of oxygen content, down to 10wt.% if pH was not modified or to 4-6% when hydrochar was produced at pH equal or lower than 3. The pH did not seem to have a significant influence on the oxygen content (Table 4) whereas it has an effect on the carbon yield. The lower the pH, the higher the carbon yield. Taking into account the whole process, HTC (or not) and carbonization at

900°C, it is surprising that the HTC step always lowered the total yield compared to direct carbonization in dry atmosphere (C100T) but the effect was less important when HTC was performed in acidic media.

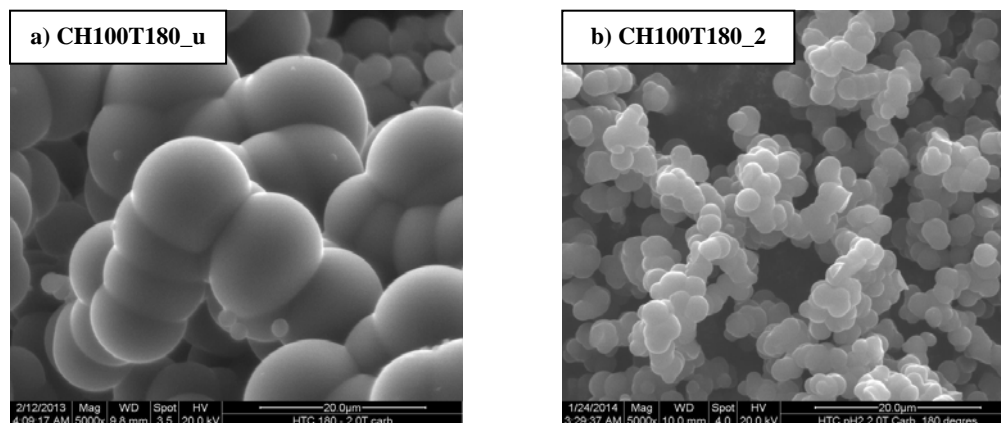


Fig. 43: SEM images of CH100T submitted to HTC at 180°C with, a) unmodified pH and b) pH=2, and further pyrolysis at 900°C.

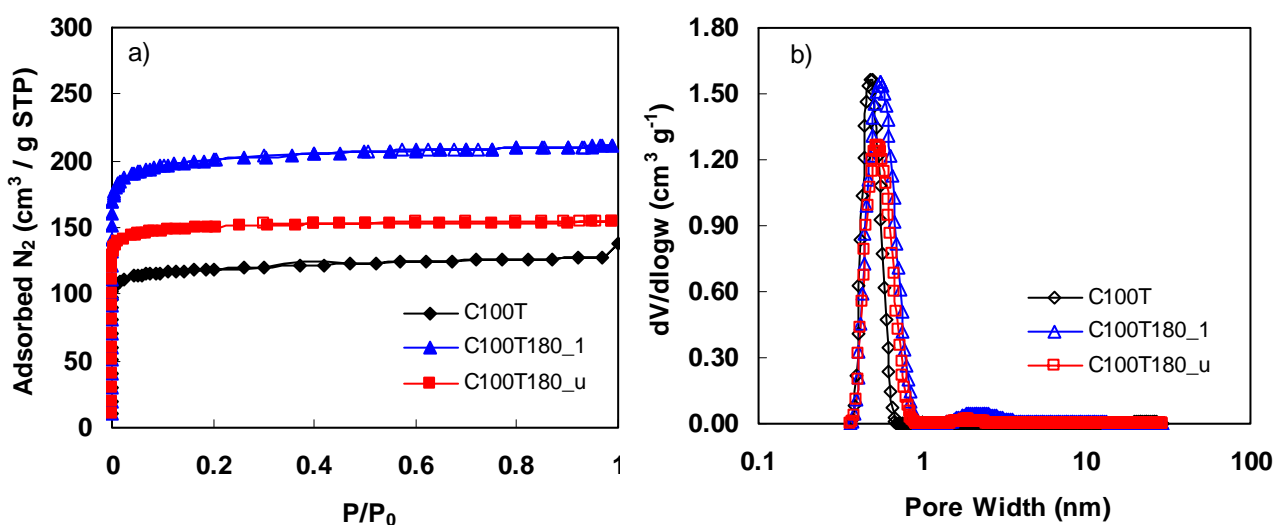


Fig. 44: a) Nitrogen adsorption-desorption isotherms (full and open symbols, respectively) at -196°C after carbonization at 900°C of pristine tannin (C100T) and of two hydrochars obtained at 180°C at pH 1 (CT100T180\_1) and unchanged (pH=4.2, CT100T180\_u ); and b) their corresponding pore size distribution obtained by DFT (slit-like pore geometry).

Fig. 44 a) shows the adsorption-desorption isotherms of nitrogen at -196°C of C100T, CH100T180\_u and CH100T180\_1 samples. All of them are type I following the IUPAC classification, without hysteresis cycle, and they are characteristic of microporous solids.

Both, HTC and pH reduction produced an increase of the pore volume and surface area while maintaining the PSD approximately unchanged (see Fig. 44 b). If we take into account the product  $S_{\text{BET}} \times \text{Total yield}$  we obtained  $210 \text{ m}^2 \text{ g}^{-1}$  for tannin directly carbonized at  $900^\circ\text{C}$  (C100T). Introducing HTC without modifying pH led to similar value ( $201 \text{ m}^2 \text{ g}^{-1}$ ) but allowed higher oxygen content, as seen in Table 4. The reduction of pH to 1 allowed increasing  $S_{\text{BET}} \times \text{Total yield}$  up to  $319 \text{ m}^2 \text{ g}^{-1}$  mainly due to the much higher  $S_{\text{BET}}$  obtained.

An important outcome of this study that must be specially pointed out is the increase of the  $S_{\text{BET}}$ . By decreasing the pH down to 1, we increased the surface area from 471 to  $796 \text{ m}^2 \text{ g}^{-1}$ . This increase cannot be only justified by the decrease of particle diameter, which accounts for less than 1% of the  $S_{\text{BET}}$  determined. However, the lower particle diameter could facilitate volatile evolution and then the development of textural properties.

### 3.3 Effect of sucrose addition

#### 3.3.1 Textural and chemical properties of 50S50T materials at different pHs

Table 5 shows the main characteristics of hydrochars and carbon materials prepared with the same weight of sucrose and tannin, materials 50S50T, at different pHs. The results of this Table should be compared to those presented in Table 4 related to 100T. Fig. 45 shows results of HTC yield and  $S_{\text{BET}}$  of the hydrochar materials derived from 100T and 50S50T submitted to HTC at pH value ranging from 4 to 1. The results on tannin are presented here for the sake of comparison to study the effect of sucrose addition. At the opposite of 100T, submission of 50S50T to HTC at different pH did not produce any change in the HTC yield, which was always below and around  $61.5 \pm 1.5 \text{ wt.}\%$ . The  $S_{\text{BET}}$  values were almost the same for 100T and 50S50T carbon derived materials, taking into account the analysis error inherent to gas adsorption techniques. It has been shown in the literature that sucrose submitted to HTC undergoes hydrolysis producing glucose and fructose, which decompose into hydroxymethylfurfural (HMF) as the main dehydration product, and organic acids (acetic, formic, levulinic acids, etc), aldehydes (formaldehyde, pyruvaldehyde, etc) producing a rapid pH change from 8 to 3. Glucose and fructose can also undergo polymerization and condensation reactions as showed elsewhere [Antal and Mok 1990; Luijckx et al. 1995; Kabyemela et al. 1997; Sasaki et al. 1998; Sevilla and Fuertes 2009].

Titirici et al. (2008) confirmed that the morphologies and chemical structures of carbons obtained from sucrose are directly related to those of carbons obtained from pure furan. Acids and aldehydes coexist with furans and they are probably responsible for particle size, powder

texture and aggregation discrepancies. Then, we can assume that several reactive germs coexist in the system of sucrose submitted to HTC. When sucrose and tannin were submitted together in HTC conditions, sugar reacts faster than tannin producing more germs and at the end, smaller spheres.

Table 5: Textural properties and elemental analysis obtained for materials 50S50T, HTC and carbon materials made at different pHs.

	Yield (wt. %)			Textural Properties					Elemental Analysis (wt %)					
	HTC	Carbon	Total	S <sub>DFT</sub> (m <sup>2</sup> g <sup>-1</sup> )	S <sub>BET</sub> (m <sup>2</sup> g <sup>-1</sup> )	V <sub>0.97</sub> (m <sup>3</sup> g <sup>-1</sup> )	V <sub>μ</sub> (cm <sup>3</sup> g <sup>-1</sup> )	V <sub>CO<sub>2</sub></sub> (cm <sup>3</sup> g <sup>-1</sup> )	C	H	N	S	O	C/O
<b>After HTC</b>														
H50S50T180_1	63.0				1.22				62.6	5.0	0.6	0.2	31.6	2.0
H50S50T 180_2	60.0				1.05				62.6	4.3	0.2	0.2	32.7	1.9
H50S50T 180_3	61.2				0.87				62.3	4.8	0.8	0.0	32.1	1.9
H50S50T 180_u	61.5				0.84				60.9	4.4	0.3	0.0	34.4	1.8
<b>After carbonization at 900°C</b>														
C100T		44.5	44.5	508	471	0.20	0.19	0.38	90.4	0.8	0.6	0.0	8.2	11.0
CH50S50T 180_1		50.4	31.8	972	809	0.35	0.31	0.36	89.9	1.5	0.8	0.0	7.8	11.5
CH50S50T 180_2		53.2	31.9	929	767	0.34	0.29	0.32	91.5	1.1	1.2	0.0	6.2	14.8
CH50S50T 180_3		48.4	29.6	790	643	0.27	0.25	0.29	90.8	2.1	0.8	0.0	6.3	14.4
CH50S50T 180_u		49.6	30.5	790	639	0.25	0.24	0.28	91.0	0.5	0.3	0.0	8.2	11.1

The microsphere diameter was reduced from 10 μm for H100T (see Fig. 43) to 2-5 μm by the simple addition of sucrose (see Fig. 46 a) for H50S50T). A similar effect was encountered by the decrease of the pH down to 2 in presence of sucrose; particles appeared smaller and more monodispersed in size (compare Fig. 46 a) and b)). Zhao et al. (2013) observed the effect of the acidic pH on the formation mechanism of carbon spheres by HTC of cellulose. The hydrolysis of cellulose produces oligo-sacharides, monomers (glucose and fructose) and by products (acetic, formic, ..., acids) as we have mentioned. These compounds rapidly react with H<sup>+</sup> present in the system through dehydration and polymerisation reactions and lead to hydrochar nucleation. In summary, they concluded that the acid concentration can control the shape and the diameter of the formation of carbon spheres.

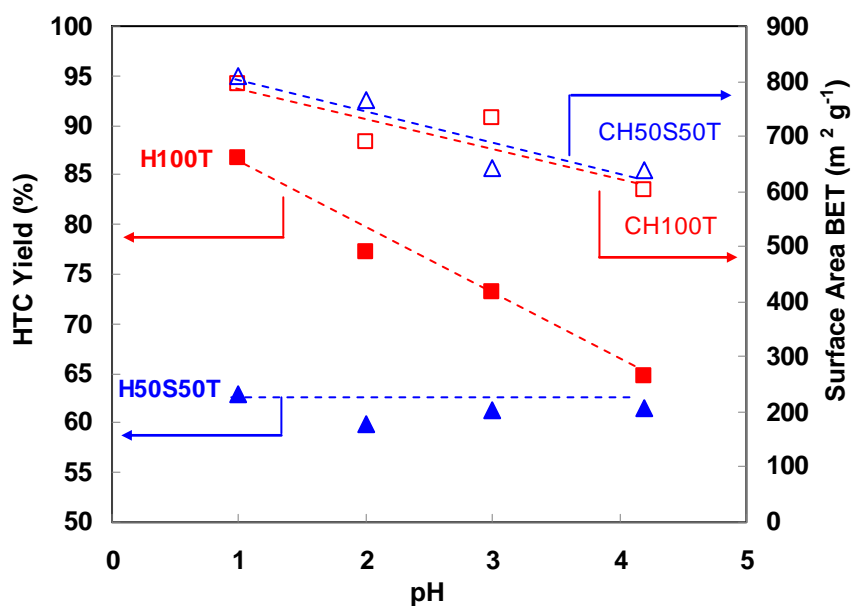


Fig. 45: HTC yield of H100T and H50S50T at different pHs and  $S_{BET}$  ( $m^2 g^{-1}$ ) of the carbon materials after posterior pyrolysis at  $900^\circ C$  (discontinuous lines are guides for the eyes).

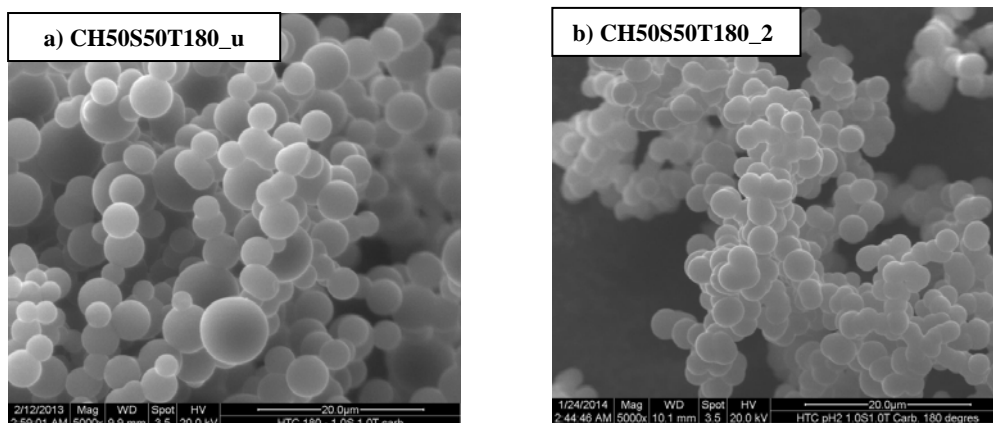


Fig. 46: SEM images of 50S50T submitted to HTC at a) unmodified pH and b) at  $pH=2$ .

### 3.3.2 Textural and chemical properties of 50S50T materials prepared at various temperatures and pHs

Fig. 47 shows the total carbon yield and the  $S_{BET}$  as a function of the temperature during HTC for samples 50S50T submitted to HTC at unchanged pH or at  $pH=2$ . HTC yield was around 60% irrespective from the temperature or the pH. After “dry” carbonization, the total carbon yield appears to be constant, around 30%, whatever the HTC temperature or the pH

used previously. In the same way,  $S_{BET}$  did not change with HTC temperature but was higher for samples prepared at  $pH=2$ . Indeed, carbons prepared from hydrochars obtained at  $pH=2$  showed a  $S_{BET}$  of  $735 \pm 32 \text{ m}^2 \text{ g}^{-1}$  while those prepared at unchanged  $pH$  showed a  $S_{BET}$  of  $629 \pm 10 \text{ m}^2 \text{ g}^{-1}$ . Fig. 48 shows that when 50S50T was submitted to HTC at different temperatures and  $pH=2$ , no changes in particle diameter were observed, their diameter was nearly constant around  $2\mu\text{m}$ . This finding was different from our previous studies on the system H100T (Chapter 2) at unchanged  $pH$ . At  $160^\circ\text{C}$ , we observed irregular spheres indicating that HTC reaction was not finished. By increasing HTC temperature from 180 to  $200^\circ\text{C}$ , bigger spheres were observed.

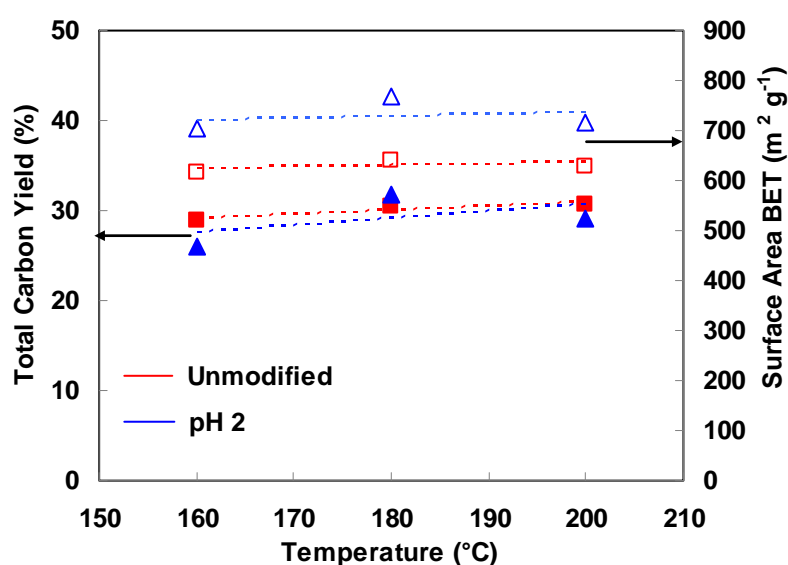


Fig. 47: Total carbon yield and surface area BET ( $\text{m}^2 \text{g}^{-1}$ ) for the carbonized ( $900^\circ\text{C}$ ) carbon samples CH50S50T prepared with different HTC temperatures and  $pH$  values.

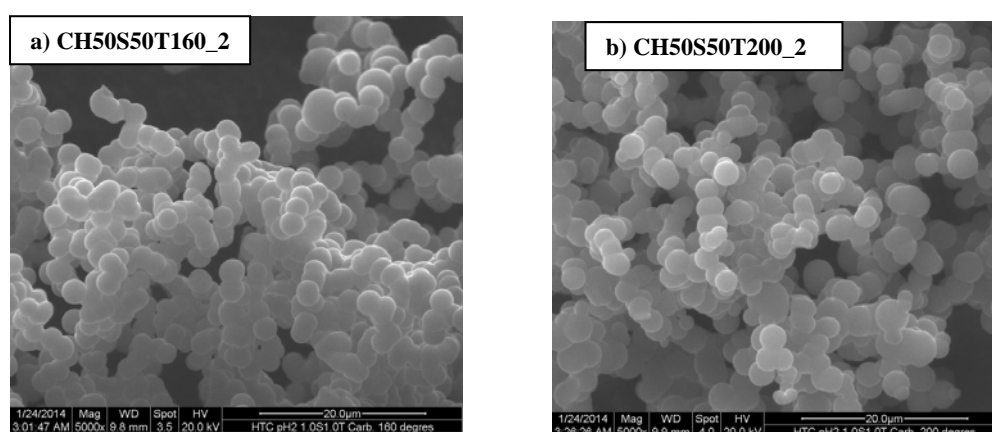


Fig. 48: SEM images of 50S50T submitted to HTC at  $pH$  2 a)  $160^\circ\text{C}$  and b)  $200^\circ\text{C}$ .



In order to study the effect of the percentage of sucrose on the hydrochar characteristics, we prepared hydrochars at different tannin to sucrose proportions, at unchanged pH and at pH equal to 2. Table 6 shows the main characteristics of hydrochars and carbon materials prepared with 50% of sucrose (50S50T) at different HTC temperatures (160, 180 and 200°C) and different pHs. The results of this Table should be compared to those presented in Table 4 related to 100T. It is also summarised in Table 7 all materials made at different percentages of S/T at unchanged pH and pH=2.

Table 6: Textural properties and elemental analysis obtained for materials 50S50T after HTC and carbonization at different temperatures and pHs.

	Yield (wt. %)			Textural Properties				Elemental Analysis (wt %)					
	HTC	Carbon	Total	S <sub>DFT</sub> (m <sup>2</sup> g <sup>-1</sup> )	S <sub>BET</sub> (m <sup>2</sup> g <sup>-1</sup> )	V <sub>0.97</sub> (m <sup>3</sup> g <sup>-1</sup> )	V <sub>μ</sub> (cm <sup>3</sup> g <sup>-1</sup> )	C	H	N	S	O	C/O
<b>After HTC</b>													
H50S50T160_u	61.0				1.33			59.0	4.4	0.3	0.0	36.3	1.6
H50S50T180_u	61.5				0.84			60.9	4.4	0.3	0.0	34.4	1.8
H50S50T200_u	59.2				0.91			62.9	4.4	0.3	0.0	32.4	1.9
H50S50T160_2	60.7				1.06			62.9	4.7	0.2	0.2	32.0	2.0
H50S50T180_2	59.9				0.41			62.6	4.3	0.2	0.2	32.7	1.9
H50S50T200_2	59.6				1.10			64.7	4.4	0.2	0.1	30.6	2.1
<b>After carbonization at 900°C</b>													
CH50S50T160_u		47.4	28.9	743	618	0.24	0.24	92.6	0.5	0.4	0.0	6.5	14.2
CH50S50T180_u		49.6	30.5	790	639	0.25	0.24	91.0	0.5	0.3	0.0	8.2	11.1
CH50S50T200_u		51.7	30.6	783	630	0.26	0.24	93.3	0.6	0.4	0.0	5.7	16.4
CH50S50T160_2		42.9	26.0	860	703	0.32	0.27	94.1	0.7	0.5	0.0	4.7	20.0
CH50S50T180_2		53.2	31.9	929	767	0.34	0.29	91.5	1.1	1.2	0.0	6.2	14.8
CH50S50T200_2		48.9	29.2	869	718	0.29	0.27	93.3	0.8	0.7	0.0	5.2	17.9

### 3.3.3 Textural and chemical properties of tannin/sucrose materials at different proportions and pHs

Fig. 49 shows SEM pictures of carbon materials derived from 100S submitted to HTC at unchanged pH (pH 8) or at pH=2. HTC of 100S at unchanged pH produces mostly monodisperse spherical particles having a size of approximately 1 μm, in accordance with other authors [Titirici et al. 2008; Sevilla et al. 2009]. Comparison of Fig. 43 and Fig. 50

shows that increasing the amount of sugar up to 75% at unchanged pH, the sphere diameter decreased from around 10  $\mu\text{m}$  to 2  $\mu\text{m}$  and they became more individualized and monodispersed in size. Then, polydispersity and bigger particles sizes appear to be the consequence of tannin presence in the system at unchanged pH. In the literature, particles morphology modification by the mixture of two carbon precursors submitted to HTC was also evidenced for microalgae in presence of glucose (mass ratio of 1). In that case, the particles morphology was that of pure glucose with larger average diameter; it changed from 1 to 2  $\mu\text{m}$ , and a rougher surface [Falco et al. 2012].

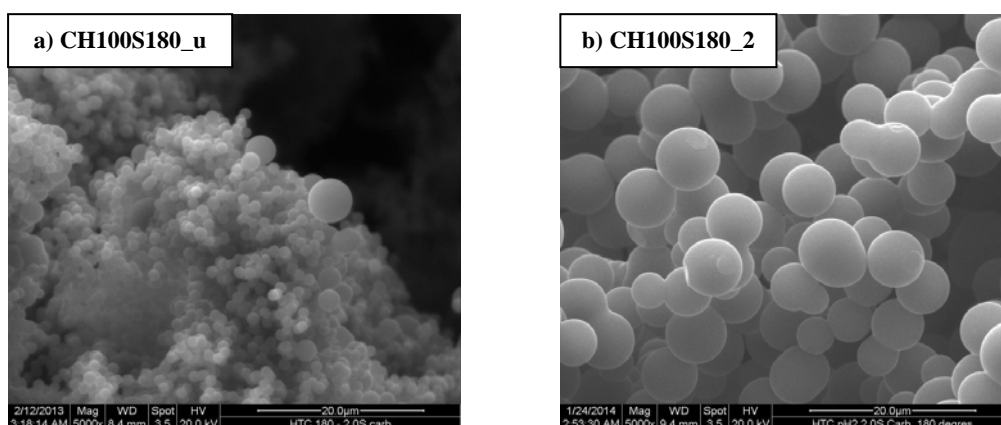


Fig. 49: SEM images of carbon materials derived from sucrose submitted at HTC at 180°C with a) unchanged pH (pH=8) and b) pH = 2 and further carbonized at 900°C.

Fig 49 b) shows the  $S_{\text{BET}}$  for the same carbon materials as in Fig. 51 a). As a general remark, the addition of sugar to tannin slightly increased the  $S_{\text{BET}}$ . The highest  $S_{\text{BET}}$  was found for the mixture 50S50T at both pHs. But the main effect on the increase of the surface area was due to the pH reduction. Carbon samples prepared from hydrochars synthesized at pH=2 showed always higher  $S_{\text{BET}}$ . Fig. 52 shows that  $S_{\text{BET}}$  and the micropore volume increased with the total carbon yield. This effect is opposite to that showed by physical and chemical activations of carbon, which produce higher surface areas when decreasing the carbon yield or increasing the burn-off. The product  $S_{\text{BET}} \times$  total carbon yield is also showed in Fig. 52.

Table 7: Textural properties and elemental analysis obtained for pristin tannin (100T), HTC materials and carbon materials.

	Yield (wt. %)			Textural Properties				Elemental Analysis (wt %)					
	HTC	Carbon	Total	S <sub>DFT</sub> (m <sup>2</sup> g <sup>-1</sup> )	S <sub>BET</sub> (m <sup>2</sup> g <sup>-1</sup> )	V <sub>0.97</sub> (m <sup>3</sup> g <sup>-1</sup> )	V <sub>μ</sub> (cm <sup>3</sup> g <sup>-1</sup> )	C	H	N	S	O	C/O
<b>After HTC</b>													
<b>Unmodified pH</b>													
H100S180_u	41.1				1.81			65.6	4.4	0.0	0.0	30.0	2.2
H75S25T180_u	55.2				1.23			62.5	4.5	0.2	0.0	32.8	1.9
H50S50T180_u	61.5				0.84			60.9	4.4	0.3	0.0	34.4	1.8
H25S75T180_u	65.5				1.01			60.1	4.3	0.4	0.0	35.2	1.7
H100T180_u	64.6				0.78			60.9	4.4	0.8	0.0	33.9	1.8
<b>pH=2</b>													
H100S180_2	34.7				0.56			66.9	4.5	0.5	0.0	28.1	2.4
H75S25T180_2	44.3				0.73			64.7	4.5	0.2	0.1	30.5	2.1
H50S50T180_2	59.9				0.41			63.4	4.4	1.0	0.0	31.2	2.0
H25S75T180_2	67.5				1.26			62.4	4.7	0.2	0.0	32.6	1.9
H100T180_2	77.3				1.25			62.3	4.3	0.5	0.2	32.7	1.9
<b>After carbonization at 900°C</b>													
<b>Unmodified pH</b>													
CH100S180_u		51.2	21.1	675	562	0.22	0.22	93.0	0.5	0.0	0.0	6.0	14.3
CH75S25T180_u		49.8	27.5	745	610	0.24	0.23	91.5	0.6	0.1	0.0	7.8	11.7
CH50S50T180_u		49.6	30.5	790	639	0.25	0.24	91.0	0.5	0.3	0.0	8.2	11.1
CH25S75T180_u		51.2	33.5	794	635	0.25	0.24	90.9	0.5	0.4	0.0	8.2	11.1
CH100T180_u		51.6	33.4	743	601	0.24	0.23	88.3	0.9	0.7	0.0	10.1	8.7
<b>pH=2</b>													
CH100S180_2		51.4	17.8	678	565	0.26	0.22	92.1	1.0	0.9	0.0	6.0	15.4
CH75S25T180_2		51.3	22.7	846	690	0.32	0.26	93.6	0.7	0.6	0.0	5.1	18.4
CH50S50T180_2		53.2	31.9	929	767	0.34	0.29	91.4	0.9	1.2	0.0	6.5	14.1
CH25S75T180_2		47.7	32.2	858	704	0.33	0.27	95.3	0.6	0.6	0.0	3.5	27.2
CH100T180_2		47.9	37.1	826	689	0.28	0.26	94.7	0.8	0.5	0.0	4.0	23.7

Fig. 51 a) shows the HTC yield of all materials at different proportions of tannin / sugar, and two pHs, unchanged and pH=2. The dotted lines represent the theoretical yield calculated

from the experimental yield of 100T and 100S, i.e. for 75S25T  $Y_{\text{HTC}, 75\text{S}25\text{T}} = (75 * Y_{\text{HTC}, 100\text{S}} / 100 + 25 * Y_{\text{HTC}, 100\text{T}} / 100)$  to see any synergic effect between tannin and sucrose during HTC. At pH=2, the experimental HTC yield is the same as that calculated and so, we can conclude that there is *no apparent* interaction between sucrose and tannin regarding the HTC yield. Acidic pH accelerates HTC reactions, both for sucrose and tannin precursors [Kim et al. 2001; Lee et al. 1999; Trajano and Wyman 2013]. Therefore, kinetics for both compounds were then levelled upward and no differences were observed. At unmodified pH, experimental HTC yield of tannin-sucrose mixtures were higher than those theoretically calculated leading to the conclusion that HTC products of sucrose interact with those of tannin. At pH around 4, sucrose yields more solid materials. Its higher kinetics of HTC compared to tannin leads to more germs with a resulting lower particles size and a enhanced HTC yield. At pH=2, however the experimental HTC yield is the same as that calculated. Acidic pH promotes fast reactions to liquid products [Kim et al. 2001; Lee et al. 1999; Trajano and Wyman 2013] that do not interact with tannin.

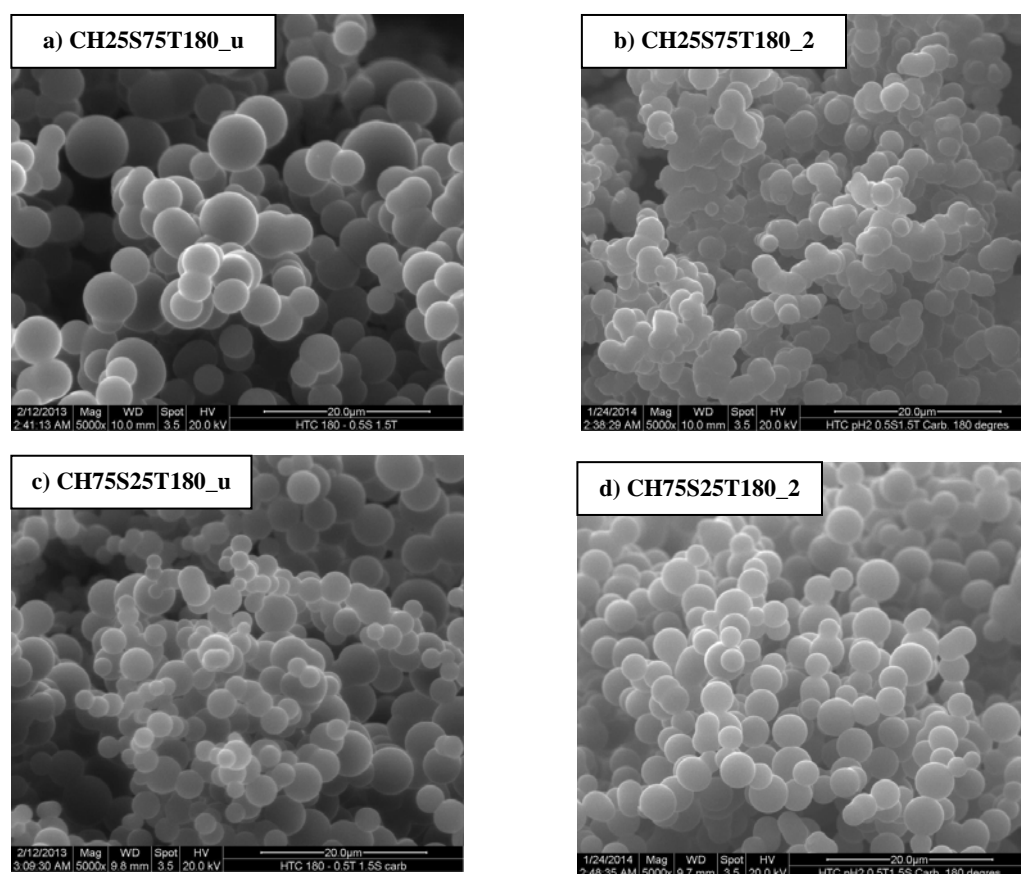
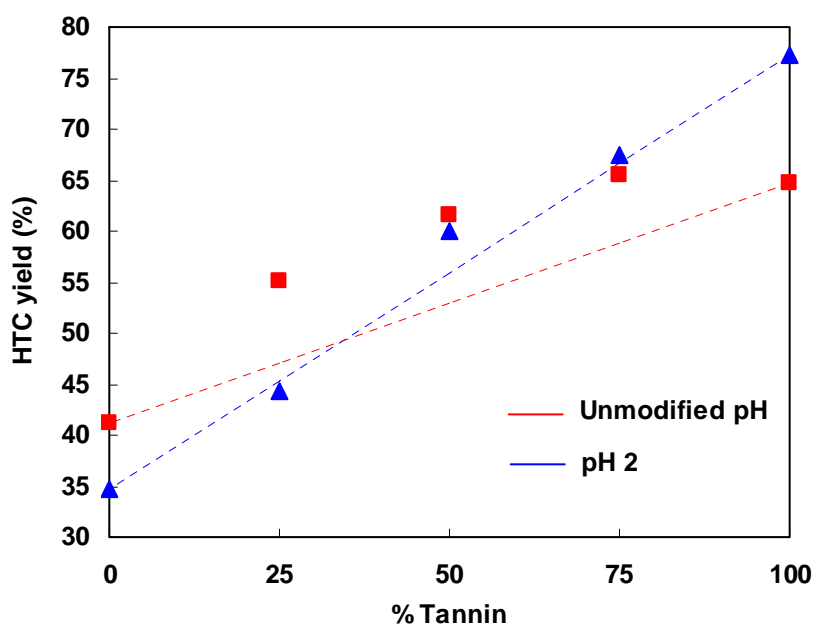


Fig. 50: SEM images of carbon materials derived made from sucrose and tannin at proportion of 25 and 75% submitted at HTC at unmodified pH (a, c) and pH = 2 (b, d) and further carbonised (900°C).

a)



b)

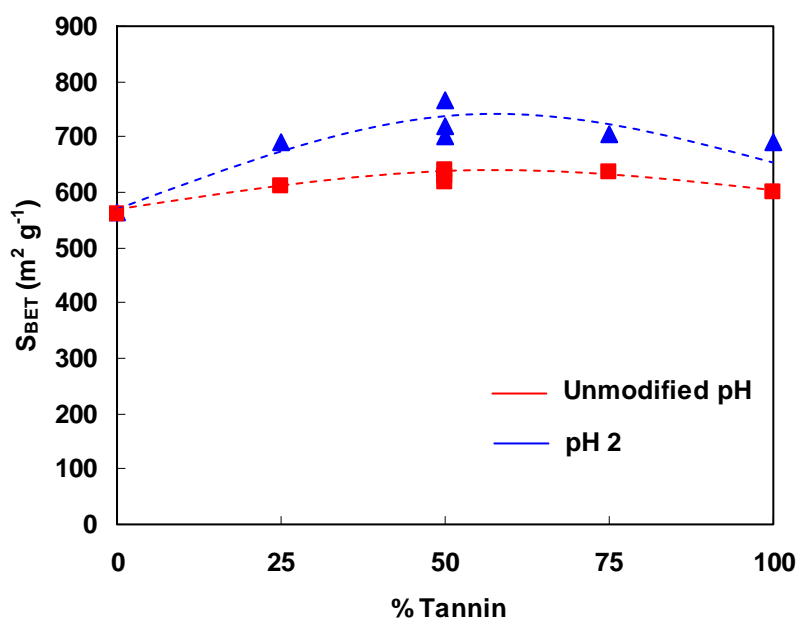


Fig. 51: a) HTC yield of all materials at different proportions of T / S; b) Surface areas  $S_{BET}$  ( $m^2 g^{-1}$ ) for the same materials after HTC and posterior carbonization at  $900^\circ C$ .

These materials are microporous confirmed by their Type I nitrogen isotherms at  $-196^\circ C$ , having a horizontal curve from  $P/P_0 = 0.02$  till  $P/P_0 = 1$  as shown in Fig. 53 a) for CH50S50T180\_2 and CH50S50T180\_u. The pore size distribution calculated by DFT is presented in Fig. 53 b) for the same samples, pore sizes were between 0.40 and 1.2 nm. The isotherm of sample prepared at  $pH=2$  presented a slight slope showing the presence of pore diameters wider than 2 nm as confirmed in Fig. 53 b). Most of the carbohydrates submitted to

HTC needed a second thermal treatment, at higher temperature, to increase the porosity of the resultant carbon materials. Glucose, chitosan and glucosamine showed very low porosity and surface areas measured around  $30\text{-}50\text{ m}^2\text{g}^{-1}$  even after pyrolysis at  $900^\circ\text{C}$ , contrary to HTC-derived material made from tannin [Zhao et al. 2010a].

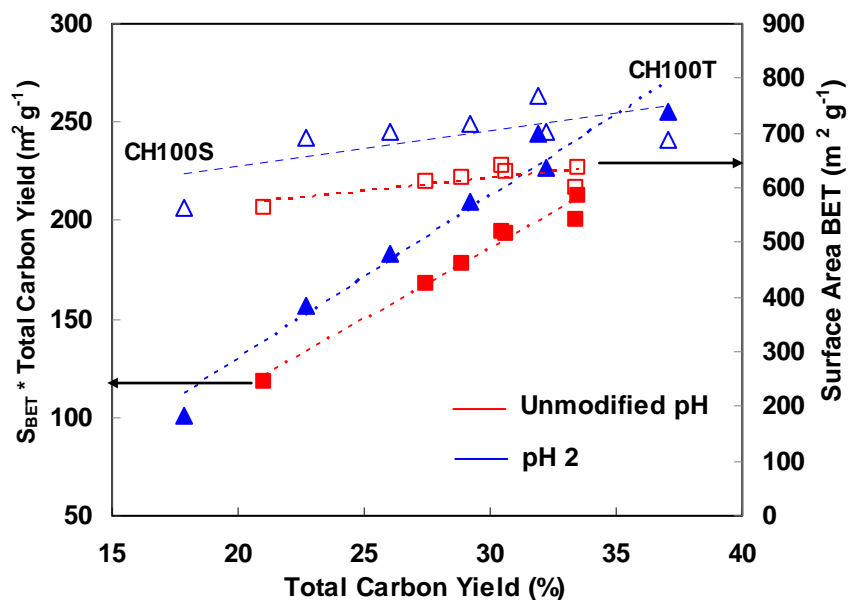


Fig. 52: Surface areas  $S_{\text{BET}}$  ( $\text{m}^2\text{g}^{-1}$ ) (open symbols) and the product Total carbon Yield  $\times S_{\text{BET}}$  (full symbols) as function of the total carbon yield for all materials at different proportions of T / S after HTC and posterior pyrolysis at  $900^\circ\text{C}$ .

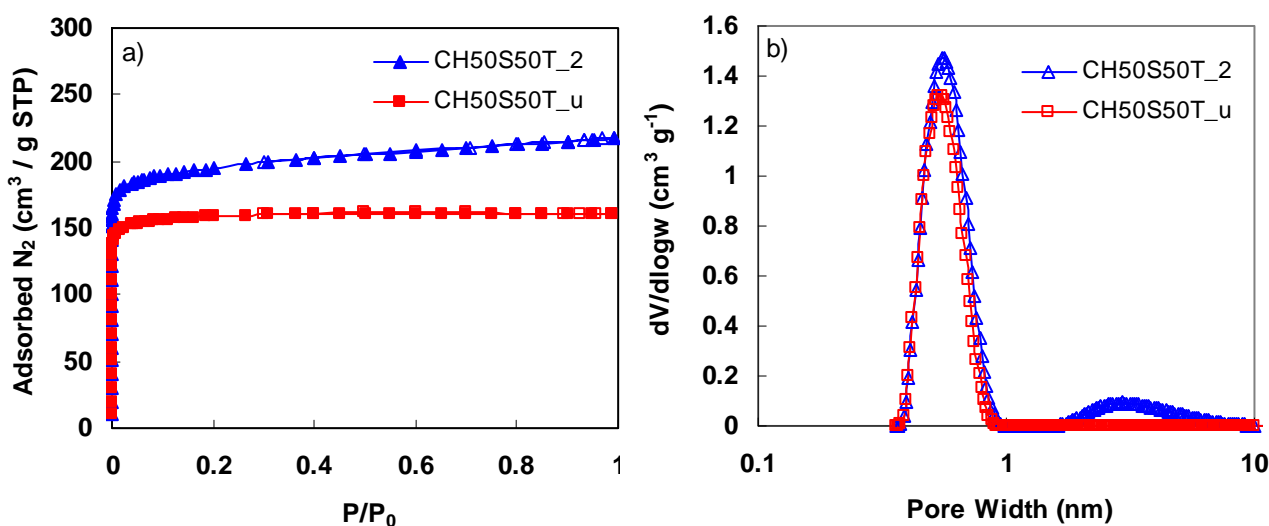


Fig. 53: a) Nitrogen adsorption-desorption isotherms (full and open symbols, respectively) at  $77\text{K}$ ; and b) their pore size distribution determined by the DFT method (slit-like geometry) for CH50S50T\_2 and CH50S50T\_u samples.

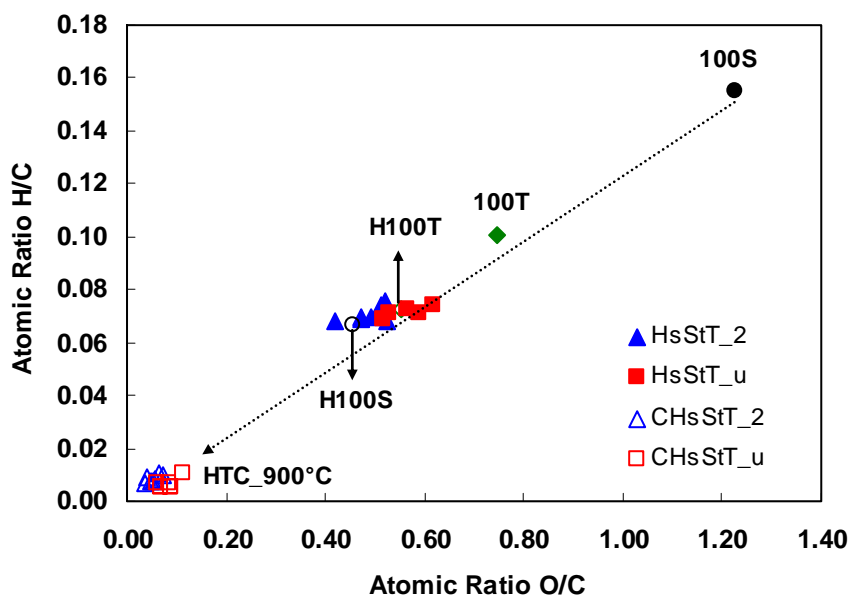
### 3.3.4 Van Krevelen diagram, TPD (Temperature Programmed Desorption) and XPS analysis

Fig. 54 a) shows the van Krevelen diagram for all hydrochars and carbon materials prepared from tannin and sucrose at different pHs and temperatures. The main arrow (from 100S to HTC\_900°C) indicates the loss of oxygen and hydrogen and therefore the augmentation of carbon content after both thermal treatments: HTC (160-200°C) and pyrolysis (900°C) [van Krevelen 1950]. The percentage of carbon increased after HTC and still more after carbonization. After HTC, samples prepared at unmodified pH retained more oxygen, 30-36%, than those prepared at pH=2, 28-33%. Even after carbonization at 900°C, carbon derived from hydrochars prepared at unmodified pH retained more oxygen, 6-10%, than those prepared at pH=2, 3-6%.

Fig. 54 b) shows the total amount of CO and CO<sub>2</sub> gases in mmol lost during a thermal treatment (TPD analysis) up to 1100°C for T/S materials at different proportions. CO<sub>2</sub> derives from precursors having carboxylic acids, lactones and anhydrides groups and CO from quinonic and phenolic groups [Figueiredo et al. 1999]. Boudouard equilibrium also takes place modifying the CO/CO<sub>2</sub> ratio. It is clear that the total percentage of gases lost is higher for materials HsStT\_2 prepared at pH 2 (2.5-2.88 mmol) compared to the materials HsStT\_u prepared without pH modification (1.12-1.45 mmol). It was shown previously that the HTC yield was better with acidic conditions compared to non modified pH conditions. Beside, for unmodified pH, the oxygen content appears higher than for pH 2. Therefore, the amount of gas released seems to be governed by the HTC yield rather than by the C/O ratio of the HTC hydrochar. The highest gas released during “dry” carbonization being promoted by a hydrochar obtained with high yield rather than a hydrochar with high oxygen content.

XPS results, C1s and O1s regions, for all materials at all proportions T/S are presented in Table 8. C1s core level spectra (not shown here) for all samples show an asymmetric peak centered at about 284.5 eV. The fitting of each peak showed the presence of various contributions with binding energies (BEs) in percentage that are given in Table 8. The BEs of the fitted peaks were assigned to different C linkages according to Perry et al. (1983), Desimoni et al. (1990) and Albers et al. (1992). Two types of carbons were found for all samples: C1 assigned to hydrocarbons (aliphatic, aromatics) and C2 assigned to C-O single bond in alcohols, phenols and carboxyls. The contribution C3 assigned to C=O double bond in carbonyls, quinones and C associated to N are seen for all materials except from C100T, H50S50T180\_2 and H50S50T180\_u. Tannin after direct pyrolysis, C100T, presented the highest amount of C1 from hydrocarbons (83.8%) and no C3 contribution.

a)



b)

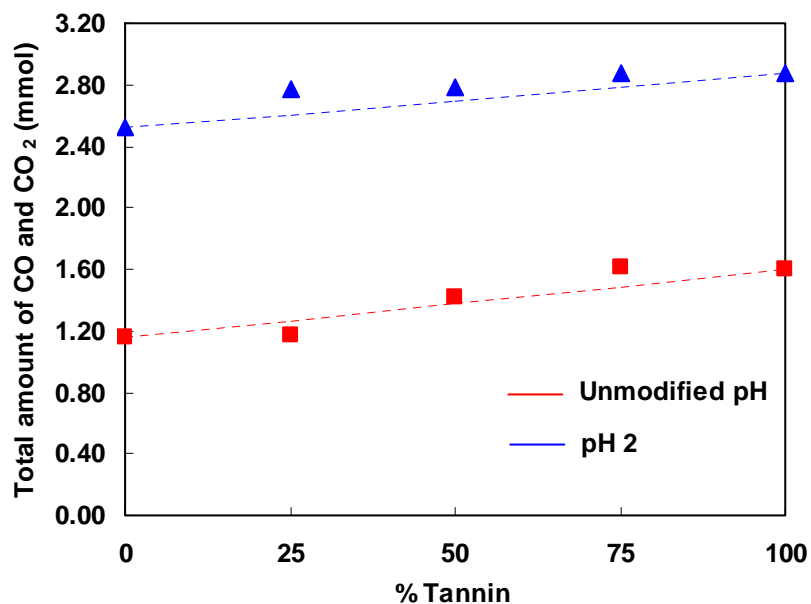


Fig. 54: a) van Krevelen diagram for all materials before (100S and 100T) and after HTC (H100S and H100T) and at unmodified pH (HsStT\_u) and at pH 2 (HsStT\_2) and posterior pyrolysis at 900°C (HTC\_900°C); and b) the total amount of CO and CO<sub>2</sub> gases produced during TPD analysis for T / S materials at different proportions.



Table 8: Contributions to the C1s O1s bands in XPS patterns.

	C1s peak Area of peak (%)			O1s peak Area of peak (%)	
	<b>C1</b> 284.4- 284.6 eV	<b>C2</b> 285.5- 286.1 eV	<b>C3</b> 287.7- 288.5 eV	<b>O1</b> 531.1- 531.8 eV	<b>O2</b> 532.3- 533.3 eV
<b>100T</b>	59.7	33.8	6.5	14.1	85.9
<b>C100T</b>	83.8	16.2	-	8.4	91.6
<b>H50S50T180_2</b>	73.0	27.0	-	-	100
<b>CH50S50T180_2</b>	50.3	39.0	10.7	11.5	88.5
<b>H100T180_2</b>	83.5	14.4	2.1	46.2	53.8
<b>CH100T180_2</b>	46.6	40.5	12.9	6.5	93.5
<b>H50S50T180_u</b>	23.6	76.4	-	-	100
<b>CH50S50T180_u</b>	48.1	41.1	10.8	9.5	90.5
<b>H100T180_u</b>	68.9	28.5	2.6	45.3	54.7
<b>CH100T180_u</b>	46.2	41.3	12.5	9.3	90.7

Table 8 also shows the O1s and O2s contributions for all materials. The first BE of the fitted peaks are between 531.1 and 531.8 eV, assigned to double C=O bonds in ketone and carboxyl acid groups, and at BE between 532.3 and 533.3 eV, assigned to single C–O bonds from alcohols, phenols and carboxyl acid groups. It is clear that C2 contributions are higher for all materials due to the presence of C–O bonds from phenol groups. However, HTC of tannin at both pHs showed the presence of almost 50% of each contribution C1 and C2. The HTC procedure also contributes to generate a surface functional material presenting stable oxygen atoms. Comparison of elemental analysis data reported in Table 4, Table 5 and Table 7, shows that HTC has the advantage to produce, after high temperature carbonization (900°C), carbon materials with the highest oxygen content with 10 wt.% (CH100T180\_u) whereas the direct carbonized tannin gave only 8 wt.% of oxygen (C100T). Nevertheless, this trend is no more valid when HTC is performed in acidic media (CH100T180\_2) or in presence of sucrose that acidified the synthesis media (CH100S180\_u) where the oxygen contents of 3.5–6.5 wt.% were lower than C100T (8.2 wt.%).

### 3.4 Effect of silver nitrate addition into HTC of tannin

Hydrothermal treatment seems to be the cheapest and low energy consumption procedure to fabricate silver nanoparticles, suitable also for industrial production. Fig. 55 shows TEM photos of the filtrates after dissolving 2.0 g of tannin in 15.5 g of water and 0.5 mL of an

aqueous solution of 0.1M of AgNO<sub>3</sub> and performing a HTC at 180°C for 1, 2 or 4h without modifying the pH. Silver nanoparticles encapsulated into hydrochar microspheres were found. These microspheres had a polydispersed size distribution. In the literature, the effects of time, temperature of HTC and concentration of AgNO<sub>3</sub> were studied by Sun and Li (2005) using glucose as reducing agent. These authors found that a low concentration of Ag<sup>+</sup> ions (0.625 10<sup>-3</sup> M) produced nanoparticles having perfect core/shell nanostructures in which Ag<sup>0</sup> was encapsulated into a shell of hydrochar produced from glucose. However, Ag<sup>+</sup> in an excessive amount (7.5 10<sup>-3</sup> M), produced nanoparticles, which were aggregated as chainlike structures similar to those showed in Fig 53 for HTC reaction times of 2 and 4h.

The HTC yield of tannin was around 7.5% at 180°C and 1.67h of reaction. Here, Ag<sup>+</sup> reduction by tannin occurs even at low residence times (i.e. 1h). The mechanism between the reaction of hydrolysable tannin and silver aqueous solution at 70-80°C was reported elsewhere [Bulut and Özacar 2009]. Tannin acts as the reducing agent because it has a great amount of hydroxyls groups that can interact to produce the reaction Ag<sup>+</sup> → Ag<sup>0</sup>. Ag metal is formed through an intermediate product of Ag<sup>+</sup> – tannin complex. Tannin oxidation produces the complex elimination; Ag<sup>+</sup> ions are converted into Ag metal. By coalescence and growth, clusters are formed leading to the formation of Ag particles [Gunckel et al. 1998; Sánchez-Cortés et al. 2000; Ortiz-Ibarra et al. 2007; Bulut et al. 2009].

Fig. 56 shows the effects of the augmentation of the added volume of 0.1M AgNO<sub>3</sub>: 1, 2 and 6 mL to a tannin aqueous solution submitted to HTC at 180°C and 24h. Having just 1 mL 0.1M AgNO<sub>3</sub> or 0.011 g of Ag<sup>+</sup> into the system produced a polydisperse distribution of microspheres, where very small spheres coexisted with much bigger ones. Increasing the amount of solution added produced more homogenous systems with smaller microspheres. These results agree well with those obtained by Sun and Li (2005) concerning the addition of Ag<sup>+</sup> to glucose. The formation of Ag@C core/shell structures involves two steps: nucleation of silver nanoparticles and, growing and thickening of the carbonaceous shell made from hydrochar of glucose. In the literature, Heparin, a sulphur-containing polysaccharide, together with a silver nitrate aqueous solution was submitted to agitation in a 70°C water bath to produce silver nanoparticles. When the concentration of Ag<sup>+</sup> ions was increased (from 2 to 5 mM), the size of silver nanoparticles also increased and therefore larger particles and Ag clusters were formed [Huang and Yang 2004; Korbekandi and Iravani 2012].

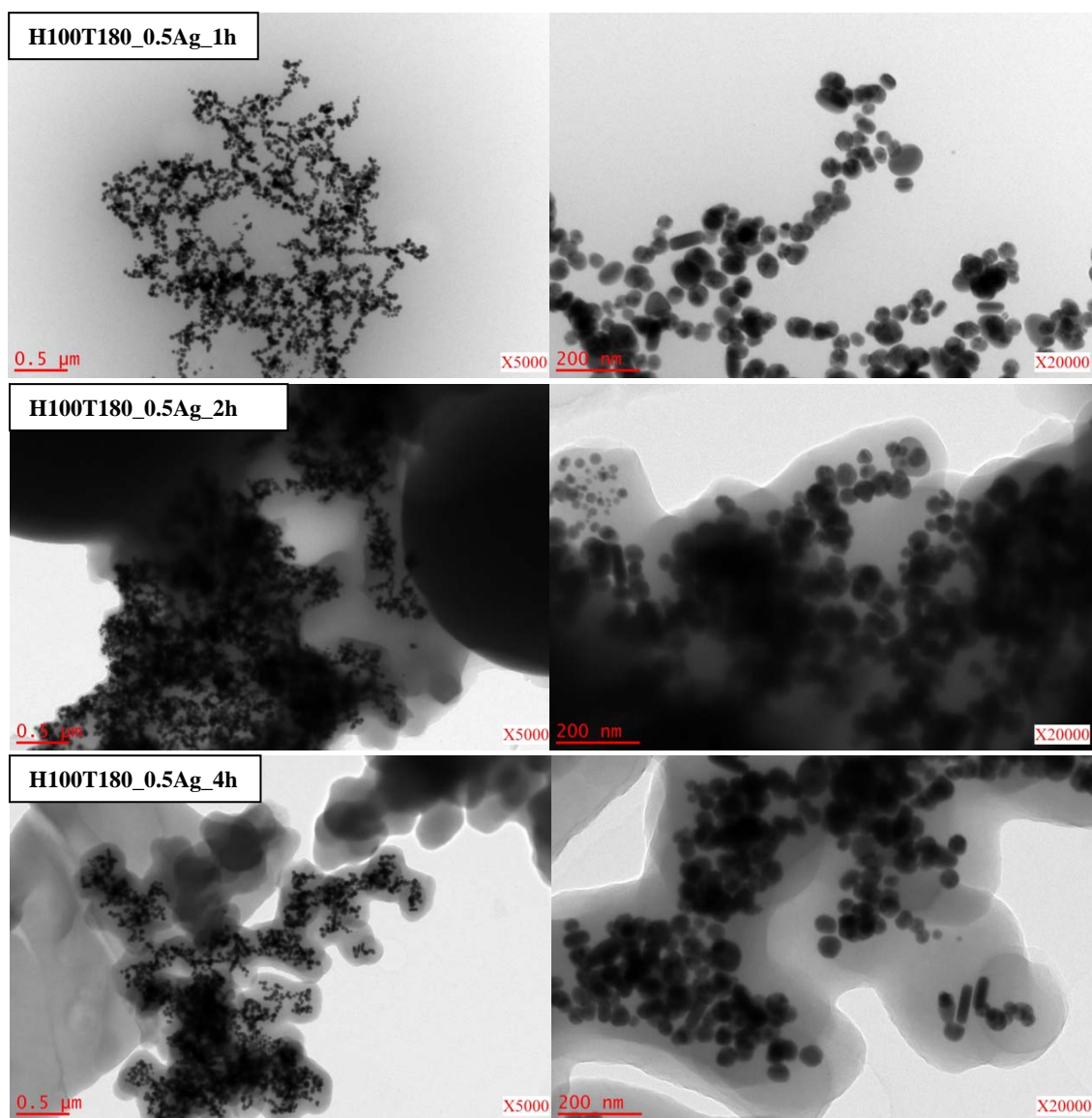


Fig. 55: TEM images of three filtrates obtained after HTC of tannin at 180°C in presence of  $AgNO_3$  solution during 1, 2 and 4h respectively.



Fig. 56: TEM images of three filtrates obtained after HTC of tannin with 1, 2 or 6 mL of 0.1M  $AgNO_3$  solution at 180°C for 24h and posterior carbonization at 900°C.

Fig. 57 shows the HTC yield and the surface area BET with increasing amounts of silver nitrate added to 2g of tannin submitted to HTC. Both parameters were calculated at different manners. The full blue symbols show the HTC yield of the whole solid material recovered including silver ( $Ag^0$ ). On the other hand, the full red symbols show the HTC yield to the solid material calculated without the presence of  $Ag^0$ , assuming that all  $Ag^+$  ions were reduced to  $Ag^0$  and remained on the hydrochar. The same was done for the surface BET, which was measured for the carbon material (empty blue symbols) and calculated per mass (g) of carbon once  $Ag^0$  was subtracted (empty red symbols). The addition of silver nitrate has an influence on both parameters: HTC yield and  $S_{BET}$  of the final carbon material. HTC yield increased with the augmentation of silver nitrate added while the  $S_{BET}$  was reduced to  $554 \text{ m}^2 \text{ g}^{-1}$ . These tendencies were observed even after subtraction of the  $Ag^0$  content.

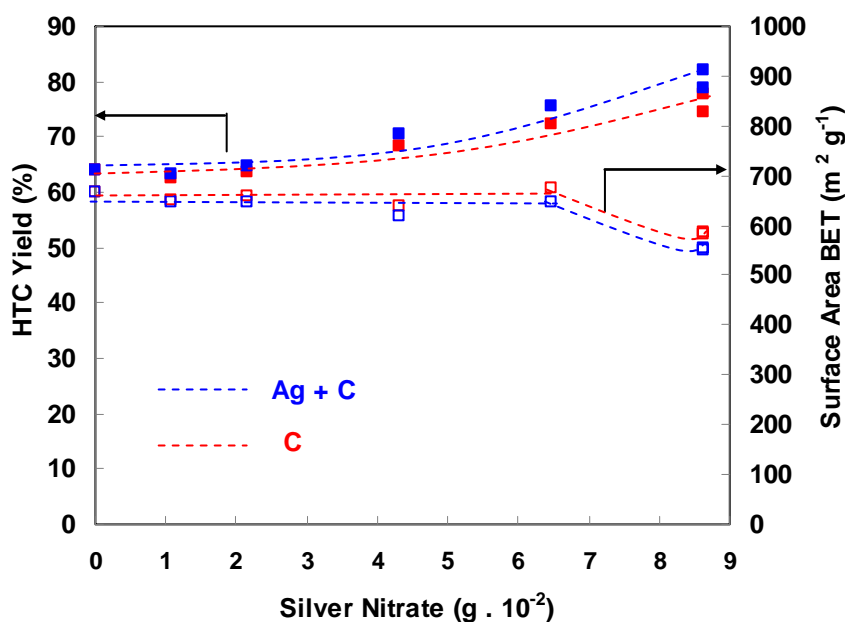


Fig. 57: HTC yield and surface area (BET) of all samples made with tannin and  $AgNO_3$  solution.

HTC yield increased from 63 to 83 % when adding 1 to 8 mL of 0.1M  $AgNO_3$  ( $\approx 0.01$  and  $\approx 0.09$  g of  $Ag^+$ , respectively) and from 63 to 78 % but just calculating the HTC yield to hydrochar without  $Ag^0$  (see Fig. 57 and Table 9). Table 9 shows the textural parameters as well as the HTC, carbon and total yield, and elemental analysis of all materials.  $S_{BET}$  was relatively constant with the augmentation of silver nitrate up to 6mL. Tannin submitted to HTC had a surface area of  $665 \text{ m}^2 \text{ g}^{-1}$ . A volume addition of 0.1M  $AgNO_3$  lower than 8ml reduced slightly the surface area but it remained in the range  $632 \pm 15 \text{ m}^2 \text{ g}^{-1}$ . The addition of 8 mL of 0.1M  $AgNO_3$  reduced the  $S_{BET}$  down to  $554 \text{ m}^2 \text{ g}^{-1}$ . The volume of micropores

determined by N<sub>2</sub> adsorption was reduced from 0.25 to 0.21 m<sup>3</sup> g<sup>-1</sup> and also that of micropores determined by CO<sub>2</sub> adsorption from 0.31 till 0.25 m<sup>3</sup> g<sup>-1</sup>. The volume of micropores determined by CO<sub>2</sub> was always higher than that determined by N<sub>2</sub>, which means that a very narrow porosity not accessible to N<sub>2</sub> at -196°C exists. The isotherms are characteristic of microporous solids, both type I following the IUPAC classification without hysteresis cycle as seen in Fig. 58 a) which is confirmed with the PSD in a range of 0.5-1.5 nm together with a slight slope showing the presence of pore diameters wider than 2 nm as confirmed in Fig. 58 b).

Table 9: Textural properties of all silver nanoparticles samples prepared after HTC and posterior pyrolysis.

				Textural Properties						Elemental Analysis (wt. %)					
	HTC* yield (%)	Carbon yield (%)	Total yield (%)	S <sub>DFT</sub> (m <sup>2</sup> g <sup>-1</sup> )	S <sub>BET</sub> (m <sup>2</sup> g <sup>-1</sup> )	V <sub>0.97</sub> (cm <sup>3</sup> g <sup>-1</sup> )	V <sub>μ</sub> (cm <sup>3</sup> g <sup>-1</sup> )	V <sub>CO2</sub> (cm <sup>3</sup> g <sup>-1</sup> )	Total yield x S <sub>BET</sub>	C	H	N	S	O	C/O
CH100T180_1Ag	62.7	53.3	33.4	618	645	0.27	0.25	0.31	218	91.2	1.5	0.8	0.0	11.2	8.2
CH100T180_2Ag	63.6	53.0	33.7	570	648	0.26	0.25	0.28	222	92.9	1.6	0.7	0.0	9.4	9.9
CH100T180_4Ag	68.3	51.8	35.4	647	618	0.25	0.23	0.28	225	91.2	1.7	0.7	0.0	6.4	14.4
CH100T180_6Ag	72.2	51.7	37.3	563	647	0.27	0.25	0.28	252	93.2	1.4	0.6	0.0	4.9	19.1
CH100T180_8Ag	77.6	52.0	40.4	576	554	0.25	0.21	0.25	236	91.2	1.3	0.5	0.0	4.9	18.4

\* HTC yield calculated without Ag<sup>0</sup>

The decrease of surface area and pore volume were also found when increasing the metal loading up to 5 wt. % during the preparation of silver colloids catalysts imbedded in alumina [Pârvulescu et al. 2010]. During the preparation of Pd nanoparticles supported on starch through overnight agitation and posterior filtration, the surface area and the mesoporous structure of the material were preserved at lower Pd content but an increase of Pd content from 2.5 to 5 wt.% resulted in a significant decrease of the S<sub>BET</sub> due to pore blocking [Budarin et al. 2008]. Using also starch to produce silver nanoparticles through agitation, White et al. (2011a) found that the pore diameter maxima in the mesopore region was sensitive to Ag<sup>+</sup> loading presumably due to pore filling with larger Ag nanoparticles. Pore size distributions become increasingly narrower and the maximum diameter became increasingly smaller with Ag<sup>+</sup> loading changing from 8.2 nm (without silver ions) to 5 nm (having 0.180 mmol g<sup>-1</sup> of AgNO<sub>3</sub> sol.) [White et al. 2011a]. In our case, with the addition of Ag<sup>+</sup> into the system, the

PSD also reduced in the region lower than 2 nm (micropores) but presents a slight slope showing the presence of mesopores (between 1 and 10 nm).

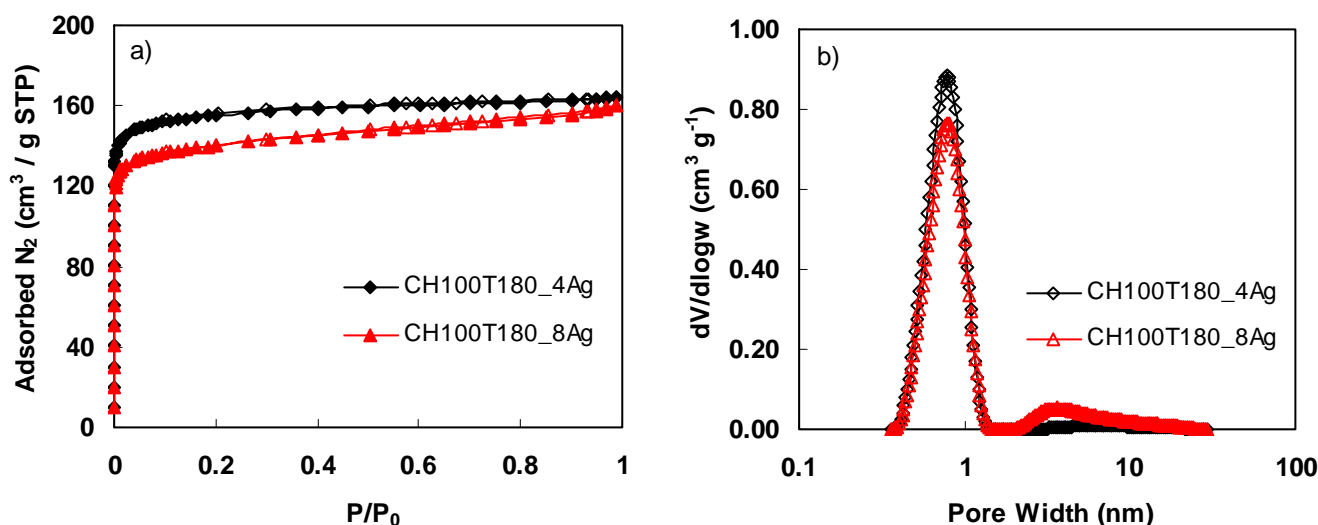


Fig. 58: a) Nitrogen adsorption-desorption isotherms (full and open symbols, respectively) at  $-196^{\circ}\text{C}$  for pristin two materials made after HTC at  $180^{\circ}\text{C}$  having 4 and 8g of an aqueous solution of  $AgNO_3$  after posterior pyrolysis at  $900^{\circ}\text{C}$ ; and b) their correspondent pore size distribution obtained by PSD.

If the hydrochar yield increased with the volume of  $AgNO_3$  solution added, the carbon yield was proximately the same (around 52-53%) for all the samples indicating that  $Ag^0$  does not have a catalytic effect during carbonization reactions. Taking into account the product Total yield  $\times S_{\text{BET}}$ , an optimum was found at the sample prepared by addition of 6 mL of 0.1M  $AgNO_3$  (sample CH100T180\_6Ag). For this sample, the  $S_{\text{BET}}$  was  $647 \text{ m}^2 \text{ g}^{-1}$  and the total yield of 37%.  $Ag^+$  addition did not have a significant effect on the elemental composition on the resultant carbon materials.

### 3.5 Conclusions

Three modifications to the system tannin in aqueous solution submitted to HTC were proposed in order to increase the carbon yield. Moreover the impact of these modifications on the textural properties of the carbon materials was studied. The main conclusions are the following:

- 1) The reduction of the pH, increased the hydrochar yield but reduced the carbon yield resulting in a positive impact on the total yield comparing to an unmodified pH. In addition, the carbon materials derived from hydrochars produced at low pH had higher

surface areas with almost the same microporous size distribution. The product total carbon yield  $\times S_{\text{BET}}$  was much higher for carbon materials prepared by reduction of pH down to 1, it increased from 220 m<sup>2</sup> g<sup>-1</sup> (unmodified pH) to 319 m<sup>2</sup> g<sup>-1</sup>. By applying a previous HTC step and decreasing the pH down to 1, surface area increased from 476 (for C100T) to 791 m<sup>2</sup> g<sup>-1</sup> (CH100T\_1).

- 2) The addition of sugar produced microspheres of lower particle size due to the increase of germs produced by sucrose HTC. Carbon yield increased only at unmodified pH and remained constant at pH=2 when compared to pure tannin submitted to HTC. The addition of sucrose produced also a slight increase of the  $S_{\text{BET}}$ . After carbonization, the surface chemistry of carbon materials prepared at pH=2 was similar to that of those materials prepared at unmodified pH.
- 3) The presence of silver nitrate in the tannin aqueous solution produced a reduction and homogenisation of the microsphere particle size. Hydrochar yield increased but surface area decreased possibly due to the presence of Ag nanoparticles blocking the porosity. Such materials containing silver nanoparticles present numerous potential applications such as in biochemistry and also as in electronic sensors.

## **Chapter 4: N-doped carbon materials and their use as electrodes for supercapacitors**





In this chapter, the preparation and characterisation of N-doped carbon spheres will be investigated including the morphology, textural characteristics and chemical composition of all materials. For that purpose, HTC of aminated tannin has been carried out as first step of carbonization and therefore NCM's were obtained (Fig. 59): as a powder by HTC of tannin in a concentrated aqueous ammonia solution (AT route); and as a gel without using any crosslinker (formaldehyde for example) by HTC in water of tannin previously aminated at room temperature (EAT route). Those materials were then submitted to a second thermal treatment to develop and increase their textural characteristics. Such a choice is justified by the easiness of the amination reaction of tannin, and by the high efficiency of nitrogen incorporation into carbon matrices offered by the HTC process. N-doped materials with high surface area and high nitrogen content were obtained and they were tested as electrodes for supercapacitors. These materials presented outstanding specific capacitances at  $2 \text{ mV s}^{-1}$ , close to those already reported for high surface area-activated carbons.

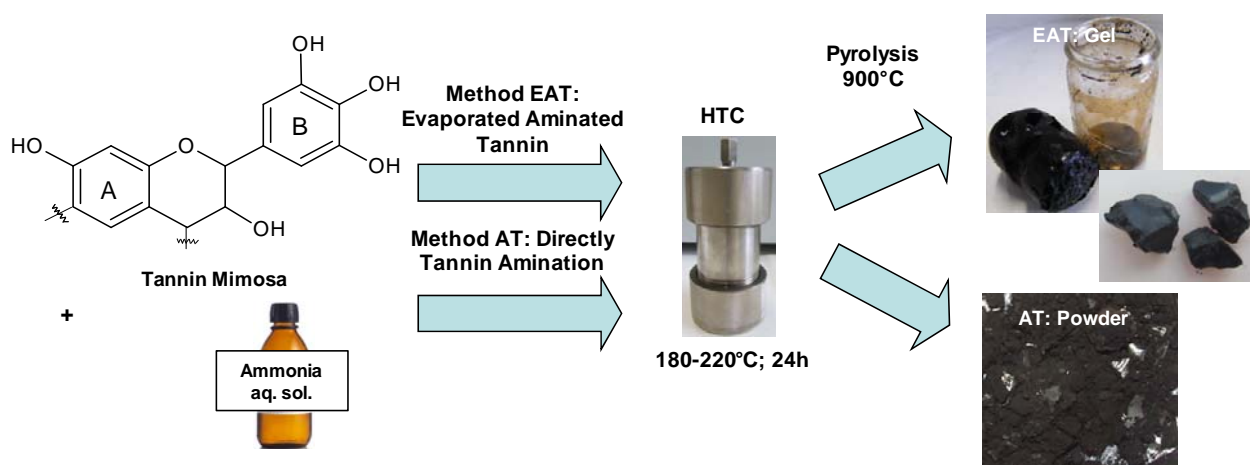


Fig. 59: Graphical procedure for the synthesis of hydrochars made from N-modified tannin.

#### 4.1 Preparation of N-doped materials by HTC

The first step for the synthesis of N-doped materials is the amination of tannin which was made through two different methods and all the textural and chemical characteristics of the final materials were compared to obtain an optimal sample. In both methods, tannin powder was dissolved into a concentrated aqueous ammonia solution at 28% as shown in Fig. 60. These samples were then carried out according to two different ways: (1) evaporation, in order to recover a dry powder subsequently submitted to HTC; (2) direct HTC of the as-obtained solution. A reference sample of pure tannin powder was also treated by HTC. The method (1) was named as: evaporated aminated tannin (EAT), prepared from 2g of tannin which was mixed with  $40 \text{ cm}^3$  of aqueous ammonia in air. The solution was sealed and stirred

for 1h at room temperature. Afterwards, the mixture was placed in a Petri dish, and left for evaporation in a fume hood during two days at room temperature, in order to remove the excess ammonia. The solid, dry residue, not completely soluble in water at room temperature, was mixed with 16g of bi-distilled water.



Fig. 60: The methods used for preparing N-doped carbon materials and their respective final products.

The method (2) was named as aminated tannin (AT) which was prepared by mixing 2g of tannin with 16 cm<sup>3</sup> of aqueous ammonia in air. The tannin was completely soluble, and the resultant solution was sealed and stirred for 1h at room temperature. A reference sample was also prepared just for the sake of comparison, one sample (T) was obtained by dissolving 2g of raw tannin in 16 g of bi-distilled water. Each solution sample was installed in a Teflon-lined autoclave for HTC. The inner volume of the autoclave was 50 cm<sup>3</sup>, so that the volume of liquid placed inside, around 16 cm<sup>3</sup>, was 1/3 of its capacity. The autoclave was directly put into a ventilated oven pre-heated at different temperatures 180, 190, 200, 210 and 220°C, and

remained inside during 24 h at the same temperature once temperatures equal or higher than 180°C and reaction time of 24h were optimal conditions for HTC of tannin.

After HTC, the autoclave was left to cool down at room temperature. The resultant dark powders or monoliths, depending on the synthesis method as shown in Fig. 60, were recovered, washed with distilled water and then placed inside of a vacuum oven at 80°C for drying during 12h. EAT, AT and T samples were labelled H-EAT, H-AT and H-T after HTC, respectively. H-EAT, H-AT and H-T samples were finally pyrolysed in high-purity nitrogen, leading to materials labelled CH-EAT, CH-AT and CH-T, respectively. Pyrolysis was carried out in the quartz tube of a tubular furnace heated at 1°C min<sup>-1</sup> up to 900 °C. The final temperature was maintained for 3h, after which the resultant carbon samples were cooled under nitrogen flow.

## 4.2 Chemical structure of hydrothermally treated tannin

### 4.2.1 <sup>13</sup>C NMR studies

Solid-state <sup>13</sup>C NMR spectra of Mimosa tannin and the hydrothermal carbons H-T, H-EAT and H-AT, obtained after HTC at 180°C are shown in Fig. 61 and 62 respectively. Table 10 shows the numbered carbons present in Mimosa tannin (see Fig. 6 a), Chapter 1) according to the peaks in ppm seen in <sup>13</sup>C NMR spectra. As it can be seen, the spectrum of H-T (Fig. 62) is typical of flavonoid Mimosa tannin (see Fig. 61 and Table 10) [Pizzi 1994], however with the distinctive feature that the peaks are much broader than usual. This finding is related to the autocondensation of tannin induced by HTC. Another difference is the absence of peaks between 60 and 80 ppm, characteristic of the carbohydrates formerly present in the tannin extract, and that have been hydrolyzed in hot pressurized water.

Additionally, the disappearance of the peak at 81-82 ppm, corresponding to the C2 site shown in Fig. 6 a), indicates that the almost totality of the heterocyclic C ring is in the open form. Simultaneously, there is a relative decrease of the band at 157-158 ppm, compared with the spectra of raw Mimosa tannin, indicating a relatively lower proportion of C5, C7 and C9. While the decrease of the C9 signal is logical due to heterocyclic ring opening, the apparent relative decrease of C5 and C7 could be due to reactions on C6 and C8, indicating that the autocondensation is likely to partially proceed between C2 (open) to C6 or C8. There is also a considerable increase of the bands between 30 and 50 ppm that are difficult to be ascribed, but probably coming from -CH<sub>2</sub>- from sugar hydrolysis due to -OH elimination from their structure. Alternatively this is a shift of the C4 peak, indicating some autocondensation taking

place on C4 to C6 and C8. Therefore, the opening of the heterocyclic C2–ring is the base of the autocondensation for the solution of tannin in water at HTC conditions.

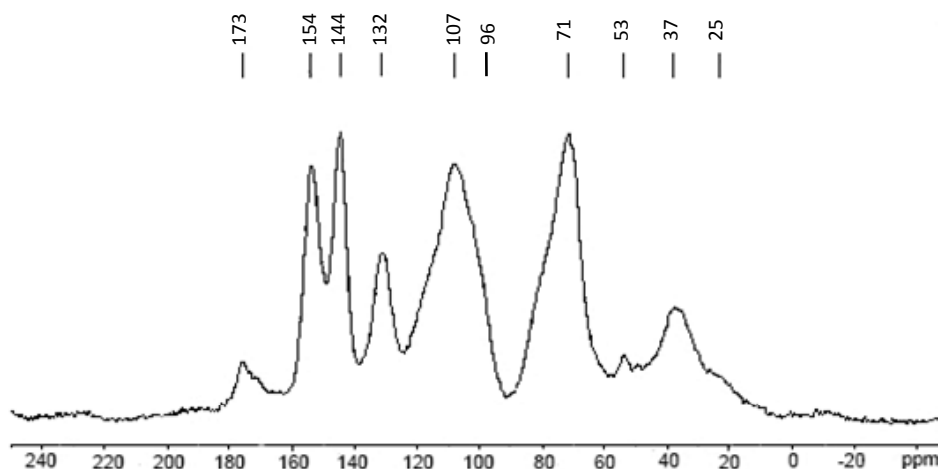


Fig. 61: The spectrum of RMN of  $C^{13}$  of tannin Mimosa in a solid state [Pizzi 1994].

Table 10:  $^{13}C$  NMR peaks in ppm of the numbered carbons and gallic acid residues present in Mimosa tannin.

<i>Numbered carbons and materials present in Mimosa tannin</i>	<i>Peaks present in <math>^{13}C</math> NMR spectra (ppm)</i>
gallic acid residues	173
C5, C7, C9	155-156
C3' and C4'	145-146
C1'	130
C4 to C6	107
C2	81-82
C3	70-72
C4	24-25

The spectrum of the H-EAT sample shears the main features of that of H-T, however with some significant differences. The intensity of the C3' and C4' bands at 145-150 ppm indicates that the –OH groups have decreased, probably through substitution by –NH– or –NH<sub>2</sub> groups. This is supported by the equivalent decrease of the C2' and C5' bands at around 110 ppm without any effect on the C6' band at 115 ppm that remains unaltered. The sugars are hydrolyzed as shown by the low 30-50 ppm bands, even more than in the H-T sample. Additionally, while the majority of heterocyclic rings are open, the C2 band is still present here, indicating that some close heterocyclic structures are still maintained after HTC. The

spectrum also shows polymerization, just like for H-T sample, but in much less extent than H-AT. H-EAT is the only one that may show condensation through –NH– bridges and therefore, this event could explain why it is the only material made from tannin and ammonia solution at 28-30 % that formed a gel whereas no additional crosslinker was present in the system. The presence of –NH<sub>2</sub> groups and –NH– bridges could confirm that, using HTC conditions such as temperature and pressure, not only the –OH at position C4' reported by Hashida et al. (2009) and Morisada et al. (2011) but other hydroxyl groups turned to –NH<sub>2</sub>.

The H-AT spectra is not interpretable. The only point that can be made is that H-AT is very polymerized due to the huge widening of the bands. It can be seen the practically disappearance of the 30-50 ppm bands indicating destruction of the carbohydrates, a wide C4 peak but much less pronounced than the H-T sample indicating that there is much less C4 to C6 and C4 to C8 autocondensation in this case. The mystifying thing of these spectra is the huge single wide peak between 90 and 180 ppm. Nothing can be distinguished here, it almost appears that the structure of the tannin itself has been lost. The fusion of all the bands indicates a very high level of polymerization and reticulation of the material. Thus condensation through N or other mechanisms is possible but can be indisputably assigned through which it is not possible to define. Another possible explanation of these poorly resolved spectra is the presence of radicals, easily formed by polyphenols and stabilized in basic media (phenolate form) as it is the case for these syntheses [Pizzi 1999].

In summary, H-T has a similar structure as that of flavonoid tannin, but presents a much higher level of polymerisation, mainly through the opening of the heterocyclic C2–ring and subsequent partial condensation between C2 (open) to C6 or C8, and partly through some autocondensation C4 to C6 and C8. H-EAT shears the main features of H-T in terms of autocondensation and heterocyclic C2-ring opening, but is also characterized by the amination of C3' and C4' sites, the preservation of some heterocyclic structures, and a lower level of polymerization. The presence of –NH– bridges is also observed, possibly explaining why H-EAT is a gel whereas no crosslinker was initially present in the system. Finally, H-AT is a highly polymerized and crosslinked material, in which the typical tannin structure is almost completely lost.

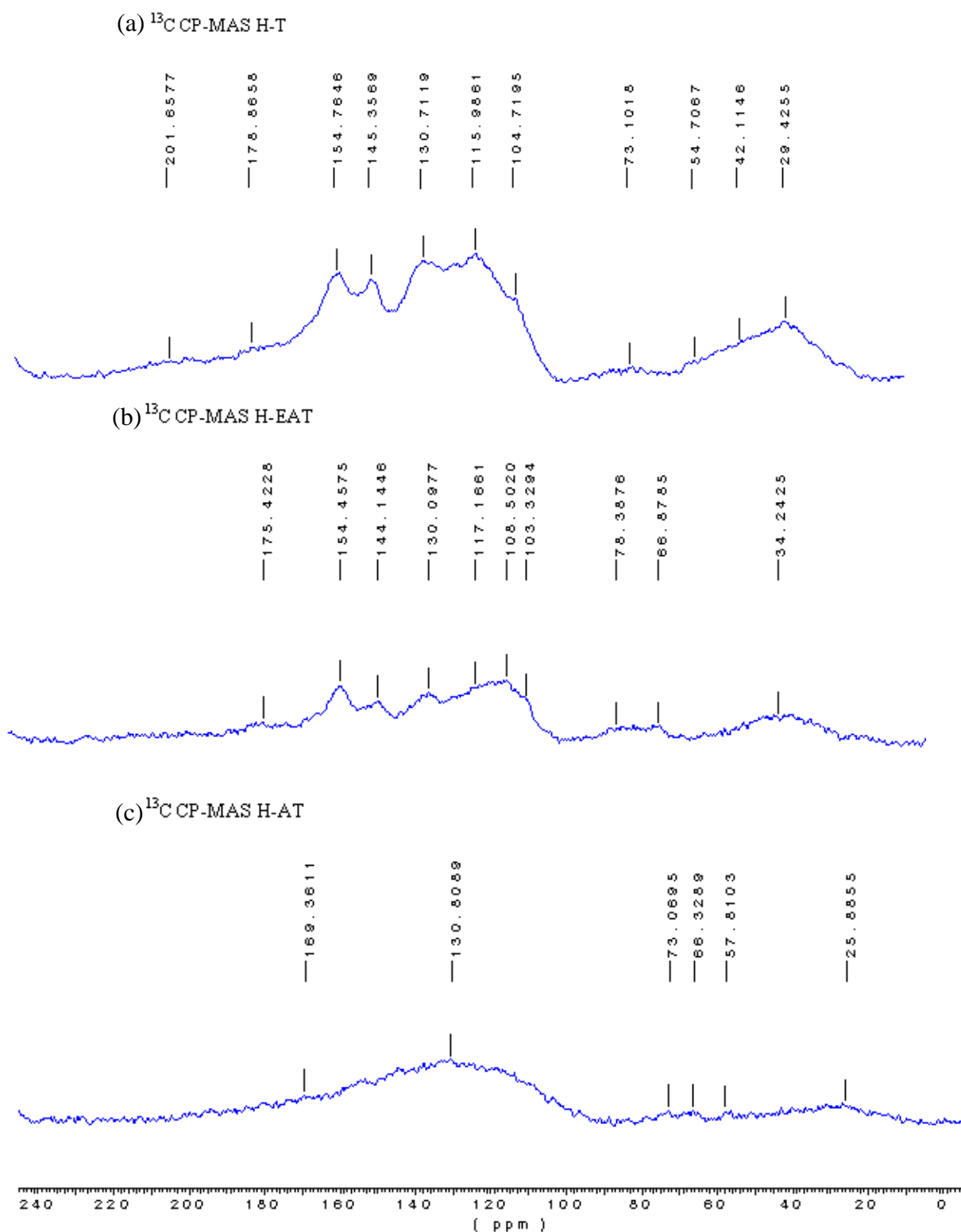


Fig. 62: Solid-state CP-MAS  $^{13}\text{C}$  NMR spectra of all materials after HTC at  $180^\circ\text{C}$ : (a) H-T; (b) H-EAT, and (c) H-AT.

### 4.2.2 MALDI-ToF studies

MALDI-ToF spectra of the HTC-derived materials and Mimosa tannin and their detailed interpretation are given in Fig. 63 and 64 respectively. The spectrum of mimosa tannin extract indicates the presence of flavonoid repeating units at a relatively important proportion of 288 Da (Fig. 64), indicating that this tannin is predominantly a prorobinetinidin [Pasch et al. 2001]. For the spectrum of H-T (Fig. 63 c)) in which nitrogen is absent, a fairly normal MALDI-ToF spectrum for flavonoid tannin appears. There is no gel here so only perhaps some low level of self polymerisation. The interpretation of the MALDI spectra can be done based on the fact that four flavonoid units may be obtained depending on the position and on the number of –OH groups. Thus, one hydroxyl at position 7 of the A-ring and two others at positions 3' and 4' of the B-ring lead to a flavonoid of molecular weight 274 Da. If three –OH are now present on the B-ring (at positions 3', 4' and 5'), the weight becomes 290 Da. The same if, instead, two –OH are present on the A-ring (at positions 5 and 7) and two other remain on the B ring (at positions 3' and 4'). Finally, if two –OH on A-ring and three –OH on B-ring are present, the molecular weight is 304 Da. Consequently, flavonoids having three different molecular weights of 273, 289 Da and 304 Da, below referred to as I, J and K, respectively, can combine with each other into oligomers detected by the MALDI spectrometer, as shown in Table 11.

The most interesting of the three spectra is the one of H-EAT (Fig. 63 a)), thus of the gel made from aminated tannin after evaporation. Indeed, only reasonably low molecular masses can be seen and the explanation is that being a gel, the material is composed of very long chains polymerized to an “infinite” three-dimensional network. Such molecules cannot be detected by MALDI-ToF as of too high molecular weight, beyond the range examinable and in this case, it can be deduced by the peaks that remain. As the mimosa extract used in the present study contains a small percentage of flavonoid monomers, mainly fisetinidin and robinetinidin, it is to be expected that some of these monomers may dimerize through the mechanisms pointed out by  $^{13}\text{C}$  NMR for both model compounds and tannins themselves. Thus, on top of the standard 553 Da peak present in all the spectra that is likely to be either a dimer of the 2,5-dihydroxybenzoic acid (DHB) calibration compound or a bifisetinidin flavonoid from which a –OH group has been lost, the two most interesting peaks showing the doping by nitrogen of the flavonoid structures are the ones at 554 Da and 555 Da.



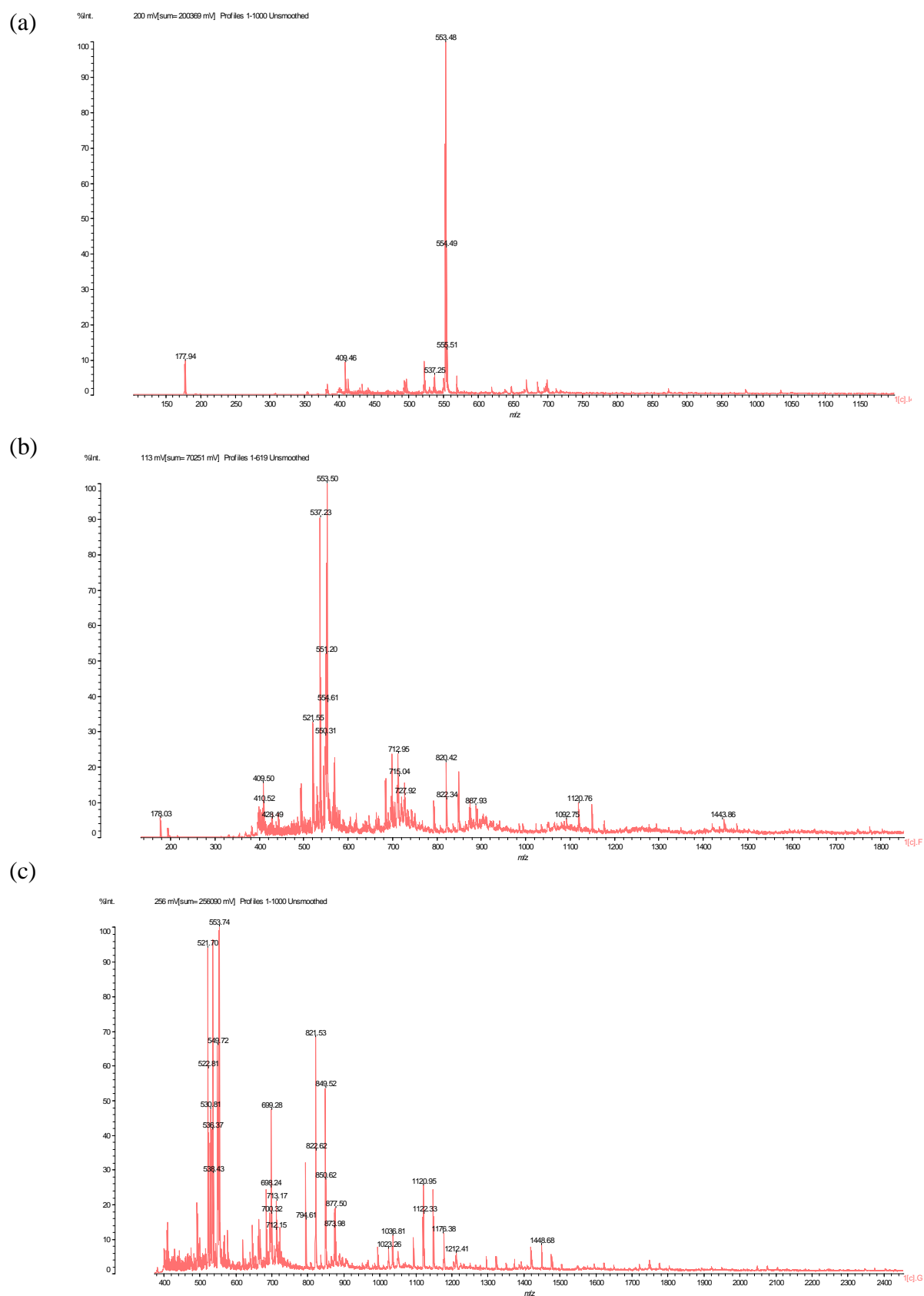


Fig. 63: MALDI-TOF spectra of all materials after HTC at 180°C: (a) H-EAT; (b) H-AT, and (c) H-T.

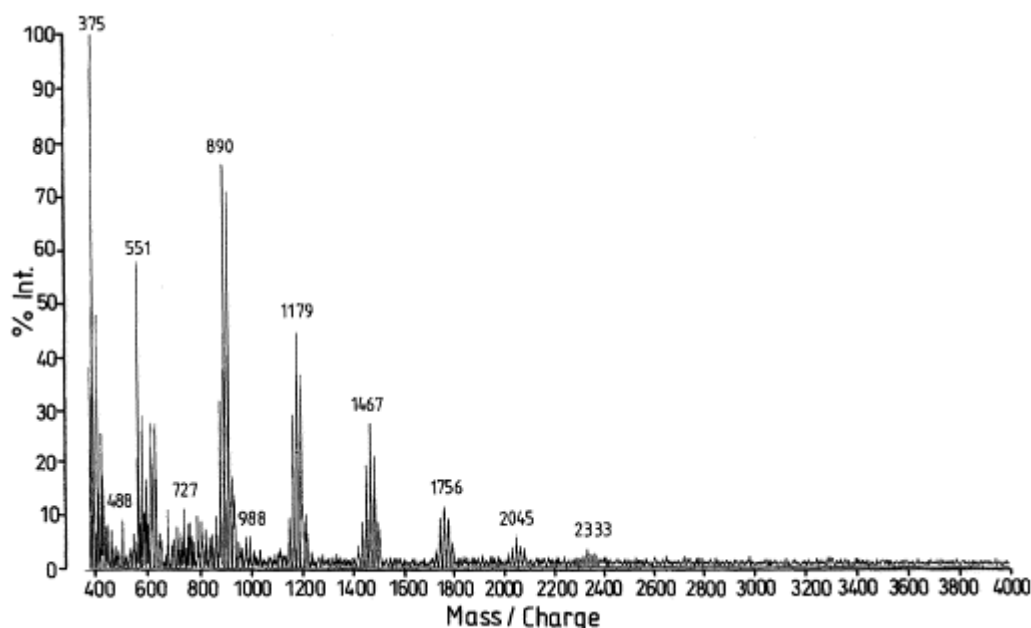


Fig. 64: MALDI mass spectrum of natural Mimosa tannin extract [Pasch et al. 2001].

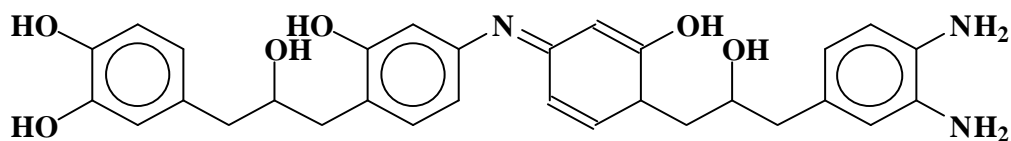
Table 11: MALDI-ToF peaks of H-T, i.e. tannin submitted to HTC at 180°C.

Experimental (Da)	Calculated (Da)	Suggested molecular species
521 and 522	518	$I_2 - 3 \times -OH + Na^+$
530	530	$I_2 - 2 \times -OH - 5 \times -H + Na^+$
536	535	$I_2 - 2 \times -OH + Na^+$
549	549	$I_2 - 1 \times -OH - 3 \times -H + Na^+$
553	552	$I_2 - 1 \times -OH + Na^+$
821	821	$I_2J - 2 \times -OH - 3 \times -H + Na^+$ or $I_3 - 1 \times -OH - 4 \times -H + Na^+$
874	874	$IJ_2 + Na^+$
1093	1093	$I_4 - 1 \times -OH - 5 \times -H + Na^+$
1147	1147	$I_2J_2 + Na^+$
1176	1179	$J_4 + Na^+$
1212	1209	$J_2K_2 + Na^+$
1448	1448	$IJ_4 - 4 \times -H + Na^+$

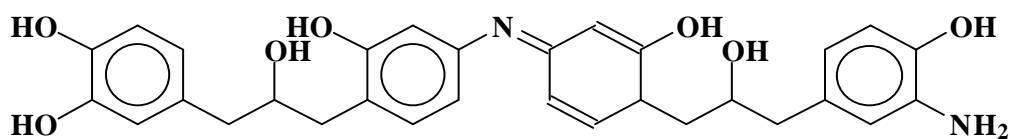
While these structures are based on a skeleton of fisetinidin, the little difference in mass confirms what observed by NMR both for the model compounds and the tannin. They are composed of two fisetinidin monomers dimerized through a  $-N=$  bridge. The structure's Da count indicates that on top of the  $-N=$  bridge between the two flavonoid units for the 554 Da peak there are two only of the  $-OH$  groups of the whole structure that are substituted by  $-NH_2$  groups, and for the 555 Da peak there is only one of the  $-OH$  groups of the whole structure that is substituted by a  $-NH_2$  group. These  $-NH_2$  groups can have substituted any one of the  $-OH$ s of the two flavonoid units and thus their distribution is likely to be variable. The 554 Da and 555 Da structures can then be interpreted as shown in Fig. 65(a) and 64(b), respectively,

with the  $\text{-NH}_2$  groups distributed in any position where there is an  $\text{-OH}$ , without further definition possible.

(a)



(b)



(c)

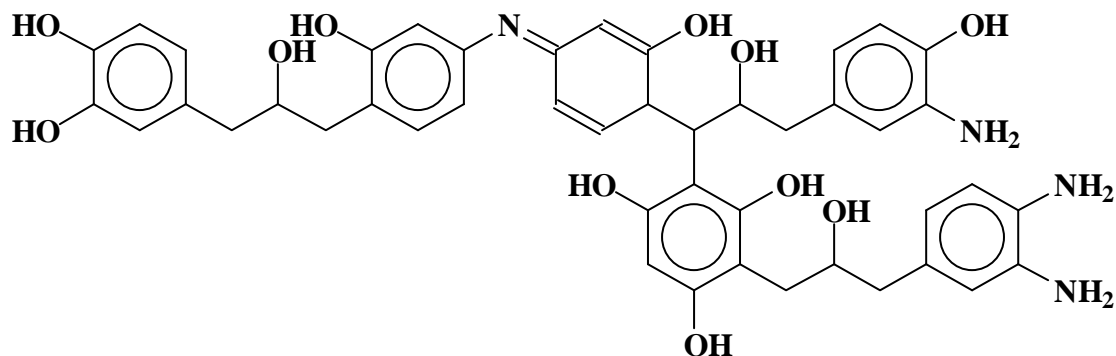


Fig. 65: Chemical species suggested from the analysis of MALDI-ToF spectra of hydrothermal aminated carbon gel before pyrolysis, H-EAT: (a) 554 Da; (b) 555 Da; (c) 843 Da (the sodium of weight 23 was implicitly taken into account).

The 537 Da peak is one 554 Da peak from which a  $\text{-OH}$  group has been lost. There is trace that higher oligomers of much higher molecular weight have been formed by observing the small peak at 843-844 Da that is the 554 and 555 Da compounds above to which has been added a  $290-1 = 289$  Da unit, either a robinetinidin or a catechin. This indicates that even higher oligomers of the flavonoid tannins such as dimmers have been able to react and presented a structure of the type shown in Fig. 65(c). The only other possible explanation for this peak being that this is a  $273 \times 3$  trimer, and the low proportion of such a peak indicates that this is highly unlikely. In the case of H-AT (Fig. 63 b)), as no gel occurred, many more species could be observed, in which the  $\text{-OH}$  groups have been substituted by  $\text{-NH}_2$  groups. Suggested chemical species have been listed in Table 12.

In summary, the spectrum of the H-EAT sample shears the main features of that of H-T, however with some significant differences. The intensity of the C3' and C4' bands at 145-150 ppm indicates that the –OH groups have decreased, probably through substitution by –NH– or –NH<sub>2</sub> groups. This is supported by the equivalent decrease of the C2' and C5' bands at around 110 ppm without any effect on the C6' band at 115 ppm that remains unaltered. The sugars are hydrolyzed as shown by the low 30-50 ppm bands, even more than in the H-T sample (Fig. 63 c)). Equally, while the majority of heterocyclic rings are open, the C2 band is still present here, indicating that some close heterocyclic structures are still maintained after HTC. The spectrum also shows polymerization, just like for H-T sample, but in much less extent than H-AT. H-EAT is the only one that may show condensation through –NH– bridges and therefore, this event could explain why it is the only material made from tannin and ammonia solution at 28-30 % that formed a gel whereas no additional crosslinker was present in the system. The presence of –NH<sub>2</sub> groups and –NH– bridges could confirm that, using HTC conditions such as temperature and pressure, not only the –OH at position C4' but other hydroxyl groups turned to –NH<sub>2</sub> as it has been reported by Hashida et al. (2009) and Morisada et al. (2011).

Table 12: MALDI-ToF peaks of H-AT, i.e. tannin aminated by direct HTC in ammonia at 180°C.

Experimental (Da)	Calculated (Da)	Suggested molecular species
521	518	I <sub>2</sub> – 3×-OH + Na <sup>+</sup>
537	535	I <sub>2</sub> – 2×-OH + Na <sup>+</sup>
551*	550	I <sub>2</sub> – 3×-OH + 2×-NH <sub>2</sub> + Na <sup>+</sup>
553	552	I <sub>2</sub> – 1×-OH + Na <sup>+</sup>
554.61*	554 or 555	Species of Fig. 4(a-b) + Na <sup>+</sup>
822*	843	Species of Fig. 4(c)
856	856 or 858	I <sub>2</sub> K – 1×-OH or I <sub>2</sub> J + Na <sup>+</sup>
888	890	J <sub>3</sub> + Na <sup>+</sup>
1145	1147	I <sub>2</sub> J <sub>2</sub> + Na <sup>+</sup>
1178	1179	J <sub>4</sub> + Na <sup>+</sup>
1444	1444 or 1452	I <sub>2</sub> -N=K <sub>2</sub> J – 4×-OH + 2×-NH <sub>2</sub> + Na <sup>+</sup> or IJ <sub>4</sub> + Na <sup>+</sup>

\* N-containing species

### 4.2.3 Elemental analysis

The elemental analyses of all materials prepared by HTC at different temperatures: 180, 190, 200, 210 and 220°C are given in Table 13 before and after pyrolysis at 900°C. The carbon content slightly increased with HTC temperature, whatever the preparation method. This finding was observed at the same small extent after pyrolysis at 900°C. The carbon content of natural tannin mimosa extract used in this work was 53.8 wt.%, and only increased

by 5-11% after HTC. As it has seen in the literature [Baccile et al. 2009 and refs. therein], the resultant microspheres or gels called hydrothermal carbons are not really carbon materials until a pyrolysis is carried out at much higher temperature (around 900°C). Indeed, and as shown in Table 13 the carbon content reached around 90 wt.% after pyrolysis.

Table 13: Elemental analyses of all samples after HTC at different temperatures, before (H-T, H-EAT and H-AT) and after pyrolysis at 900°C (CH-T, CH-EAT and CH-AT).

Sample	HTC T(°C)	C (wt.%)	H (wt.%)	N (wt.%)	S (wt.%)	O (wt.%)	C/O	C/N
<i>H-T</i>	180	60.9	4.4	0.8	0.0	33.9	1.8	76.1
	190	61.6	4.2	0.9	0.0	33.3	1.8	68.4
	200	63.3	3.9	0.6	0.0	32.2	2.0	105.5
	210	63.9	4.1	1.0	0.0	31.0	2.1	63.9
	220	64.1	3.8	0.9	0.0	31.2	2.1	71.2
<i>H-EAT</i>	180	58.3	4.3	3.3	0.1	34.0	1.7	17.7
	190	58.9	4.3	3.4	0.1	33.3	1.8	17.3
	200	59.3	4.2	3.7	0.1	32.7	1.8	16.0
	210	60.1	4.1	4.0	0.0	31.8	1.9	15.0
	220	60.6	4.1	3.5	0.1	31.7	1.9	17.3
<i>H-AT</i>	180	59.0	3.7	11.6	0.0	25.7	2.3	5.1
	190	59.8	3.9	12.0	0.0	24.3	2.5	5.0
	200	61.0	4.1	12.2	0.0	22.7	2.7	5.0
	210	61.1	4.1	12.7	0.0	22.1	2.8	4.8
	220	61.1	4.1	13.6	0.0	21.2	2.9	4.5
<i>CH-T</i>	180	88.3	0.9	0.7	0.0	10.1	8.7	126.1
	190	91.0	0.9	0.7	0.0	7.4	12.3	130.0
	200	91.6	0.7	0.6	0.0	7.1	12.9	152.7
	210	92.1	0.9	0.7	0.0	6.3	14.6	131.6
	220	92.9	0.7	0.8	0.0	5.6	16.50	116.1
<i>CH-EAT</i>	180	80.4	0.8	2.9	0.0	15.9	5.1	27.7
	190	80.9	0.9	2.0	0.0	16.2	5.0	40.5
	200	81.1	1.0	2.1	0.0	15.8	5.1	38.6
	210	81.7	0.9	1.9	0.0	15.5	5.3	43.0
	220	82.4	0.7	2.3	0.1	14.5	5.7	35.8
<i>CH-AT</i>	180	76.2	1.1	7.5	0.0	15.2	5.0	10.2
	190	80.0	1.0	8.0	0.0	11.0	7.3	10.0
	200	80.9	1.0	7.0	0.0	11.1	7.3	11.6
	210	81.5	1.0	7.5	0.0	10.0	8.2	10.9
	220	81.9	1.0	8.1	0.0	9.0	9.15	10.1

More interesting is the nitrogen content, which has been reported in Fig. 66 for N-doped materials only, before and after pyrolysis. Tannin contains naturally nitrogen due to the presence of amino and imino acids. H-T materials had nitrogen content lower than 1%, which still decreased after pyrolysis. As expected, pyrolysis at 900°C produced a significant decrease of the nitrogen content. Nitrogen is indeed a volatile element, which evolves as more easily as the heat-treatment temperature and/or the porosity of the material in which it is contained is high. The challenge was thus to prepare materials having both a high porosity

and a high nitrogen content. Fig. 66 shows that the H-EAT gel, having a nitrogen content around 4 wt.%, led to a carbon xerogel CH-EAT after pyrolysis whose N content was close to 2 wt.%, irrespective to the HTC temperature as a first approximation. In contrast, increasing HTC temperature produces a nitrogen enrichment of H-AT, with an outstanding N content ranging from 12 to 14 wt.%. After pyrolysis, a roughly constant but still amazing 8 wt.%, on average, was obtained.

The percentage of nitrogen after amination of tannin would have been 4.8 wt.% if only the site 4' of the B-ring (see again Fig. 6 a) Chapter 1) was aminated, which situation happens in room conditions according to Hashida et al. (2009) and Morisada et al. (2011). This statement is consistent with the results for H-EAT. However, as suggested by the previous NMR and MALDI-ToF spectra, tannin can be aminated on both A and B rings, and can also bear  $-N=$  bridges between flavonoid units as seen in Fig. 66, thereby justifying higher nitrogen contents. However, for the sample having the highest N content, H-AT, the NMR spectrum was hardly interpreted and the MALDI-ToF studies did not help much, as  $-NH_2$  and  $-OH$  have very close molecular weights, and cannot be separated in oligomers prone to be partly deprotonated. The molecular structure of N-doped tannin after direct HTC in concentrated ammonia is still unknown, but should explain so high nitrogen contents ranging from 11 to 13 wt.% before pyrolysis.

The literature reports that nitrogen-doped carbon materials were also prepared by HTC of chitosan and subsequent pyrolysis at 750°C, having carbon and nitrogen contents of 79.2% and around 9.0%, respectively. The same method applied to glucosamine led to C and N contents of 81.6 and 6.6 wt.%, respectively [Zhao et al. 2010b]. Such N contents are similar or below than those measured in CH-AT, despite the significantly lower temperature of pyrolysis, 750°C, in favour of a much lower loss of nitrogen during the heat treatment. Zhang et al. (2012a) studied the amination of sucrose by HTC in ammonia at 160, 180 and 200°C, followed by pyrolysis at 900°C. The resultant materials can thus be compared to H-AT and CH-AT and their C and N contents were around 64 and 20 wt.% before pyrolysis, respectively, and 94.8 and 4.4 wt.% after pyrolysis, respectively. Reaching around 8 wt.% of nitrogen in CH-AT even after heat-treatment at 900°C suggests that nitrogen was well stabilized in the carbonaceous structure.

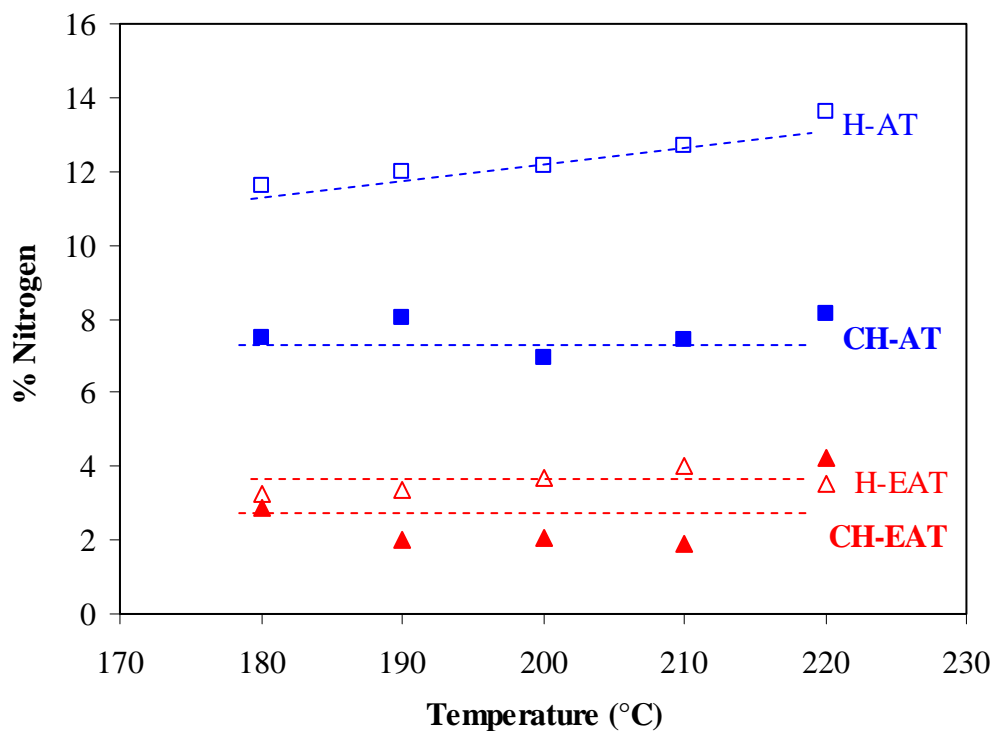


Fig. 66: Nitrogen content of N-doped materials prepared by HTC at different temperatures, before and after pyrolysis.

#### 4.2.4 XPS technique

The chemical analysis of the surface of the aminated tannin (EAT), dried hydrogels (H-AT, H-EAT) and carbon gels (CH-AT, CH-EAT) was investigated by XPS. XPS spectra of N-doped materials, with emphasis on the energy range corresponding to N1s with the corresponding curve fits allowing the deconvolution of the peaks. The corresponding data are given in Table 14 and 15. Caution should be taken regarding the assignment of XPS peaks to chemical groups since the low abundance of N increases the uncertainty of the multi-component curve-fitting peak and, non-conductive samples (EAT, H-AT and H-EAT) could lead to local charging effect with shifted binding energy to higher values. Moreover, the assignment is complicated by the location of N within the polyaromatic network and the degree of condensation of the graphene layer [Lahaye et al. 1999]. For instance, N in pyridinic groups has its core level binding energy that lies from 398.3 eV for conducting samples (e.g. N-doped graphite) up to 399.3 eV for isolated pyridine group within the non-conducting poly(2-vinylpyridine) polymers or pyridinic N located in a border of a polyaromatic cycle. A common way to assign peaks and especially N in pyridinic group is to determine the energy difference  $|\Delta E_{N1s - C1s}|$  between the binding energy of N1s and

reference C1s taken at the maximum of the C1s envelope for C-C or C=C bonds. For different reference compounds containing pyridinic N,  $\Delta$  values range from 113.7 to 114.3 eV [Lahaye et al. 1999]. Assignment of other peaks could then be done by the relative shift to that N-pyridinic reference.

Table 14: Contributions to the N1s bands in XPS patterns of HTC-derived materials.

	<b>Binding energy (eV)</b>	<b>(at. %)</b>		
		<b>Isolated Pyridinic (N-6) and/ or Neutral amines</b>	<b>N<sub>XPS</sub></b>	<b>C<sub>XPS</sub></b>
H-AT_180°C	399.2	7.9	76.4	15.6
H-AT_190°C	399.1	8.1	78.7	13.2
H-AT_210°C	399.3	9.4	78.6	12.0
H-EAT_180°C	399.1	2.5	76.6	18.3
H-EAT_190°C	399.5	3.2	78.5	18.3
H-EAT_210°C	399.3	3.4	78.2	18.4

Table 15: Contributions to the N1s bands in XPS patterns of carbonised HTC samples.

	<b>Binding energy (eV) and area of the peak (%)</b>			<b>(at. %)</b>		
	<b>Pyridinic (N-6)</b>	<b>Pyrrolic (N-5) or pyridonic</b>	<b>Quaternary N-Q or oxydised pyridinic N</b>	<b>N<sub>XPS</sub></b>	<b>C<sub>XPS</sub></b>	<b>O<sub>XPS</sub></b>
CH-AT_180°C	398.1 (35.7)	400.6 (55.3)	402.8 (9.0)	4.9	90.8	4.3
CH-AT_190°C	398.1 (38.2)	400.7 (57.7)	402.7 (4.1)	2.8	92.4	4.8
CH-AT_210°C	398.1 (39.2)	400.7 (59.2)	402.7 (1.6)	4.0	90.2	5.8
CH-EAT_180°C	398.1 (33.1)	400.7 (60.1)	402.8 (6.8)	1.6	95.8	2.6
CH-EAT_190°C	398.0 (36.7)	400.6 (60.9)	402.6 (2.4)	2.1	92.1	5.8
CH-EAT_210°C	398.1 (37.1)	400.7 (61.2)	402.7 (1.7)	1.9	94.4	3.7

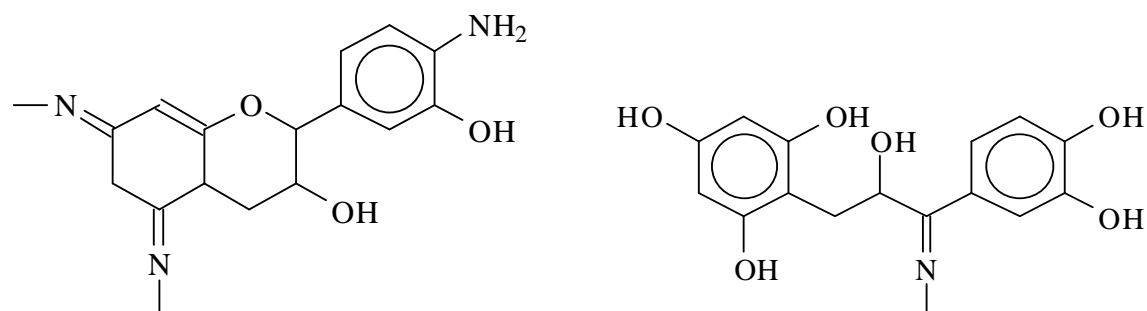
For tannin modified with ammonia at room temperature (EAT), XPS composition reveals a high fraction of O (28 at.%), a minor amount of N (3 at.%) and traces of K (0.65 at.%). The N1s peak exhibits two components at 399.9 and 402.1 eV. Based on the previous discussion,



$|\Delta(N1s - C1s)|$  was calculated with the binding energy of 399.9 eV and 284.7 eV for N1s and C1s respectively. It leads to a value of 115.2 eV, outside the range of 113.7 to 114.3 eV expected for N pyridine species [Lahaye et al. 1999]. It suggests that the main peak at 399.9 eV could not be attributed to pyridinic N species but rather to functional groups having slightly higher binding energy, around +1.1 eV with respect to the averaged N pyridinic binding energy ( $398.8 \pm 0.5$  eV). Moreover, it is well known in the literature that conversion of carbonaceous materials containing no pyridinic groups (e.g cellulose) to pyridinic nuclei is supposed to occur at temperature higher than 250°C in presence of gaseous  $NH_3$  [Cagniant et al. 2002]. Therefore, the possible N-containing chemical groups are attributed mainly to neutral amine and/or amide since both functions could have their binding energy in the range around 399.9 eV. Regarding imine groups, only traces could be present if we consider their classical binding energy around 398.5 eV. They could more significantly be present by considering their assignment at  $399.0 \pm 0.1$  eV as performed by Cagniant et al. (2002) by coupling XPS and IR spectroscopies for ammonia-treated cellulose at low temperature (250°C).

In that case, these data appear in agreement with the characterization of EAT. For that purpose, catechin was used as a flavonoid model compound and treated in similar conditions. Solid state CP-MAS  $^{13}C$  NMR and MALDI-ToF spectroscopy studies revealed that, amination is not always regioselective and leading to the conversion of one single -OH group in C4' into  $NH_2$ . New reactions have been evidenced, clearly leading to (i) multiamination of a great proportion of phenolic hydroxygroups, and these both on the A and B-rings of the flavonoid structure contrary to the amination of a single hydroxygroup on the B-ring as previously theorised; and (ii) oligomerisation and cross-linking through the formation of -N= bridges between flavonoid units explaining the gelation of the tannin/ammonia mixture in water (Fig. 67) and oxidation of phenolic-OH groups to quinone were observed. The latter point could explain the high oxygen content determined by XPS at the surface of the sample. The peak at 402.1 eV was attributed to quaternary nitrogen such as protonated amides or amines.

(i)



(ii)

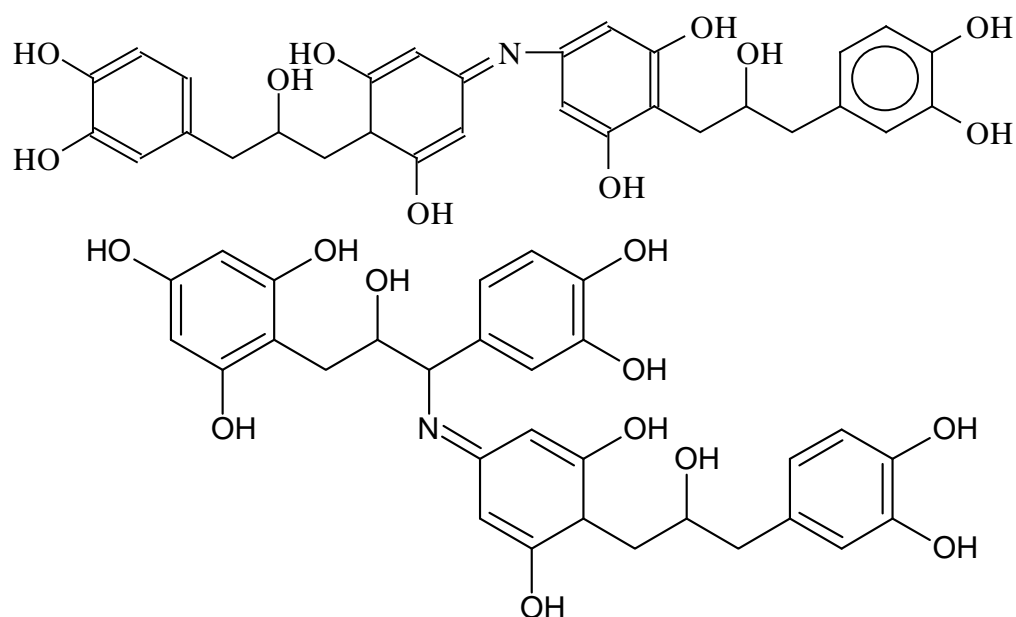


Fig. 67: Chemical species suggested from the analysis of MALDI-ToF spectra of catechin treated with an aqueous ammonia solution.

When tannin and EAT were submitted to hydrothermal treatment in concentrated aqueous ammonia (H-AT) or in water (H-EAT) respectively, the XPS compositions evolve as shown in Table 14, with a decrease of the oxygen content in both cases and a significant nitrogen enrichment, around 3 at% for H-EAT up to 8-9 at% for H-AT compared to 0.6 at% for natural tannin and 1 at% after HTC of tannin. Presence of Si (0.7 at % for H-EAT) could also be detected when silica vials were used in the autoclave during HTC.

Based on the literature, the presence of pyridinic species is now possible since it is well known that HT process promotes the carbonization of carbohydrates with polycondensation of aromatic units and formation of N-containing cycles such as pyridinic species [Baccile et al. 2011]. For instance, Cagniant et al. (2002), have proposed the formation of pyridinic group

during the carbonization of cellulose at 250°C in ammonia atmosphere [Cagniant et al. 2002]. The N1s XPS spectra shown an asymmetry of the main peak associated with a shift to lower binding energy compared to EAT sample (399.3 eV instead of 399.9 eV). The  $\Delta|N1s - C1s|$  values were around 114.8 eV, outside the expected range for pyridinic species, suggesting that the N- pyridinic species are not the main contribution to this peak. Indeed, its presence could not be excluded since the N1s binding energy domains of pyridinic groups are scattered in a large range (1eV).

After carbonization at 900°C, no amines were present, as expected, and they were mainly replaced by pyridinic N-6 and to a lower other species such as pyrrolic (N-5) or pyridonic (not distinguishable by XPS measurements), quaternary pyridinic nitrogen (N-Q) [Lahaye et al. 1999] or pyridine oxide groups (Table 15). Despite the high purity of the inert gases used for carbonization, the presence of oxide forms (pyridone, pyridine oxide) could be ascribed to the reactivity of carbonized materials with air as previously observed in the works of Pels et al. (1995) and Lahaye et al. (1999).

### 4.3 Materials' morphology and porous texture

#### 4.3.1 Morphological characteristics: TEM and SEM photos

TEM pictures of the samples CH-T, CH-EAT and CH-AT prepared after HTC firstly at 180°C and pyrolysis at 900°C have been presented in Fig. 68. CH-T presented monodisperse spherical particles with diameters around 5  $\mu\text{m}$ . In aminated materials, CH-EAT and CH-AT, the presence of ammonia changed the cross-linking process so that spherical particles with different diameters were obtained in agreement with Wang et al. (2012). CH-EAT showed the typical structure of a carbon gel derived from phenolic precursors, i.e. was a monolith based on micro nodules (with diameters around 50 nm) connected to each others. CH-AT had an intermediary structure between CH-T and CH-EAT, presenting a mixture of both structures.

Fig. 69 shows the effects of the HTC temperature, which was changed from 190 to 210°C for all materials, aminated or not, and submitted to pyrolysis at 900°C. Although comparisons are made all along the present work with materials derived from HTC of polysaccharides, for which the literature is the most abundant, tannin treated in similar conditions behaves differently in some aspects. For example, amino-functionalised materials prepared by HTC of glucose in ammonia at pH 11 at 150°C were obtained in the form of spheres having a very narrow distribution of diameters centred on around 2-3  $\mu\text{m}$  [Wang et al. 2012]. In the case of tannin, most spherical particles were obtained at 180 – 190°C, lower temperatures within the

range 130 – 160°C leading to much more irregular and polydisperse spheres as confirmed in Chapter 2.

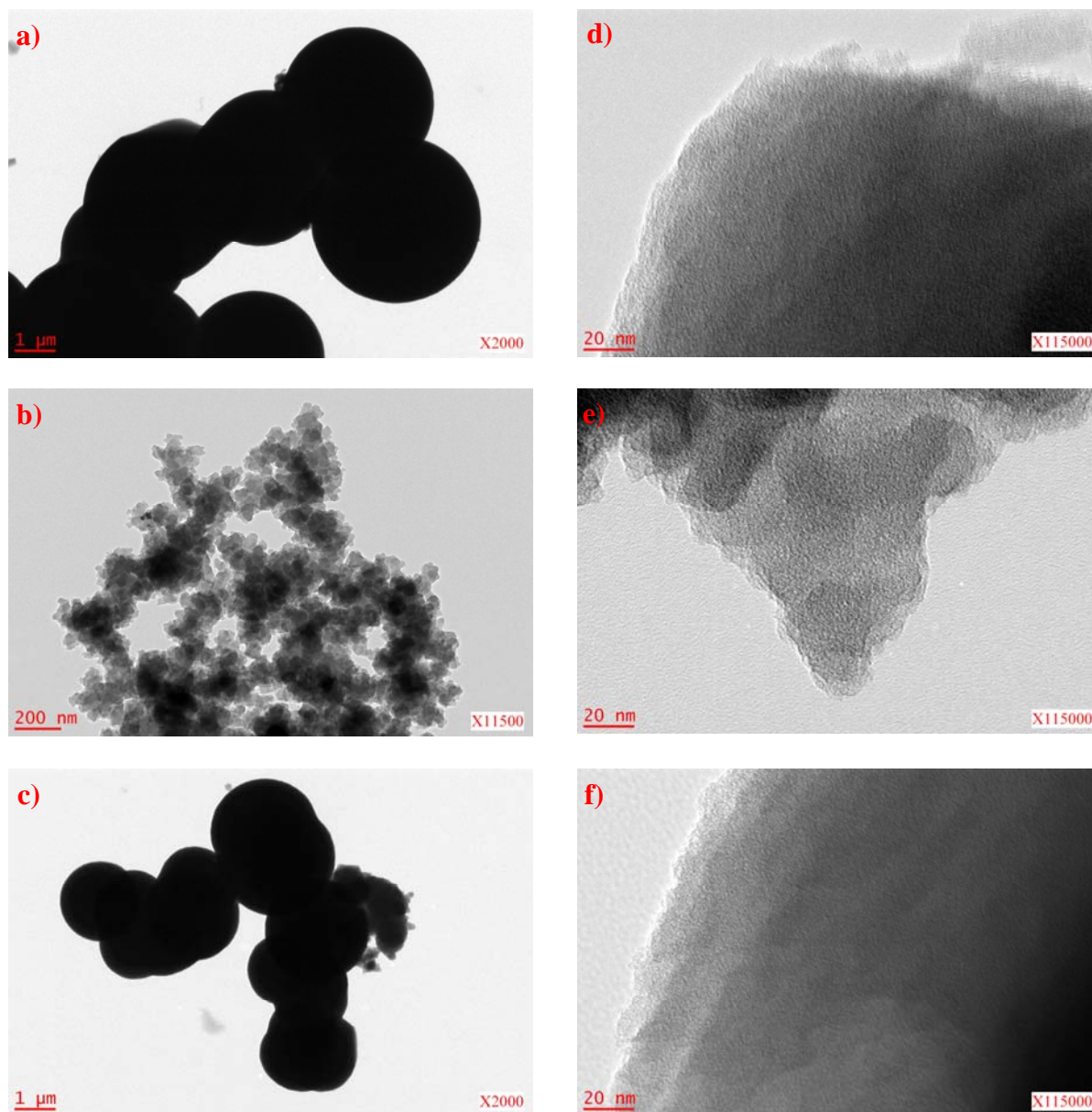
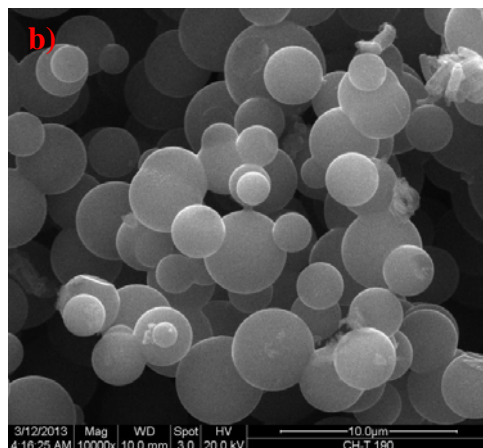
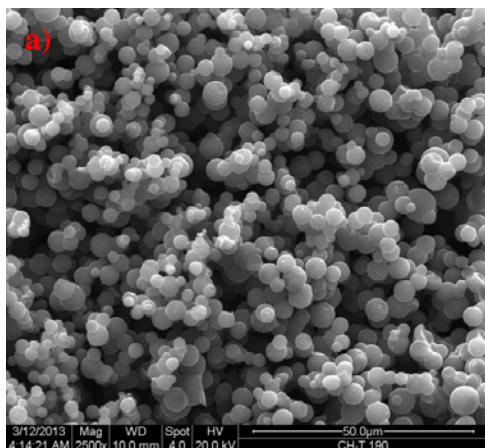
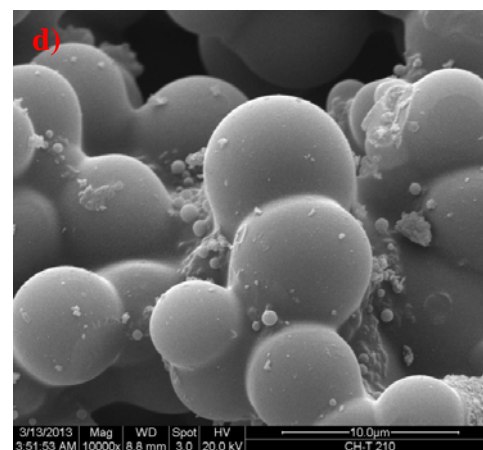
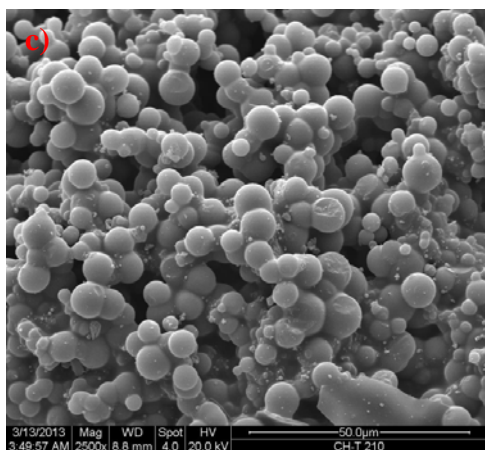


Fig. 68: TEM images of the samples after HTC at 180°C and subsequent pyrolysis at 900°C: CH-T (a and d), CH-EAT (b and e) and CH-AT (c and f).

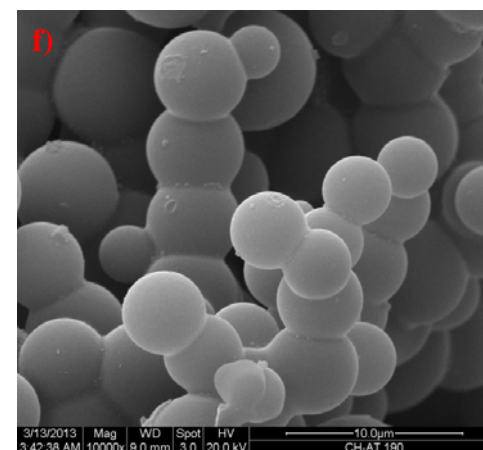
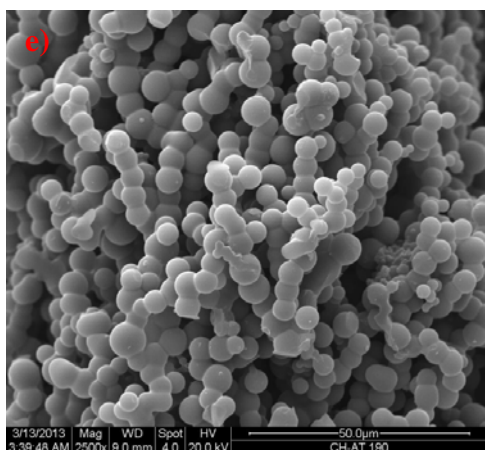
CH-T 190°C



CH-T 210°C



CH-AT 190°C





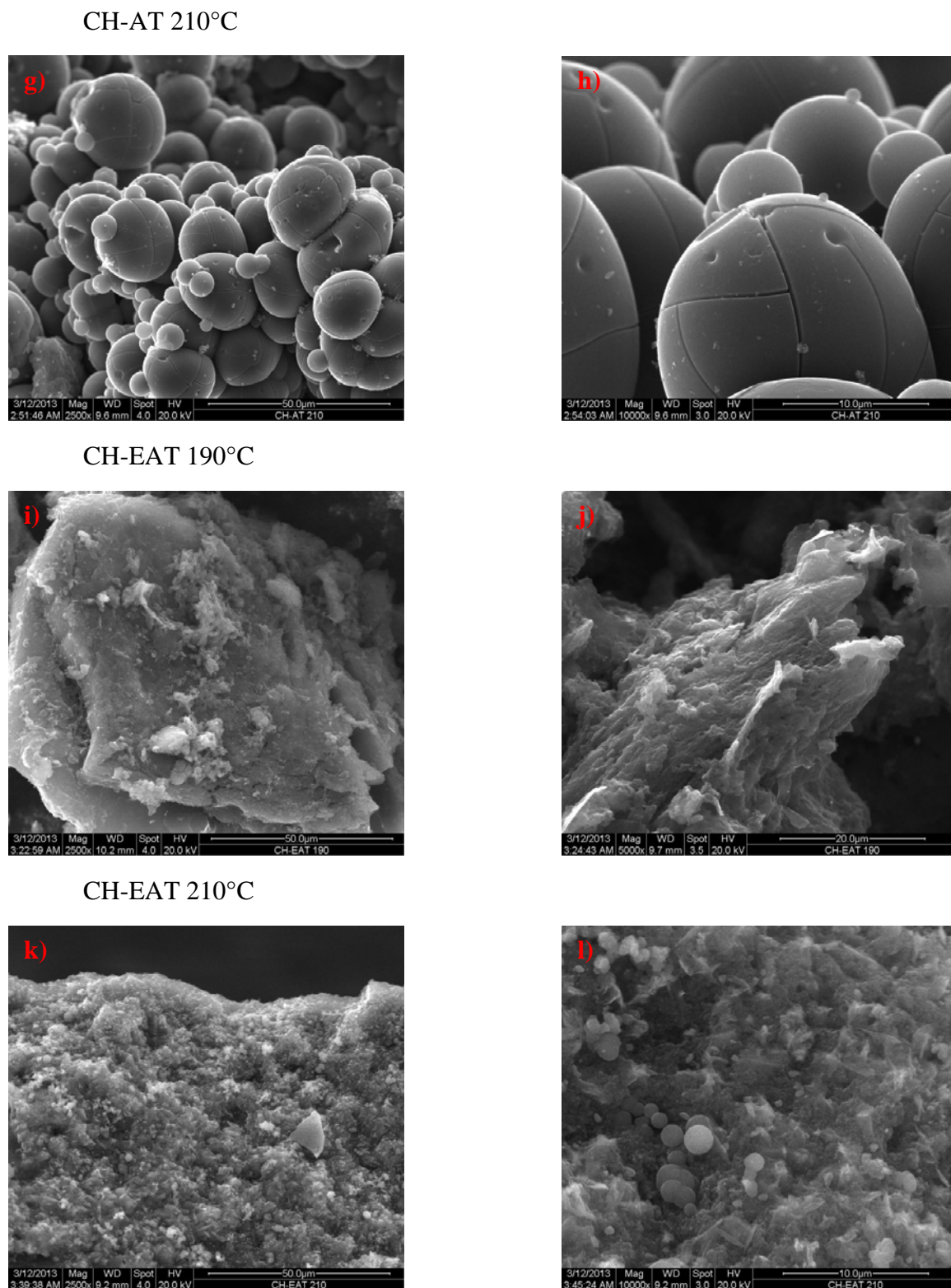


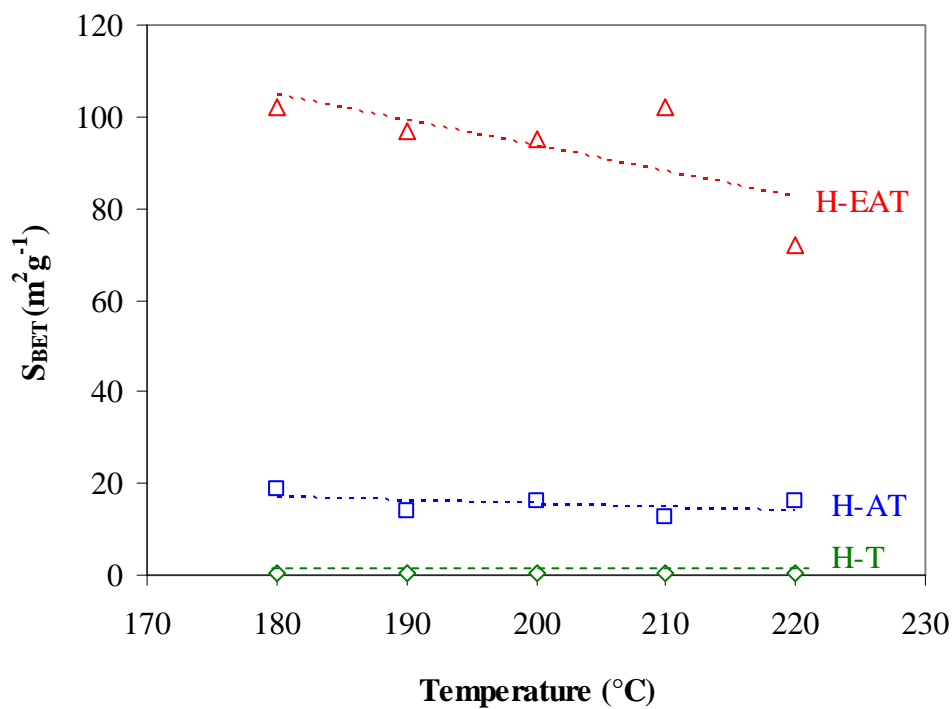
Fig. 69: SEM images of tannin-based materials after HTC and posterior pyrolysis at 900°C: (a, b) CH-T prepared at 190°C; (c, d) prepared at 210°C; (e,f) CH-AT prepared at 190°C; (g,h) CH-AT prepared at 210°C; (i,j) CH-EAT 190°C; (k,l) and 210°C.

CH-T (Fig. 69(a-d)) showed spherical particles, more or less connected with each other, whose average diameter and agglomeration state increased with HTC temperature. Li et al. (2011) also found that, in the case of HTC of glucose, the most spherical particles were formed at lower temperatures of 180-190°C, whereas more polydisperse spheres with broken shapes appeared at higher temperatures such as 210°C. The same was observed for the material directly aminated by HTC, CH-AT (Fig. 69(e-h)), but the polydispersity was much higher at 210°C. Indeed, whereas the particles were rather monodisperse at 190°C, a mixture of small and very big particles was found after HTC at 210°C. Fig. 69(h) even shows big, basket ball-like, spheres. Finally, for the carbon gel CH-EAT (Fig. 69(i-l)), in fact a carbon xerogel as the material was dried in vacuum oven at 80°C before pyrolysis at 900°C, the spherical nodules were so small that they were hardly observed at the magnifications used in Fig. 69. Again, when the temperature increased, bigger particles were obtained with a higher polydispersity, as seen in Fig. 69(l). This finding is somewhat different from that of Titirici (2013) in the case of glucose treated by HTC between 120 and 280°C, who found that higher temperatures led to larger but more homogeneous particles.

### 4.3.2 Textural properties

Fig. 70 shows the specific surface areas of all materials prepared at different HTC temperatures, measured before and after pyrolysis at 900°C. Before pyrolysis, the gel H-EAT was the material having the highest surface area, around  $100 \text{ m}^2 \text{ g}^{-1}$ , see Fig. 70(a). This is a logical result, considering that such material comprises the smallest particles. In contrast, H-T was the one having the lowest surface area, less than  $1 \text{ m}^2 \text{ g}^{-1}$ , due to his rather monodisperse, solid and big, spherical particles. As expected, H-AT had values of surface area between those of the former two materials, slightly lower than  $20 \text{ m}^2 \text{ g}^{-1}$ , since its structure is intermediary between a powder and a gel. All the materials had surface areas which decreased slightly when the HTC temperature increased, due to both growth and agglomeration of the particles. The effect was the most significant in the case of H-EAT, whose very small nodules were more affected by particle growth and Ostwald ripening.

a)



b)

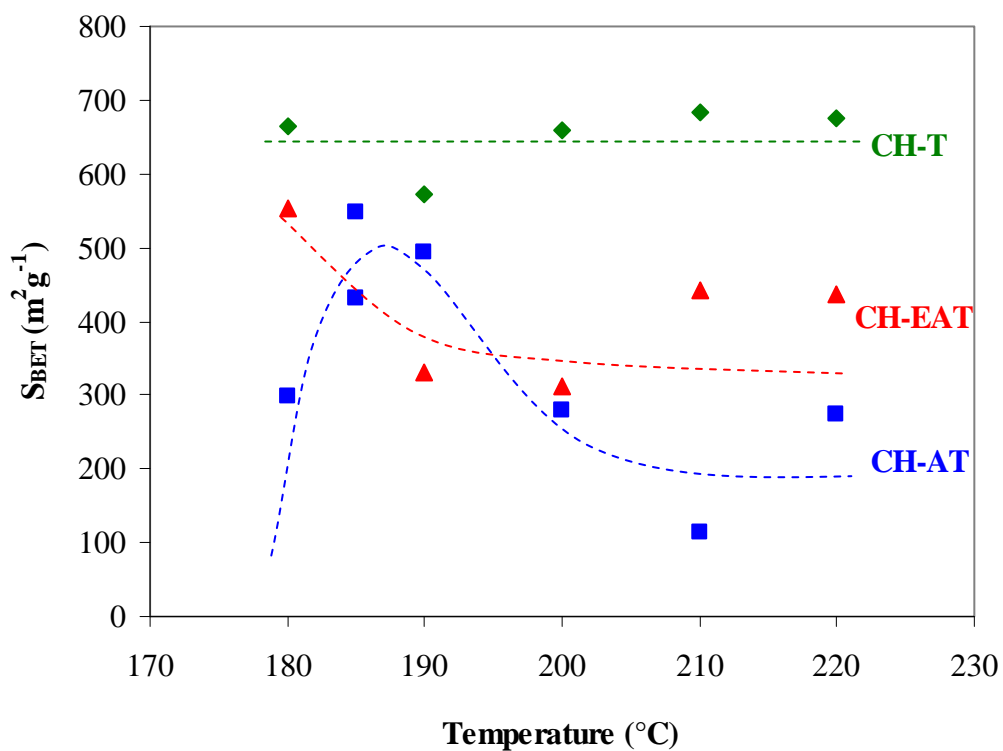


Fig. 70: Surface areas,  $S_{BET}$ , of all materials obtained after HTC at different temperatures: (a) before, and (b) after pyrolysis at 900  $^\circ\text{C}$ .



After pyrolysis at 900°C, the materials CH-T, CH-AT and CH-EAT presented developed porosity and significantly higher surface areas, as shown in Fig. 70(b). Depending on the preparation method, different effects of the HTC temperature were observed. CH-T presented the highest surface areas, around 700 m<sup>2</sup> g<sup>-1</sup>, which did not change much when the HTC temperature increased. Such values are higher than most results reported so far for carbohydrates submitted to HTC and subsequently pyrolysed at high temperature. Glucose, chitosan and glucosamine indeed presented low porosity not only after HTC, but also after pyrolysis, so that the resultant measured surface areas were around 30-50 m<sup>2</sup> g<sup>-1</sup> in general [Zhao et al. 2010a]. In the case of CH-AT, the materials obtained after HTC at 185-190°C and after subsequent pyrolysis had the highest value of surface area, up to 550 m<sup>2</sup> g<sup>-1</sup>. Higher HTC temperatures led to lower surface areas, as seen in Fig. 70(b), probably due to the formation of bigger and less porous carbon spheres, as suggested by Fig. 69(h).

The surface areas of the carbon gel CH-EAT presented the same trends as for CH-AT, but the changes were lower, and the minimum at low HTC temperature was not observed. On average, the surface area of CH-EAT was around 400 m<sup>2</sup> g<sup>-1</sup>. Fig. 71 shows the nitrogen adsorption-desorption isotherms at -196°C for the materials shown in Fig. 69 together with their respective distribution of pores (DFT). Nitrogen adsorption isotherms of CH-T materials were type I, according to the IUPAC classification, with a sharp increase of the nitrogen amount adsorbed at P/P<sub>0</sub> lower than 0.05, a narrow knee and a plateau up to P/P<sub>0</sub> equal to 0.99. These isotherms are characteristic of purely microporous solids.

Nitrogen adsorption isotherms of CH-AT materials were similar to those of CH-T but presented a lower volume adsorbed at low P/P<sub>0</sub> < 0.05, indicating a lower microporosity than CH-T materials, and a sudden increase of the nitrogen uptake P/P<sub>0</sub> < 0.95, indicating capillary condensation in wide mesopores. Nitrogen adsorption isotherms of CH-EAT materials were combinations of types I and IV, for which adsorption of nitrogen takes place in both micro and mesopores. The existence of a well-developed mesoporosity is also indicated by the slope of the adsorption isotherms, in the P/P<sub>0</sub> range from 0.05 to 0.7, and by the large hysteresis cycle. Textural parameters of all the carbon materials prepared are given in Table 16.

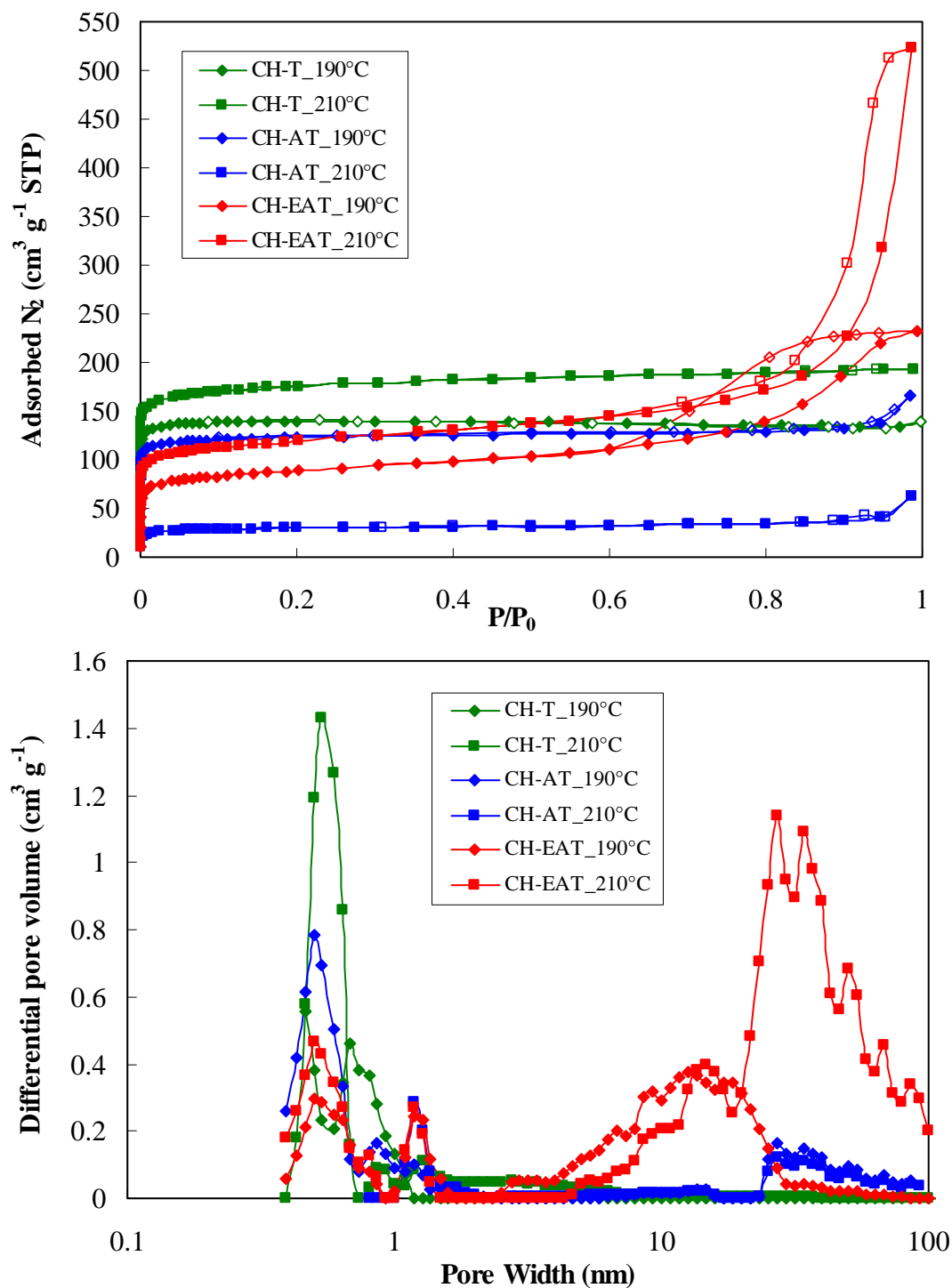


Fig. 71: Nitrogen adsorption-desorption isotherms (full and open symbols, respectively) at 77K of tannin-based carbon materials, i.e. after HTC at 190 and 210°C followed by pyrolysis at 900°C; and their respective DFT.

The carbon xerogels, CH-EAT materials, were those materials presenting the highest proportion of mesopores, between 66 and 76% of the total pore volume. Whereas these

materials were xerogels, i.e. were not submitted to supercritical drying after synthesis, a significant amount of mesoporosity was thus maintained. N-doped carbon materials were also prepared by White et al. (2011b) from the HTC of glucose and ovalbumin. A gel was obtained, which was dried by exchange with supercritical CO<sub>2</sub>, and then pyrolysed. The resultant carbon aerogel also presented a high mesopore volume of 0.51 cm<sup>3</sup> g<sup>-1</sup>, and its surface area was 310 m<sup>2</sup> g<sup>-1</sup>. These characteristics are thus similar to those of our CH-EAT\_200°C sample, but in our case a simple subcritical drying was carried out. Therefore, our process is expected to be much more convenient and cheaper for preparing N-doped porous carbon materials.

Table 16: Surface areas and pore volumes of all materials pyrolysed at 900°C, determined by N<sub>2</sub> adsorption at -196°C.

Sample	HTC T(°C)	S <sub>DFT</sub> (m <sup>2</sup> g <sup>-1</sup> )	S <sub>BET</sub> (m <sup>2</sup> g <sup>-1</sup> )	V <sub>0.97</sub> (cm <sup>3</sup> g <sup>-1</sup> )	V <sub>m</sub> (cm <sup>3</sup> g <sup>-1</sup> )	V <sub>μ</sub> (cm <sup>3</sup> g <sup>-1</sup> )
CH-T	180	803	665	0.26	0.01	0.25
	190	372	571	0.21	0.00	0.21
	200	784	658	0.26	0.01	0.25
	210	775	684	0.30	0.04	0.26
	220	810	675	0.27	0.02	0.25
CH-EAT	180	470	552	0.62	0.41	0.21
	190	315	330	0.35	0.22	0.13
	200	227	311	0.51	0.38	0.13
	210	438	442	0.62	0.44	0.18
	220	447	436	0.57	0.40	0.17
CH-AT	180	314	297	0.16	0.04	0.12
	185	669	547	0.25	0.04	0.21
	190	578	494	0.24	0.05	0.19
	200	293	280	0.15	0.04	0.11
	210	47	113	0.08	0.03	0.05
	220	449	386	0.19	0.03	0.16

#### 4.4 Comparison of NCM's made from tannin and other precursors

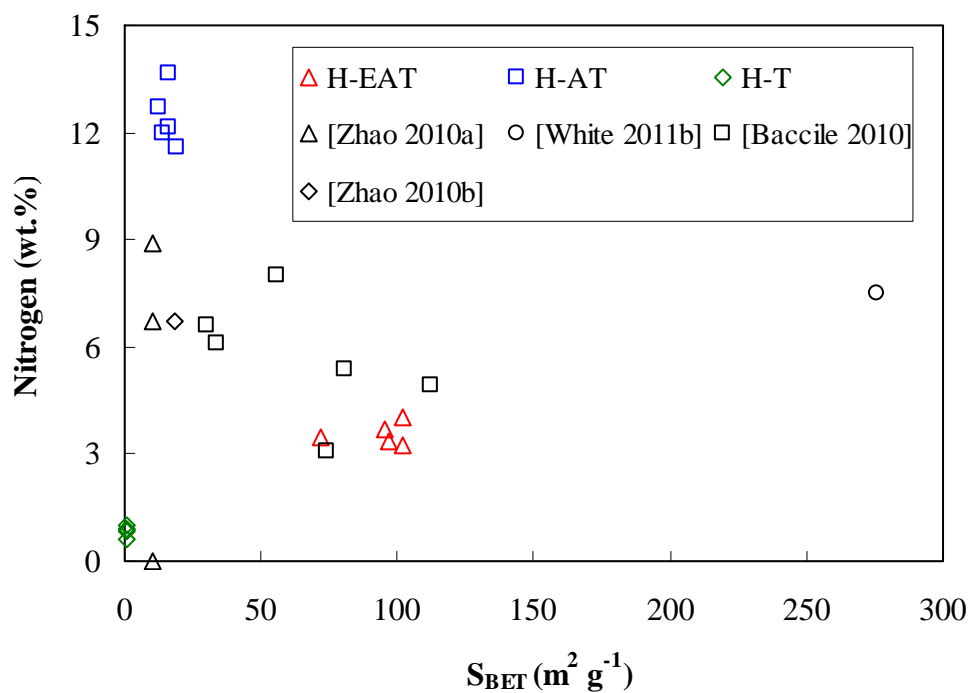
Fig. 72(a) gathers the data of surface area and nitrogen content of all the tannin-derived materials prepared in the present work. The same kind of data is also given on the same plot for other carbonaceous materials also produced by HTC of various precursors, such as chitosan, glucose and glucosamine [Zhao et al. 2010a], glucose and albumin [Baccile et al. 2010], glucose and ovalbumin [White et al. 2011b], D-glucosamine [Zhao et al. 2010b]. H-T presented both low surface area and very low nitrogen content, but their aminated

counterparts were among the materials having either the highest N content (H-AT) or the highest surface area (H-EAT). But none presented both characteristics at the same time. The H-EAT gel was comparable to the material obtained by HTC of a mixture of glucose and albumin [Baccile et al. 2010], having values of  $S_{BET}$  and N content around  $100 \text{ m}^2 \text{ g}^{-1}$  and 4-5 %, respectively.

Fig. 72(b) shows results for the same precursors as in Fig. 72(a) and a few others more, such as cystine and T-cystine [Wohlgemuth et al. 2012b] and prawn shells [White et al. 2009] after HTC and posterior pyrolysis at different temperatures: 550 [Wohlgemuth et al. 2012b], 750 [Baccile et al. 2010; White et al. 2009; 2011b; Zhao et al. 2010a], 900 [Wohlgemuth et al. 2012b] and 950°C [Baccile et al. 2010; White et al. 2011b]. After KOH activation at 600°C of D-glucosamine submitted to HTC [Zhao et al. 2010b],  $S_{BET}$  as high as  $600 \text{ m}^2 \text{ g}^{-1}$  was obtained but N content was only 2.3 wt.%. Even higher  $S_{BET}$ ,  $730 \text{ m}^2 \text{ g}^{-1}$ , was obtained after carbonization at 900°C of T-cystine submitted to HTC but N content was lower than 4 wt.% [Wohlgemuth et al. 2012b]. Pyrolysis obviously led to a significant decrease of nitrogen content, and especially at the highest temperatures. However, it is important to point out that despite H-AT was heat-treated at 900°C, the resultant carbon CH-AT was among the materials presenting the highest N content, around 8 wt.%, with a surface area as high as  $500 \text{ m}^2 \text{ g}^{-1}$ .

In this study, we obtained carbon materials with simultaneously high nitrogen content and high surface areas. Specially tannin directly submitted to HTC in concentrated ammonia at 190°C and pyrolysed at 900°C presented  $S_{BET}$  and nitrogen content of  $500 \text{ m}^2 \text{ g}^{-1}$  and 8 wt.%, respectively. The incorporation of nitrogen in the carbonaceous structure is indeed expected to increase its electrical conductivity and provide pseudofaradaic reactions, thus further increasing the capacitance and the performances of the porous electrode. Therefore, this material is foreseen to be tested in several applications, in particular as electrode of electric double-layer capacitor.

a)



b)

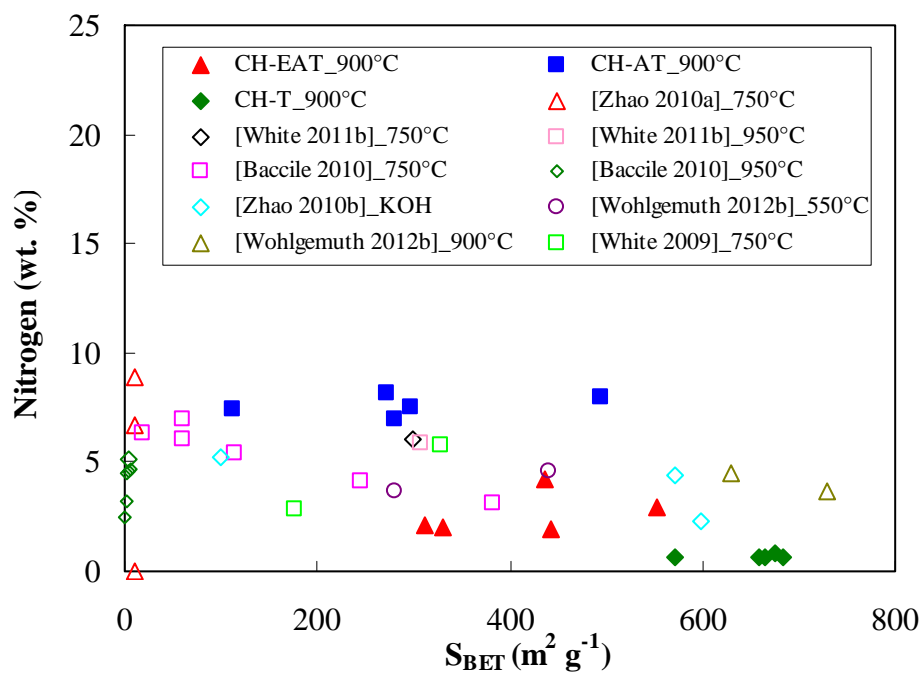


Fig. 72: Surface areas,  $S_{BET}$ , and nitrogen content of our materials: (a) before pyrolysis (H-T  $\diamond$ , H-AT  $\square$  and H-EAT  $\triangle$ ); (b) after pyrolysis (CH-T  $\blacklozenge$ , CH-AT  $\blacksquare$  and CH-EAT  $\blacktriangle$ ) compared to results reported in literature.

## 4.5 Electrochemical performances of N-doped, tannin-based, hydrothermal carbons

### 4.5.1 Electrochemical experiments

Porous electrodes were prepared by pressing together a mixture of 75 wt% of finely ground carbon, 5 wt% of acetylene black and 20 wt% of polyvinylidene fluoride (PVDF, Sigma Aldrich). The as-prepared pellets were investigated with a typical three-electrode configuration using Teflon Swagelok<sup>®</sup> cells working at room temperature, seen in Fig. 73. The positive and negative electrodes of comparable mass, ranging from 10.0 to 18.0 mg, were electrically isolated by a glassy fibrous paper separator. Both Teflon Swagelok<sup>®</sup> cells were filled with 4 mol L<sup>-1</sup> H<sub>2</sub>SO<sub>4</sub> aqueous solution. The reference electrode was Ag/AgCl (KCl saturated). The electrochemical characterizations were performed by the voltammetric technique and cyclic voltammograms were obtained within 0.05 – 1.05V versus reference electrode at scan rates ranging from 2 to 50 mV s<sup>-1</sup>. The specific capacitance of the carbon material,  $C$  (F g<sup>-1</sup>), was estimated from the aforementioned method, the currents,  $I$  [A], for calculations were taken at 0.55 V in third cycle of measurement, then  $C$  was calculated as:

$$C = \frac{2I}{m s},$$

where  $I$  is the current (A),  $m$  the mass of active material in the electrode (g) and  $s$  the scan rate (V s<sup>-1</sup>). The samples were named as i.e. H-EAT1 or H-EAT2 respectively for H-EAT materials depending of the temperature used around 180 or 210°C respectively.

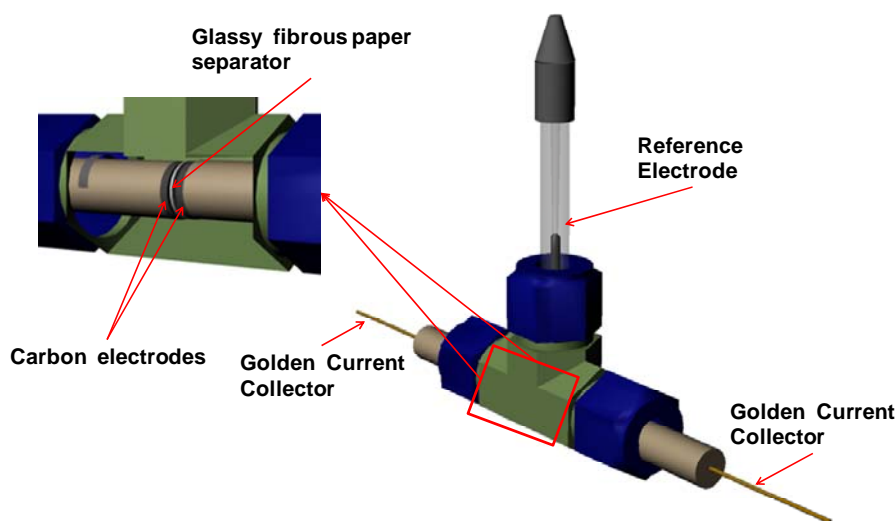


Fig. 73: Three – electrode cell for measuring electrochemical properties of carbon materials.

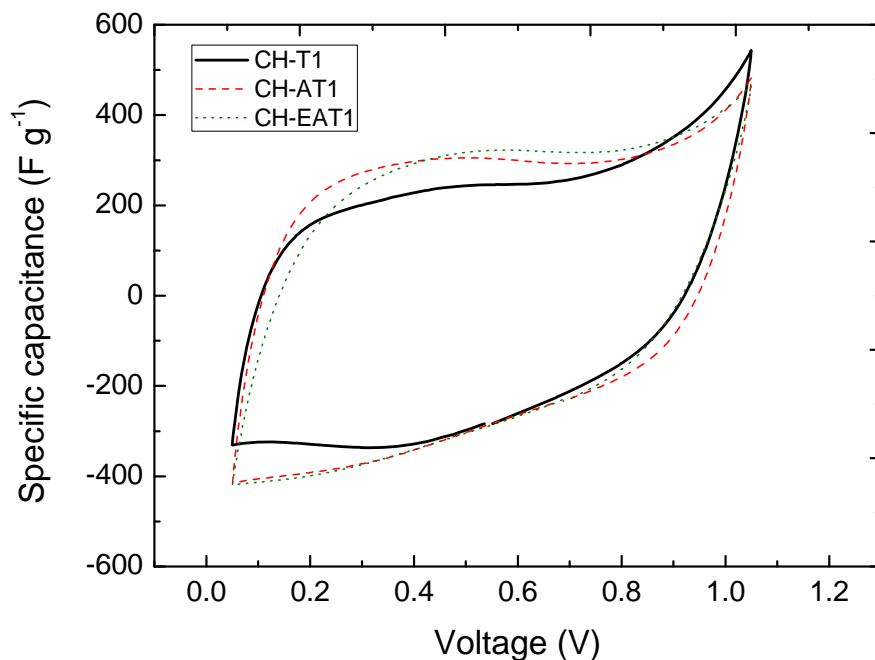
Fig. 74 a) shows the cyclic voltammograms (CV) obtained with a scan rate of  $2 \text{ mV s}^{-1}$  for CH-T1, CH-AT1 and CH-EAT1 samples. They present an asymmetric shape, typical of many carbonaceous electrodes having a resistance, either internal or at the contact between electrode and current collector, or both and, a small hump characteristic of Faradic pseudocapacitance. The appearance of such hump in the CV curves within the range  $0.2 - 0.6\text{V}$ , indicates that the overall capacitive response combines both ideal capacitive behaviour and redox reactions, the latter being related to the heteroatom-containing functional groups of the hydrothermal carbons [Conway et al. 1997; Frackowiak and Béguin 2001; Zhao et al. 2010b; Si et al. 2013]. Zhao et al. (2010b) submitted D-glucosamine to HTC and activation with KOH, the resultant materials showed almost similar CV curve in  $1\text{M H}_2\text{SO}_4$ . Those materials had moderate surface area, around  $600 \text{ m}^2 \text{ g}^{-1}$ , and 4.4 wt. % nitrogen content, almost the same scenario as in this study.

Fig. 74 b) shows that a further increase of scan rate implies a decrease of specific capacitance. Such decrease can be attributed to internal resistances in the tested capacitors and in particular to the carbon porous texture, which is characterised in the present case by a significant microporosity with pore width in the range  $0.5 - 1.5 \text{ nm}$ . Thus, the diffusion of the electrolyte ions is the easiest at the lowest scan rate, but is progressively hindered when the scan rate increases, despite the presence of large mesopores which act as transportation channels [Frackowiak and Béguin 2001; Xing et al. 2006; Amaral-Labat et al. 2012b]. The difficulty for the electrolyte to diffuse in the smallest pores at high scan rate leads to a lower available electroactive surface area.

The internal resistance is thus significantly increased, further deviating the cycles from the ideal rectangular shape. Therefore, a drop of capacitance is observed when the scan rate increases, for the three materials prepared at HT temperature of around  $180^\circ\text{C}$  (CH-T1, CH-AT1 and CH-EAT1). Despite its remarkable decrease, the capacitance remains high at moderate scan rates, up to  $322$  and  $198 \text{ F g}^{-1}$  at  $2$  and  $10 \text{ mV s}^{-1}$ , respectively. Many overlapping factors, such as carbon internal resistance, wettability, heteroatom content, micropore volume and surface area, influence the capacitive properties of pyrolysed hydrothermal carbons. The decrease of capacitance at high scan rate may be related to a decrease of internal Ohmic resistance or due to the interaction of the electrolyte with the functional groups present in the carbon electrode [Jurewicz et al. 2004; Vix-Guterl et al. 2004; 2005; Portet et al. 2007; 2008]. We assume that the observed changes at increasing scan rate

are related to the low amount of mesopores within the range 3-13 nm able to quickly lead the electrolyte ions to the electrode surfaces [Amaral-Labat et al. 2012b].

a)



b)

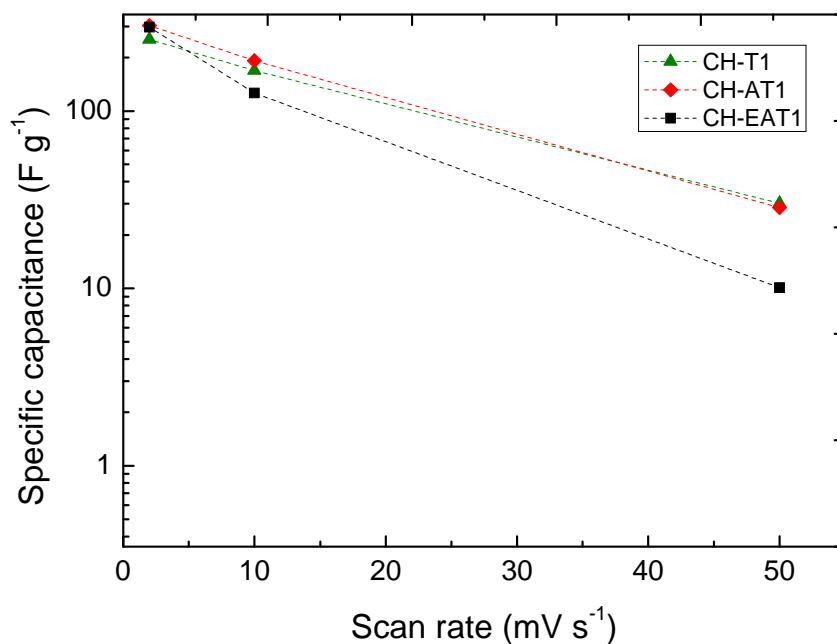


Fig. 74: a) Cyclic voltammograms of CH-T1, CH-AT1 and CH-EAT1 samples, at a scan rate of  $2 mV s^{-1}$ ; b) Specific capacitance of samples CH-T1, CH-AT1 and CH-EAT1 as a function of scan rate.



The mesopore size distributions of CH-AT and CH-EAT have their maxima located at 27 – 34 nm, but such mesopores are useless for capacitive properties [Amaral-Labat et al. 2012b]. Indeed some authors claimed that porous carbons having pore diameters within the range 3-13 nm are those showing the highest capacitance values [Escribano et al. 1998]. Lower capacitances, although decreasing much more slowly with scan rate, were achieved with tannin-formaldehyde (TF) carbon cryogels, based on narrow and well interconnected mesoporosity, not only giving access to micropores but also having a significant contribution to the active surface area [Amaral-Labat et al. 2012b].

Table 17 gathers the values of specific capacitance obtained at  $2 \text{ mV s}^{-1}$  for our six materials. The specific capacitance changed from 181 to  $322 \text{ F g}^{-1}$ . The normalized capacitance, simply calculated by dividing the specific capacitance by the BET surface area, is also reported and the highest value is close to  $60 \text{ } \mu\text{F cm}^{-2}$ . The most important parameters influencing the specific capacitance are surface area, micropore volume and pore size distribution, which provide the available volume in which ions can be transported and stored. It is well known that surface area is not enough for understanding the changes of specific capacitance. Thus, for samples CH-EAT and CH-AT, the specific capacitance increased with surface area, whereas samples CH-T presented the opposite trend. Table 17 also shows that the specific capacitance decreased with the increase of HT temperature in each of group of samples. This could be explained by the corresponding widening of the PSD and the related shift towards the mesopore range.

Table 17: Main characteristics of the six carbon materials tested.

Scan rate	$2\text{mVs}^{-1}$	
	Specific Capacitance $\text{Fg}^{-1}$	Normalized Capacitance $\mu\text{Fcm}^{-2}$
Sample		
CH-T1	246	36,96
CH-T2	181	26,50
CH-AT1	303	55,47
CH-AT2	253	51,10
CH-EAT1	322	58,34
CH-EAT2	230	52,11

### 4.5.2 Effect of oxygen and nitrogen-containing functional groups

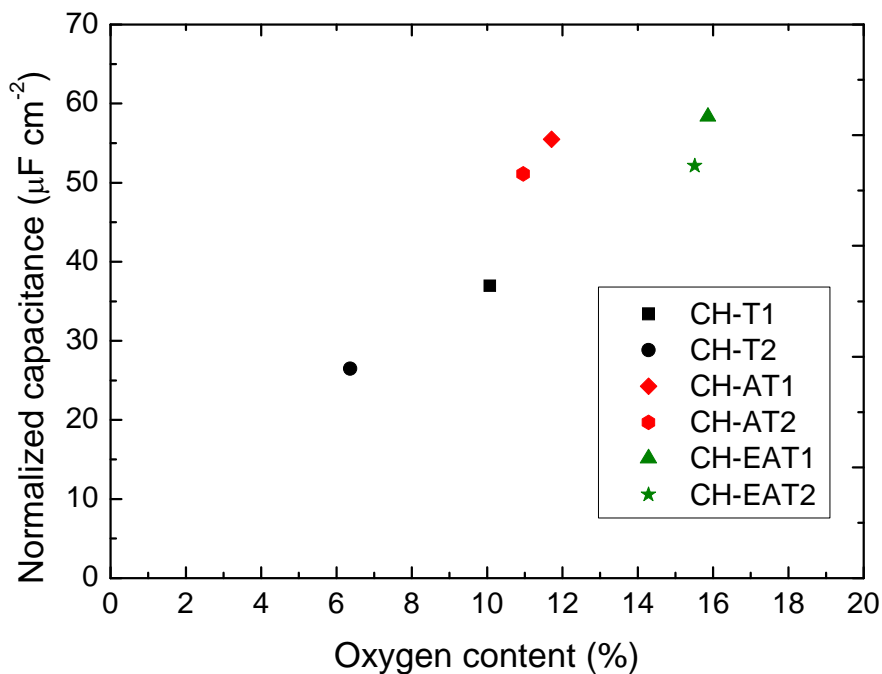
The presence of oxygen- and nitrogen-containing functional groups might also have a positive effect on specific capacitance of carbon. On the one hand, the formation of polar functional groups enhances the surface wettability of electrodes and thus leads to an increased exposed surface for charge storage [Frackowiak and Béguin 2001; Zhao et al. 2010b; Si et al. 2013]. On the other hand, the redox reactions of oxygen- and nitrogen-containing functional groups can enhance the specific capacitance. Oxygen-containing functional groups are typical electron acceptors, while nitrogen-containing functional groups work as electron donors. A previous work dealing with other tannin-based porous carbons evidenced a linear relationship between micropore volume and specific capacitance [Amaral-Labat et al. 2012b]. In the present case, the range of micropore volumes is much narrower but no linear trend could be found, especially at low scanning rate. In contrast, some trends are observed as soon as the heteroatom content is considered. Fig. 75 a) and 75 b) thus show the normalized capacitance, i.e. the capacitance measured at  $2 \text{ mV s}^{-1}$  and normalized by the BET surface area, plotted as a function of oxygen and nitrogen contents, respectively.

Although the micropore volume was not constant, normalized capacitance seems to increase linearly with the oxygen amount. The effect of nitrogen content is more complex. For example, the sample CH-AT2 presents a normalized capacitance which is 1.4 times higher than that of sample CH-T1, whereas its micropore volume is lower and its oxygen content is very similar to that of CH-T1. The main difference between these two samples is the nitrogen content, which is close to 8 wt. % in CH-AT2 against less than 1 wt. % in CH-T1. But a too high nitrogen content does not seem to be too favorable either, unlike what was found with oxygen, as an optimum of nitrogen content can be seen in Fig. 75 b). An intermediate nitrogen content ranging from 3 to 6 wt. %, combined with an appropriate pore size distribution and a high oxygen amount, can thus enhance the capacitor performances through extra redox reactions of Faradic pseudo-capacitance.

N6 or N5 nitrogen at the edges of the graphitic layers is mainly responsible of the pseudo-capacitance rather than the NQ quaternary nitrogen located inside the graphitic layers [Ra et al. 2009; Si et al. 2013]. It can be seen that N6+N5 functional groups were dominant (>90%) and so we can assume that N species present in our carbon gels produced pseudocapacitance. Concerning oxygen, Moreno-Castilla et al. (2012) showed that normalized capacitance had a linear relationship with the areal oxygen concentration up to 10.7 wt. %, and CO and CO<sub>2</sub>

evolving groups equally contributed. Our results are in well agreement with these findings; we observed a linear increase of capacitance up to 18% of oxygen content.

a)



b)

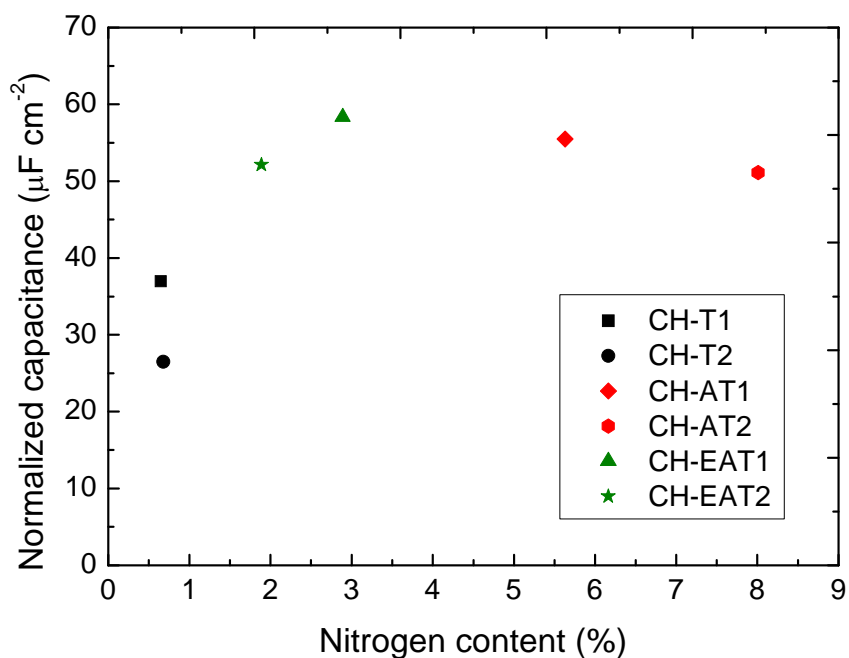


Fig. 75: The relationship between oxygen a) and nitrogen b) content and specific capacitance.

Similar trends were also found for scan rates  $10 \text{ mV s}^{-1}$  and  $50 \text{ mV s}^{-1}$  indicating positive influence of functional groups on specific capacitance of hydrothermal carbons. The presence

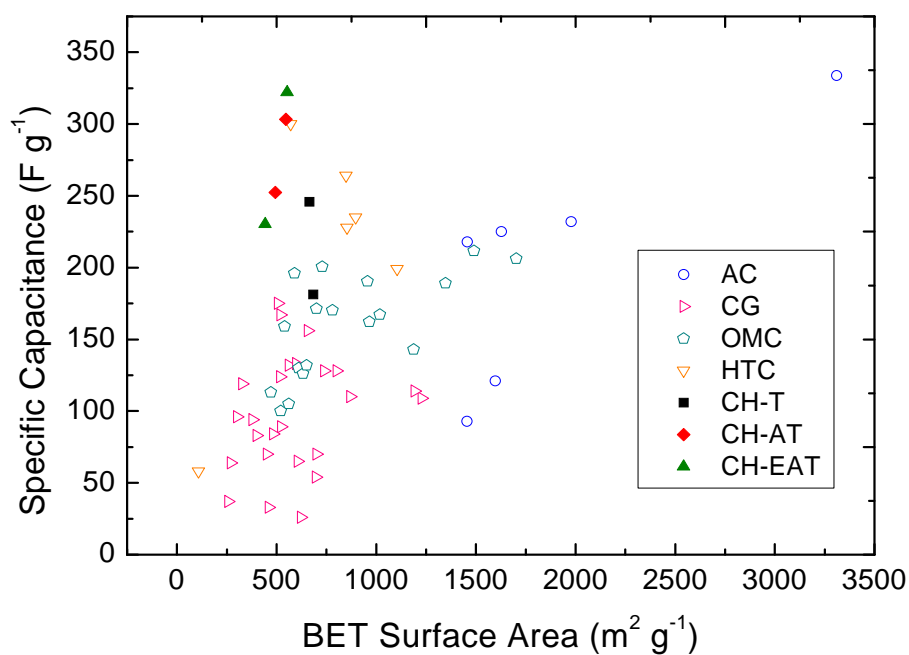
of oxygen and nitrogen functional groups in the carbon matrix provides additional pseudocapacitance to the capacitor. Activated carbons having high surface areas were oxidised with  $\text{HNO}_3$  and  $\text{H}_2\text{O}_2$  and the oxidised carbons obtained higher capacitance due to the pseudo-faradaic redox reactions [Khomenko et al. 2010]. The same tendency was observed for carbon materials having high nitrogen contents [Zhao et al. 2010b; Si et al. 2013; Shen and Fan 2013]. Wang et al. (2010) also observed that, in doped activated carbons, nitrogen- and oxygen-containing functional groups can bring pseudocapacitance contribution to the overall capacitance. However, such moieties are prone to block the ions of the electrolyte in the pores. Such effect may explain why too high N contents are less favourable when a significant amount of oxygen is already present and might justify that capacitances decreased faster for N-doped materials when increasing scan rate.

### 4.5.3 Comparison with previous studies

Fig. 76 a) shows the specific capacitance as a function of BET surface area for our materials as well as for other data reported in the literature for activated carbons (AC) [Frackowiak and Béguin 2001; Babel and Jurewicz 2004; Kumagai et al. 2013], carbon gels (CG) [Yoshizawa et al. 2003; Babic et al. 2004; Szczurek et al. 2010; Moreno-Castilla et al. 2011; 2012; Amaral-Labat et al. 2012b; Lu et al. 2012b], ordered mesoporous carbons (OMC's) [Xing et al. 2006; Wang et al. 2011; Lu et al. 2012a; Matsui et al. 2013] and HTC-derived materials [Zhao et al. 2010b; Si et al. 2013]. In this figure, only the data obtained at a scan rate of 1, 2, 4 and 5  $\text{mV s}^{-1}$  in acid and/or basic inorganic electrolytes ( $\text{H}_2\text{SO}_4$ ,  $\text{HClO}_4$  and  $\text{KOH}$ ) at different concentrations are given. As underlined by Stoller et al. (2010), the measurements of capacitance are highly dependent on the electrochemical setup, 3-electrode systems showing higher capacitances than the corresponding 2-electrode symmetrical cell. Consequently, we selected only studies using similar systems of 3-electrodes for the sake of comparison.

As stated above, our six materials were characterized by moderate values of  $S_{\text{BET}}$ , ranging from 442 to 684  $\text{m}^2\text{g}^{-1}$ , comparable to those of carbon gels prepared from tannin- or phenolic-based precursors [Babic et al. 2004; Szczurek et al. 2011a; 2011b; Amaral-Labat et al. 2012]. Moreover, their pore size distribution was very similar to those obtained for carbon gels, with a mixed micro-mesoporous texture [Szczurek et al. 2011a; 2011b; Amaral-Labat et al. 2012b]. The heteroatom doping might explain that the specific capacitances of our hydrothermal carbons are 2 to 8 times higher than those found for carbon gels [Babic et al. 2004; Szczurek et al. 2010; Amaral-Labat et al. 2012b].

a)



b)

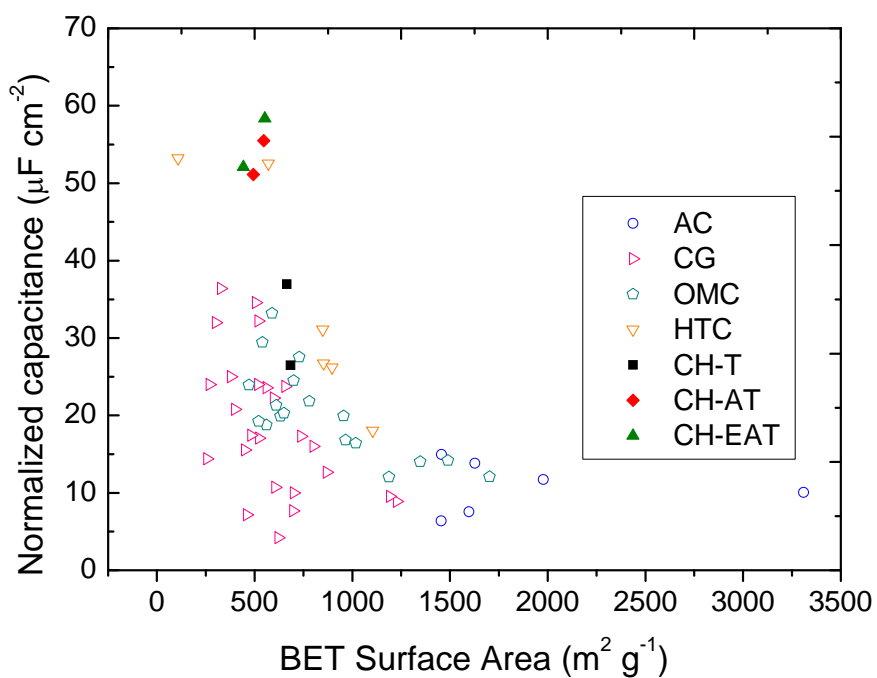


Fig. 76: a) Comparison, at a constant scan rate of at  $2 \text{ mV s}^{-1}$ , of a) specific capacitances and b) normalized EDLC capacitance of our materials with those of other carbonaceous materials as a function of their BET surface area (AC: Activated carbons, CG: Carbon gels, OMC: Ordered mesoporous carbons, HTC: Hydrothermal carbons).

Furthermore, the capacitances of tannin-based doped hydrothermal carbons are in the same range of magnitude as those found for activated carbons possessing apparent surface areas often higher than  $3000 \text{ m}^2 \text{ g}^{-1}$  [Frackowiak and Béguin 2001; Babel and Jurewicz 2004; Jurewicz et al. 2008]. Fig. 76 b) shows the normalized capacitance as a function of surface area for the same materials as in Fig. 76 a). The average values of our materials, close to 47 and  $28 \mu\text{F cm}^{-2}$  for scan rates of 2 and  $10 \text{ mV s}^{-1}$ , respectively, are significantly higher to those of activated carbons [Frackowiak and Béguin 2001; Jurewicz et al. 2008], carbon cryogels [Szczurek et al. 2010; Amaral-Labat et al. 2012b] or ordered mesoporous carbons prepared by a templating procedure [Qu and Shi 1998; Jurewicz et al. 2004].

These average values are also higher than the normalized capacitance generally accepted for a clean graphite surface,  $20 \mu\text{F cm}^{-2}$  [Saliger et al. 1998; Babic et al. 2004]. Fig. 76 b) shows that the highest values of normalized capacitance were found for other hydrothermally prepared carbons [Zhao et al. 2010b; Si et al. 2013], and for  $\text{RuO}_2$  deposited on graphene [Lin et al. 2013]. The active surface of hydrothermal carbons thus seems to be highly available at  $2 \text{ mV s}^{-1}$ , as non-doped materials (CH-T1 and CH-T2) already present excellent specific capacitances compared to carbon gels of similar surface area. Heteroatom-containing functional groups further improve the results by inducing extra pseudo-capacitance, and therefore allow increasing significantly the performances of capacitors.

## 4.6 Conclusions

N-doped carbon materials were prepared from Mimosa tannin in water or in 28 – 30 wt.% ammonia solution, and at temperatures ranging from 180 to  $220^\circ\text{C}$ . N-doped materials were obtained either by tannin amination in ammonia in room conditions followed by HTC in distilled water (H-EAT), or by direct HTC in ammonia (H-AT). The former method led to a hydrogel despite no crosslinker was present, and the latter led to microspheres. All were based on autocondensed and partly dehydrated tannin, mainly through heterocycle opening, the level of polymerisation depending on the preparation method. The N-doped materials presented rather low surface areas, but H-AT had outstanding nitrogen contents as high as almost 14 wt.%. Most of the nitrogen was in the form of amines, with some possible pyridinic N. MALDI-Tof and NMR studies proved that nitrogen was incorporated at several sites of the flavonoid units. Pyrolysis at  $900^\circ\text{C}$  systematically decreased the N content, as expected, given the volatility of this element, but simultaneously led to a significant porosity development. As a consequence, the CH-AT material prepared by HTC at  $190^\circ\text{C}$  presented N content and BET surface area of 8.01 wt.% and around  $500 \text{ m}^2 \text{ g}^{-1}$ , respectively.

When tested as electrodes for supercapacitors, these materials presented outstanding specific capacitances at  $2 \text{ mV s}^{-1}$ , close to those already reported for high surface area-activated carbons. The specific capacitances obtained with our hydrothermal carbons are among the highest ever reported so far. Further improvements are needed to maintain capacitance at high scan rates and mesostructuration, within the range 3-13 nm, of such materials is under study. Nitrogen doping, when combined with oxygen groups, can further increase the capacitance through Faradaic effects. The presence of such functional groups, however, hinder the diffusion of ions throughout the porosity, so that the capacitance decreased faster when the scan rate increased than what is observed for non-doped materials. We confirmed the beneficial role of oxygen up to 18 wt. % while an optimum in nitrogen content exists from 3 to 6 wt. %.

**Chapter 5: Synthesis of N-doped carbon  
gels and their use as electrodes for  
supercapacitors**





Brinker and Scherer (1990) defined a gel as a semi-solid system containing two phases: liquid and solid in which the pores of the solid are saturated by a solvent in a colloidal dimension. Fig. 77 summarizes the three main steps related to its synthesis: i) a starting solution having soluble reactive precursors is prepared and then, ii) it is transformed into a colloidal suspension of very fine solid particles in a liquid (sol). During the sol-gel process for the formation of an oxide gel (i.e. silica gel), the first reaction is the precursor hydrolysis, which leads to reactive species that further condense forming low molecular weight oligomers. Sol particles are so small that during constant agitation they are not subject to gravity. By extending and/or branching, polymer chains are formed. They become insoluble and extremely small solid particles appear; iii) so that in the end a giant cluster, having the size of the container, suddenly appears, the gel [Brinker and Scherer 1990]. Beyond the gel point, it is no longer possible to measure viscosity but an elastic modulus [Hench and West 1990].

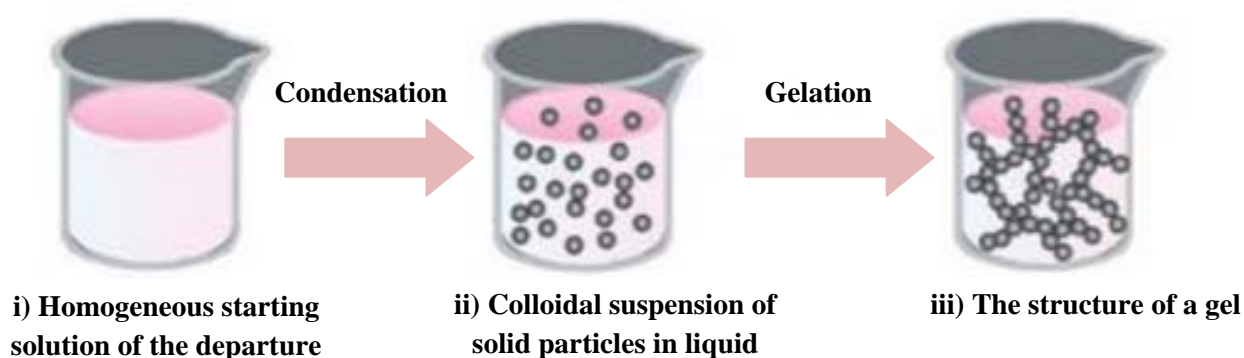


Fig. 77: Principle of a sol-gel reaction: i) starting solution with precursor, ii) sol system and iii) gel.

In a conventional procedure, there is also a fourth step which is the maturation. These gels, placed inside a tube slightly closed, spend normally few days in an oven at moderate temperatures, i.e. 85°C to reach the highest possible degree of polymerization. The formation of the polymer network generally increases the gels' density and their mechanical properties, and reduces the shrinkage during drying.

### 5.1 Introduction to gel drying

The gel drying process is the final and the most critical step if monoliths are expected. Solvent in pores must be replaced by air and the challenge here is to remove solvent without collapsing their brittle nanostructure. Shrinkage produces structure collapsing and cracking after drying [García-González et al. 2012]. Such fragile materials must be dried under mild

conditions to avoid detrimental shrinkage and to preserve, as much as possible, the morphology and the size of the gel [Aegerter et al. 2011]. Therefore, three different kinds of drying methods were applied here in which; 1) the solvent in liquid phase was transformed to gas phase by evaporation (xerogels); 2) the solvent was frozen into a solid phase and sublimated to gas (cryogels) and finally, 3) the solvent in liquid phase was transformed into gas under supercritical conditions ( aerogels). The three methods with their specific pressure and temperature pathway are illustrated in Fig. 78.

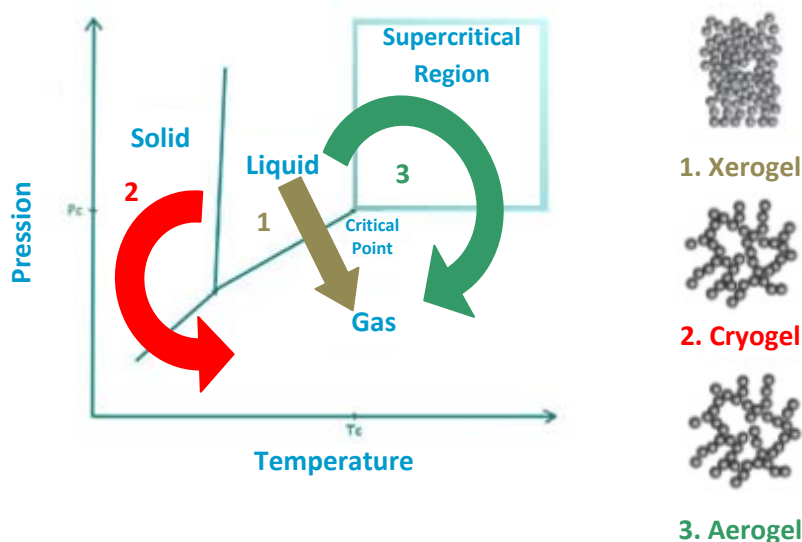


Fig. 78: Phase diagram of the solvent present in the gel and the corresponding drying pathways used for the formation of xerogel (grey), aerogel (green) and cryogel (red) and their corresponding drying nodular structure of the resulting porous materials.

### 5.1.1 Subcritical Drying or xerogels synthesis

The traditional method of drying under atmospheric conditions or under subcritical conditions leads to the formation of xerogels (from the Greek "xeros" means dry). This traditional drying is the easiest and also the cheapest. It is based on the evaporation of the solvent either at room temperature or in an oven. Water is used during the synthesis and it is usually also a by-product of the crosslinking reactions. The main problem found during the water removal is that the capillary forces applied in the pores of small diameters may reach values between 100 and 200 MPa and such forces are responsible for the closure of the pores resulting in very high shrinkage and therefore xerogels are often cracked. In order to reduce these capillary forces, water is exchanged by an organic solvent exchange i.e. ethanol, acetone, before the drying step. These solvents, having a surface tension lower than that of water, are supposed to limit the loss of porosity because capillary forces exerted in the pores

are lower than those produced by water [Scherer and Smith 1995; Job et al. 2006]. After sub-critical drying, xerogels are denser and their porosity is lower than those of cryogels and aerogels. In summary, xerogels show the greatest shrinkage.

### 5.1.2 Freeze-drying or Cryogels synthesis

The word “cryo” is derived from Greek which means cold or icy. Lyophilization or freeze-drying process is carried out at low temperatures, below the freezing point of the solvent, and therefore the liquid present in the pores are removed by sublimation under reduced pressure and it turns directly to the gaseous phase from the solid phase. For that, the best known and most used solvent having high vapour pressure to facilitate its sublimation process is tert-butanol (2-methyl-2-propanol). Its freezing temperature is around 26°C, the density variation freezing is  $-0.00034 \text{ g cm}^{-3}$  and vapour pressure at 821Pa at 26°C against  $-0.075 \text{ g cm}^{-3}$  and 61 Pa respectively for water at 0°C [Daraoui et al. 2010].

The freeze-drying process is divided into four parts. Firstly, the water present in the pores is exchanged with tert-butanol at 50°C during three days with agitation. Then, the solvent is frozen at very low temperatures such as -90°C and then submitted to a vacuum drying to sublimate the interstitial tert-butanol ice formed. The last part is a second drying process for extracting the solvent found on the surface of the dried gels. The main drawback of such drying process is that the solvent, t-butanol, is frozen in the pores and this can modify the materials' porous structure by the large ice crystals growth that leads to cracks which formation of megalopores (pores  $> 10\mu\text{m}$ ), macropores (pores  $> 50\text{nm}$ ) and regular mesopores ( $2 < \text{pores} < 50\text{nm}$ ) [Tamon et al. 1999; Job et al. 2005].

### 5.1.3 Supercritical Drying or Aerogel synthesis

The third kind of drying process is the supercritical drying leading to aerogels in which “aēr” in Greek means air. The method comprises the increasing of the pressure and temperature simultaneously beyond the critical point of the solvent. Water is not the best option because of its high critical point so the use of high temperature leads to loss of porosity. Therefore, other kinds of organic solvents can be applied during this method such as: acetone, isopropanol, ethanol and methanol but also carbon dioxide [Job et al. 2006]. This technique requires two exchanges: the first being the exchange of water with an organic solvent, acetone for example and the second, is the solvent exchange with CO<sub>2</sub> liquid. The exchange of water by CO<sub>2</sub> is not feasible due to the too low solubility of CO<sub>2</sub> in water. For the second step, CO<sub>2</sub> seems to be the best option among the other possible solvents since its

critical point is one of the lowest (its critical temperature is around 40°C) [García-González et al. 2012]. This process avoids the formation of a liquid-vapour meniscus in the pores of the wet gels because the transition from liquid to gas is carried out outside of the phase diagram of the solvent. The supercritical phase is obtained in the supercritical region as seen in Fig. 78. This technique is the most commonly used to minimize gels' shrinkage obtaining remarkable values of surface area and pores volume [Aegerter et al. 2011; Baetens et al. 2011]. With this method, great porous materials are obtained keeping the typical pearl necklace structure but it is costly and requires well-controlled safety conditions because of the high pressure used (around 100 bars) [Job et al. 2005].

The hydrogels produced here were fragile and broke into pieces so it was not possible to observe visually the difference between these three kinds of drying method mentioned above. Fig. 79 shows the dimensions of an aerogel (left), cryogel (center) and xerogel (right) produced from the hydrogel formulation of tannin and formaldehyde. It illustrates the typical physical appearance of the dried gels based on their drying method [Amaral-Labat 2013].



Fig. 79: The three dried gels made from tannin and formaldehyde resin and dried in supercritical CO<sub>2</sub> conditions (aerogel) on the left; freeze-drying conditions (cryogel) on the centre and subcritical conditions (xerogel) on the right.

## 5.2 N-doped carbon gel synthesis by HTC

In this work, HTC allowed synthesizing gels in easier and shorter time: i) first a solution containing reactants was prepared and ii) the solution was submitted to HTC at 180°C for 24h. Thanks to the autocondensation reactions that take place with tannin, a gel could be formed without the conventional use of any crosslinker such as formaldehyde.

In a typical synthesis, evaporated aminated tannin (EAT) was first prepared by dissolving 2.0 g of tannin in 40 cm<sup>3</sup> of 28% aqueous ammonia solution, as described in Chapter 4. The mixture was sealed and stirred for 1 h at room temperature, and subsequently left for

evaporation in a fume hood for two days. Amounts of 2.0, 3.5 or 6.0 g of EAT were then mixed with 16.0 g of bi-distilled water in a glass vial. Those mixtures correspond to EAT concentrations of 11, 18 or 27 wt. %, respectively. The vial was placed in a Teflon-lined autoclave and directly put in a ventilated oven pre-heated at 180°C and let for HTC for 24 h. After that time, the autoclave was removed from the oven and cooled down to room temperature. A dark brown gel was obtained (Fig. 80), which was removed from the vial. At this step, the gel pores are saturated with water, some residual unreacted tannin and/or other by-products of the tannin autocondensation. The wet gel was soaked in dry ethanol to remove those soluble species and also to decrease the surface tension of the solvent and limit the crack formation. Ethanol was replaced daily with fresh one. After three days, the solvent exchange was assumed to be complete, and then the following drying processes were applied to produce xerogels, cryogels and aerogels.

**Aerogels:** gels were cut into small pieces, i.e. less than 1 cm along the largest side, and were introduced in the chamber of an automatic supercritical point dryer apparatus (Autosamdri-815, Tousimis, USA), in which ethanol was first fully exchanged by liquid CO<sub>2</sub> before the latter being submitted to supercritical conditions. The depressurization was carried out at a controlled rate of 0.45 MPa min<sup>-1</sup>. The aerogels prepared from initial EAT concentrations of 11, 18 or 27 wt. % were labelled A11, A18 and A27, respectively.

**Cryogels:** gels were immersed in a large excess of tert-butanol (melting point: 26°C) to exchange ethanol. Fresh tert-butanol was replaced every day by fresh one during three days. The samples were next installed into a deep-freezer at -90 °C for 24h and then into a freeze-dryer (Heto PowerDry PL6000, Thermo Scientific, France) for 72 h. During the freeze-drying process, the working pressure and the temperature were around 0.12–0.20 mbar and -96.5 °C, respectively. The cryogels prepared from initial EAT concentrations of 11, 18 or 27 wt. % were labelled C11, C18 and C27, respectively.

**Xerogels:** gels were left in a vacuum oven at 80°C overnight for drying. The xerogels prepared from initial EAT concentrations of 11, 18 or 27 wt. % were labelled X11, X18 and X27, respectively.

After drying, the gels were submitted to pyrolysis in a quartz tube installed in a tubular furnace and continuously flushed with high-purity nitrogen at 50 mL min<sup>-1</sup>. The heating rate was 1°C min<sup>-1</sup>, the set point was 900 °C and the dwell time was 3h. After carbonization, the letter “C” (for “carbon” gels) was added to the sample label, so that the following samples were recovered: CA11, CA18, CA27, CC11, CC18, CC27, CX11, CX18 and CX27.

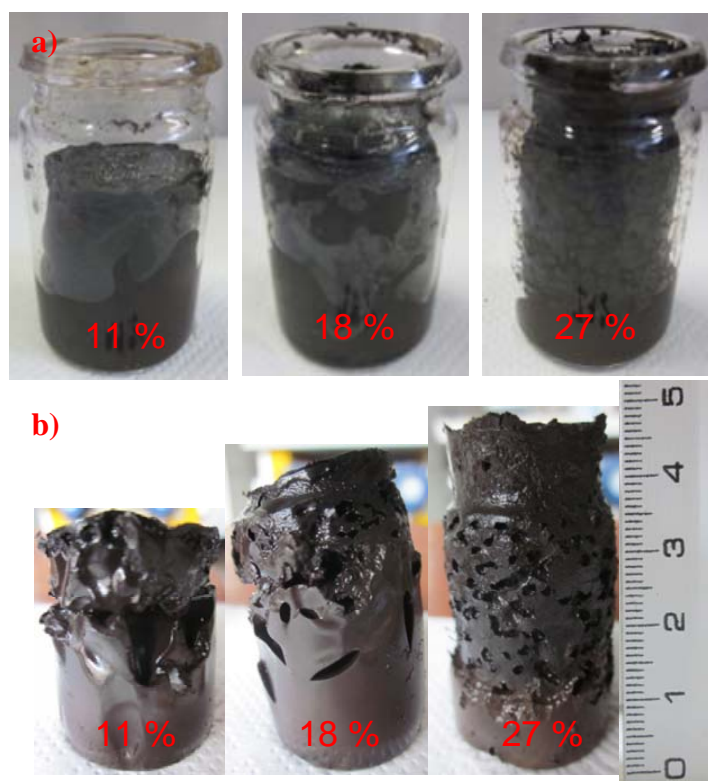


Fig. 80: The three gels made from evaporate aminated tannin (EAT) and water after HTC at 180°C and 24h a) in and b) outside of a glass vial at different initial concentrations of 11, 18 and 27%.

### 5.3 Morphology of carbon gels

Fig. 81 shows SEM images of one series of carbon gels only, CX27, CC27, and CA27, as rather similar images were obtained for the other materials. The typical granular structure of carbon aero, xero or cryogels based on phenolic precursors cross-linked with formaldehyde [Petričević et al. 1998; Horikawa et al. 2004; Czakkel et al. 2005; Szczurek et al. 2011a, 2011b] is clearly evidenced. The materials are indeed based on a set of roughly spherical nodules of rather small size due to the pH used, around 7. It is indeed well known that, in phenolic gels, the higher the pH, the lower the nodule size [Job et al. 2005; Szczurek et al. 2011a, 2011b].



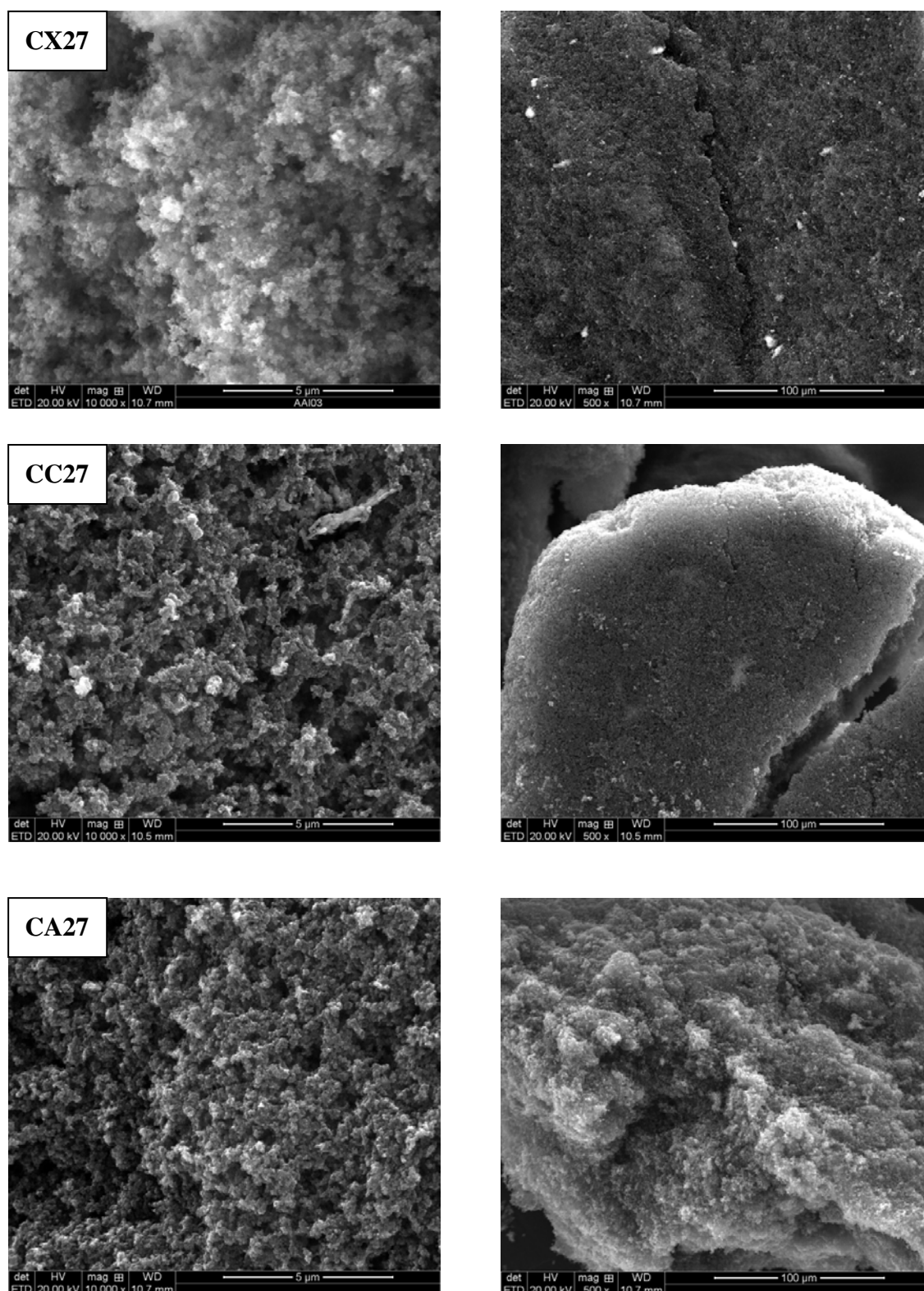


Fig. 81: SEM images of all samples after HTC and posterior pyrolysis at 900°C for all carbon gels: CA, CC and CX at 27%.

After HTC, gels as-obtained from the autoclave had monolithic shapes, were homogenous, but presented some cracks here and there. Mercury porosimetry was tried as an additional characterisation technique, but all (organic and carbon) gels were cracked into



smaller pieces during the tests. Careful examination of the samples showed that mercury intrusion did not occur into the samples. Therefore, macro/mesopore volumes and distribution of sizes could not be determined by porosimetry. However, missing this information was not that important as carbon gels were ground to prepare electrodes, and the macroporosity was expected to be lost during the grinding process as already observed elsewhere [Szczyrek et al. 2010; Amaral-Labat et al. 2012b].

### 5.4 Porous texture of organic and carbon gels

Fig. 82(a) shows the BET surface area of the nine dried gels, obtained after HTC of EAT solutions at different concentrations (11, 18 or 27 wt. %) and after drying by the three different methods (A, C and X). Xerogels had the lowest  $S_{\text{BET}}$  values,  $112 \pm 10 \text{ m}^2/\text{g}$ , irrespective to the initial EAT concentration. Cryogels had  $S_{\text{BET}}$  values between 155 and  $243 \text{ m}^2 \text{ g}^{-1}$ ; the lowest  $S_{\text{BET}}$  was that of sample C27, whereas C11 and C18 had similar  $S_{\text{BET}}$ , 219 and  $243 \text{ m}^2 \text{ g}^{-1}$ , respectively. Aerogels had  $S_{\text{BET}}$  values between 295 and  $129 \text{ m}^2 \text{ g}^{-1}$  for A11 and A27, respectively. The impact of the drying method was the highest for the most diluted gels, i.e. for those prepared at the lowest EAT concentration, 11 wt. %. For these gels, the BET surface area increased as  $X11 < C11 < A11$ . In contrast, the less diluted gels, i.e. those prepared from the highest EAT concentration, 27 wt. %. presented rather similar  $S_{\text{BET}}$  values, whatever the drying method.

After pyrolysis at  $900^\circ\text{C}$ ,  $S_{\text{BET}}$  increased considerably as a consequence of evolution of volatiles and related creation of microporosity, as evidenced in Fig. 82(b). A value as high as  $860 \text{ m}^2 \text{ g}^{-1}$  was indeed obtained for CA27. However, if this general trend is well obeyed, the effects of both drying method and initial resin concentration on the surface area of the resultant carbon gels are not readily predictable. The mechanical properties of the gels before pyrolysis indeed play a significant role, the most diluted gels being more prone to shrinkage during pyrolysis, and being therefore those whose porosity can collapse more easily. As a consequence, the most porous organic gels are often not those leading to the carbon gels of highest surface areas, as observed previously [Amaral-Labat et al. 2012b]. From Fig. 82(b) it appears that carbon xerogels, cryogels and aerogels have  $S_{\text{BET}}$  values within the ranges  $521 - 585 \text{ m}^2 \text{ g}^{-1}$ ,  $496 - 754 \text{ m}^2 \text{ g}^{-1}$  and  $557 - 864 \text{ m}^2 \text{ g}^{-1}$ , respectively. Unlike organic gels, the highest surface areas of carbon gels were obtained when using the highest EAT concentration, 27 wt. %.

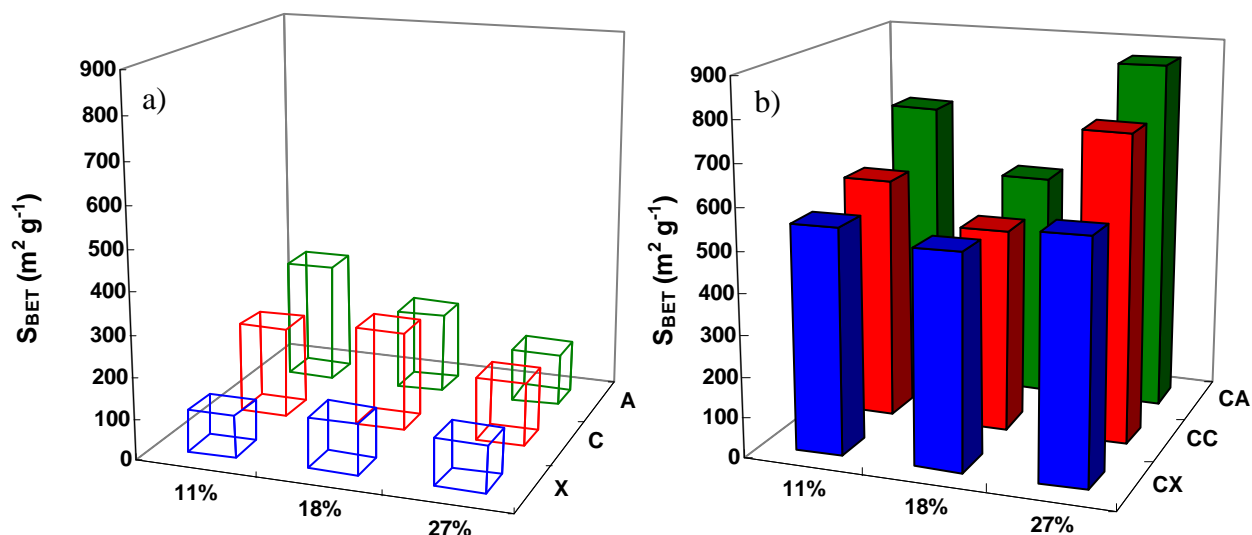


Fig. 82: BET surface area of all gels: a) before pyrolysis (A, C and X), and b) after pyrolysis (CA, CC and CX).

Fig. 83 shows nitrogen adsorption-desorption isotherms and pore size distributions (PSDs) of the carbon gels series prepared with an initial concentration of evaporated aminated tannin of all carbon gels CA, CC and CX prepared at 11, 18 and 27 wt. %. Nitrogen adsorption isotherms were a combination of types I and IV. They presented an important nitrogen uptake at relative pressures  $P/P_0$  lower than 0.01, indicating the existence of a well-developed narrow microporosity, and a slight slope up to  $P/P_0=0.9$  which indicates the development of wider microporosity and mesoporosity. All the samples presented a narrow hysteresis loop, assigned to capillary condensation in mesopores. PSD's obtained by DFT method are in good agreement with qualitative conclusions derived from the above analysis of nitrogen isotherms. PSD's were indeed bimodal with significant pore volumes centred on around 0.6 nm (micropores) and 50 nm (upper limit of mesopores). In the case of our best materials (at 27 wt. %), the microporosity decreased according to  $\text{CA}_{27} > \text{CC}_{27} > \text{CX}_{27}$ , i.e. in the expected order of  $S_{\text{BET}}$  values, see Table 18.

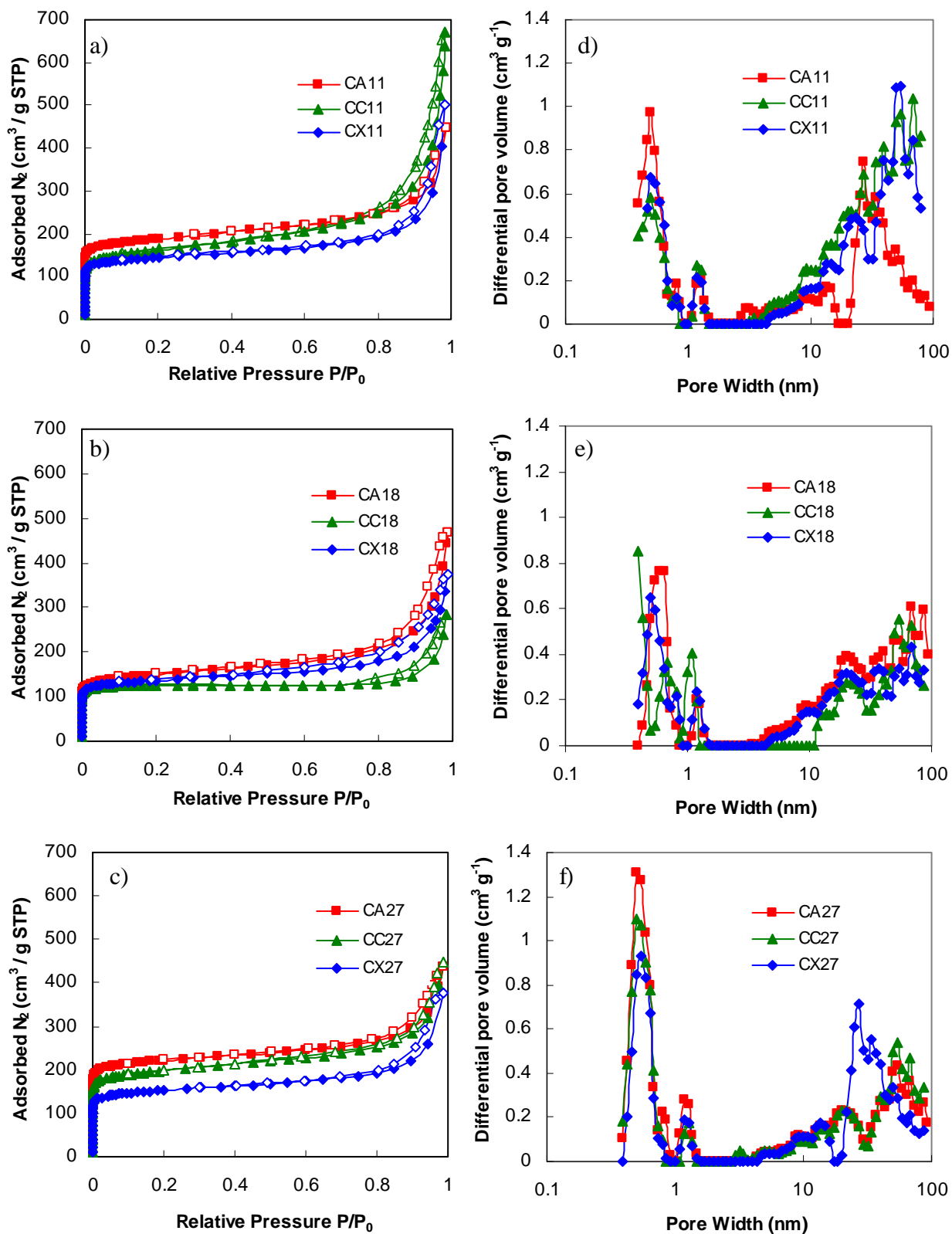


Fig. 83: (a), (b) and (c) Nitrogen adsorption-desorption isotherms at -196 °C of CA, CC and CX carbon gels at different percentages 11, 18 and 27%, and (d), (e) and (f) their corresponding pore size distributions.

Table 18: Main characteristics of all organic and carbon gels synthesized.

	Textural Properties						Electrochemical performances		Elemental Composition		
	$S_{DFT}$ ( $m^2 g^{-1}$ )	$S_{BET}$ ( $m^2 g^{-1}$ )	$V_{0.97}$ ( $cm^3 g^{-1}$ )	$V_{\mu}$ ( $cm^3 g^{-1}$ )	$V_m$ ( $cm^3 g^{-1}$ )	$L_0$ (nm)	Specific Capacitance ( $F g^{-1}$ )	Volumetric specific capacitance ( $\mu F cm^{-2}$ )	N (%)	C (%)	O (%)
<b>A11</b>	79	295	0.67	0.10	0.57	2.20			3.1	55.4	37.1
<b>C11</b>	72	219	0.38	0.06	0.32	1.59			3.0	54.4	37.7
<b>X11</b>	32	102	0.35	0.04	0.31	3.84			3.0	56.8	35.5
<b>CA11</b>	789	714	0.59	0.27	0.32	0.61	349.9	49.0	2.5	78.3	17.2
<b>CC11</b>	571	592	0.81	0.23	0.58	0.82	255.4	43.1	2.6	77.1	18.7
<b>CX11</b>	470	552	0.62	0.21	0.41	0.67	399.3	72.3	2.5	78.3	17.6
<b>A18</b>	47	198	0.42	0.06	0.36	2.19			3.6	56.5	35.2
<b>C18</b>	55	243	0.48	0.08	0.40	2.06			3.6	55.5	36.0
<b>X18</b>	44	122	0.46	0.04	0.42	3.21			3.7	56.9	34.7
<b>CA18</b>	515	557	0.60	0.22	0.38	0.73	358.9	64.4	2.9	78.8	16.5
<b>CC18</b>	537	496	0.37	0.20	0.17	0.64	347.4	70.0	3.0	79.3	15.8
<b>CX18</b>	532	521	0.52	0.20	0.32	0.69	277.9	53.3	2.8	81.4	14.1
<b>A27</b>	31	129	0.31	0.04	0.27	2.38			3.7	56.7	34.7
<b>C27</b>	38	155	0.35	0.05	0.30	2.13			3.8	56.8	34.7
<b>X27</b>	32	112	0.28	0.04	0.24	2.30			3.4	54.3	37.4
<b>CA27</b>	915	860	0.61	0.33	0.28	0.60	403	46.9	2.6	81.3	13.9
<b>CC27</b>	797	754	0.61	0.29	0.32	0.58	409.5	54.3	1.9	78.2	17.3
<b>CX27</b>	601	585	0.46	0.23	0.23	0.64	350.3	59.9	2.4	78.8	16.4

## 5.5 Elemental composition of organic and carbon gels

Fig. 84(a) shows the van Krevelen diagram of raw tannin and of organic and carbon gels. As expected, tannin showed the highest O/C and H/C ratios, 0.75 and 0.10, respectively. After HTC, O/C and H/C ratios decreased to  $0.65 \pm 0.05$  and  $0.08 \pm 0.01$ , respectively, but remained rather close to those of pristine tannin. After pyrolysis at  $900^\circ C$ , the evolution of volatiles made the O/C and H/C ratios decrease to  $0.20 \pm 0.04$  and  $0.02 \pm 0.01$ , respectively. The average, absolute C and O contents after HTC were 56 and 36 wt. %, respectively, and these values became 79 and 16 wt. % after pyrolysis at  $900^\circ C$ , respectively. Similar trends were found for different kinds of biomass: wheat straw, poplar wood, olive residues [Wiedner et al. 2013] or hazelnut shells [Unur 2013]. Fig. 84(b) shows the nitrogen content of all gels, before and after pyrolysis at  $900^\circ C$ , as a function of their  $S_{BET}$ . The highest nitrogen contents, between 3.0 and 3.7 wt. %, were obtained before pyrolysis, as N is a volatile element. Pyrolysis thus produced an increase of  $S_{BET}$  but also a decrease of nitrogen content to 1.9 – 3.0 wt. %. A roughly linear relationship between  $S_{BET}$  and N can be observed, and therefore

the lowest N contents were found for CA27, CC27 and CX27, which had the highest  $S_{\text{BET}}$  of each series of drying mode. Table 18 summarises the results of elemental composition and of textural properties of organic and carbon gels.

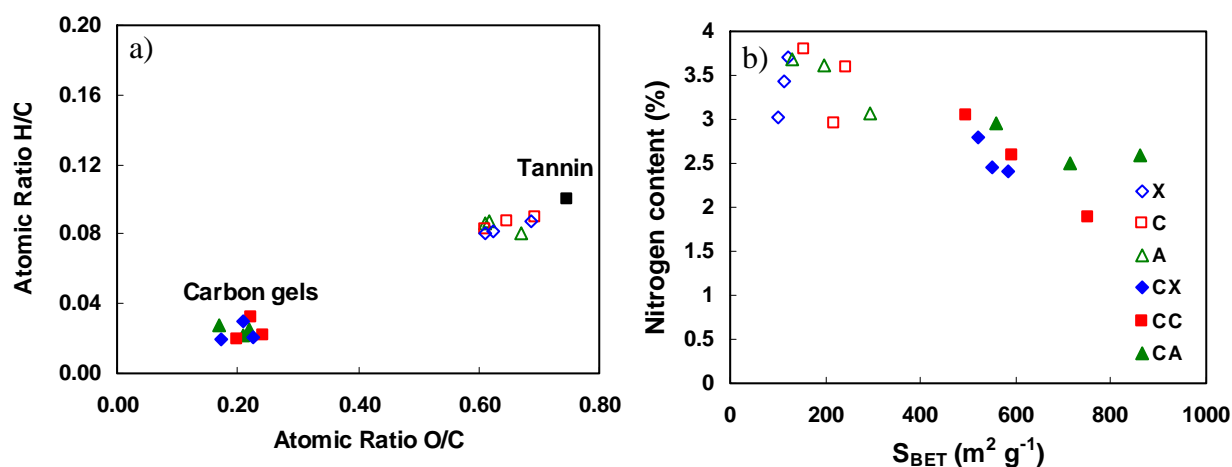


Fig. 84: a) Van Krevelen diagram for all materials including the pristine tannin, and b) relationship between the nitrogen content and the BET surface area for all materials.

Table 19 shows the results of XPS analysis of X11 and CX11 materials after peaks deconvolution, with emphasis on the energy range corresponding to N1s and O1s. X11 had 2.5 at.% N in the form of isolated pyridinic (N-6) and/or neutral amines. Based on the literature, the presence of pyridinic species is possible since it is well known that HTC process promotes polycondensation of aromatic units and formation of N-containing cycles such as pyridinic species [Baccile et al. 2011]. For instance, Cagniant et al. (2002) proposed the formation of pyridinic group during the carbonization of cellulose at 250°C in ammonia atmosphere. After carbonization at 900°C, no amines were present in CX11, as expected, as they were mainly replaced by pyridinic (N-6) and by other species such as pyrrolic (N-5) or pyridonic (not distinguishable by XPS measurements), quaternary pyridinic nitrogen (N-Q) or pyridine oxide groups [Lahaye et al. 1999]. Despite the high purity of the inert gas used for carbonization, the presence of oxide forms (pyridone, pyridine oxide) could be ascribed to the reactivity of carbonized materials with air as previously observed [Pels et al. 1995; Lahaye et al. 1999].

The atomic content of oxygen was 18.3 at.% for X11 and it decreased down to 2.6 at.% for CX11 after carbonization. Observing the high-resolution O1s spectra, we found three main peaks: OI due to carbonyls from quinines, pyridones, quinones and ketones; OII due to carbonyls from esters and anhydrides and from hydroxyl groups; OIII due non-carbonyls

(ether type) found in esters and anhydrides [Biniak et al. 1997; Zhou et al. 2007]. Before carbonization, we found essentially OII (30.9 at.%) and OIII (69.1 at.%) types of oxygen. After carbonization, OI groups appeared (23 at.%), and OII gained importance (55.1 at.%) compared to OIII (21.9 at.%) due to gas evolution and related aromatization during carbonization.

Table 19: Contributions to N1s and O1s bands in XPS patterns of X11 and CX11 materials.

	Binding energy (eV) and area of the peak (%)							(at. %)		
	Isolated Pyridinic (N-6) and/ or Neutral amines	Pyridinic (N-6)	Pyrrolic (N-5) or pyridonic	Quaternary N-Q or oxydised pyrinic N	OI	OII	OIII	N <sub>XPS</sub>	C <sub>XPS</sub>	O <sub>XPS</sub>
<b>H-EAT_180°C</b>	399.1 (100)					531.9 (30.9)	533.3 (69.1)	2.5	76.6	18.3
<b>CH-EAT_180°C</b>		398.1 (33.1)	400.7 (60.1)	402.8 (6.8)	530.7 (23.0)	532.4 (55.1)	533.6 (21.9)	1.6	95.8	2.6

Synthesis of carbon aerogels by HTC has been reported elsewhere. For example, when a mixture of glucose and ovalbumin was submitted to HTC at 180°C, aerogels presented a  $S_{\text{BET}}$  value of 276 m<sup>2</sup> g<sup>-1</sup> and a nitrogen content of 7.5 wt. %. After carbonization at 900°C,  $S_{\text{BET}}$  increased up to 308 m<sup>2</sup> g<sup>-1</sup> and nitrogen content decreased to 5.9 wt. % [White et al. 2011b]. When glucose together with borax were submitted to HTC at 180°C, aerogels having  $S_{\text{BET}}$  value of 233 m<sup>2</sup> g<sup>-1</sup> were produced, and  $S_{\text{BET}}$  increased up to 600 m<sup>2</sup> g<sup>-1</sup> after pyrolysis at 550°C [Fellinger et al. 2012]. Aerogels were also produced by HTC using S-(2-thienyl)-L-cysteine and 2-thienyl carboxaldehyde as precursors, leading to values of  $S_{\text{BET}}$  and N content of 263 m<sup>2</sup> g<sup>-1</sup> and 5.9 wt. %, respectively. After carbonization at 900°C, these values became 322 m<sup>2</sup> g<sup>-1</sup> and 4.3 wt. %, respectively [Wohlgemuth et al. 2012a]. The addition of phenolic compounds such as phenol and phloroglucinol together with glucose, fructose and xylose, produced gels with BET surface areas up to 1100 m<sup>2</sup> g<sup>-1</sup> after HTC, and 700 m<sup>2</sup> g<sup>-1</sup> after pyrolysis but without the presence of nitrogen atoms [Brun et al. 2013a]. Compared to the HTC-derived carbon gels mentioned in the literature, the present carbon aerogels have high  $S_{\text{BET}}$ , up to 860 m<sup>2</sup> g<sup>-1</sup>, a reasonably high nitrogen content of 2.6 wt. %, and the advantage of being synthesised from non-toxic and renewable raw materials, in the absence of crosslinking agent. The electrochemical properties of carbon gels prepared in this study are now analysed.

## 5.6 Electrochemical performances of carbon gels

Electrochemical experiments were carried out using the same technique as described in Chapter 4. Fig. 85(a) shows the voltammograms of all nine carbon gels CA, CC and CX prepared at initial EAT concentrations of 11, 18 and 27 wt. %, obtained at a scan rate of  $2 \text{ mV s}^{-1}$ . The specific capacitances of all carbon gels at  $2 \text{ mV s}^{-1}$  were also gathered in Table 18. The curves show an asymmetric shape with a small hump in the range of 0.2 – 0.6 V, characteristic of Faradaic pseudo-capacitance due to redox reactions, and which can be correlated to the high level of functional groups (oxygen and nitrogen, see Table 18) [Fraczkowiak and Béguin 2001; Conway and Pell 2003]. The same behaviour was reported for other carbon materials prepared by HTC [Zhao et al. 2010b; Si et al. 2013]. The following redox reactions involving N and O are possible, among others where  $>\text{C}$  stands for the carbon network) [Fraczkowiak and Béguin 2001; Li et al. 2007]. Above 0.85V, the increase of the signal is related to the oxidation of water. The same behaviour was also reported for activated carbons investigated in a similar range of potential in acidic medium, e.g. in the work of Demarconnay et al. (2010).

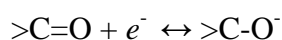
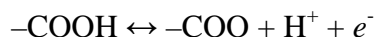
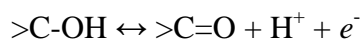
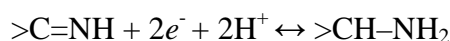


Fig. 85(b) shows the changes of specific capacitance as a function of scan rate. At 27 wt. %, CC27 got the highest values of capacitance at 2 and  $10 \text{ mV s}^{-1}$ , 409 and  $213 \text{ F g}^{-1}$ , respectively, whereas CA27 got the highest value of capacitance at  $50 \text{ mV s}^{-1}$ ,  $37 \text{ F g}^{-1}$ . The specific capacitance of a material corresponds to its ability of storing electrical charge per unit mass. Several materials' characteristics have an impact on specific capacitance, such as  $S_{\text{BET}}$ , PSD, pore volume and amount and nature of functional groups. The drop of capacitance observed for all samples at higher scan rates may be related to a series of factors: i) increase of internal Ohmic resistance during the ions transport throughout the micropores; ii) interaction of the electrolyte with the functional groups present at the surface of hydrothermal carbons electrodes; iii) presence of dangling bonds existing on carbon surfaces [Jurewicz et al. 2004; Vix-Guterl et al. 2004, 2005; Portet et al. 2007, 2008]; iv) insufficient amount of

mesopores for conveying the ions from the electrolyte to the electrode surfaces [Wei et al. 2011; Amaral-Labat et al. 2012b].

Fig. 86(a) presents the relationship between BET surface area and specific capacitance for all prepared carbon gels. Despite the significant scattering of the data points, it can be clearly seen that, on average, increasing  $S_{\text{BET}}$  roughly led to higher capacitances, as already observed in previous studies [Frackowiak and Béguin 2001; Conway and Pell 2003; Moreno-Castilla et al. 2012; Shen and Fan 2013]. However, though presenting rather different  $S_{\text{BET}}$  values (552, 754 and 860  $\text{m}^2 \text{g}^{-1}$ ), CX11, CC27 and CA27 exhibited similar specific capacitance (399.3, 409.5 and 403  $\text{F g}^{-1}$ , respectively) at  $2 \text{ mV s}^{-1}$ . Therefore, surface area is important but is obviously not the only factor affecting the electrochemical performances. CX11 is especially interesting as it combines high dilution (only 11 wt. % of EAT in water), easy and fast synthesis (drying in oven at  $80^\circ\text{C}$ ), and high capacitance. Therefore, HTC-derived carbon xerogels may have as good textural properties as aerogels, and therefore they should be interesting materials to be applied in electrochemistry applications [Frackowiak and Béguin 2001; Moreno-Castilla et al. 2005, 2012].

Fig. 86(b) shows the specific capacitance as a function of different pore volumes classified according to their corresponding pore width: lower than 0.7 nm ( $V_{0.7}$ , ultramicropores), lower than 2 nm ( $V_2$ , micropores), lower than 10 nm ( $V_{10}$ , micropores + narrow mesopores) and total ( $V_t$ ). Applying a linear fit to each set of pore volumes (not shown for clarity), the correlation factors were low and were found to decrease in the order  $V_{0.7} > V_2 > V_{10} > V_t$ . Taking into account  $V_{0.7}$  only, an increase of specific capacitance was found up to  $0.2 \text{ cm}^3 \text{ g}^{-1}$ , above which a constant value around  $400 \text{ F g}^{-1}$  was observed for higher ultramicropore volumes.

The presence of nitrogen and also oxygen functional groups might induce pseudocapacitance effects due to Faradaic redox reactions [Toupin et al. 2005]. Fig. 87(a) presents the normalised capacitance as a function of nitrogen content for the present carbon gels, as well as for previous materials also obtained by HTC of aminated tannin or not (TM: Tannin Materials) synthesized and discussed in Chapter 4. Fig. 87(b) is the same as Fig. 87(a) but for oxygen content. For both plots, optimal values of nitrogen and oxygen contents could be observed at 2-3% and 17-18%, respectively. Nitrogen and oxygen moieties thus seem to have a positive effect on capacitance values, until they block the pores and therefore hinder the diffusion of ions throughout the porosity, hence the observed maxima.



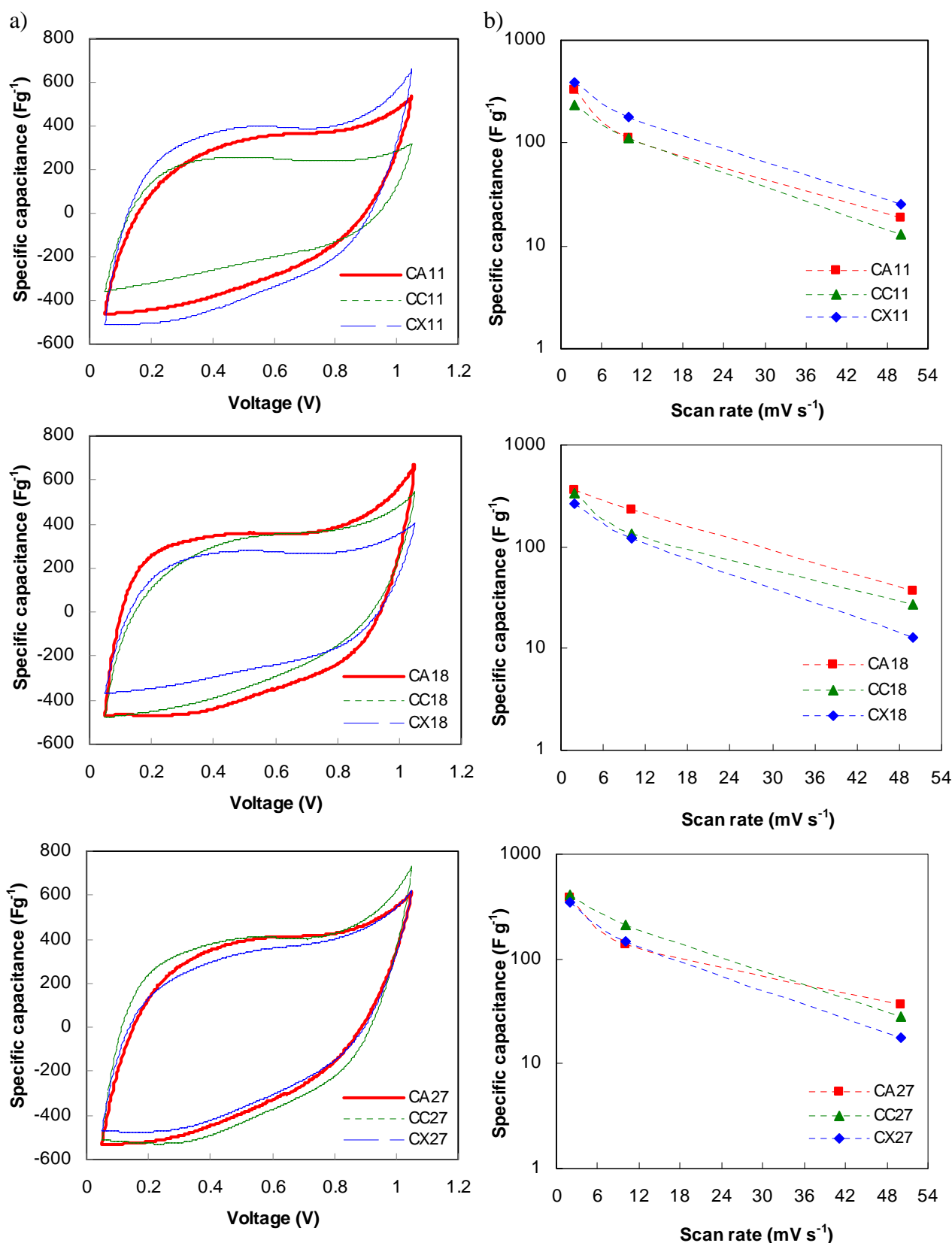


Fig. 85: a) Cyclic voltammograms of CA, CC and CX carbon gels at different percentages of tannin: 11, 18 and 27% at a scan rate of  $2 \text{ mV s}^{-1}$ , and b) their corresponding specific capacitance at different scan rates (the dotted lines are just guides for the eye).

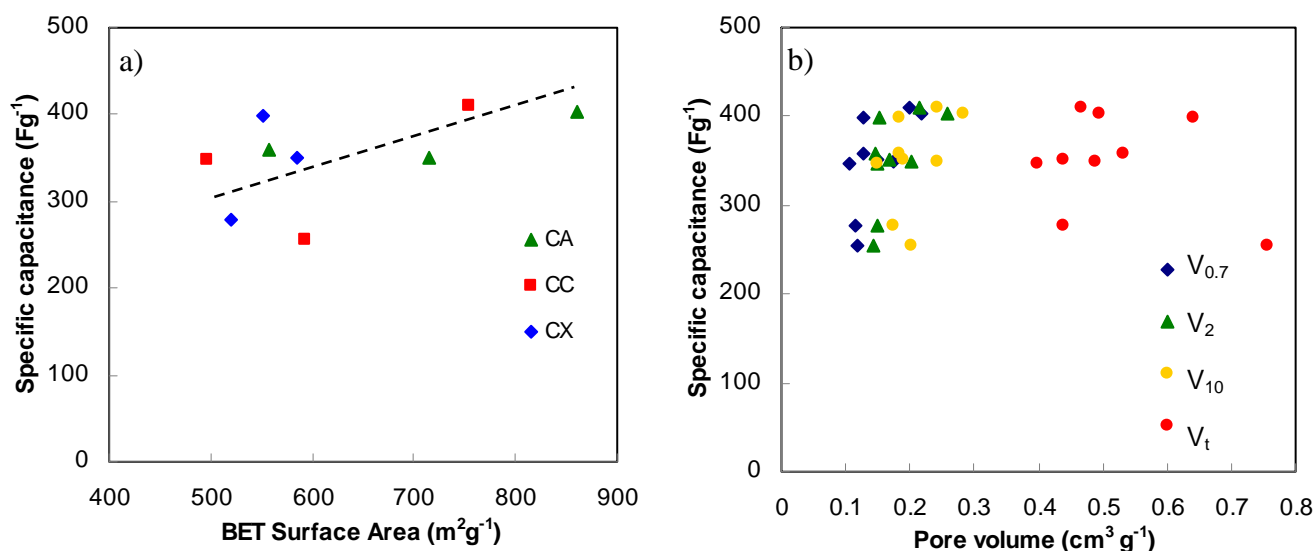


Fig. 86: Specific capacitance of all prepared, HTC-derived, carbon gels plotted as a function of: a) BET surface area, and b) pore volumes classified according to pore widths: below 0.7 nm ( $V_{0.7}$ , ultramicropores), below 2 nm ( $V_2$ , micropores), below 10 nm ( $V_{10}$ , micropores and narrow mesopores) and total ( $V_t$ ).

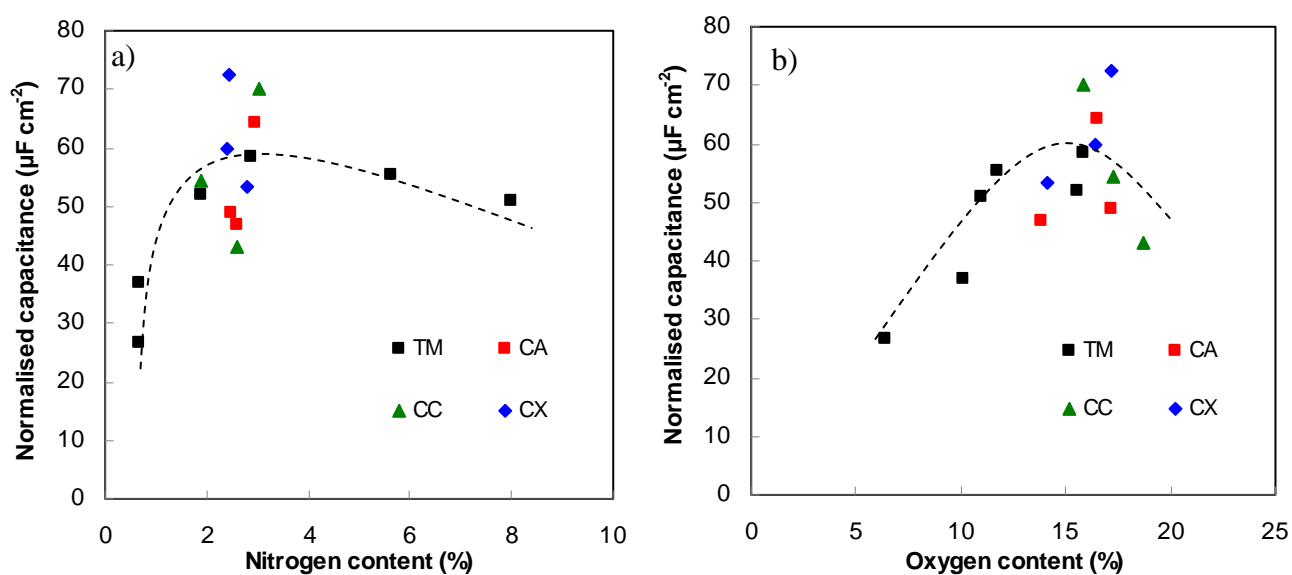


Fig. 87: Normalised capacitance of all prepared, HTC-derived (TM), carbon gels plotted as a function of: a) nitrogen, and b) oxygen functional groups.

CX27, CC18 and CA11 were dried according to different methods, and presented different BET surface areas ( $585$ ,  $496$  and  $714 \text{ m}^2 \text{ g}^{-1}$ , respectively) but similar specific capacitances ( $350$ ,  $347.4$  and  $349.9 \text{ F g}^{-1}$ , respectively). CX27, CC18 and CA11 had N contents of  $2.41$ ,  $3.04$  and  $2.49 \text{ wt. } \%$ , respectively. O contents of  $16.4$ ,  $15.84$  and  $17.16 \text{ wt. } \%$ .

%, respectively, and micropore fractions of 49, 53 and 46%, respectively. These values suggest that N and O contents, and  $S_{\text{BET}}$  and micropore fractions, compensate more or less but are all important to give good electrochemical performances. For example, CC18 has the lowest  $S_{\text{BET}}$  but also the highest N content and micropore fraction.

N6 or N5 nitrogen at the edges of the graphitic layers is mainly responsible of the pseudocapacitance, unlike the NQ quaternary nitrogen located inside the carbon sheets [Ra et al. 2009; Si et al. 2013]. As shown in Table 19, N6+N5 functional groups were clearly dominant (93%) and so we can assume that N species present in our carbon gels accounted for the observed pseudocapacitance. As for oxygen, it has been reported that oxygen-containing functional groups can be categorized into CO-desorbing and CO<sub>2</sub>-desorbing species, the former (such as carbonyl, hydroxyl and quinone groups) being more likely to produce pseudocapacitance than the latter (carboxyl, lactones and anhydrides) [Li et al. 2007; Sun et al. 2011a]. However, others authors stated that both CO-desorbing and CO<sub>2</sub>-desorbing groups can induce pseudo-capacitance [Zhao et al. 2010b; Moreno-Castilla et al. 2012]. For instance, Moreno-Castilla et al. (2012) concluded that normalized capacitance was linearly correlated with the surface oxygen concentration up to oxygen content of 10.7 wt.%, and that CO- and CO<sub>2</sub>-desorbing groups equally contributed. In fact, CO<sub>2</sub>-desorbing groups have acidic character and induce electron-acceptor properties in the carbon surface that also contribute to the overall capacitance through pseudo-capacitance interactions. Our results agree with these last findings, as we observed a linear increase of capacitance up to 17-18 wt.% of oxygen content.

The above trends are in good agreement with previous studies [Zhao et al. 2010b; Shen and Fan 2013; Si et al. 2013]. For instance, human hair submitted to HTC and subsequent KOH activation led to materials whose highest specific capacitance, 264 F g<sup>-1</sup>, was obtained for those having the highest levels of nitrogen, as high as 3.1% [Si et al. 2013]. Two materials made by HTC of D-glucosamine and posterior KOH activation were also prepared, having similar surface areas, but the highest capacitance (300 F g<sup>-1</sup>) was obtained with the material having again the highest nitrogen content (4.4%) [Zhao et al. 2010b]. Shen and Fan (2013) reported that carbon materials made from different precursors containing nitrogen showed better electrochemical performances than those not containing nitrogen.

Fig. 88 (a) presents the specific capacitance as a function of  $S_{\text{BET}}$  for the nine carbons gels studied herein, as well as for other carbon materials such as: other kinds of carbons gels (CG) [Yoshizawa et al. 2003; Babic et al. 2004; Szczurek et al. 2010; Moreno-Castilla et al. 2011,

2012; Amaral-Labat et al. 2012b; Lu et al. 2012b); hydrothermal carbons (HTC) [Zhao et al. 2010b; Si et al. 2013]; tannin-based carbon materials prepared by HTC (TM) synthesized and discussed in Chapter 4 and activated carbons (AC) [Conway et al. 1997; Frackowiak and Béguin 2001; Xing et al. 2006]. The data gathered in this figure correspond to specific capacitances recorded at scan rates of 1, 2 or 5  $\text{mV s}^{-1}$  in acid or basic inorganic electrolytes at different concentrations, and measured with similar three-electrode systems. The highest normalised capacitances were observed for the N-doped carbon gels synthesised in the present work, definitely higher than those exhibited by AC with apparent  $S_{\text{BET}}$  higher than  $3000 \text{ m}^2 \text{ g}^{-1}$ . Fig. 88 (b) shows the normalised capacitance, obtained by dividing the specific capacitance by  $S_{\text{BET}}$  for the same materials as in Fig. 88 (a). The normalised capacitance of our materials, from 43.1 to  $72.3 \mu\text{F cm}^{-2}$ , were also higher than the normalised capacitance generally accepted for a clean graphite surface,  $20 \mu\text{F cm}^{-2}$  [Babic et al. 2004; Saliger et al. 1998]. The active surface of hydrothermal carbons thus seems to be highly available at  $2 \text{ mV s}^{-1}$ , and the presence of heteroatom-containing functional groups further improves the results by inducing extra pseudo-capacitance, and therefore allows increasing significantly the electrochemical performances.

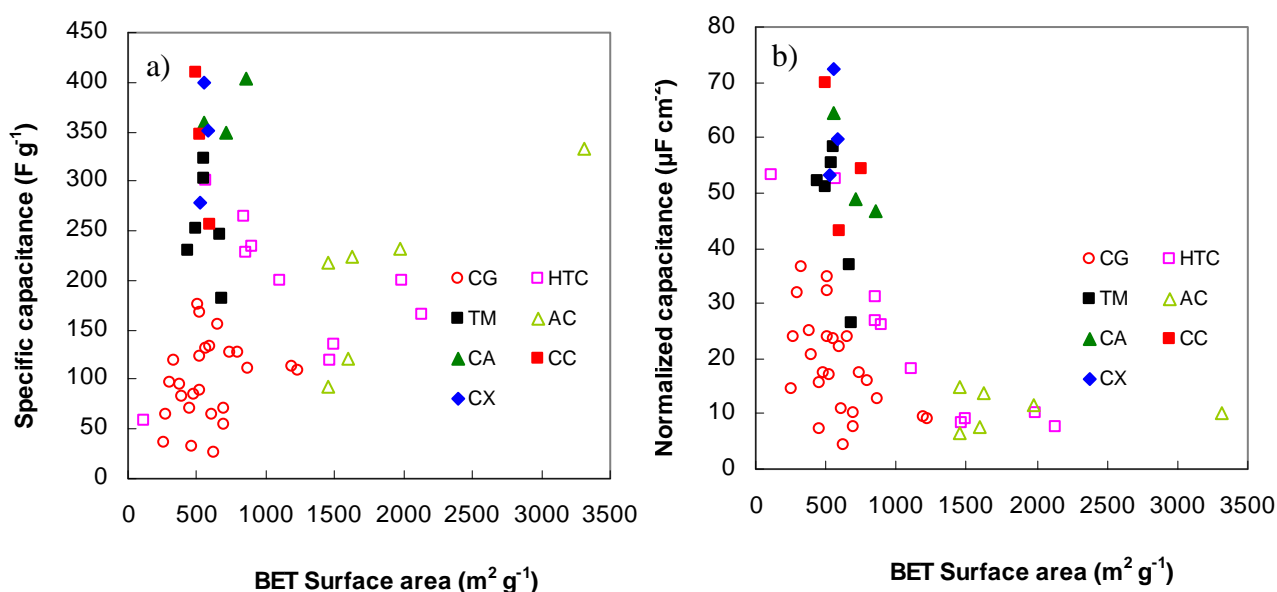


Fig. 88: a) Specific capacitance, and b) normalised capacitance, both plotted as a function of BET surface area for all carbon gels and other materials from the literature (CG: other carbon gels; HTC: HTC-derived materials; TM: HTC-derived tannin-based materials; AC: activated carbons).

Unfortunately, increasing the scan rate made the electrochemical capacitances decrease rapidly. Lower capacitances, although decreasing much more slowly with scan rate, were achieved with tannin-formaldehyde (TF) carbon cryogels. The latter were based on narrow and well interconnected mesoporosity, not only giving access to micropores but also having a significant contribution to the active surface area [Amaral-labat et al. 2012b]. Indeed, some authors claimed that porous carbons having pore diameters within the range 3-13 nm are those showing the highest capacitance values [Escribano et al. 1998]. We assume that the observed changes at increasing scan rate are related to the low amount of mesopores having the most relevant range of pore diameters for rapidly leading the electrolyte ions to the electrode surfaces [Amaral-labat et al. 2012b]. Therefore, further improvements are still needed to maintain high capacitances at high scan rates. Mesostructuration of such materials, within the range 3-13 nm, is one possible way of meeting better performances at high scan rates, and is presently under study.

## 5.7 Conclusions

Nitrogen-doped carbon aerogels, cryogels and xerogels were prepared from aminated tannin submitted to hydrothermal carbonization, followed by relevant drying mode and subsequent pyrolysis at 900°C. Materials based on spherical nodules, typical of carbon gels of phenolic origin, were obtained. The preparation method presented here produced cheaper and greener carbon gels than those produced by more conventional routes. The dehydrating and self-crosslinking reactions occurring during HTC might have improved the hydrogels resistance to shrinkage during drying, so that highly porous xerogels could be obtained. After pyrolysis at 900°C, carbon gels with developed surface areas and porosity, and with nitrogen contents between 1.9 and 3.0 wt. %, were produced. These materials were tested as electrodes of supercapacitor in a three-electrode system. High specific capacitances, ranging from 255.4 to 409.5 F g<sup>-1</sup>, and high normalised capacitance, from 43.1 to 72.3 μF cm<sup>-2</sup>, were reached at a scan rate of 2 mV s<sup>-1</sup>. These performances are much higher than those reported for high surface area-activated carbons. The presence of functional groups, based on nitrogen and oxygen heteroelements, partly accounted for such performances through Faradaic effects. However, optimal values in nitrogen and oxygen contents, 2-3 and 17-18 wt. %, respectively, were observed. Further improvements might be achieved in terms of capacitance decrease at higher scan rates through a suitable mesostructuration of such materials, which is presently under study.

**Chapter 6: Synthesis of mesoporous  
carbons by a soft-templating route using  
tannin as a carbon precursor**



Carbonization and, eventually, further activation of biomass increase the surface and porosity of the final carbon materials however, it is difficult to control their size and it is impossible regarding their shape and connectivity. If mesoporosity is formed, the pore size distribution (PSD) is usually wide. Different strategies have been developed to tailor the pore size of carbon materials especially in the mesoporous range. One of them, the nanocasting route, is based on the negative replication of a porous host matrix filled with carbon. If an ordered mesoporous silicate materials is as a (hard)-template, ordered mesoporous carbons (OMC's) can be produced with a partly controlled mesoporosity regarding size and morphology. Nevertheless, this process is tedious, time-consuming and it is not environmentally friendly (use of fluorhydric acid to remove the hard template). Another process, developed more recently, is based on the use of surfactants, as endo-structurant or soft-templates for the preparation of OMC's. This route is interesting since it is more environmentally friendly and it can be considered as a direct route compared to the multiple-step of the nanocasting process. This soft-templating route is based on the self-assembly of a surfactant, acting as a pore structuring agent, with a soluble carbon precursor (i.e. a resin). These compounds yield to composite mesophase (precursor/surfactant) having well-defined symmetry like similar to liquid crystals.

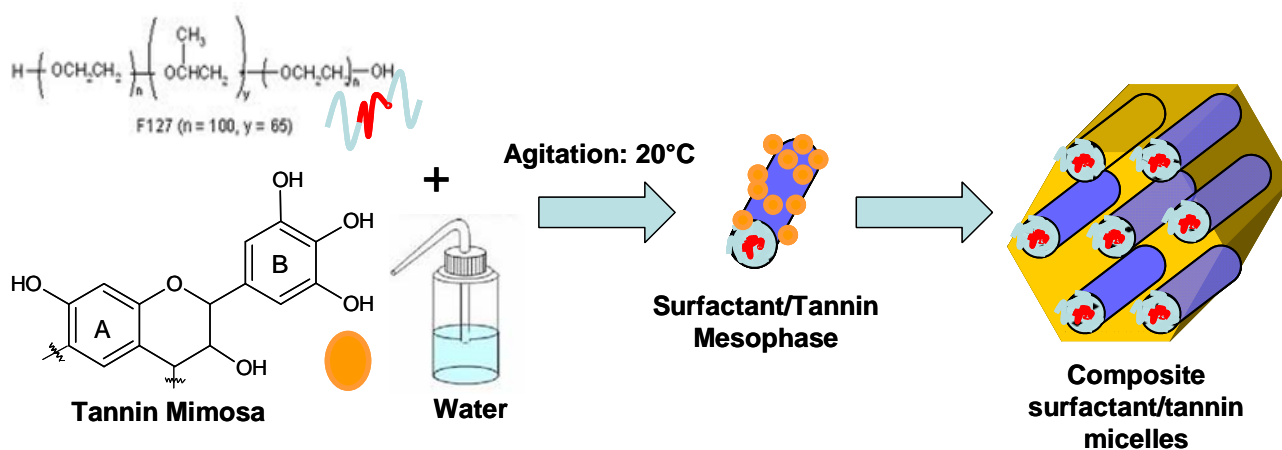


Fig. 89: Schematic approach for the production of OMC's using tannin Mimosa (adapted from Schlienger et al. (2012)).

These mesostructures are converted to OMC's by carbonization in inert atmosphere, the soft-template being pyrolysed during this step and yielding the mesoporosity. The mechanisms of formation of those mesostructures are still under investigation. They occur in aqueous media or in alcoholic media through an Evaporation-Induced Self-Assembly process (EISA). This chapter will be devoted to the direct synthesis of OMC's in aqueous phase with the use of surfactants and tannin as the carbon precursor (Fig. 89).



## 6.1 F-127 Pluronic<sup>®</sup> and OMC synthesis

Surfactants have two main parts: one hydrophilic and one hydrophobic, which lead to self-assembly and micelle formation. Fig. 90 shows various kinds of surfactants, classified according to the nature of their hydrophilic portion. The four main types of surfactants are: ionic, including anionic, cationic and amphoteric surfactants, and non-ionic or neutral surfactants. In this study, we used a non-ionic surfactant in which the hydrophilic part is water-soluble and the hydrophobic portion is capable of interacting with materials/solvents immiscible in water [Förster and Plantenberg 2002]. The surfactant chosen was: F-127 Pluronic<sup>®</sup> from BASF, also commercially available under the name Poloxamer 407, supplied by Sigma-Aldrich and quite well known due to its large application in OMC's synthesis. F-127 Pluronic is a non-ionic triblock copolymer composed of hydrophilic polyethylene oxide (PEO) and hydrophobic polypropylene oxide (PPO) chains [Escobar-Chavez et al. 2006; Perry et al. 2011]. Its molecular weight and chemical formula are 12.6 kDa and  $\text{HO}(\text{EO})_{\sim 100}(\text{PO})_{\sim 65}(\text{EO})_{\sim 100}\text{OH}$  respectively. In aqueous solution, the PEO-PPO-PEO chain has a natural tendency to self-associate and form spherical micelles having a central core of hydrophobic chains surrounded by heads of hydrophilic chains [Park et al. 2007; Jiang et al. 2012].

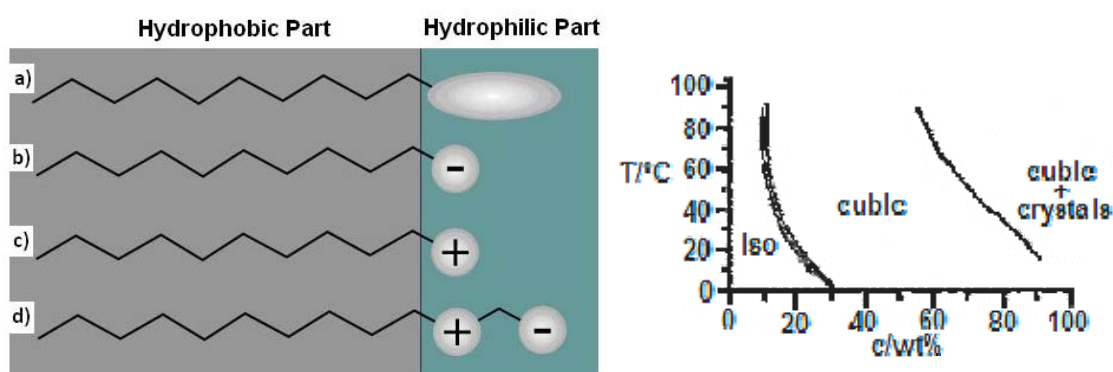


Fig. 90: Schematic representation of the four main types of surfactants a) neutral, b) anionic, c) cationic and d) amphoteric on the left and the phase diagram of Pluronic F127 in aqueous medium on the right [Wanka et al. 1994].

Fig. 90 also shows the phase diagram of F127, where *c* stands for concentration (wt.%) and *T* stands for temperature (°C), as determined by Wanka et al. (1994). The temperature for the micelle formation (*T<sub>m</sub>*) is of 23.1°C, having a critical micelle concentration (CMC) of 1 wt.%. At temperatures lower than *T<sub>m</sub>*, micelles are not formed and the block copolymer molecules are present in the solution only as unimers. However, in a transition region around *T<sub>m</sub>*, micellar size strongly increases with temperature. When the temperature is 20°C higher

than  $T_m$ , the size of the micelle is independent of the concentration and temperature. By increasing the concentration and temperature, the micelles arrange themselves to form a mesophase having a cubic symmetry [Wanka et al. 1994].

The formation of micelles through self-assembly of amphiphilic block copolymer is a crucial step during the synthesis [Huang et al. 2008; Liu et al. 2011]. Therefore, the choice of the synthesis temperature or the surfactant concentration is very important for the micelles formation and the synthesis of OMC's [Wanka et al. 1994]. Schlienger et al. (2014) observed that the mixing temperature is a parameter very important during micelles formation and different formation pathways are seen depending on the temperature chosen. Finally, heating treatment under inert atmosphere at temperatures higher than 400°C allows totally removing the template and revealing regular nanostructures [Escobar-Chávez et al. 2006; Ma et al. 2013].

OMC's were produced from phenol [Zhang et al. 2007; Huang et al. 2008; Fang et al. 2010], resorcinol [Wang et al. 2008] or phloroglucinol [Liang and Dai 2006] together with formaldehyde. Schlienger et al. (2012) explored the synthesis of OMC's from tannin using PF127 and a water/alcohol solution in very acidic medium to synthesize the first "green" OMC's. They observed that the pH is one important factor to be taken into consideration in relation to resins autocondensation and crosslinking reactions. Amaral-Labat et al. (2013) also observed that the gelation time of xerogels made from tannin-formaldehyde-F127 system was correlated to the pH. In the range of pH equal to 4-5, the highest gelation time was reached, which means that the crosslinking and condensation reactions were the least favourable. On the contrary, those reactions are very fast at very acidic pH, lower pH= 2, or basic pH, i.e. pH= 10.

Wang et al. (2008) and Schlienger et al. (2012) stated that the interactions between the surfactant and the organic precursor are mainly through hydrogen bonds but secondary Coulombic interactions could also occur depending on the pH used. At pH between 3 and 7, below the tannin's pKa (around 8), the surfactant (S) and the organic precursor (O) are neutral and develop interactions *via* H-bond which are noted  $S^0O^0$ . For those pH, especially at pH 4-4.5, tannin self-condenses slowly. At very acid pH (below 1.5), autocondensation seems to be very faster and with the introduction of high concentration of chloride ions ( $X^-$ ) and  $H^+$  in the system, interactions of  $S^+X^-O^+$  or  $S^+X^-O^0$  types could probably occur. However, the autocondensation of the phenolic precursor may be too fast and may limit rearrangements during the self-assembly with micelles [Wang et al. 2008; Schlienger et al. 2012]. The

inconvenient of the materials produced by Schlienger et al. (2012) is that mesoporosity disappeared after carbonization at 900°C. We decided to modify the OMC's synthesis, eliminating ethanol in order to see the effect on the resultant carbon materials.

## 6.2 Synthesis of OMC's from tannin and F127

In a typical synthesis, 1,0g of tannin was dissolved in 8mL of water and the pH was set adding hydrochloric acid (HCl 12N) for  $\text{pH} \leq 2$  or NaOH to set  $\text{pH} = 5$ . Separately, a second solution was prepared dissolving 1,0g of F127 in 8g of water. After complete dissolution, both solutions were mixed together. The final mixture was instantaneously insoluble and a reddish resin appeared at the bottom of the glass vial. The initially salmon coloured liquid became reddish transparent after total phase separation. After 5 days, the liquid was removed and the solid was dried in a vacuum oven at 80°C (Fig. 91).



Fig. 91: Schematic approach of OMC's synthesis using tannin and F127.

The dried samples were then carbonised at 400 and 900°C (sample prepared at  $\text{pH} < 1$  was also carbonised at 700°C). The samples were placed in an oven up to the final carbonization temperature that was held for 3h (heating rate:  $1^\circ\text{C min}^{-1}$ ). The entire process, heating and cooling, was carried out under nitrogen flow. The materials were named according to the pH and temperature of pyrolysis i.e. PTW\_1\_400°C stand for a carbon material prepared from Pluronic\_Tannin\_Water at  $\text{pH}=1$  and calcined at 400°C.

### 6.2.1 Effect of the pH

Fig. 92 shows TEM photos of two materials synthesized at pH equal to 1 and 5 after carbonization at 400°C. TGA analysis is not shown here but the template (F127) was gradually eliminated from 250°C up to 400°C permitting the formation of the ordered structures [Liang et al. 2004; Liang and Sheng 2006; Schlienger et al. 2012]. The structures seen are typically of mesoporous materials having a more or less organised mesostructure depending on the pH. Mesoporosity presents a hexagonal symmetry (honey comb type) for the material prepared at pH 1 whereas wormlike structures are obtained for other pHs (pH<1 and pH>2). Thus, pH 1 appears as the optimal pH for the ordering of the mesostructure with a hexagonal symmetry. The same trend was observed by Wang et al. (2008) and Schlienger et al. (2012) who observed that for very acid medium, the fast autocondensation reaction of the phenolic precursors could affect ordering during the composite mesophase formation.

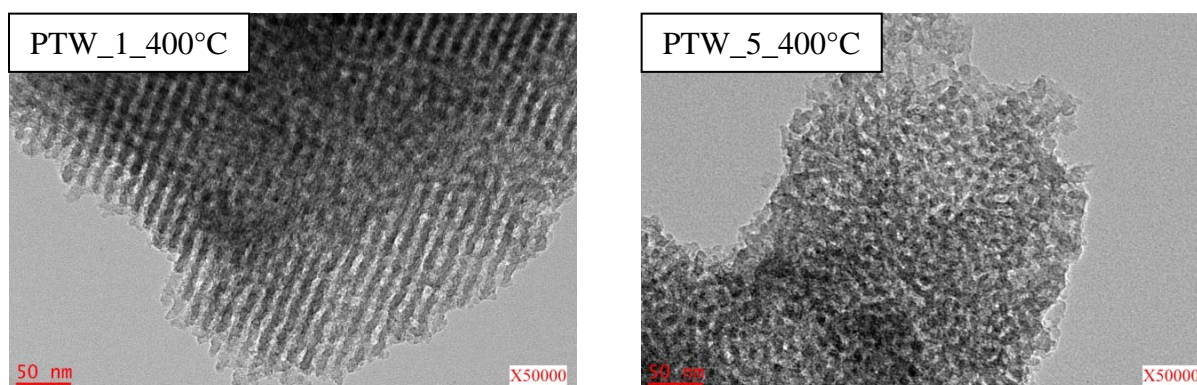


Fig. 92: TEM images of some PTW samples synthesized after agitation at pH 1 (on the left) and pH 5 (on the right), drying at 80°C and posterior pyrolysis at 400°C.

Table 20 shows the textural properties as well as the elemental analysis of the OMC's. Samples had a very similar  $S_{\text{BET}}$ , between 433-472  $\text{m}^2 \text{g}^{-1}$  after a thermal treatment at 400°C. The rest of textural properties were also very similar and did not vary with the pH. At 400°C, very narrow porosity was not present as the micropore volume determined by nitrogen was always higher than the one determined by carbon dioxide. Elemental analysis is also given in the same table; carbon content is around 70%, having a high proportion of oxygen around 23%. In order to increase the conductivity of the materials, higher carbonization temperatures i.e. 900°C were necessary.

Table 20: Textural properties and elemental analysis of all carbon materials synthesized.

	<i>Textural Properties</i>						<i>Elemental Analysis</i>			
	$S_{BET}$ ( $m^2 g^{-1}$ )	$V_{0.97}$ ( $cm^3 g^{-1}$ )	$V_{\mu}$ ( $cm^3 g^{-1}$ )	$V_{CO_2}$ ( $cm^3 g^{-1}$ )	$V_{meso}$ ( $cm^3 g^{-1}$ )	$Meso_{size}$ (nm)	C (%)	H (%)	O (%)	N (%)
PTW_<1_400°C	433	0.51	0.17	0.13	0.35	7.3	72.5	3.5	23.9	0.1
PTW_<1_700°C	624	0.53	0.24	0.24	0.29	6.5	87.6	1.8	10.5	0.1
PTW_<1_900°C	717	0.61	0.27	0.32	0.34	5.2	94.9	1.5	3.5	0.1
PTW_1_400°C	447	0.50	0.18	0.12	0.32	6.8	74.3	3.4	22.1	0.1
PTW_1_900°C	699	0.56	0.27	0.28	0.29	5.4	90.5	1.6	7.7	0.2
PTW_2_400°C	469	0.50	0.17	0.12	0.33	5.1	74.7	3.6	21.6	0.1
PTW_2_900°C	723	0.64	0.28	0.25	0.36	4.6	89.2	1.4	9.3	0.1
PTW_5_400°C	472	0.49	0.16	0.14	0.33	4.7	71.7	4.0	24.2	0.1
PTW_5_900°C	685	0.52	0.26	0.26	0.26	4.8	90.9	1.1	7.6	0.7

Fig. 93 a) to d) shows  $N_2$  adsorption isotherms depending of the pH. Nitrogen adsorption-desorption isotherms for all materials are of type I and IV, characteristic of a combination of micro-mesoporous volumes. Fig. 93 e) shows  $CO_2$  adsorption isotherms, decreasing the pH increases the amount of  $CO_2$  adsorbed at very low pressures, indicating the development of very narrow porosity. Fig. 93 f) shows the PSD calculated by the application of the DFT model to  $N_2$  and  $CO_2$  isotherms. Additionally, these PSD showed three maximums at 0.7, 2 and 8 nm. Liang and Dai (2009) studied the synthesis of bimodal meso-/microporous carbon monoliths of phloroglucinol-formaldehyde resins prepared with different copolymers, including PF127. They paid special attention to the factors significantly interfering in the phase separation such as: reaction temperature, solvent composition and polymerisation time. All these parameters are quite important during the synthesis of OMC's as well as having a homogenous phase before polymerisation occurs. It means that before the formation of the polymeric resin, the system should be completely miscible and then spinodal decomposition, a mechanism developed during the rapid demixing between non miscible liquids, is gradually developed through the polymer crosslinking reactions. Water has also a great influence on the spinodal decomposition and it was therefore excluded from the system [Liang and Dai 2009] or used in small concentrations [Constant et al. 1996]. In the case of PTW samples using 100% of water, spinodal decomposition occurred instantly. It is worth noting that, owing to the very fast phase separation observed whatever the pH, those spinodal decomposition is rather induced here by the strong interaction

between the PF127 and the tannin. This “complex” is no more soluble in water and lead to a liquid/liquid phase separation.

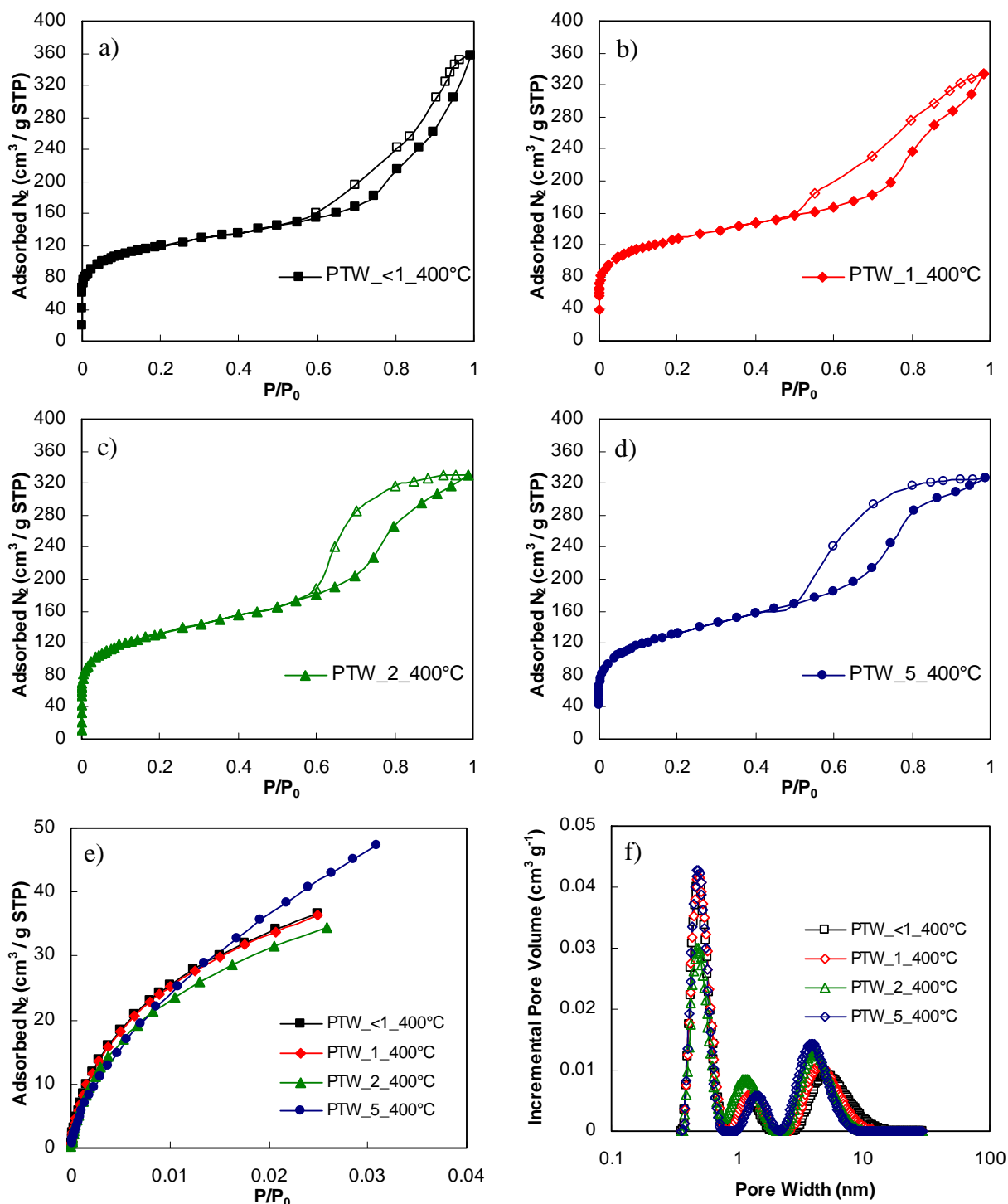


Fig. 93: a) to d) Nitrogen adsorption-desorption isotherms (full and open symbols, respectively) at  $-196^\circ C$  for different pHs; e)  $CO_2$  adsorption isotherms at  $0^\circ C$  for PTW carbon materials at different pHs after pyrolysis at  $400^\circ C$ ; and f) pore size distribution calculated by DFT model for all samples prepared at different pHs and calcined at  $400^\circ C$ .



## 6.2.2 Effect of the carbonization temperature

After a second thermal treatment at 900°C, there was an increase of the  $S_{\text{BET}}$  for all materials, the values varied from 685 to 723  $\text{m}^2 \text{g}^{-1}$ . The outstanding material presenting the most organised mesostructures had  $S_{\text{BET}}$  of 699  $\text{m}^2 \text{g}^{-1}$  obtained at pH 1. Micropore volume increased with the carbonization temperature but mesopore volume remained approximately constant around  $0.30 \pm 0.05 \text{ cm}^3 \text{g}^{-1}$ . Schlienger et al. (2012) observed the lost of mesoporosity when increasing the carbonization temperature from 400 to 850°C, which is contrary to our findings. Fig. 94 shows the TEM photos of materials prepared at pH very acidic (<1) at different temperatures of carbonization (400, 700 and 900°C). All materials seem to present a worm-like structure in all cases.

Fig. 95 a) to c) shows  $\text{N}_2$  adsorption isotherms depending of carbonization temperatures, 400, 700 and 900°C respectively. The elbows of the isotherms are shifted to higher  $\text{N}_2$  adsorbed volumes with an increase of carbonization temperature, which in an evidence of microporosity development. Fig. 95 d) shows  $\text{CO}_2$  adsorption isotherms. With increasing the carbonization temperatures, an increase of the  $\text{CO}_2$  amount adsorbed at very low pressures is observed, indicating the development of very narrow porosity. Fig. 95 e) shows the PSD calculated by the application of the DFT model to  $\text{N}_2$  and  $\text{CO}_2$  isotherms. These PSD showed three maxima when carbonization temperature was 400 or 700°C but only 2 when carbonization temperature was 900°C.

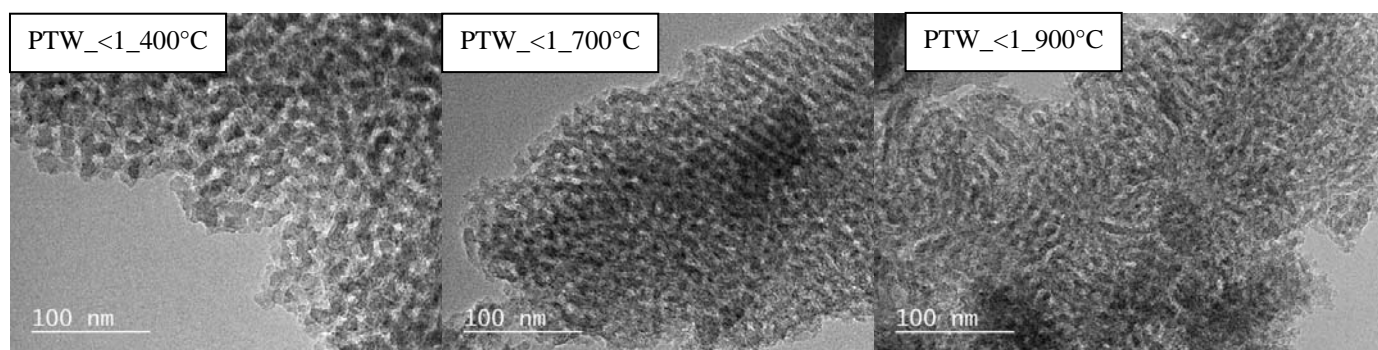


Fig. 94: TEM images of PTW samples at pH<1 synthesized after agitation, drying at 80°C and posterior pyrolysis at 400, 700 and 900°C.

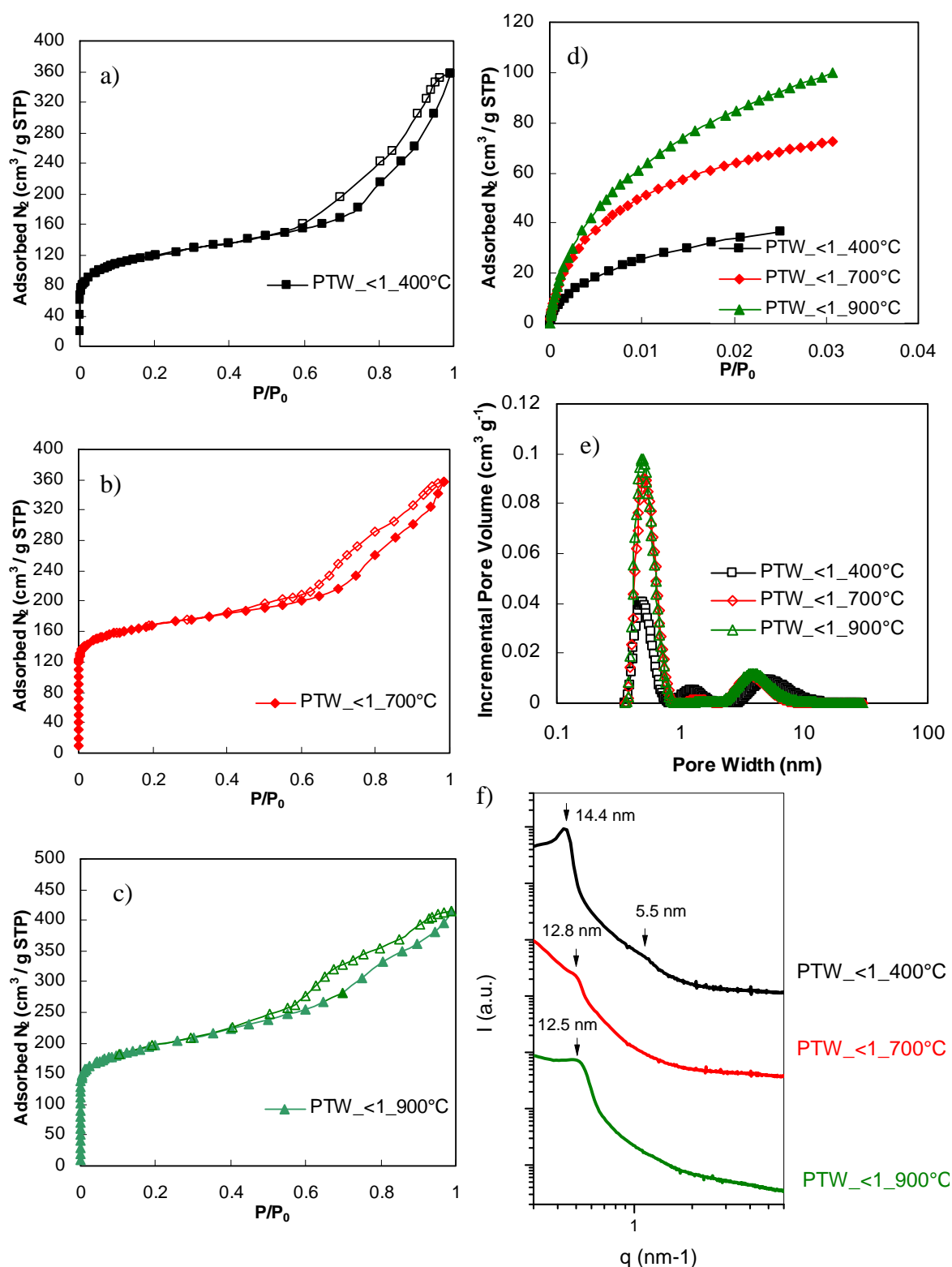


Fig. 95: a) to c) Nitrogen adsorption-desorption isotherms (full and open symbols, respectively) at -196°C; d) CO<sub>2</sub> adsorption isotherms at 0°C for PTW carbon materials at different pHs after pyrolysis; e) pore size distribution calculated by DFT model for the samples prepared at different pHs and calcined at 900°C; f) SAXS patterns for the same samples in d) and e).



After carbonization at 900°C, carbon content increased to 92 and oxygen content was reduced to 6-7% (see Table 20). Fig. 95 f) shows the SAXS diffractograms for materials synthesized at pH<1 and carbonized at 400, 700 and 900°C. At pH <1, diffractograms of OMC's obtained at 700 and 900°C showed that the materials are wormlike and the repeat distance between the pores is almost identical (12.5-12.8 nm), whereas at 400°C the material had a greater organization, which could correspond to a hexagonal structure due to the presence of two peaks at 14.4 and 5.5 nm. This long-range ordering is partly destroyed by heat-treatment at higher temperature (700 and 900°C). Materials carbonized at temperatures higher than 400°C did not show such a clear structure.  $S_{\text{BET}}$  were very similar and independent on the pH when the samples were carbonised at 400°C. Increasing the temperature, the  $S_{\text{BET}}$  was increased and a maximum was found for sample prepared and carbonised at 900°C. With the increase of the temperature, there is an increase of their volume of pores from 400 to 700 and 900°C.

Fig. 96 a) shows  $\text{N}_2$  adsorption isotherms depending of the pH for all materials pyrolysed at 900°C. Nitrogen adsorption-desorption isotherms for these materials have the same behaviour that shown in Fig. 90 for materials calcined at 400°C. Isotherms are a combination of type I and IV, characteristic of micro-mesoporous solids. As it has been mentioned before, the PSD calculated by the application of the DFT model to  $\text{N}_2$  and  $\text{CO}_2$  isotherms (Fig. 96 b)) showed two maxima (between 0.5 and 1 nm and 8 nm) when the carbonization temperature was 900°C. The peaks of SAXS showed in Fig. 96 c) are almost identical from 11.2-12.3 nm. TEM photos (Fig. 96 d) to g)) show that the materials present a wormlike structure but a more organised structure was obtained at pH 1.

In the literature, D-fructose together with F127 were submitted to HTC to produce ordered nanostructures. After carbonization at around 550°C, the surfactant was removed but limited total pore volume ( $0.14 \text{ cm}^3 \text{ g}^{-1}$ ) and surface area ( $257 \text{ m}^2 \text{ g}^{-1}$ ) were obtained [Kubo et al. 2011]. Schlienger et al. (2012) obtained materials having  $S_{\text{BET}}$  of  $534 \text{ m}^2 \text{ g}^{-1}$  and total pore volume as high as  $0.86 \text{ cm}^3 \text{ g}^{-1}$  when mixing tannin and F127 together with ethanol followed by evaporation (EISA). Our materials showed greater textural properties such as  $S_{\text{BET}}$  up to  $700 \text{ m}^2 \text{ g}^{-1}$ , mesopore volume equal to  $0.29 \text{ cm}^3 \text{ g}^{-1}$  and total pore volume equal to  $0.56 \text{ cm}^3 \text{ g}^{-1}$ , which are outstanding results when using natural phenolic precursors and only water as solvent.

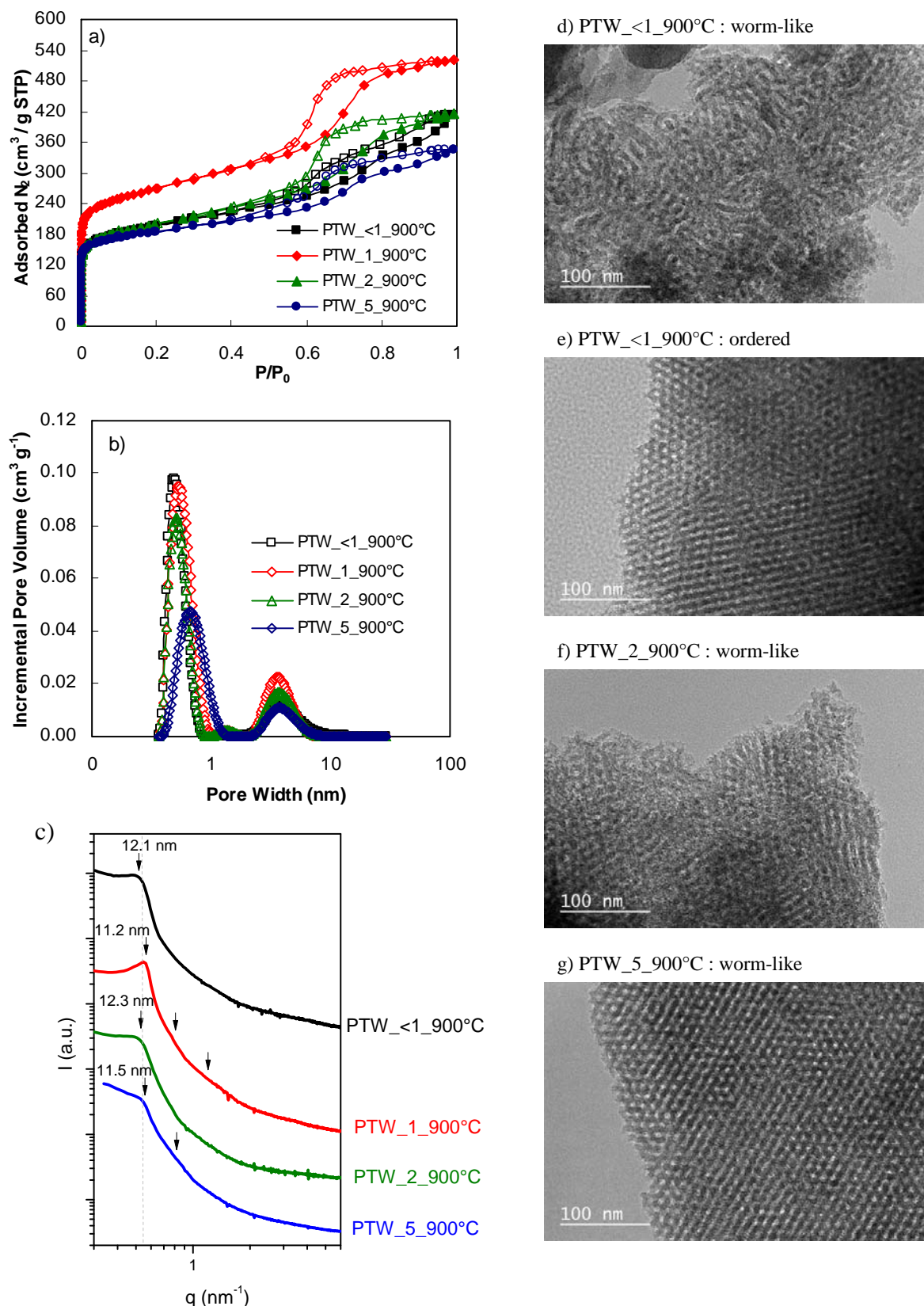


Fig. 96: a) Nitrogen adsorption-desorption isotherms (full and open symbols, respectively) at  $-196^\circ C$ ; b) pore size distribution calculated by DFT model for the samples prepared at different pHs and calcined at  $900^\circ C$ ; c) SAXS patterns for the same samples in a) and b); d) to g) TEM photos of all PTW samples after pyrolysis at  $900^\circ C$ .

Liang and Dai 2009 used phloroglucinol and formaldehyde and they got  $S_{\text{BET}}$  up to  $420 \text{ m}^2 \text{ g}^{-1}$  and total pore volume equal to  $0.56 \text{ cm}^3 \text{ g}^{-1}$ . Using a resorcinol-formaldehyde system, Wang et al. 2008 reach a  $S_{\text{BET}}$  of  $607 \text{ m}^2 \text{ g}^{-1}$  and a total pore volume of  $0.58 \text{ cm}^3 \text{ g}^{-1}$ . Huang et al. 2008 obtained materials with  $S_{\text{BET}}$  up to  $620 \text{ m}^2 \text{ g}^{-1}$  and total pore volume of  $0.36 \text{ cm}^3 \text{ g}^{-1}$  when using a phenol-formaldehyde resin as carbon precursor. Synthetic phenolic molecules are more expensive and they are non-renewable sources which are for some of them toxic or dangerous to the environment. We succeeded in producing OMC's with high surface area and mesoporosity even after carbonization at  $900^\circ\text{C}$  from bio-sourced precursor.

### 6.3 Conclusions

Ordered mesoporous carbon (OMC's) materials were successfully synthesized with a low-cost and by an eco-friendly manner. High-surface area materials were obtained by mixing tannin and a soft template, PF127, with water under agitation at room temperature ( $20^\circ\text{C}$ ) and different initial pHs. By reducing the pH of the system around one, self-assembly between surfactant and tannin seems to be optimum for the preparation of ordered mesostructures. Contrary to previous synthesis, mesoporosity is preserved after carbonization at high temperatures and narrow microporosity is developed. Highly porous materials were obtained having a  $S_{\text{BET}}$  up to  $700 \text{ m}^2 \text{ g}^{-1}$ , a total pore volume equal to  $0.56 \text{ cm}^3 \text{ g}^{-1}$  and a mesopore volume equal to  $0.29 \text{ cm}^3 \text{ g}^{-1}$ , after carbonization at  $900^\circ\text{C}$ . These OMC's, when carbonized at  $400^\circ\text{C}$ , presented an ordered hexagonal mesoporous structure which is progressively disorganized to a wormlike structure when increasing the carbonization temperature as confirmed by TEM and SAXS analysis.

## **Conclusions and Perspectives**



This PhD work focuses research on “green chemistry” field that aims to develop new processes in a sustainable manner by producing compounds or materials having similar or even enhanced properties compared to existing ones, while limiting strongly their negative impact on environment. Such new processes have also to be economically viable for being transferred at the industrial scale, so the use of low cost and largely available precursor had also to be taken into account. In this context, we have explored the high potentialities of synthesis in aqueous media including hydrothermal carbonization (HTC) and used a versatile carbon precursor, tannin, which reaches most of the expected criteria for a green and sustainable bio-sourced precursor.

The systematic study of the HTC conditions of tannin (concentration, temperature, duration) helped us to understand its behavior during this treatment and to propose original HTC synthesis that led to new hydrochars and carbon materials (after a second carbonization in inert atmosphere) with peculiar physico-chemical properties and sometimes unusual performances for specific applications. The versatility of tannin has been explored in this work mainly through its ability to undergo multi-amination reactions and also to auto-condense during HTC. The highlights concerning those two aspects are detailed bellow:

- i) According to the synthesis conditions (pH, tannin concentration, temperature), modification of the nucleation-growth mechanism led to gel or powder composed of spherical particles arranged in a necklace. They were obtained without the need of any carcinogenic cross-linker such as formaldehyde. The ability to form gel was taken into account to produce dry gels by different ways (aerogel, cryogels and xerogels) in order to get various levels of porosity and a monolithic shape for the final carbon materials.
- ii) The reactional mechanism of tannin submitted to HTC can be also modified by the addition of sucrose or  $\text{Ag}^+$  salt. Peculiar nanostructures and sometimes increased yield, could then be obtained.
- iii) Tannin contains a high portion of oxygen due to its high portion of phenolic and ether groups. After HTC, the resulting hydrochars still contain a high portion of oxygenated groups (~ 33 wt.%). These groups seems to be stabilized by the HTC since they are only removed at high temperature during a second carbonization step in inert atmosphere, generating thus a significant porosity in the microporous range without any needs of a carbon activation procedure.

iv) The polyphenolic nature of tannin can advantageously be used to deeply modify its structure by a simple contact with a concentrated ammonia solution. Reactions that take place are among others, amination reactions, rings opening and cross-linking with formation of imine bonds between flavonoid units. This modified tannin has shown a reactivity in HTC conditions that led to hydrogels or powders containing high portions of O (21.2 – 34.0 wt.%) and of N (3.3 – 13.6 wt.%) with presence of amine groups and possible pyridinic groups. Those N- groups, as shown previously for O-groups in HTC of tannin, have a strong thermal stability. One of the highest ever reported nitrogen content (8 wt.%), mainly in pyridinic form, could be obtained after a second carbonization step in inert atmosphere at high temperature 900°C. During carbonization, a high surface area is created without any activation agent.

Thanks to the interesting properties of tannin (pure and modified) and the advantages of the HTC processes, numerous interesting carbon materials were prepared after carbonization of the hydrochars at 900°C in inert atmosphere. The major development was achieved in the field of supercapacitors where the dry carbonization of N-modified tannin hydrochars led to microporous carbons with a high surface area and optimized amount of O and N heteroatoms. Outstanding capacitances were then obtained with values as high as 409 F g<sup>-1</sup> (scan rate of 2 mV s<sup>-1</sup>) for carbonized N-doped xerogels. That value was much higher than those reported for high surface area-activated carbons. The mesostructuration of those materials could even increase their performances at high scan rates.

Another interesting feature of tannin evidenced during this work is its ability of strongly interaction *via* hydrogen bonds with triblock surfactant having a hydrophilic part composed of polyethylene oxide. Their association (complexation) in water led instantaneously to a liquid/liquid phase separation. After separation and subsequent carbonization (in dry atmosphere) of the organic part, a mesostructured carbon showing mesopores arranged in a honey comb structure together with micropores were obtained. Without activation, a surface area as high as 700 m<sup>2</sup> g<sup>-1</sup> was obtained. The remarkable simplicity and low cost of this process, compared to the resulting advanced mesoporous material produced, opens many opportunities to the industrial development of such materials.

Even if a lot of work has been done on the HTC of tannin during this PhD, the potentialities of tannin treated by HTC have been only glimpsed. Indeed, many studies still remain to be done to fully explore the other multifaceted nature of tannin when used in such conditions: its reducing and/or its complexing properties have been barely approached here.

Prospective trials have shown for instance that catalytic trace of transition metal (TM) salts were able to deeply modified the mechanism of formation of hydrochars from tannin with formation of different particle morphologies (see Fig. 97). This feature associated with the complexing and reducing properties of tannin pave the way to new synthesis for the preparation of interesting porous carbon-based nanocomposites with TM at a metallic state or in the form of carbide, nitride, oxide and sulphide forms for instance. Those materials, prepared by a low cost and a green process could have potential applications in the field of electrochemical energy storage, gas storage or catalysis.

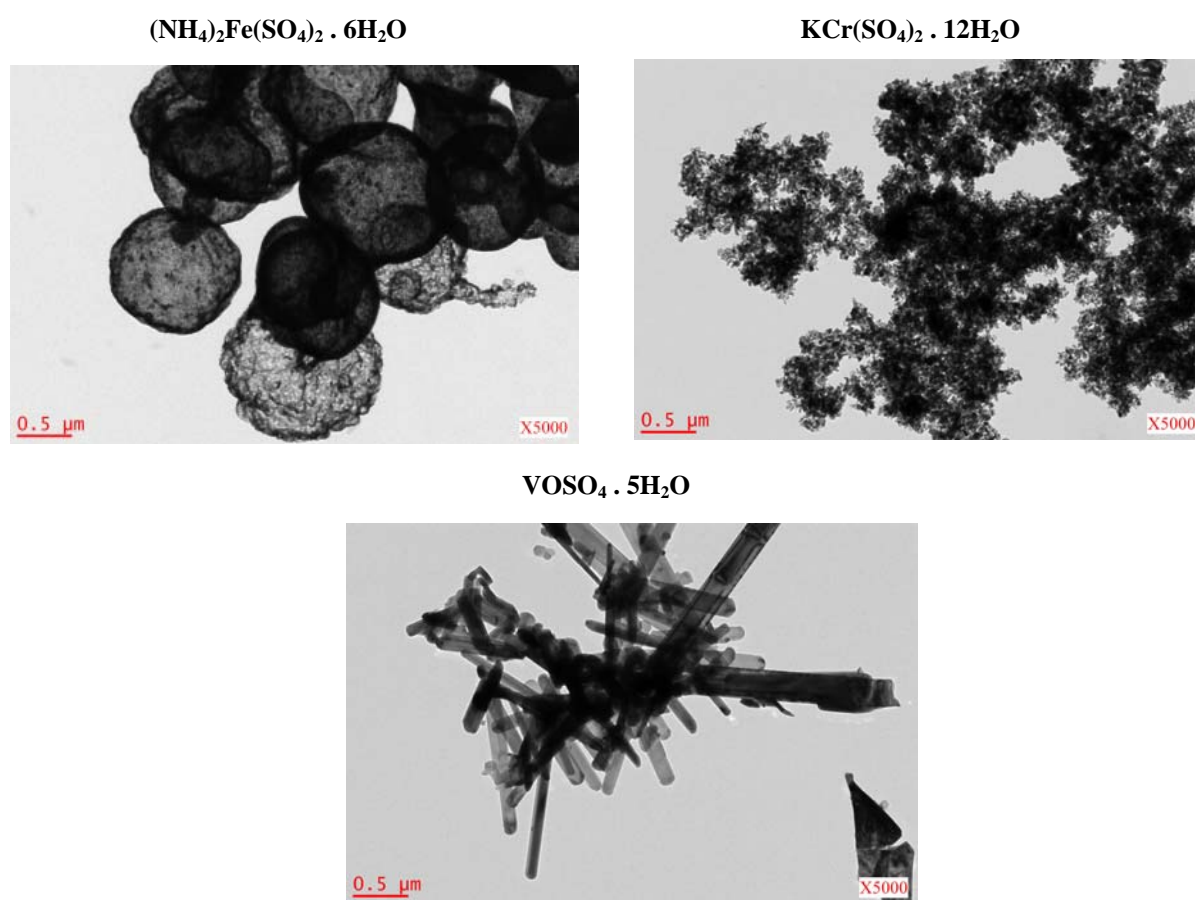


Fig. 97: Metal oxide nanoparticles made from HTC of tannin together with metal salts and oxidized in air at 550°C.





# **Annexes**



## Annex 1: Techniques of characterisation

This annex briefly describes the main experimental techniques used for the characterisation of the materials synthesised in this work. They will be divided in three: chemical, physical and electrochemical characterisation.

### A1. Chemical characterisation

#### A1.1 Elemental Analysis (EA)

Elemental analysis is a technique that provides the total content of carbon, hydrogen, nitrogen and sulfur from any organic or carbonaceous materials. The technique is based on the complete and instantaneous oxidation of the sample by combustion with oxygen excess at a temperature of approximately 1000°C. During oxydated combustion the elements C, H, N and S produce – in addition to the molecular nitrogen ( $N_2$ ) – the oxidation products  $O_2$ ,  $H_2O$ ,  $NO_x$ ,  $SO_2$  and  $SO_3$  [Speight 2005]. Two equipments were used in this work. The first one, the samples prepared were analysed through an apparatus microanalysis Thermo Flash 1112 (Fig. A1), with a detection range from 0.05% to 99.95% for determining the content of carbon, hydrogen, nitrogen and sulfur. The oxygen content was obtained by the difference with the other elements.



Thermo Flash 1112



vario El cube (Elementar)

Fig. A1: Elemental analysis equipments: Thermo Flash 1112 and vario El cube (Elementar) used in this PhD work.

The second equipment, the elemental analysis were performed using the vario EI cube equipment (Elementar) CHNS system in which the samples were submitted to a combustion in a quartz tube at 1150°C (He flow of 230 ml min<sup>-1</sup>; Oxygen (99.995%) flow of 35-38 ml min<sup>-1</sup>). After combustion, the samples were converted in a form of oxides such as: CO<sub>2</sub>, O<sub>2</sub>, H<sub>2</sub>O, NO<sub>x</sub>, SO<sub>2</sub>, SO<sub>3</sub> which were reduced to CO, H<sub>2</sub>O, N<sub>2</sub> and SO<sub>2</sub> respectively and quantified as C, H, N and S elements for each sample. The oxygen was analysed with the same equipment by pyrolysis in a quartz tube and the oxygen element was quantified by the thermal conductivity detector (TCD).

### A1.2 Mass Spectrometry - MALDI ToF

The Matrix-Assisted Laser Desorption/Ionization - Time of Flight (MALDI-ToF) spectrometry has been used since its introduction by Karas et al. (1987) for characterizing synthetic and natural polymers by assessing their molecular weight. Fig. A2 shows the schematic principle of MALDI-ToF instrument where the sample plate is irradiated with a laser pulse promoting desorption of singly charged ions matrix through high voltage acceleration region. The ions formed will be then separated in the ToF electric field and detected in a form of peaks in the ToF detector. This soft ionization technique in large part is combined with mass analyzers time of flight (ToF), which has the advantage of providing a full spectrum of an unlimited range of masses through very little amount of sample. The investigation of these materials prepared using tannin as precursor through MALDI-ToF is quite useful once tannin is a macromolecule and it was quite helpful to understand its polymerisation reactions [Pizzi and Meikleham 1995; Merlin and Pizzi 1996; Garcia and Pizzi 1998; Waver et al. 2006].

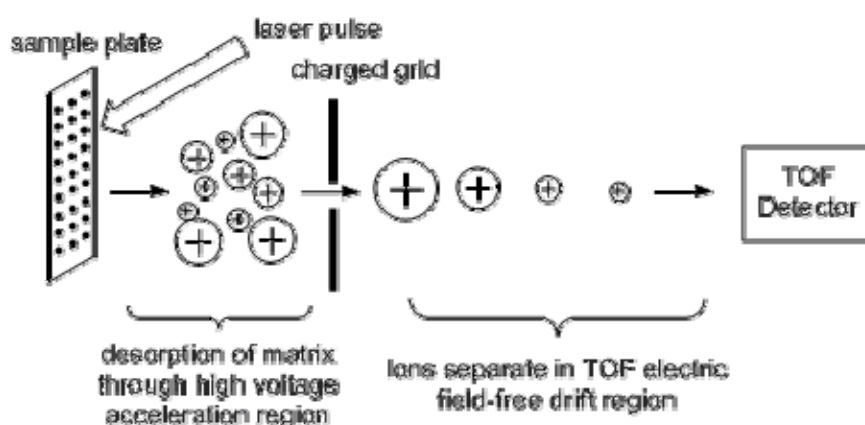


Fig. A2: Schematic principle of a MALDI-TOF instrument operation.

MALDI-ToF spectra were recorded on a Shimadzu Axima Precision instrument. 5 mg of each sample were dissolved in 1 mL of an aqueous solution acetone:water (1:1), and then mixed with a matrix, 2,5-dihydroxy benzoic acid/tetrahydrofuran. For the enhancement of ion formation, NaCl was added to the matrix and the resulting solution was placed on the MALDI target. After evaporation of the solvent, the MALDI target was introduced into the spectrometer. The irradiation source was a pulsed nitrogen laser with a wavelength of 337 nm. The length of one laser pulse was 3 ns. The measurements were carried out using the following conditions: polarity-positive, flight path-linear, mass-high (20 kV acceleration voltage), 100 – 150 pulses per spectrum. The delayed extraction technique was used applying delay times of 200 – 800 ns.

### A1.3 Nuclear Magnetic Resonance Spectroscopy (NMR) $^{13}\text{C}$

Nuclear magnetic resonance (NMR) is a method widely used for characterizing synthetic and natural materials for identifying their chemical structures giving some information of the chemical properties of atoms present within a molecule. It allows the specification of the formula and the stereochemistry of the compound. Fig. A3 shows the schematic principle of NMR functioning which is based on the information produced by the absorption of electromagnetic radiation by the nuclei of some atoms of the sample analysed. The interpretation of the signals or radio frequency (RF) generated such as position, aspect and intensity leads to a set of information giving the structural details about the sample. If the sample is a pure compound, its structure will be easier deduced [Breitmaier and Voelter 1986].

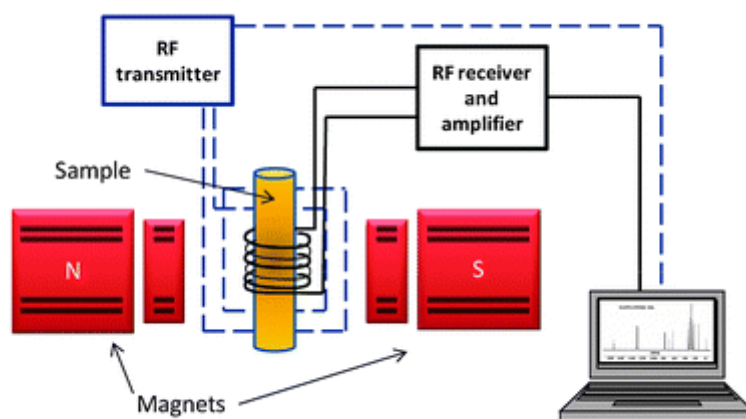


Fig. A3: Schematic principle of NMR spectroscopy.

Solid-state CP-MAS (cross-polarisation/magic angle spinning)  $^{13}\text{C}$  NMR spectra for H-T, H-AT and H-EAT were recorded on a Bruker MSL 300 FT-spectrometer at a frequency of 75.47 MHz. Chemical shifts were calculated relative to tetramethyl silane (TMS). The rotor was spun at 4 kHz on a double-bearing 7 mm Bruker probe. The spectra were acquired with 5 s recycle delays, a  $90^\circ$  pulse of 5  $\mu\text{s}$  and a contact time of 1 ms. The number of transients was 3000, and the decoupling field was 59.5 kHz.

#### A1.4 Temperature Programmed Desorption (TPD)

This method is based on monitoring and evaluating the decomposition of different oxygenated groups present on the surface of the materials with the increase of the temperature. As it can be seen in Fig. A4, the gases  $\text{CO}$  and  $\text{CO}_2$  are desorbed depending on the oxygenated groups linked into the surface of the carbon matrix. At the same time, this characterization is complex firstly because carbonyl groups, ether and quinone decompose to the same product,  $\text{CO}$  for example and secondly, the temperature of decomposition of the same type of group is not unique, it depends on their status in the graphitic sheet and the interaction with neighbouring groups [Rodriguez-Reinoso and Molina-Sabio 2004; Figueiredo et al. 2007; Shen et al. 2008].

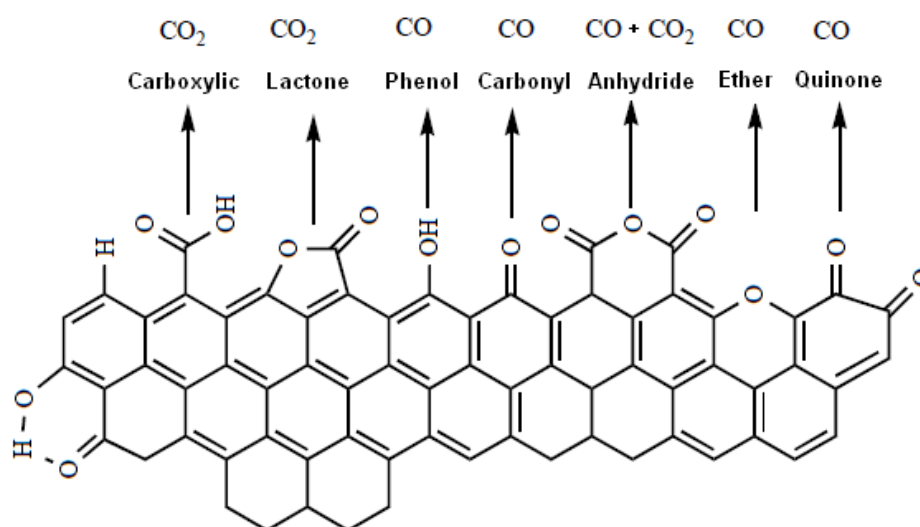


Fig. A4: The conversion of the oxygenated groups present in HTC-derived materials into  $\text{CO}$  and  $\text{CO}_2$  gases [Rodriguez-Reinoso and Molina-Sabio 2004].

TPD experiments were performed in a quartz tube placed within an electric furnace in which 0.5g of each sample was placed in a tube under argon flow of  $30 \text{ mL min}^{-1}$ . Samples were heated to  $1100^\circ\text{C}$  with a heating rate of  $10^\circ\text{C min}^{-1}$  and a mass spectrometer Pfeiffer

recorded the amounts of CO and CO<sub>2</sub> detached during the pyrolysis. Calibrations for CO and CO<sub>2</sub> gases were provided in argon.

### A1.5 Thermogravimetric Analysis (TGA)

The TGA is a method used for determining the thermal degradation of a sample or its weight loss behaviour during pyrolysis in an inert atmosphere. The loss weight of the samples is recorded as the temperature is raised at a uniform rate. According to the temperature range, different types of reactions and different materials will be released such as solvent, water and especially gases CO and CO<sub>2</sub> and/or CH<sub>4</sub> and other organic volatile gases. Between 150°C and 200°C, this range normally corresponds to the release of the remaining solvent or water formed by the condensation of -OH groups. At higher temperatures (400-500°C), the organic volatile gases are released [Job et al. 2004; Singh et al. 2012] so all of these weigh losses are recorded. For the realization of TGA experiments, a scale SDT Q600 (TA Instruments) was used. The essays were performed using N<sub>2</sub> gas as entrainment with a flow of 100 mL min<sup>-1</sup>. The amount of sample used was around 20 mg which was placed into a platinum crucible to minimize temperature gradients. The temperature was increased up to 1000°C and the heating rate applied of 20°C min<sup>-1</sup>.

### A1.6 X-ray photoelectron spectroscopy (XPS)

X-ray photoelectron spectroscopy (XPS) is used to measure the elemental composition of the surface of the materials. XPS spectra are obtained by irradiating a material with a beam of X-rays. The spectra were recorded with an ESCAPlus OMICROM system equipped with a hemispherical electron energy analyser. The spectrometer was operated at 10 kV and 15 mA, using a non-monochromatized Mg K $\alpha$  X-ray source ( $h\nu = 1253.6$  eV) under vacuum ( $< 5 \times 10^{-9}$  Torr). Analyzer pass energy of 50 and 20 eV was used for survey scans and detailed scans, respectively. The C1s peak at 284.5 eV was used for binding energy correction. A survey scan (1 sweep/200 ms dwell) was acquired between 1100 and 0 eV. Current region sweeps for N1s, O1s and C1s were obtained. The CASA data processing software allowed smoothing, Shirley type background subtraction, peak fitting and quantification.

## A2. Physical characterisation

### A2.1 Adsorption - desorption of gases

Gas adsorption measurements are used to determine the most important textural parameters characteristic of solids: the specific surface area, the total surface area of a



material per unit of mass ( $S_{\text{BET}}$  as it is called - method calculated by Brunauer, Emmett and Teller equation and normally measured in  $\text{m}^2 \text{g}^{-1}$ ) [Brunauer et al. 1938] and the pore size distribution of these solid materials. From the adsorption of  $\text{N}_2$  and Kr at  $-196.5^\circ\text{C}$  and  $\text{CO}_2$  at  $0^\circ\text{C}$ , it is possible to understand the porous texture [Garrido et al. 1987; Rodriguez-Reinoso and Linares-Solano 1989; Lozano-Castello et al. 2002]. It is therefore particularly well suited for studying the textural properties of high porous HTC-derived carbon materials. For samples that showed a very low specific surface area, Kr was used as a probe molecule instead of nitrogen to obtain the most accurate results. Therefore,  $S_{\text{BET}}$  was determined by Kr adsorption for organic samples or samples made after HTC having very lower porosity which were degassed for 48h under vacuum at  $60^\circ\text{C}$  before analysis. Gels and carbon materials made after HTC and pyrolysis respectively, were degassed for 48h at  $270^\circ\text{C}$ . The adsorption-desorption of nitrogen was carried out using a Micromeritics ASAP 2020 automatic apparatus (Fig. A5). Micromeritics ASAP 2420 apparatus was used for obtaining  $\text{CO}_2$  adsorption (for assessing microporosity) and Kr adsorption.  $\text{CO}_2$  and  $\text{N}_2$  adsorption isotherms were used to determine the PSD by utilizing the AERIUS® software provided by Micromeritics, which allows obtaining a only PSD from the two isotherms.

From the modelling isotherms obtained (see Fig. 14, Chapter 1) between relative pressures typical between  $10^{-7}$  and 0.99, the following parameters were determined:

- Specific surface area ( $S_{\text{BET}}$  ( $\text{m}^2 \text{g}^{-1}$ ): the total surface of the cavities of a porous material calculated from the Brunauer - Emmett - Teller (BET) [Brunauer et al. 1938] at a relative pressure of  $P/P_0$  between 0.01 – 0.05. Owing to the simultaneous presence of micropores and mesopores, the selected domain emphasis rather the contribution of the surface area of the micropores and the  $S_{\text{BET}}$  values are only indicative. In this case, surface area  $S_{\text{DFT}}$  determined by the DFT method [Tarazona 1995] was also measured considering a slit-like pore geometry.
- The total pore volume ( $V_{\text{T}}$  ( $\text{cm}^3 \text{g}^{-1}$ ): the volume is calculated by the nitrogen adsorption up to relative pressure  $P/P_0 = 0.99$  [Gregg and Sing 1991], 0.97 or 0.95 [Gregg and Sing 1982] according to the shape of the isotherm;
- Micropore volume ( $V_{\mu}$  or  $V_{\text{CO}_2}$  ( $\text{cm}^3 \text{g}^{-1}$ ): calculated by the equation of Dubinin-Radushkevich (DR) [Dubinin 1989] at  $P/P_0$  between 0.009 till 0.0007;
- Pore size distribution (DFT): calculated from DFT (Density Functional Theory) method for isotherms type I [Tarazona 1995];

- Pore size distribution (BJH): calculated from BJH (Barret, Joyner and Halenda) method from the desorption branch isotherms type IV [Barret et al. 1951];
- Mesopore volume ( $V_m$  ( $\text{cm}^3 \text{g}^{-1}$ )): calculated as the difference  $V_T - V_\mu$ .



Fig. A5: Micromeritics ASAP 2020 instrument used for the adsorption-desorption experiments.

## A2.2 Scanning and Transmission Electron Microscopy (SEM and TEM)

Light scanning electron microscopy (SEM) is undoubtedly the most widely used of all electron beam instruments. SEM is a method used for producing images of the surface of a sample with a wide range of magnifications, which varies from 5 to 500000 x giving access to nearly nanometer dimensions. SEM shows only the morphology of samples and their preparation is much simpler allowing a large amount of them to be analysed at a time. The HTC-derived materials and carbons were observed at various magnifications by a SEM (FEI-Quanta 400) with or without metallization. SEM microscopy has several features accountable for its popularity, such as the versatility of its various modes of imaging, the excellent spatial resolution now achievable, the very simple sample preparation and condition, and the relatively straightforward interpretation of the acquired images.

Transmission electron microscopy (TEM) is a technique in which an electron beam passes through a very thin sample and provides the details about its internal composition. The image resolution is much better and can reach  $10^{-2}$  nm. The sample in TEM has to be cut thinner and only a small amount of sample can be analysed at a time. The images show its morphology, crystallization or even about magnetic domains. Viewing TEM samples was performed with a FEI-Philips microscopy CM200 at a voltage of 200 kV. They were ground and then dispersed in chloroform by sonication. A drop of the dispersion was laid down on a TEM grid and dried before observation. As a result of elastic scattering of electrons by atoms of the sample, backscattered electrons (BSE) are emitted. The ability of sample atoms to scatter electrons principally depends on their atomic number  $Z$  and increases with it. Difference in  $Z$ , and hence in composition, gives visible BSE image contrast, areas of lower atomic numbers being darker, and vice-versa.

### A2.3 Small Angle X-rays Scattering (SAXS)

SAXS (the "SAXSess mc2" equipment) is a small-angle scattering technique used for studying the structural determination of colloidal systems (i.e. micelles, microemulsions, emulsions, liquid crystals, vesicles, liposomes) and nanostructured materials (i.e. mesoporous nanoparticles). It is equipped with a X-ray tube and a copper anode collinearly adjusted having two dispositives of detection: i) a CCD camera (24x24 pixel  $\mu\text{m}^2$ ) allowing to perform measurements at small angles (range of wave vectors ( $q$ ) from 0.04 to 6  $\text{nm}^{-1}$ ) to highlight the nanoscale sample' structure; ii) a flat image which can be scanned from small to large wave vectors ( $q$ ) from 0.04  $\text{nm}^{-1}$  to 27  $\text{nm}^{-1}$ , corresponding to dimensions of 0.2 nm to 150 nm, and thus to provide simultaneously information ranging from the nanoscale to the atomic scale of the system. This angular range contains information about the shape and size of the materials, characteristic distances of partially ordered materials, pore sizes, among others.

The samples were placed in a solid support, either in a cell for solids or in a capillary in quartz for liquids, before being introduced into the sample holder at temperature controlled in a range from -30 to 120°C and exposed to X-rays for a period of typically from 5 minutes to 1 hour, depending on the nature of the sample. The scattering spectra obtained can then be analyzed by the method of Generalized Indirect Fourier Transformation (GIFT) in order to obtain the structural parameters of the particle (size, shape) or the interfacial film.

## A2.4 Determination of the skeletal density and the particle size

Helium pycnometer was used for determining the skeletal density of HTC-derived materials and carbons. Fig. A6 shows the differences between the bulk, the skeletal and the pore volumes. Most of the samples synthesized after HTC and pyrolysis did not present an homogeneous structure. Some of them were powder and the others had an homogenous monolithic shape presenting some cracks therein due to the temperature and pressure generated by the method of HTC and therefore, the bulk density was not measured. The true or skeletal density  $\rho_s$  ( $\text{g cm}^{-3}$ ) was obtained with a helium pycnometer AccuPyc II 1340 (Micromeritics, USA). The samples were previously ground in an agate mortar to avoid any error related to closed porosity and then the powder was dried at  $80^\circ\text{C}$  under vacuum overnight. The powder was then placed in a standard chamber of  $1 \text{ cm}^3$  and the variation of helium pressure was measured with high accuracy including 10 helium flushes in order to clean the volume chamber removing contaminants and gases that could eventually be found on the surface of the sample or in the room and then 50 analytical runs. The particle size of the spherical microspheres of HTC-derived materials was measured using the equation (A1). The equivalent average diameters,  $d$  ( $\mu\text{m}$ ) of hydrothermal carbon particles assumed to be non-porous were estimated according to Rouquerol et al. (1999):

$$d = \frac{6}{\rho_s S_{BET}} \quad (\text{A1})$$

In a few cases for which the particles were almost spherical, the average sizes could be also measured using the Image Pro-Plus 6.0 software applied to TEM images. Particle size was also determined with a Beckman Coulter LS 13 320 apparatus equipped with a Universal Liquid Module, and using calculations from  $0.040 \mu\text{m}$  to  $2000 \mu\text{m}$  and Fraunhofer optical model. A small amount of sample was dispersed in water, to which a drop of a silicon surfactant was added for avoiding particle agglomeration. Then, the suspension was introduced in the universal liquid (water) module of the apparatus.

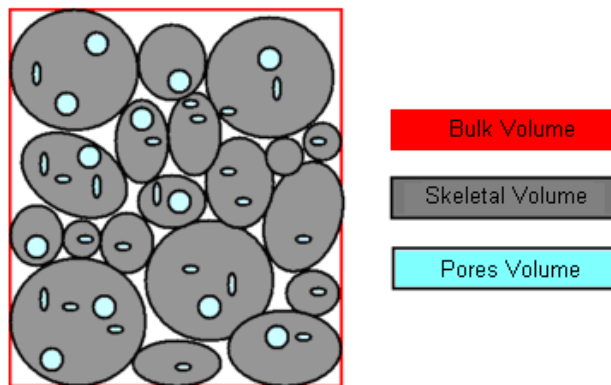


Fig. A6: Definition of bulk, skeletal and pore volumes.

### A3. Electrochemical characterization

#### A3.1 Electrical Double-Layer Capacitors (EDLC)

The electrochemical properties of HTC-derived materials and carbon gels were determined only in terms of capacity of the electric double - layer that develops at the interface electrode / electrolyte. Porous electrodes were prepared by pressing together a mixture of 75 wt. % of finely ground pyrolysed hydrothermal carbon, 5 wt. % of acetylene black and 20 wt. % of polyvinylidene fluoride (PVDF, Sigma Aldrich) used as binder. The as-prepared pellets were investigated with a typical three-electrode configuration using a Teflon Swagelok<sup>®</sup> cell working at room temperature (Fig. 70, Chapter 4). The positive and negative electrodes of identical mass, ranging from 10.0 to 18.0 mg, were electrically isolated by a glassy fibrous paper separator. The Teflon Swagelok<sup>®</sup> cell was finally filled with 4 mol L<sup>-1</sup> H<sub>2</sub>SO<sub>4</sub> aqueous solution. The reference electrode was Ag/AgCl (KCl saturated). The electrochemical characterizations were performed by cyclic voltammetry (Biologic VSP potentiostat), and the voltammograms were obtained within the range 0.05 – 1.05V versus reference electrode at scan rates ranging from 2 to 50 mV s<sup>-1</sup>. The specific capacitance of the carbon material,  $C$  (F g<sup>-1</sup>), was calculated as:

$$C = \frac{2 I}{m s} \quad (\text{A2})$$

where  $I$  is the current (A) taken at 0.55 V in the third measurement cycle,  $m$  is the mass of active material in the electrode (g), and  $s$  is the scan rate (V s<sup>-1</sup>).

## Annex 2: Published materials

This annex includes all of the work that was published and presented before and after the thesis from 2002 till 2014. Most of the work published was related to materials made with tannin as precursor such as foams, gels and hydrothermal carbon materials. The published materials and presentations made or submitted or being written during this thesis are highlighted in green.

### A2.1 List of Publications in scientific journals:

1. Braghiroli FL, Fierro V, Izquierdo MT, Parmentier J, Celzard A. Carbons produced from tannin/sucrose system through two steps: Hydrothermal Carbonization (HTC) and pyrolysis at 900°C; in preparation.
2. Braghiroli FL, Fierro V, Izquierdo MT, Parmentier J, Celzard A. Carbons produced from tannin by alteration of the HTC reactional environment: addition of H<sup>+</sup>, sucrose and Ag<sup>+</sup>; in preparation.
3. Braghiroli FL, Fierro V, Pasc A, Parmentier J, Celzard A. Low-cost and eco-friendly synthesis of ordered porous carbon materials by a soft-templating route using tannin as a carbon precursor; in preparation.
4. Hawelek L, Balin K, Szade J, Braghiroli FL, Fierro V, Celzard A, Burian A. Conversion of natural tannin to hydrothermal and graphene-like carbons studied by wide-angle X-ray scattering; Carbon 2014; submitted.
5. Braghiroli FL, Fierro V, Szczurek A, Stein N, Parmentier J, Celzard A. Hydrothermally-treated aminated tannin as precursor of N-doped carbon gels for supercapacitors. Carbon 2014; submitted.
6. Braghiroli FL, Fierro V, Szczurek A, Stein N, Parmentier J, Celzard A. Electrochemical performances of hydrothermal tannin-based carbons doped with nitrogen. Ind Crop Prod 2015; accepted.
7. Braghiroli FL, Fierro V, Izquierdo MT, Parmentier J, Pizzi A, Delmotte L, Fioux P, Celzard A. High surface - highly N-doped carbons from hydrothermally-treated tannin. Ind Crop Prod 2015;66:282-290.
8. Braghiroli FL, Fierro V, Izquierdo MT, Parmentier J, Pizzi A, Celzard A. Kinetics of the hydrothermal treatment of tannin for producing carbonaceous microspheres. Bioresource Technol 2014;151:271-277.
9. Braghiroli F, Fierro V, Pizzi A, Rode K, Radke W, Delmotte L, Parmentier J, Celzard, A. Reaction of condensed tannins with ammonia. Ind Crop Prod 2013;44:330-5.
10. Toniazzo L, Fierro V, Braghiroli FL, Amaral G, Celzard A. Biosorption of model pollutants in liquid phase on raw and modified rice husks. J Phys: Conf Ser 2013;416:1-5.
11. Celzard A, Fierro V, Amaral-Labat G, Szczurek A, Braghiroli F, Parmentier J, Pizzi A, Grishechko LI, Kuznetsov BN. Carbon gels derived from natural resources. Bol Grupo Español Carbon 2012;26:2-7.

12. [Braghiroli F.L.](#), Fierro V, Izquierdo MT, Parmentier J, Pizzi A, Celzard, A. Nitrogen-doped carbon materials produced from hydrothermally treated tannin. *Carbon* 2012;50(15):5411–20.

13. Li X, Basso MC, [Braghiroli FL](#), Fierro V, Pizzi A, Celzard A. Tailoring the structure of cellular vitreous carbon foams. *Carbon* 2012;50:2026-2036.

14. [Braghiroli FL](#), Barboza JCS, Serra AA. Sonochemical epoxidation of cyclohexene in R–CN/H<sub>2</sub>O<sub>2</sub> system. *Ultrason Sonochem* 2006;13(5):443-445.

## **A2.2 Articles in Conference**

1. [Braghiroli FL](#), Zhao W, Celzard A, Fierro V. Rice husk activated carbons for the removal of model pollutants in liquid phase: batch and continuous experiments. Proceedings of the International Conference Carbon - 2011, Shangai (China), 24 – 29 July 2011.

## **A2.3 Oral Communications**

1. Fierro V, [Braghiroli FL](#), Celzard A, Vidal L, Parmentier J. (oral presentation). One-pot hydrothermal synthesis of ordered porous carbon materials from tannin. International Conference on Electron Microscopy and XXXV Annual Meeting of the Electron Microscope Society of India (EMSI), Delhi, India, 09-11 2014.

2. Fierro V, [Braghiroli FL](#), Celzard A, Parmentier J, Izquierdo MT. (oral presentation). Optimisation of one-pot process conditions to obtain highly N-doped carbon materials from tannins. International Conference Carbon'13, Rio de Janeiro, Brazil, 14-19 July 2013.

3. [Braghiroli FL](#), Fierro V, Izquierdo MT, Parmentier J, Pizzi A, Celzard, A. (oral presentation) Traitement hydrothermal du tannin pour produire des matériaux carbonés poreux. Journées Scientifiques du Groupe Français d'Étude des Carbones: GFEC 2013, Voreppe, France 13 – 16 May 2013.

4. [Braghiroli FL](#), Barboza JCS, Serra AA. (oral presentation) Reação de epoxidação sob influência de ondas ultrassônicas: substituição de solvente orgânico por água. VII Encontro de Iniciação Científica - UNITAU – Taubaté, Brazil, 2003.

5. [Braghiroli FL](#), Barboza JCS, Serra AA. (oral presentation) Estudo do efeito de ondas ultrassônicas em reações de epoxidação em meio aquoso empregando Cl<sub>3</sub>CCN/H<sub>2</sub>O<sub>2</sub>/KHCO<sub>3</sub>. VII Encontro de Iniciação Científica - UNIVAP – São José dos Campos, Brazil, 2003.

6. [Braghiroli FL](#), Barboza JCS, Serra AA. (oral presentation) Estudo do efeito de ondas ultrassônicas em reações de epoxidação em meio aquoso empregando R-CN/H<sub>2</sub>O<sub>2</sub>/KHCO<sub>3</sub>. Iniciação Científica - SEQVAP – USP – Lorena, Brazil, 2002.

## **A2.4 Communications by Poster**

1. Fierro V, Amaral-Labat G, [Braghiroli FL](#), Szczurek A, Grischechko LI, Pizzi A, Celzard A. (poster) Versatility of tannins as precursors of new carbon materials. 8<sup>th</sup> Japanese-French Frontiers of Science symposium (JFFoS), Metz, France, 23-27 January 2014.

2. Braghiroli FL, Fierro V, Izquierdo MT, Parmentier J, Pizzi A, Celzard, A. (poster) Two strategies to prepare N-doped carbons from tannins by Hydrothermal Carbonisation (HTC). International Conference Carbon'13, Rio de Janeiro, Brazil, 14-19 July 2013.
3. Braghiroli FL, Fierro V, Amaral-Labat G, Celzard A. (poster) Biosorption of methylene blue in liquid phase on raw and modified rice husks. Woodchem 2011, Strasbourg, France, 1 – 2 December 2011.
4. Braghiroli FL, Zhao W, Celzard A, Fierro V. (poster) Rice husk activated carbons for the removal of model pollutants in liquid phase: batch and continuous experiments". International Conference Carbon '11, Shanghai, China, 24 – 29 July 2011.
5. Braghiroli FL, Fierro V, Zhao W, Amaral-Labat G, Celzard A. (poster) Adsorption de polluants en phase aqueuse par un charbon actif produit à partir d'écorces de riz. Journées Scientifiques du Groupe Français d'Étude des Carbones : GFEC 2011, Orbey, Haut-Rhin, 4 – 7 April 2011.
6. Toniazzi L, Fierro V, Braghiroli FL, Amaral G, Celzard A. (poster) Biosorption of model pollutants in liquid phase on raw and modified rice husks". IV France – Russia. Conference NAMES'10 (New Achievements in Materials and Environmental Science), Nancy, France, 26-29 October 2010.
7. Braghiroli FL, Barboza JCS, Serra AA. (poster) Epoxidação sob sonicação em presença do ácido benzoperoxidocarboximídico preparado in situ. 3º Congresso Nacional de Iniciação Científica (CONIC/SEMESP) – São Paulo, Brazil, 2003.





## **Bibliography**



- Abdullah MO, Tan IAW, Lim LS. Automobile adsorption air-conditioning system using oil palm biomass-based activated carbon: A review. *Renewable and Sustainable Energy Reviews* 2011;15:2061-2072.
- Achaw OW. A study of the porosity of activated carbons using the scanning electron microscope. In: Kazmiruk V, editor. *Scanning Electron Microscopy, InTech*; 2012, p. 473-490.
- Aegerter MA, Leventis N, Koebel MM. *Aerogels Handbook. Advances in sol-gel derived materials and technologies*. New York: Springer-Verlag; 2011.
- Akperov OG, Dzhafarova EA, Tairov SA. The kinetics of polycondensation of 9-bromofluorene in the molten state. *Polym Sci USSR* 1974;16:2016-2019.
- Albers P, Deller K, Despeyroux BM, Schäfer A, Seibold K. XPS-SIMS study on the surface chemistry of commercially available activated carbons used as catalyst supports. *J Catal* 1992;133(2):467-478.
- Al-Muhtaseb SA, Ritter JA. Preparation and properties of resorcinol–formaldehyde organic and carbon gels. *Adv Mater* 2003;15(2):101-114.
- Amaral-Labat G, Grishechko LI, Szczurek A, Fierro V, Pizzi A, Kuznetsov BN, Celzard A. Highly mesoporous organic aerogels derived from soy and tannin. *Green Chem* 2012a;14(11):3099-3106.
- Amaral-Labat G, Szczurek A, Fierro V, Stein N, Boulanger C, Pizzi A, Celzard A. Pore structure and electrochemical performances of tannin-based carbon cryogels. *Biomass Bioenerg* 2012b;39:274-282.
- Amaral-Labat G. Gels poreux biosourcés : production, caractérisation et applications. Université de Lorraine, France, PhD thesis, 2013.
- Amaral-Labat G, Grishechko LI, Fierro V, Kuznetsov BN, Pizzi A, Celzard A. Tannin-based xerogels with distinctive porous structure. *Biomass Bioenerg* 2013;56:437-445.
- Antal MJ, Mok WSL. Mechanism of formation of 5-(hydroxymethyl)-2-furaldehyde from d-fructose and sucrose. *Carbohydr Res* 1990;199(1):91-109.
- Antonietti M, Titirici MM. Coal from carbohydrates: The "chimie douce" of carbon. *Comptes Rendus Chimie* 2010;13:167-173.
- Aron PM, Kennedy JA. Flavan-3-ols: nature, occurrence and biological activity. *Mol Nutr Food Res* 2007;52(1):79-104.
- Asghari FS, Yoshida H. Acid-catalyzed production of 5-hydroxymethyl furfural from d-fructose in subcritical water. *Ind Eng Chem Res* 2006;45(7):2163-2173.
- Babel K, Jurewicz K. KOH activated carbon fabrics as supercapacitor material. *J Phy Chem Solids* 2004;65:275-280.
- Babic B, Kaluderovic B, Vracar L, Krstajic N. Characterization of carbon cryogel synthesized by sol-gel polycondensation and freeze-drying. *Carbon* 2004;42(12-13):2617-2624.

- Baccile N, Laurent G, Babonneau F, Fayon F, Titirici MM, Antonietti M. Structural characterisation of hydrothermal carbon spheres by advanced solid-state MAS  $^{13}\text{C}$  NMR investigations. *J Phys Chem C* 2009;113:9644-9654.
- Baccile N, Antonietti M, Titirici MM. One-step hydrothermal synthesis of nitrogen-doped nanocarbons: albumine directing the carbonization of glucose. *ChemSusChem* 2010;3(2):246-253.
- Baccile N, Laurent G, Coelho C, Babonneau F, Zhao L, Titirici MM. Structural insights on nitrogen-containing hydrothermal carbon using solid-state Magic angle spinning  $^{13}\text{C}$  and  $^{15}\text{N}$  nuclear magnetic resonance. *J Phys Chem* 2011;115(18):8976-8982.
- Baetens R, Jelle BP, Gustavsen A. Aerogel insulation for building applications: A state-of-the-art review. *Energ Buildings* 2011;43(4):761-769.
- Balat M, Balat M, Kırtay E, Balat H. Main routes for the thermo-conversion of biomass into fuels and chemicals. Part 1: Pyrolysis systems. *Energ Convers Manage* 2009;50(12):3147-3157.
- Barbehenn RV, Constabel CP. Tannins in plant - herbivore interactions. *Phytochemistry* 2011;72(13):1551-1565.
- Barin GB, Gimenez IF, Costa LP, Filho ATGS, Barreto LS. Hollow carbon nanostructures obtained from hydrothermal carbonization of lignocellulosic biomass. *J Mater Sci* 2014;49(2):665-672.
- Barret EP, Joyner LG, Halenda PP. The determination of pore volume and area distributions in porous substances. Computations from nitrogen isotherms. *J Am Chem Soc* 1951;73:373-380.
- Basu P. Biomass gasification and pyrolysis - Practical design and theory. Elsevier; 2010.
- Bauer I. Process for the hydrothermal carbonization of biological material and use of the obtained water for fermentation. EP patent 2640812 A1, 2013.
- Bej B, Basu RK, Ash SN. Kinetic studies on acid catalysed hydrolysis of starch. *JSIR* 2008;67(4):295-298.
- Berge ND, Ro KS, Mao J, Flora JRV, Chappell MA, Bae S. Hydrothermal carbonization of municipal waste streams. *Environ Sci Technol* 2011;45(13):5696-5703.
- Bergius F. *Zeitschrift für Komprimierte und Flüssige Gase*. 1915, p. 17.
- Bergius F. Beiträge zur Theorie der Kohleentstehung. *Naturwissenschaften* 1928;16:1-10.
- Berl E, Schmidt A. Über das Verhalten der Cellulose bei der Druckerhitzung mit Wasser. *Justus Liebigs Ann Chem* 1928;461(1):192-220.
- Berl E, Schmidt A, Koch H. Über die Entstehung der Kohlen. *Angew Chem* 1932;45:517-519.
- Bimer J, Salbut PD, Berlozecki S, Boudou JP, Broniek E, Siemieniowska T. Modified active carbons from precursors enriched with nitrogen functions: sulphur removal capabilities. *Fuel* 1998;77(16):519-525.
- Biniak S, Szymański G, Siedlewski J, Świątkowski A. The characterization of activated carbons with oxygen and nitrogen surface groups. *Carbon* 1997;35(12):1799-1810.

- Bobleter O, Bonn G. The hydrothermolysis of cellobiose and its reaction-product d-glucose. *Carbohydr Res* 1983;124(2):185-193.
- Bonn G, Bobleter O. Determination of the hydrothermal degradation products of D-(U-14C) glucose and D-(U-14C) fructose. *JRNC* 1983;79(2):171-177.
- Breitmaier E, Voelter W. Carbon-13 Nmr spectroscopy: High-resolution methods and applications in organic chemistry and biochemistry. Wiley-VCH; 1986.
- Brinker CJ, Scherer GW. Sol – gel science. The physics and chemistry of sol–gel processing. Academic Press Inc.; 1990.
- Brun N, Garcia-González CA, Smirnova I, Titirici MM. Hydrothermal synthesis of highly porous carbon monoliths from carbohydrates and phloroglucinol. *RSC Advances* 2013a;3:17088-17096.
- Brun N, Wohlgemuth SA, Osiceanu P, Titirici MM. Original design of nitrogen-doped carbon aerogels from sustainable precursors: application as metal-free oxygen reduction catalysts. *Green Chem* 2013b;15:2514-2524.
- Brunauer S, Emmet PH, Teller E. Adsorption of gases in multimolecular layers. *J Am Chem Soc* 1938;60:309-319.
- Bruno MM, Cotella NG, Miras MC, Koch T, Seidler S, Barbero C. Characterization of monolithic porous carbon prepared from resorcinol/formaldehyde gels with cationic surfactant. *Colloid Surface A* 2010;358:13-20.
- Budarin VL, Clark JH, Hardy JJE, Luque R, Milkowski K, Tavener SJ, Wilson AJ. Starbons: New starch-derived mesoporous carbonaceous materials with tunable properties. *Angew Chem Int Ed* 2006;45(23): 3782-3786.
- Budarin VL, Clark JH, Luque R, Macquarrie DJ, White RJ. Palladium nanoparticles on polysaccharide-derived mesoporous materials and their catalytic performance in C–C coupling reactions. *Green Chem* 2008;10:382-387.
- Bulut E, Özacar M. Rapid, facile synthesis of silver nanostructure using hydrolyzable tannin. *Ind Eng Chem Res* 2009;48(12):5686-5690.
- Burchell TD. Carbon Materials for Advanced Technologies. Kidlington: Elsevier; 1999.
- Cagniant D, Magri P, Gruber R, Berlozecki S, Salbut PD, Bimer J, Nansé G. Ammoxidation of cellulose - a structural study. *J Anal Appl Pyrol* 2002;65:1-23.
- Castillo F, Hernández D, Gallegos G, Rodríguez R, Aguilar CN. Antifungal properties of bioactive compounds from plants. In: Dhanasekaran D, Thajuddin N, Panneerselvam A, editors. *Fungicides for Plant and Animal Diseases*, InTech; 2012, p. 81-106.
- Celzard A, Fierro V, Marêché JF, Furdin G. Advanced Preparative Strategies for Activated Carbons Designed for the Adsorptive Storage of Hydrogen. *Adsorpt Sci Technol* 2007;25(3):129-142.
- Celzard A, Fierro V, Amaral-Labat G, Szczurek A, Braghiroli F, Parmentier J, Pizzi A, Grishechko LI, Kuznetsov BN. Carbon gels derived from natural resources. *Boletín del Grupo Español del Carbon* 2012;26:2-7.

- Chang H, Joo SH, Pak C. Synthesis and characterization of mesoporous carbon for fuel cell applications. *J Mater Chem* 2007;17:3078-3088.
- Chen Z, Ma L, Li J, Geng J, Song Q, Liu J, Wang C, Wang H, Li J, Qin Z, Li S. Simple approach to carboxyl-rich materials through low-temperature heat treatment of hydrothermal carbon in air. *Appl Surf Sci* 2011;257(20):8686-8691.
- Cherubini F. The biorefinery concept: Using biomass instead of oil for producing energy and chemicals. *Energy Convers Manage* 2010;51(7):1412-1421.
- Chesebrough RA. Improvement in products from petroleum. Letters Patent 127568, 1872.
- Child M. Industrial - scale hydrothermal carbonization of waste sludge materials for fuel production. Lappeenranta University of Technology, Finland, Master of Science Thesis, 2014.
- Chow S. Thermal reactions and industrial uses of bark. *Fall* 1972;4(3):130-138.
- Cleaner Production Germany; Available at: <http://www.cleaner-production.de/en.html> [Accessed 7 Oct. 2014].
- Constant KP, Lee J-R, Chiang Y-M. Microstructure development in furfuryl resin-derived microporous glassy carbons. *J Mater Res* 1996;11(9):2338-2345.
- Conway BE, Birss V, Wojtowicz J. The role and utilization of pseudocapacitance for energy storage by supercapacitors. *J Power Sources* 1997;66(1-2):1-14.
- Conway BE, Pell WG. Double-layer and pseudocapacitance types of electrochemical capacitors and their applications to the development of hybrid devices. *J Solid State Electrochem* 2003;7:637-644.
- Côté WA. Chemical composition of wood. In: Kollmann FFP, Côté WA, editors. *Principles of wood science and technology, I Solid Wood*, Springer-Verlag; 1968; p. 55-78.
- Cowlard FC, Lewis JC. Vitreous carbon – A new form of carbon. *J Mater Sci* 1967;2(6):507-512.
- Cui X, Antonietti M, Yu SH. Structural effects of iron oxide nanoparticles and iron ions on the hydrothermal carbonization of starch and rice carbohydrates. *Small* 2006;2(6):756-759.
- Czakkel O, Marthi K, Geissler E, László K. Influence of drying on the morphology of resorcinol-formaldehyde-based carbon gels. *Microporous Mesoporous Mater* 2005;86(1-3):124-133.
- Dai M, Song L, LaBelle JT, Vogt BD. Ordered Mesoporous Carbon Composite Films Containing Cobalt Oxide and Vanadia for Electrochemical Applications. *Chem Mat* 2011;23(11):2869-2878.
- Dalahmeh SS, Pell M, Vinneras B, Hylander LD, Oborn I, Jonsson H. Efficiency of bark, activated charcoal, foam and sand filters in reducing pollutants in gray water. *Water Air Soil Poll* 2012;223(7):3657-3671.
- Damartzis T, Vamvuka D, Sfakiotakis S, Zabaniotou A. Thermal degradation studies and kinetic modeling of cardoon (*Cynara cardunculus*) pyrolysis using thermogravimetric analysis (TGA). *Bioresource Technol* 2011;102(10):6230-6238.

- Danso-Boateng E, Holdich RG, Shama G, Wheatley AD, Sohail M, Martin SJ. Kinetics of faecal biomass hydrothermal carbonisation for hydrochar production. *Appl Energ* 2013;111:351-357.
- Daraoui N, Dufour P, Hammouri H, Hottot A. Model predictive control during the primary drying stage of lyophilisation. *Control Eng Pract* 2010;18(5):483-494.
- Debeaujon I, Nesi N, Perez P, Devic M, Grandjean O, Caboche M, Lepiniec L. Proanthocyanidin-accumulating cells in *Arabidopsis thaliana*: Regulation of differentiation and role in seed development. *Plant Cell* 2003;15(11):2514-2531.
- de Boer B, Stalmach U, Nijland H, Hadziioannou G. Microporous honeycomb-structured films of semiconducting block copolymers and their use as patterned templates. *Adv Mater* 2000;12(21):1581-1583.
- Deglise X, Donnot A. Dossier techniques de l'ingénieur. In: Deglise X, Donnot A, editors. *Bois énergie*, Paris; 2004, p. 1-21.
- Demarconnay L, Raymundo-Piñero E, Béguin F. A symmetric carbon/carbon supercapacitor operating at 1.6 V by using a neutral aqueous solution. *Electrochem Commun* 2010;12(10): 1275-8.
- Demirbaş A. Biomass resource facilities and biomass conversion processing for fuels and chemicals. *Energ Convers Manage* 2001;42(11):1357-1378.
- Demir-Cakan R, Baccile N, Antonietti M, Titirici MM. Carboxylate-rich carbonaceous materials via one-step hydrothermal carbonization of glucose in the presence of acrylic acid. *Chem Mater* 2009;21(3):484-490.
- Deshmukh AA, Mhlanga SD, Coville NJ. Carbon spheres. *Mat Sci Eng R*. 2010;70(1-2):1-28.
- Dessimoni E, Casella GI, Morone A, Salvi AM. XPS determination of oxygen-containing functional groups on carbon-fibre surfaces and the cleaning of these surfaces. *Surf Interface Anal* 1990;15(10):627-634.
- Donnet JB. *Carbon black: science and technology*. New York: CRC Press; 1993.
- Du S, Wang L, Fu X, Chen M, Wang C. Hierarchical porous carbon microspheres derived from porous starch for use in high-rate electrochemical double-layer capacitors. *Bioresour Technol* 2013;139:406-409.
- Dubinin MM. Fundamentals of the theory of adsorption in micropores of carbon adsorbents - characteristics of their adsorption properties and microporous structures. *Carbon* 1989;27:457-467.
- Ebbesen TW. *Carbon nanotubes: preparation and properties*. USA: CRC Press, Inc.; 1997.
- Ebelmen JJ. *Ann* 1846;57:331.
- El-Ansary A, Faddah LM. Nanoparticles as biochemical sensors. *Nanotechnol Sci Appl* 2010;3:65-76.
- Escobar-Chávez JJ, López-Cervantes M, Naik A, Kalia YN, Quintanar-Guerrero D, Ganem-Quintanar A. Applications of thermo-reversible Pluronic Fe<sub>127</sub> gels in pharmaceutical formulations. *J Pharm Pharm Sci* 2006;9(3):339-358.



- Escribano JS, Berthon S, Ginoux JL, Achard P. Characterisation of carbon aerogels. Extended Abstracts, Eurocarbon'98. Strasbourg, France, 1998; p. 841-842.
- Falco C, Baccile N, Titirici MM. Morphological and structural differences between glucose, cellulose and lignocellulosic biomass derived hydrothermal carbons. *Green Chem* 2011;13:3273-3281.
- Falco C, Sevilla M, White RJ, Rothe R, Titirici MM. Renewable nitrogen-doped hydrothermal carbons derived from microalgae. *ChemSusChem* 2012;5:1834-1840.
- Falco C, Marco-Lozar JP, Salinas-Torres D, Morallón E, Cazorla-Amorós D, Titirici MM, Lozano-Castelló D. Tailoring the porosity of chemically activated hydrothermal carbons: Influence of the precursor and hydrothermal carbonization temperature. *Carbon* 2013;62:346-355.
- Fang Y, Gu D, Zou Y, Wu Z, Li F, Che R, Deng Y, Tu B, Zhao D. Mesoporous carbon nanospheres with tunable and uniform size. *Angew Chem Int Edit* 2010;49(43):7987-7991.
- Fellinger TP, White RJ, Titirici MM, Antonietti M. Borax-mediated formation of carbon aerogels from glucose. *Adv Funct Mater* 2012;22(15):3254-3260.
- Feng S, Cheng S, Yuan Z, Leitch M, Xu C. Valorization of bark for chemicals and materials: a review. *Renew Sust Energ Rev* 2013;26:560-578.
- Figueiredo JL, Pereira MFR, Freitas MMA, Orfao JJM. Modification of the surface chemistry of activated carbons. *Carbon* 1999;37:1379-1389.
- Figueiredo JL, Pereira MFR, Freitas MMA, Orfao JJM. Characterization of active sites on carbon catalysts. *Ind Eng Chem Res* 2007;46(12):4110-4115.
- Fischer U, Saliger R, Bock V, Petricevic R, Fricke J. Carbon aerogels as electrode material in supercapacitors. *J Porous Mater* 1997;4:281-285.
- Förster S, Plantenberg T. From self-organizing polymers to nanohybrid and biomaterials. *Angew Chem Int Ed* 2002;41(5):688-714.
- Frackowiak E, Béguin F. Carbon materials for the electrochemical storage of energy in capacitors. *Carbon* 2001;39(6):937-950.
- Frackowiak E, Lota G, Machnikowski J, Kierzek K, Vix C, Béguin F. Optimisation of supercapacitors using carbons with controlled nanotexture and nitrogen content. *Electrochim Acta* 2006;51(11):2209-2214.
- Freire RM, Batista AHM, Filho AGS, Filho JM, Saraiva GD, Oliveira AC. High catalytic activity of nitrogen-containing carbon from molecular sieves in fine chemistry. *Catal Lett* 2009;131(1-2):135-145.
- Funke A, Ziegler F. Hydrothermal carbonization of biomass: A summary and discussion of chemical mechanisms for process engineering. *Biofuels Bioprod Bioref* 2010;4(2):160-177.
- Garcia R, Pizzi A. Polycondensation and autocondensation networks in polyflavonoid tannins I. Final networks. *J Appl Polym Sci* 1998;70:1083-1091.

- García-González CA, Camino-Rey MC, Alnaief M, Zetzl C, Smirnova I. Supercritical drying of aerogels using CO<sub>2</sub>: Effect of extraction time on the end material textural properties. *J Supercrit Fluids* 2012;66:297-306.
- Garrido J, Linares-Solano A, Martín-Martínez JM, Molina-Sabio M, Rodríguez-Reinoso F, Torregrosa R. Use of N<sub>2</sub> vs CO<sub>2</sub> in the characterisation of activated carbons. *Langmuir* 1987;3:76-81.
- Garsuch A, Klepel O. Synthesis of ordered carbon replicas by using Y-zeolite as template in a batch reactor. *Carbon* 2005;43(11):2330-2337.
- Gonzalez JF, Encinar JM, Canito JL, Sabio E, Chacon M. Pyrolysis of cherry stones: energy uses of the different fractions and kinetic study. *J Anal Appl Pyrolysis* 2003;67:165-190.
- Gregg SJ, Sing KSW. Adsorption, surface area and porosity. London: Academic Press Inc.; 1982.
- Gregg SJ, Sing KSW. Adsorption, surface area and porosity. New York: Academic Press Inc.; 1991.
- Grishechko LI, Amaral-Labat G, Szczurek A, Fierro V, Kuznetsov BN, Pizzi A, Celzard A. New tannin – lignin aerogels. *Ind Crop Prod* 2013;41:347-355.
- Gross G. Biosynthesis of hydrolysable tannins. In: Nakanishi K, Pinto BM, Meth-Cohn O, Barton D, editors. *Comprehensive Natural Product Chemistry: Carbohydrates and their derivatives including tannins, cellulose and related lignings*. UK: Pergamon; 1999, p. 799-826.
- Gunckel S, Santander P, Cordano G, Ferreira J, Muñoz S, Nunez-Vergara LJ, Squella JA. Antioxidant activity of gallates: an electrochemical study in aqueous media. *Chem Biol Interact* 1998;114(1-2):45-59.
- Haenel MW. Recent progress in coal structure research. *Fuel* 1992;71(11):1211-1223.
- Harbertson JF, Parpinello GP, Heymann H, Downey MO. Impact of exogenous tannin additions on wine chemistry and wine sensory character. *Food Chem* 2012;131(3):999-1008.
- Hasan Z, Hwang JS, Jung SH. Liquid-phase dehydration of 1-phenylethanol to styrene over sulfonated D-glucose catalyst. *Catal Commun* 2012;26:30-33.
- Hashida K, Makino R, Ohara S. Amination of pyrogallol nucleus of condensed tannins and related polyphenols by ammonia water treatment. *Holzforschung* 2009;63(3):319-326.
- Haykiri-Acma H, Yaman S, Kucukbayrak S. Effect of heating rate on the pyrolysis yields of rapeseed. *Renew Energ* 2006;31:803-810.
- Heath L, Thielemans W. Cellulose nanowhisker aerogels. *Green Chem* 2010;12(8):1448-1453.
- Hench LJ, West JK. The sol – gel process. *Chem Rev* 1990;90:33-72.
- Hernández-Montoya V, García-Servín J, Bueno-López JI. Thermal treatments and activation procedures used in the preparation of activated carbons. In: Hernández-Montoya V, Petriciolet AB, editors. *Lignocellulosic precursors used in the synthesis of activated carbon - characterization techniques and applications in the wastewater treatment*, InTech; 2012, p. 1-36.
- Höök M, Tang X. Special section: transition pathways to a low carbon economy. *Energy Policy* 2013;52:797-809.

- Horikawa T, Hayashi J, Muroyama K. Controllability of pore characteristics of resorcinol–formaldehyde carbon aerogel. *Carbon* 2004;42(8-9):1625-1633.
- Huang H, Yang X. Synthesis of polysaccharide-stabilized gold and silver nanoparticles: A green method. *Carbohydr Res* 2004;339;2627-2631.
- Huang Y, Cai H, Feng D, Gu D, Deng Y, Tu B, Wang H, Webley PA, Zhao D. One-step hydrothermal synthesis of ordered mesostructured carbonaceous monoliths with hierarchical porosities. *Chem Commun* 2008;2641-2643.
- Hu B, Yu SH, Wang K, Liu L, Xu XW. Functional carbonaceous materials from hydrothermal carbonization of biomass: an effective chemical process. *Dalton Trans* 2008;40:5414-5423.
- Hu B, Wang K, Wu L, Yu SH, Antonietti M, Titirici MM. Engineering carbon materials from the hydrothermal carbonization process of biomass. *Adv Mater* 2010;22:813-828.
- Hulicova D, Kodama M, Hatori H. Electrochemical performance of nitrogen-enriched carbons in aqueous and non-aqueous supercapacitors. *Chem Mater* 2006;18(9):2318-2326.
- Hulicova-Jurcakova D, Seredych M, Lu GQ, Bandosz TJ. Combined effect of nitrogen- and oxygen-containing functional groups of microporous activated carbon on its electrochemical performance in supercapacitors. *Adv Funct Mater* 2009;19(3):438-447.
- Hwang IH, Aoyama H, Matsuto T, Nakagishi T, Matsuo T. Recovery of solid fuel from municipal solid waste by hydrothermal treatment using subcritical water. *Waste Manage* 2012;32(3):410-416.
- Inagaki M. Pores in carbon materials-importance of their control. *New Carbon Mater* 2009;24(3):193-232.
- Jiang H, Wang T, Wang L, Sun C, Jiang T, Cheng G, Wang S. Development of an amorphous mesoporous TiO<sub>2</sub> nanosphere as a novel carrier for poorly water-soluble drugs: Effect of different crystal forms of TiO<sub>2</sub> carriers on drug loading and release behaviors. *Microporous Mesoporous Mater* 2012;153:124-130.
- Job N, Pirard R, Marien J, Pirard JP. Porous carbon xerogels with texture tailored by pH control during sol–gel process. *Carbon* 2004;42(3):619-628.
- Job N, Théry A, Pirard R, Marien J, Kocon L, Rouzaud JN, Béguin F, Pirard JP. Carbon aerogels, cryogels and xerogels: Influence of the drying method on the textural properties of porous carbon materials. *Carbon* 2005;43(12):2481-2494.
- Job N, Sabatier F, Pirard JP, Crine M, Léonard A. Towards the production of carbon xerogel monoliths by optimizing convective drying conditions. *Carbon* 2006;44(12):2534-2542.
- Job N, Gomme CJ, Pirard R, Pirard JP. Effect of the counter-ion of the basification agent on the pore texture of organic and carbon xerogels. *J Non-Cryst Solids* 2008;354(40-41):4698-4701.
- Jung SM, Jung HY, Dresselhaus MS, Jung YJ, Kong J. A facile route for 3D aerogels from nanostructures 1D and 2D materials. *Sci Rep* 2012;849(2):1-5.

- Junpirom S. Activated carbon from longan seed: its activation model and adsorption of water vapor and benzene. Suranaree University of Technology, Thailand, PhD thesis, 2006.
- Jurewicz K, Vix-Guterl C, Frackowiak E, Saadallah S, Reda M, Parmentier J, Patarin J, Béguin F. Capacitance properties of ordered porous carbon materials prepared by a templating procedure. *J Phys Chem Solids* 2004;65(2-3):287-293.
- Jurewicz K, Pietrzak R, Nowicki P, Wachowska H. Capacitance behaviour of brown coal based active carbon modified through chemical reaction with urea. *Electrochim Acta* 2008;53:5469-5475.
- Kabyemela BM, Adschiri T, Malaluan RM, Arai K. Degradation kinetics of dihydroxyacetone and glyceraldehyde in subcritical and supercritical water. *Ind Eng Chem Res* 1997;36(6):2025-2030.
- Kanungo M, Kumar A, Contractor AQ. Studies on electropolymerization of aniline in the presence of sodium dodecyl sulfate and its application in sensing urea. *J Electroanal Chem* 2002;528(1-2):46-56.
- Karas M, Bachmann D, Bahr U, Hillenkamp F. Matrix-assisted ultraviolet laser desorption of non-volatile compounds. *Int J Mass Spectrom Ion Proc* 1987;78:53-58.
- Khanbabaee K, Ree TV. Tannins: classification and definition. *Nat Prod Rep* 2001;18:641-649.
- Khomenko V, Raimundo-Piñero E, Béguin F. A new type of high energy asymmetric capacitor with nanoporous carbon electrodes in aqueous electrolyte. *J Power Sources* 2010;195(13):4234-4241.
- Kim JS, Lee YY, Torget RW. Cellulose hydrolysis under extremely low sulfuric acid and high-temperature conditions. *Appl Biochem Biotechnol* 2001;91-93(1-9):331-340.
- Kinoshita K. Carbons. In: Daniel C, Besenhard JO, editors. *Handbook of battery materials*, Wiley-VCH; 1999, p. 269-283.
- Kistler SS. Coherent expanded-aerogels. *J Phys Chem* 1932;34:52-64.
- Korbekandi H, Irvani S. The delivery of nanoparticles. In: Hashim AA, editor. *Silver nanoparticles, Croatia: InTech; 2012, p. 3-34.*
- Kraiwatanawong K, Mukai SR, Tamon H, Lothongkum AW. Preparation of carbon cryogels from wattle tannin and furfural. *Micropor Mesopor Mater* 2007;98(1-3):258-266.
- Kruse A, Funke A, Titirici MM. Hydrothermal conversion of biomass to fuels and energetic materials. *Curr Opin Chem Biol* 2013;17(3):515-521.
- Ku CS, Jang JP, Mun SP. Exploitation of polyphenol-rich pine barks for potent antioxidant activity. *Wood Sci Technol* 2007;53:524-528.
- Kubo S, White R, Yoshizawa N, Antonietti M, Titirici MM. Ordered carbohydrate-derived porous carbons. *Chem Mater* 2011;23(22):4882-4885.
- Kumagai S, Sato M, Tashima D. Electrical double-layer capacitance of micro- and mesoporous activated carbon prepared from rice husk and beet sugar. *Electrochim Acta* 2013;114:617-626.

- Kumar S, Loganathan VA, Gupta RB, Barnett MO. An Assessment of U(VI) removal from groundwater using biochar produced from hydrothermal carbonization. *J Environ Manage* 2011;92(10):2504-2512.
- Kyotani T, Nagai T, Inoue S, Tomita A. Formation of new type of porous carbon by carbonization in zeolite nanochannels. *Chem Mater* 1997;9:609-615.
- La Mer VK. Nucleation in phase transitions. *Ind Eng Chem* 1952;44(6):1270-1277.
- Lahaye J, Nanse G, Fioux Ph, Bagreev A, Broshnik A, Strelko V. Chemical transformation during the carbonisation in air and the pyrolysis under argon of a inylpyridine–divinylbenzene copolymer by X-ray photoelectron spectroscopy. *Appl Surf Sci* 1999;147:153-174.
- Lauri P, Havlík P, Kindermann G, Forsell N, Böttcher H, Obersteiner M. Woody biomass energy potential in 2050. *Energ Policy* 2013;66:19-31.
- Lee YY, Iyer P, Torget RW. Dilute-Acid Hydrolysis of Lignocellulosic Biomass. *Adv Biochem Eng/Biotechnol* 1999;65:93-115.
- Legendre A. Le matériau carbone. Des céramiques noires aux fibres de carbone. Paris: Eyrolles; 1992.
- Leibnitz E, Könnecke HG, Schröter M. Zur Kenntnis der Druckinkohlung von Braunkohlen in Gegenwart von Wasser. IV. *J Prakt Chem* 1958;6:18-24.
- Léonard AF, Gommès CJ, Piedboeuf ML, Pirard JP, Job N. Rapid aqueous synthesis of ordered mesoporous carbons: Investigation of synthesis variables and application as anode materials for Li-ion batteries. *Microporous and Mesoporous Mater* 2014;195:92-101.
- Liang CD, Hong KL, Guiochon GA, Mays JW, Dai S. Synthesis of a large-scale highly ordered porous carbon film by self-assembly of block copolymers. *Angew Chem Int Ed* 2004;43(43):5785-5789.
- Liang C, Dai S. Synthesis of mesoporous carbon materials via enhanced hydrogen-bonding interaction. *J Am Chem Soc* 2006;128(16):5316-5317.
- Liang C, Dai S. Dual phase separation for synthesis of bimodal meso-/macroporous carbon monoliths. *Chem Mater* 2009;21:2115-2124.
- Libra JA, Ro KS, Kammann C, Funke A, Berge ND, Neubauer Y, Titirici MM, Fühner C, Bens O, Kern J, Emmerich KH. Hydrothermal carbonization of biomass residuals: a comparative review of the chemistry, processes and applications of wet and dry pyrolysis. *Biofuels* 2011;2(1):71-106.
- Li K, Ling L, Lu C, Qiao W, Liu Z, Liu L, Mochida I. Catalytic removal SO<sub>2</sub> over ammonia-activated carbon fibers. *Carbon* 2001;39(12):1803-1808.
- Li W, Chen D, Li Z, Shi Y, Wan Y, Huang J, Yang J, Zhao D, Jiang Z. Nitrogen enriched mesoporous carbon spheres obtained by a facile method and its application for electrochemical capacitor. *Electrochem Commun* 2007;9(4):569-573.
- Li M, Li, W, Liu S. Hydrothermal synthesis, characterization, and KOH activation of carbon spheres from glucose. *Carbohydr Res* 2011;346:999-1004.

- Lin N, Tian J, Shan Z, Chen K, Liao W. Hydrothermal synthesis of hydrous ruthenium oxide/graphene sheets for high-performance supercapacitors. *Electrochim Acta* 2013;99:219-224.
- Liu X, Tian B, Yu C, Gao F, Xie S, Tu B, Che R, Peng LM, Zhao D. Room-temperature synthesis in acidic media of large-pore three-dimensional bicontinuous mesoporous silica with *Ia3d* symmetry. *Angew Chem Int Ed* 2002;41:3876-3878.
- Liu HJ, Cui WJ, Jin LH, Wang CX, Xia YY. Preparation of three-dimensional ordered mesoporous carbon sphere arrays by a two-step templating route and their application for supercapacitors. *J Mater Chem* 2009;19:3661-3667.
- Liu RL, Wu DQ, Feng XL, Mullen K. Nitrogen-doped ordered mesoporous graphitic arrays with high electrocatalytic activity for oxygen reduction. *Angew Chem Int Ed* 2010a;49(14):2565-2569.
- Liu Z, Zhang FS, Wu J. Characterization and application of chars produced from pinewood pyrolysis and hydrothermal treatment. *Fuel* 2010b;89(2):510-514.
- Liu D, Lei JH, Guo LP, Deng KJ. Simple hydrothermal synthesis of ordered mesoporous carbons from resorcinol and hexamine. *Carbon* 2011;49(6):2113-2119.
- Lozano-Castello D, Cazorla-Amoros D, Linares-Solano A, Quinn DF. Micropore size distributions of activated carbons and carbon molecular sieves assessed by high-pressure methane and carbon dioxide adsorption isotherms. *J Phys Chem B* 2002;106(36):9372-9379.
- Lue JT. Physical Properties of Nanomaterials. In: Nalwa HS, editor. *Encyclopedia of Nanoscience and Nanotechnology*, American Scientific Publishers; 2007, p. 1-46.
- Luijkx GCA, van Rantwijk F, van Bekkum H, Antal MJ. The role of deoxyhexonic acids in the hydrothermal decarboxylation of carbohydrates. *Carbohydr Res* 1995;272(2):191-202.
- Lu J, Liong M, Zink JI, Tamanoi F. Mesoporous silica nanoparticles as a delivery system for hydrophobic anticancer drugs. *Small* 2007;3:1341-1346.
- Lu L, Lu X, Ma N. Kinetics of non-catalyzed hydrolysis of tannin in high temperature liquid water. *J Zhejiang Univ Sci B* 2008;9:401-406.
- Lu H, Dai W, Zheng M, Li N, Ji G, Cao J. Electrochemical capacitive behaviors of ordered mesoporous carbons with controllable pore sizes. *J Power Sources* 2012a;209:243-250.
- Lu X, Shen J, Ma H, Yan B, Li Z, Shi M, Ye MJ. A cost-effective way to maintain metal-doped carbon xerogels and their applications on electric double-layer capacitors. *J Power Sources* 2012b;201:340-346.
- Ma TY, Liu L, Yuan ZY. Direct synthesis of ordered mesoporous carbons. *Chem Soc Rev* 2013;42:3977-4003.
- Makowski P, Cakan RD, Antonietti M, Goettmann F, Titirici MM. Selective partial hydrogenation of hydroxy aromatic derivatives with palladium nanoparticles supported on hydrophilic carbon. *Chem Commun* 2008;999-1001.
- Manocha SM. Porous carbons. *Sadhana* 2003;28:335-348.
- Marsh H, Rodriguez-Reinoso F. *Activated Carbon*. Elsevier; 2006.

- Matos I, Fernandes S, Guerreiro L, Barata S, Ramos AM, Vital J, Fonseca IM. The effect of surfactants on the porosity of carbon xerogels. *Microporous Mesoporous Mater* 2006;92:38-46.
- Matsui T, Tanaka S, Miyake Y. Correlation between the capacitor performance and pore structure of ordered mesoporous carbons. *Adv Powder Technol* 2013;24(4):737-742.
- Meikleham NE, Pizzi A. Acid- and alkali-catalyzed tannin-based rigid foams. *J Appl Polym Sci* 2003;53(11):1547-1556.
- Merlin A, Pizzi, A. An ESR study of the silica-induced autocondensation of polyflavonoid tannins. *J Appl Polym Sci* 1996;59:945-952.
- Mochidzuki K, Sakoda A, Suzuki M. Liquid-phase thermogravimetric measurement of reaction kinetics of the conversion of biomass wastes in pressurized hot water: a kinetic-study. *Adv Environ Res* 2003;7:421-428.
- Molan AL, Liu Z, De S. Effect of pine bark (*Pinus radiata*) extracts on sporulation of coccidian oocysts. *Folia Parasit* 2009;56(1):1-5.
- Moreno-Castilla C, Maldonado-Hódar FJ. Carbon aerogels for catalysis applications: an overview. *Carbon* 2005;43(3):455-465.
- Moreno-Castilla C, Dawidziuk MB, Carrasco-Marin F, Zapata-Benabithé Z. Surface characteristics and electrochemical capacitances of carbon aerogels obtained from resorcinol and pyrocatechol using boric and oxalic acids as polymerization catalysts. *Carbon* 2011;49(12):3808-3819.
- Moreno-Castilla C, Dawidziuk MB, Carrasco-Marin F, Morallon E. Electrochemical performance of carbon gels with variable surface chemistry and physics. *Carbon* 2012;50:3324-3332.
- Morisada S, Kim YH, Ogata T, Marutani Y, Nakano Y. Improved adsorption behaviors of amine-modified tannin gel for palladium and platinum ions in acidic chloride solutions. *Ind Eng Chem Res.* 2011;50(4):1875-1880.
- Mumme J, Eckervogt L, Pielert J, Diakite M, Rupp F, Kern J. Hydrothermal carbonization of anaerobically digested maize silage. *Bioresource Technol* 2011;102(19):9255-9260.
- Nakano Y, Takeshita K, Tsutsumi T. Adsorption mechanism of hexavalent chromium by redox within condensed-tannin gel. *Water Res* 2001;35(2):496-500.
- Oberlin A. Carbonization and graphitization. *Carbon* 1984;22(6):521-541.
- O'Connor P. A general introduction to biomass utilization possibilities. In: Triantafyllidis K, Lappas A, Stöcker M, editors. *The Role of Catalysis for the Sustainable Production of Bio-fuels and Bio-chemicals*, Oxford: Elsevier; 2013; p. 1-25.
- Oganov AR, Hemley RJ, Hazen RM, Jones AP. Structure, bonding, and mineralogy of carbon at extreme conditions. *Rev Mineral Geochem* 2013;75:47-77.
- Ogata T, Nakano Y. Mechanisms of gold recovery from aqueous solutions using a novel tannin gel adsorbent synthesized from natural condensed tannin. *Water Res* 2005;39(18):4281-4286.
- Oliveira I, Blöhse D, Ramke HG. Hydrothermal carbonization of agricultural residues. *Bioresource Technol* 2013;142:138-146.

- Ortiz-Ibarra H, Casillas N, Soto V, Barcena-Soto M, Torres-Vitela R, de la Cruz W, Gómez-Salazar S. Surface characterization of electrodeposited silver on activated carbon for bactericidal purposes. *J Colloid Interface Sci* 2007;314(2):562-571.
- Ounas A, Aboulkas A, El harfi K, Bacaoui A, Yaacoubi A. Pyrolysis of olive residue and sugar cane bagasse: Non-isothermal thermogravimetric kinetic analysis. *Bioresource Technol* 2011;102(24):11234-11238.
- Pandolfo AG, Hollenkamp AF. Carbon properties and their role in supercapacitors. *J Power Sources* 2006;157(1):11-27.
- Park SY, Lee Y, Bae KH, Ahn CH, Park TG. Temperature/pH-Sensitive Hydrogels Prepared from Pluronic Copolymers End-Capped with Carboxylic Acid Groups via an Oligolactide Spacer. *Macromol Rapid Commun* 2007;28:1172-1176.
- Parshetti GK, Liu Z, Jain A, Srinivasan MP, Balasubramanian R. Hydrothermal carbonization of sewage sludge for energy production with coal. *Fuel* 2013;111:201-210.
- Pârvulescu VI, Cojocaru B, Pârvulescu V, Richards R, Li Z, Cadigan C, Granger P, Miquel P, Hardacre C. Sol-gel-entrapped nano silver catalysts-correlation between active silver species and catalytic behaviour. *J Catal* 2010;272(1):92-100.
- Pasch H, Pizzi A, Rode K. MALDI-TOF mass spectrometry of polyflavonoid tannins. *Polymer* 2001;42(18):7531-7539.
- Patten AM, Vassão DG, Wolcott MP, Davin LB, Lewis NG. Trees: A remarkable biochemical bounty. In: Reedijk J, editor. *Chemistry, Molecular Sciences and Chemical Engineering, USA: Elsevier*; 2010; p. 1173-1296.
- Pels JR, Kapteijn F, Moulijn JA, Zhu Q, Thomas KM. Evolution of nitrogen functionalities in carbonaceous materials during pyrolysis. *Carbon* 1995;33(11):1641-1653.
- Perry DL, Grint A. Application of XPS to coal characterization. *Fuel* 1983;62:1024-1033.
- Perry CC, Sabir TS, Livingston WJ, Milligan JR, Chen Q, Maskiewicz V, Boskovic DS. Fluorescence of commercial Pluronic F127 samples: Temperature-dependent micellization. *J Colloid Interface Sci* 2011;354(2):662-669.
- Peters EC, Svec F, Frechet JMJ. Rigid macroporous polymer monoliths. *Adv Mater* 1999;11(14):1169-1181.
- Peterson AA, Vogel F, Lachance RP, Fröling M, Antal MJ. Thermochemical biofuel production in hydrothermal media: A review of sub- and supercritical water technologies. *Energy Environ Sci* 2008;1:32-65.
- Petričević R, Reichenauer G, Bock V, Emmerling A, Fricke J. Structure of carbon aerogels near the gelation limit of the resorcinol-formaldehyde precursor. *J Non-Cryst Solids* 1998;225(1):41-45.
- Pizzi A. Tannin-based wood adhesives. In: Pizzi A, editor. *Wood Adhesives: Chemistry and Technology*, New York: Marcel Dekker; 1983, p. 177-246.
- Pizzi A. *Advanced wood adhesives technology*. New York: Marcel Dekker Inc.; 1994.



- Pizzi A, Meikleham N. Induced accelerated autocondensation of polyflavonoid tannins for phenolic polycondensates. III. CP-MAS  $^{13}\text{C}$ -NMR of different tannins and models. *J Appl Polym Sci* 1995;55:1265-1269.
- Pizzi A. Plant Polyphenols 2. In: Gross GG, Hemingway RW, Yoshida T, Branham SJ, editors. Tannin autocondensation and polycondensation for zero emission tannin wood adhesives, London: Kluwer Academic/Plenum Publishers; 1999, p. 805-821.
- Pizzi A. Tannins: Major Sources, Properties and Applications. In: Belgacem MN, Gandini A, editors. Monomers, Polymers and Composites from Renewable Resources, Oxford: Elsevier; 2008, p. 179-199.
- Pizzi A. Polyflavonoid tannins self-condensation adhesives for wood particleboard. *J Adhesion* 2009;85(2-3):57-68.
- Portet C, Yushin G, Gogotsi Y. Electrochemical performance of carbon onions, nanodiamonds, carbon black and multiwalled nanotubes in electrical double layer capacitors. *Carbon* 2007;45(13):2511-2518.
- Portet C, Chmiola J, Gogotsi Y, Park S, Lian K. Electrochemical characterizations of carbon nanomaterials by the cavity microelectrode technique. *Electrochim Acta* 2008;53(26):7675-7680.
- Przepiórski J. Enhanced adsorption of phenol from water by ammonia-treated activated carbon. *J Hazard Mater* 2006;135(1-3):453-456.
- Qu D, Shi H. Studies of activated carbons used in double layers capacitors. *J Power Sources* 1998;74:99-107.
- Qu LT, Liu Y, Baek JB, Dai LM. Nitrogen-doped graphene as efficient metal-free electrocatalyst for oxygen reduction in fuel cells. *ACS Nano* 2010;4(3):1321-1326.
- Ra J, Raymundo-Piñero E, Lee YH, Béguin F. High power supercapacitors using polyacrylonitrile-based carbon nanofiber paper. *Carbon* 2009;47(13):2984-2992.
- Rafique MMA, Iqbal J. Production of carbon nanotubes by different routes – a review. *JEAS* 2011;1:29-34.
- Ramke HG, Blöhse D, Lehmann HJ, Fettig J. Hydrothermal carbonization of organic waste. In: Cossu R, Diaz LF, Stegmann R, editors. Twelfth International Waste Management and Landfill Symposium. Sardinia, Italy, International Waste Working Group, 2009.
- REN21. Renewables 2013 Global Status Report. Paris: REN21; 2013a.
- REN21. Renewables Global Futures Report. Paris: REN21; 2013b.
- Richter A, Ries R, Smith R, Henkel M, Wolf B. Nanoindentation of diamond, graphite and fullerene films. *Diamond Relat Mater* 2000;9(2):170-184.
- Riling MC, Wagner M, Salem M, Antunes PM, George C, Ramke HG, Titirici MM, Antonietti M. Material derived from hydrothermal carbonization: effects on plant growth and arbuscular mycorrhiza. *Appl Soil Ecol* 2010;45(3):238-242.

- Robb SA, Lee BH, McLemore R, Vernon BL. Simultaneously physically and chemically gelling polymer system utilizing a poly (NIPAAm-co-cysteamine)-based copolymer. *Biomacromolecules* 2007;8(7):2294-2300.
- Rodríguez-Reinoso F, Linares-Solano A. Microporous structure of activated carbons as revealed by adsorption methods. *Chem Phys Carbon* 1989;21:1-146.
- Rodríguez-Reinoso F, Molina-Sabio M. El carbón activado como adsorbente en descontaminación ambiental. *Adsorbentes en la solución de algunos problemas ambientales*. Spain: CYTED; 2004, p. 163-168.
- Rouquerol F, Rouquerol J, Sing K. *Adsorption by powders & porous solids*. London: Academic Press; 1999.
- Roux DG, Ferreira D, Hundt HK, Malan E. Structure, stereochemistry, and reactivity of natural condensed tannins as basis for their extended industrial application. *Appl Polym Symp*; 1975, p. 335-353.
- Roy M. Nanocrystalline and disordered carbon materials. In: Banerjee S, Tyagi AK, editors. *Functional Materials: Preparation, Processing and Applications*, London: Elsevier Insights; 2012, p. 675-706.
- Ryoo R, Joo SH, Jun S. Synthesis of highly ordered carbon molecular sieves via template-mediated structural transformation. *J Phys Chem B* 1999;103(37):7743-7746.
- Ryu J, Suh YW, Suh DJ, Ahn DJ. Hydrothermal preparation of carbon microspheres from monosaccharides and phenolic compounds. *Carbon* 2010;48:1990-1998.
- Saddawi A, Jones JM, Williams A, Wojtowicz MA. Kinetics of the thermal decomposition of biomass. *Energ Fuel* 2010;24:1274-1282.
- Sagan M, Morandi D, Tarengi E, Du G. Selection of nodulation and mycorrhizal mutants in the model plant *Medicago truncatula* (Gaertn.) after  $\gamma$ -ray mutagenesis. *Plant Sci* 1995;111(1):63-71.
- Saliger R, Fischer U, Herta C, Fricke J. High surface area carbon aerogels for supercapacitors. *J Non-Cryst Solids* 1998;225:81-85.
- Sánchez-Cortés S, García-Ramos JV. Adsorption and chemical modification of phenols on a silver surface. *J Colloid Interface Sci* 2000;231(1):98-106.
- Sánchez-Martín J, Beltrán-Heredia J, Solera-Hernández C. Surface water and wastewater treatment using a new tanning-based coagulant. Pilot plant trials. *J Environ Manage* 2010;91(10):2051-2058.
- Sasaki M, Kabyemela B, Malaluan R, Hirose S, Takeda N, Adschiri T, Arai K. Cellulose hydrolysis in subcritical and supercritical water. *J Supercrit Fluids* 1998;13(1-3):261-268.
- Scherer GW, Smith DM. Cavitation during drying of a gel. *J Non-Cryst Solids* 1995;189(3):197-211.
- Schumacher JP, van Vucht HA, Groenewege MP, Blom L, van Krevelen DW. *Fuel* 1956;35:281-290.
- Schumacher JP, Huntjens FJ, van Krevelen DW. Chemical structure and properties of coal XXVI studies on artificial coalification. *Fuel* 1960;39:223-234.

- Schlienger S, Graff AL, Celzard A, Parmentier J. Direct synthesis of ordered mesoporous polymer and carbon materials by a biosourced precursor. *Green Chem* 2012;14:313-316.
- Schlienger S, Ducrot-Boisgontier C, Delmotte L, Guth JL, Parmentier J. History of the micelles: A key parameter for the formation mechanism of ordered mesoporous carbons via a polymerized mesophase. *J Phys Chem C* 2014;118(22):11919-11927.
- Schwalbe CG, Neumann KE. Künstliche Inkohlung von Sphagnummoos, Kiefern und Buchenholz. *Angew Chem* 1933;46:177-179.
- Sealy-Fisher VJ, Pizzi A. Increased pine tannins extraction and wood adhesives development by phlobaphenes minimization. *Holz Roh Werkstoff* 1992;50:212-220.
- Seo DK, Park SS, Kim YT, Hwang J, Yu TU. Study of coal pyrolysis by thermo-gravimetric analysis (TGA) and concentration measurements of the evolved species. *J Anal Appl Pyrolysis* 2011;92(1):209-216.
- Sevilla M, Fuertes AB. Chemical and structural properties of carbonaceous products obtained by hydrothermal carbonization of saccharides. *Chem Eur J* 2009a;15(16):4195-4203.
- Sevilla M, Fuertes AB. The production of carbon materials by hydrothermal carbonization of cellulose. *Carbon* 2009b;47:2281-2289.
- Sevilla M, Fuertes AB. Sustainable porous carbons with a superior performance for CO<sub>2</sub> capture. *Energy Environ Sci* 2011a;4:1765-1771.
- Sevilla M, Fuertes AB, Mokaya R. High density hydrogen storage in superactivated carbons from hydrothermally carbonized renewable organic materials. *Energy Environ Sci* 2011b;4:1400-1410.
- Sevilla M, Falco C, Titirici MM, Fuertes AB. High-performance CO<sub>2</sub> sorbents from algae. *RSC Adv* 2012;2:12792-12797.
- Shah YT. Water for energy and fuel production. In: Shah YT, editor. *Energy recovery for benign hydrothermal processes*, CRC Press; 2014, p. 33-46.
- Shahat AA, Marzouk MS. Medicinal Plant Research in Africa, Pharmacology and Chemistry. In: Kuete V, editor. *Tannins and related compounds from medicinal plants of Africa*, Elsevier Inc.; 2013, p. 479-555.
- Shen W, Li Z, Liu Y. Surface chemical functional groups modification of porous carbon. *Recent Patents on Chemical Engineering* 2008;27-40.
- Shen W, Fan W. Nitrogen-containing porous carbons: synthesis and application. *J Mater Chem A* 2013;1:999-1013.
- Shukla AK, Banerjee A, Ravikumar MK, Jalajakshi A. Electrochemical capacitors: Technical challenges and prognosis for future markets. *Electrochim Acta* 2012;84:165-173.
- Si W, Zhou J, Zhang S, Li S, Xing W, Zhuo S. Tunable N-doped or dual N, S-doped activated hydrothermal carbons derived from human hair and glucose for supercapacitor applications. *Electrochim Acta* 2013;107:397-405.

- Sing KSW. Reporting physisorption data for gas/solid systems with special reference to the determination of surface area and porosity. *Pure Appl Chem* 1985;57:603-619.
- Sing KSW. The use of physisorption for the characterization of microporous carbons. *Carbon* 1989;27(1):5-11.
- Singh S, Wu C, Williams PT. Pyrolysis of waste materials using TGA-MS and TGA-FTIR as complementary characterisation techniques. *J Anal Appl Pyrol* 2012;94:99-107.
- Sironmani A, Daniel K. Silver nanoparticles – universal multifunctional nanoparticles for bio sensing, imaging for diagnostics and targeted. Drug delivery for therapeutic applications. In: Kapetanovic IM, editor. *Drug discovery and development – present and future*, Intech; 2011, p. 463-488.
- Sivasankar M, Kumar BP. Role of nanoparticles in drug delivery system. *IJRPBS* 2010;1(2):41-66.
- Si W, Zhou J, Zhang S, Li S, Xing W, Zhuo S. Tunable N-doped or dual N, S-doped activated hydrothermal carbons derived from human hair and glucose for supercapacitor applications. *Electrochim Acta* 2013;107:397-405.
- Soorholtz M, White RJ, Zimmermann T, Titirici MM, Antonietti M, Palkovits R, Schüth F. Direct methane oxidation over Pt-modified nitrogen-doped carbons. *Chem Commun* 2013;49:240-242.
- Speight JG. *Handbook of Coal Analysis*. Wiley-Interscience; 2005.
- Sreeram KJ, Ramasami T. Sustaining tanning process through conservation, recovery and better utilization of chromium. *Resour Conserv Recy* 2003;38(3):185-212.
- Stokke DD, Wu Q, Han G. Adhesives used to bond wood and lignocellulosic composites. In: Stokke DD, Wu Q, Han G, editors. *Introduction to wood and natural fiber adhesives*, Wiley; 2014, p. 169-208.
- Stoller MD, Ruoff RS. Best practice methods for determining an electrode material's performance for ultracapacitors. *Energy Environ Sci* 2010;3:1294-1301.
- Sun X, Li Y. Ag@C core/shell structured nanoparticles: controlled synthesis, characterization, and assembly. *Langmuir* 2005;21:6019-6024.
- Sun G, Long D, Liu X, Qiao W, Zhan L, Liang X, Ling L. Asymmetric capacitance response from the chemical characteristics of activated carbons in KOH electrolyte. *J Electroanal Chem* 2011a;659(2):161-167.
- Sun K, Ro K, Guo M, Novak J, Mashayekhi H, Xing B. Sorption of bisphenol A, 17 $\alpha$ -ethinyl estradiol and phenanthrene on thermally and hydrothermally produced biochars. *Bioresour Technol* 2011b;102(10):5757-5763.
- Szczurek A, Jurewicz K, Amaral-Labat G, Fierro V, Pizzi A, Celzard A. Structure and electrochemical capacitance of carbon cryogels derived from phenol–formaldehyde resins. *Carbon* 2010;48(13):3874-3883.
- Szczurek A, Amaral-Labat G, Fierro V, Pizzi A, Masson E, Celzard A. The use of tannin to prepare carbon gels: Part I. Carbon aerogels. *Carbon* 2011a;49(8):2773-2784.

- Szczurek A, Amaral-Labat G, Fierro V, Pizzi A, Celzard A. The use of tannin to prepare carbon gels. Part II. Carbon cryogels. *Carbon* 2011b;49(8):2785-2794.
- Szczurek A, Fierro V, Pizzi A, Celzard A. Mayonnaise, whipped cream and meringue, a new carbon cuisine. *Carbon* 2013;58:245-248.
- Tamon H, Ishizaka H, Yamamoto T, Suzuki T. Preparation of mesoporous carbon by freeze drying. *Carbon* 1999;37(12):2049-2055.
- Tanev PT, Pinnavaia TJ. A neutral templating route to mesoporous molecular sieves. *Science* 1995;267:865-867.
- Tang MM, Bacon R. Carbonization of cellulose fibers—I. Low temperature pyrolysis. *Carbon* 1964;2(3):211-214.
- Tang YF, Allen BL, Kauffman DR, Star A. Electrocatalytic activity of nitrogen-doped carbon nanotube cups. *J Am Chem Soc* 2009;131(37):13200-13201.
- Tang K, White RJ, Mu X, Titirici MM, van Aken PA, Maier J. Hollow Carbon Nanospheres with a High Rate Capability for Lithium-Based Batteries. *ChemSusChem* 2012;5(2):400-403.
- Tarazona P. Solid–fluid transition and interfaces with density functional approaches. *Surf Sci* 1995;331-333:989-994.
- Terrones M, Ajayan PM, Banhart F, Blase X, Carroll DL, Charlier JC, Czerw R, Foley B, Grobert N, Kamalakaran R, Kohler-Redlich P, Rühle M, Seeger T, Terrones H. N-doping and coalescence of carbon nanotubes: synthesis and electronic properties. *Appl Phys A: Mater Sci Proc* 2002;74(3):355-361.
- Tian X, Li J, Pan S. Facile synthesis of single-crystal silver nanowires through a tannin-reduction process. *J Nanopart Res* 2009;11:1839-1844.
- Titirici MM, Antonietti M, Thomas A. A generalized synthesis of metal oxide hollow spheres using a hydrothermal approach. *Chem Mater* 2006;18(16):3808-3812.
- Titirici MM, Thomas A, Antonietti M. Back in the black: hydrothermal carbonization of plant material as an efficient chemical process to treat the CO<sub>2</sub> problem? *New J Chem* 2007a;31:787-789.
- Titirici MM, Thomas A, Yu SH, Muller JO, Antonietti M. A direct synthesis of mesoporous carbons with bicontinuous pore morphology from crude plant material by hydrothermal carbonization. *Chem Mater* 2007b;19:4205-4212.
- Titirici MM, Antonietti M, Baccile N. Hydrothermal carbon from biomass: a comparison of the local structure from poly- to monosaccharides and pentoses/hexoses. *Green Chem* 2008;10:1204-1212.
- Titirici MM, Antonietti M. Chemistry and materials options of sustainable carbon materials made by hydrothermal carbonization. *Chem Soc Rev* 2010;39:103-116.
- Titirici MM, White RJ, Falco C, Sevilla M. Black perspectives for a green future: hydrothermal carbons for environment protection and energy storage. *Energy Environ Sci* 2012;5:6796-6822.
- Titirici MM. Sustainable carbon materials from hydrothermal processes. London: Wiley; 2013.

- Tiwari GN, Mishra RK. Advanced renewable energy sources. RSC Publishing; 2011.
- Tondi G, Pizzi A, Masson E, Celzard A. Analysis of gases emitted during carbonization degradation of polyflavonoid tannin/furanic rigid foams. *Polym Degrad Stabil* 2008;93(8):1539-1543.
- Tondi G. Développement de résines de polycondensation à base de tanins pour produits industriels écologiques et innovants. Université de Lorraine, France, PhD thesis, 2009.
- Toupin M, Bélanger D, Hill IR, Quinn D. Performance of experimental carbon blacks in aqueous supercapacitors. *J Power Sources* 2005;140(1):203-210.
- Trajano HL, Wyman CE. Aqueous pretreatment of plant biomass for biological and chemical conversion to fuels and chemicals. In: Wyman CE, editor. *Fundamentals of biomass pretreatment at low pH*, John Wiley & Sons; 2013, p. 103-128.
- Unur E. Functional nanoporous carbons from hydrothermally treated biomass for environmental purification. *Microporous Mesoporous Mater* 2013;168:92-101.
- US DOE. Results of screening for potential candidates from sugars and synthesis gas. In: Werpy T, Peterson G, editors. *Top value added chemicals from biomass, USA: PNNL and NREL*; 2004, p. 1-76.
- van Krevelen DW. Graphical-statistical method for the study of structure and reaction processes of coal. *Fuel* 1950;29:269-284.
- Vazquez G, Gonzalez-Alvarez G, Garcia AI, Freire MS, Antorrena G. Adsorption of phenol on formaldehyde-pretreated *Pinus pinaster* bark: equilibrium and kinetics. *Bioresour Technol* 2007;98:1535-1540.
- Vix-Guterl C, Saadallah S, Jurewicz K, Frackowiak E, Reda M, Parmentier J, Patarin J, Béguin F. Supercapacitor electrodes from new ordered porous carbon materials obtained by a templating procedure. *Mater Sci Eng* 2004;108(1-2):148-155.
- Vix-Guterl C, Frackowiak E, Jurewicz K, Friebe M, Parmentier J, Béguin F. Electrochemical energy storage in ordered porous carbon materials. *Carbon* 2005;43(6):1293-1302.
- Walker PL, Rakszawski JF, Armington AF. Distinguishing between graphitic and amorphous carbon. *ASTM Bulletin* 1955;208:52-54.
- Wang Q, Li H, Chen L, Huang X. Monodispersed hard carbon spherules with uniform nanopores. *Carbon* 2001;39:2211-2214.
- Wang X, Bozhilov KN, Feng P. Facile preparation of hierarchically porous carbon monoliths with well-ordered mesostructures. *Chem Mater* 2006;18:6373-6381.
- Wang X, Liang C, Dai S. Facile synthesis of ordered mesoporous carbons with high thermal stability by self-assembly of resorcinol-formaldehyde and block copolymers under highly acidic conditions. *Langmuir* 2008;24:7500-7505.
- Wang H, Gao Q, Hu J. Preparation of porous doped carbons and the high performance in electrochemical capacitors. *Microporous Mesoporous Mater* 2010;131(1-3):89-96.
- Wang L, Guo Y, Zou B, Rong C, Ma X, Qu Y, Li Y, Wang Z. High surface area porous carbons prepared from hydrochars by phosphoric acid activation. *Bioresour Technol* 2011;102(2):1947-1950.

- Wang X, Liu J, Xu W, Liu S. One-step hydrothermal preparation of amino-functionalized carbon spheres at low temperature and their enhanced adsorption performance towards Cr(VI) for water purification. *Colloid Surface A* 2012;415:288-294.
- Wanka G, Hoffmann H, Ulbricht W. Phase diagrams and aggregation behavior of poly(oxyethylene)-poly(oxypropylene)-poly(oxyethylene) triblock copolymers in aqueous solutions. *Macromolecules* 1994;27:4145-4159.
- Waver I, Wolniak M, Paradowska K. Solid state NMR study of dietary fiber powders from aronia, bilberry, black currant and apple. *Solid State Nucl Mag* 2006;30:106-113.
- Wei L, Sevilla M, Fuertes AB, Mokaya R, Yushin G. Hydrothermal carbonization of abundant renewable natural organic chemicals for high-performance supercapacitor electrodes. *Adv Energy Mater* 2011;1(3):356-361.
- Wiedner K, Naisse C, Rumpel C, Pozzi A, Wieczorek P, Glaser B. Chemical modification of biomass residues during hydrothermal carbonization – What makes the difference, temperature or feedstock? *Org Geochem* 2013;54:91-100.
- White RJ, Antonietti M, Titirici MM. Naturally inspired nitrogen doped porous carbon. *J Mater Chem* 2009;19(45):8645-8650.
- White RJ, Budarin VL, Moir JWB, Clark JH. A sweet killer: mesoporous polysaccharide confined silver nanoparticles for antibacterial applications. *Int J Mol Sci* 2011a;12:5782-5796.
- White RJ, Yoshizawa N, Antonietti M, Titirici MM. A sustainable synthesis of nitrogen-doped carbon aerogels. *Green Chem.* 2011b;13(9):2428-2434.
- Wohlgemuth SA, White RJ, Willinger MG, Titirici MM, Antonietti M. A one-pot hydrothermal synthesis of sulfur and nitrogen doped carbon aerogels with enhanced electrocatalytic activity in the oxygen reduction reaction. *Green Chem* 2012a;14:1515-1523.
- Wohlgemuth SA, Vilela F, Titirici MM, Antonietti M. A one-pot hydrothermal synthesis of tunable dual heteroatom-doped carbon microspheres. *Green Chem* 2012b;14:741-749.
- Wu SY, Ding YS, Zhang XM, Tang HO, Chen L, Li BX. Structure and morphology controllable synthesis of Ag/carbon hybrid with ionic liquid as soft-template and their catalytic properties. *J Solid State Chem* 2008;181(9):2171-2177.
- Xing W, Qiao SZ, Ding RG, Li F, Lu GQ, Yan ZF, Cheng HM. Superior electric double layer capacitors using ordered mesoporous carbons. *Carbon* 2006;44(2):216-224.
- Xing W, Huang CC, Zhuo SP, Yuan X, Wang GQ, Hulicova-Jurcakova D, Yan ZF, Lu GQ. Hierarchical porous carbons with high performance for supercapacitor electrodes. *Carbon* 2009;47(7):1715-1722.
- Xu YJ, Weinberg G, Liu X, Timpe O, Schlögl R, Su DS. Nanoarchitecturing of activated carbon: new facile strategy for chemical functionalization of the surface of activated. *Adv Funct Mater* 2008;18:3613-3619.
- Yang W, Feller TP, Antonietti M. Efficient metal-free oxygen reduction in alkaline medium on high-surface-area mesoporous nitrogen-doped carbons made from ionic liquids and nucleobases. *J Am Chem Soc* 2011;133(2):206-209.
- Yoshizawa N, Hatori H, Soneda Y, Hanzawa Y, Kaneko K, Dresselhaus MS. Structure and electrochemical properties of carbon aerogels polymerized in the presence of Cu<sup>2+</sup>. *J Non-Cryst Solids* 2003;330(1-3):99-105.

- Yu Y, Lou X, Wu H. Some recent advances in hydrolysis of biomass in hot-compressed, water and its comparisons with other hydrolysis methods. *Energ Fuel* 2008;22:46-60.
- Yu DS, Dai LM. Self-assembled graphene/carbon nanotube hybrid films for supercapacitors. *J Phys Chem Lett* 2010;1(2):467-70.
- Yu S, Zhang Q, Dai LM. Highly efficient metal-free growth of nitrogen-doped single-walled carbon nanotubes on plasma-etched substrates for oxygen reduction. *J Am Chem Soc* 2010;132(43):15127-9.
- Yu L, Falco C, Weber J, White RJ, Howe JY, Titirici MM. Carbohydrate-derived hydrothermal carbons: a thorough characterization study. *Langmuir* 2012;28(33):12373-12383.
- Zhang F, Gu D, Yu T, Zhang F, Xie S, Zhang L, Deng Y, Wan Y, Tu B, Zhao D. Mesoporous carbon single-crystals from organic-organic self-assembly. *J Am Chem Soc* 2007;129(25):7746-7747.
- Zhang D, Hao Y, Ma Y, Feng H. Hydrothermal synthesis of highly nitrogen-doped carbon powder. *Appl. Surf. Sci.* 2012a;258(7):2510-2514.
- Zhang Z, Wang K, Atkinson J, Yan X, Li X, Rood MJ, Yan Z. Sustainable and hierarchical porous *Enteromorpha prolifera*-based carbon for CO<sub>2</sub> capture. *J Hazard Mater* 2012b;229-230:183-191.
- Zheng J, Liu Z, Liu X, Yan X, Li D, Chu W. Facile hydrothermal synthesis and characteristics of B-doped TiO<sub>2</sub> hybrid microspheres with higher photo-catalytic activity. *J Alloy Compd* 2011;509(9):3771-3776.
- Zhao D, Feng J, Huo Q, Melosh N, Fredrickson GH, Chmelka BF, Stucky GD. Triblock copolymer syntheses of mesoporous silica with periodic 50 to 300 Angstrom pores. *Science* 1998;279:548-552.
- Zhao J, Xiao H, Qiu G, Zhang Y, Huang N, Tang Z. Solid-state polycondensation of poly(ethylene terephthalate) modified with isophthalic acid: kinetics and simulation. *Polym* 2005;46:7309-7316.
- Zhao L, Baccile N, Gross S, Zhang Y, Wei W, Sun Y, Antonietti M, Titirici MM. Sustainable nitrogen-doped carbonaceous materials from biomass derivatives. *Carbon* 2010a;48(13):3778-3787.
- Zhao L, Li-Zhen F, Zhou MQ, Guan H, Qiao S, Antonietti M, Titirici MM. Nitrogen-containing hydrothermal carbons with superior performance in supercapacitors. *Adv Mater* 2010b;22(45):5202-6.
- Zhao Y, Li W, Zhao X, Wang DP, Liu SX. Carbon spheres obtained via citric acid catalysed hydrothermal carbonisation of cellulose. *Mater Res Innov* 2013;17(7):546-551.
- Zhao P, Shen Y, Ge S, Yoshikawa K. Energy recycling from sewage sludge by producing solid biofuel with hydrothermal carbonization. *Energ Convers Manage* 2014;78:815-821.
- Zhou JH, Sui ZJ, Zhu J, Li P, Chen D, Dai YC, Yuan WK. Characterization of surface oxygen complexes on carbon nanofibers by TPD, XPS and FT-IR. *Carbon* 2007;45(4):785-796.
- Zhou X, Yang Z, Nie H, Yao Z, Zhang L, Huang S. Catalyst-free growth of large scale nitrogen-doped carbon spheres as efficient electrocatalysts for oxygen reduction in alkaline medium. *J Power Sources*. 2011;196(23):9970-4.





## Résumé

Les ressources renouvelables sont considérées comme des alternatives durables, et parfois moins chères, aux matières premières d'origine pétrochimique. Dans cette thèse, on a utilisé du tanin provenant d'écorces de Mimosa comme précurseur de matériaux carbonés. La synthèse de ces nouveaux matériaux carbonés comprend un processus en deux étapes: la première étape est un traitement hydrothermal à des températures modérées, de 180 à 200°C, ce qui permet l'enrichissement en carbone ainsi que la fixation des hétéroatomes et la production de différentes morphologies: microsphères ou gels. La deuxième étape est une carbonisation à une température plus élevée, à savoir 900°C, ce qui permet d'augmenter la surface spécifique, la porosité ainsi que la conductivité électrique. La préparation d'un carbone poreux présentant des mésopores parfaitement définis en taille et dans leur organisation a été réalisée en associant le tanin, précurseur de carbone, à un tensio-actif structurant de la porosité, le copolymère Pluronic F127. Ces nouveaux matériaux carbonés ont été testés comme des électrodes de supercondensateur.

## Summary

Renewable resources are considered as sustainable, and sometimes cheaper, alternatives to substitute raw materials of petrochemical origin. We used tannins extracted from Mimosa barks. Tannin is an attractive precursor to synthesize new organic porous materials due to the presence of highly reactive phenolic molecules. The synthesis of these new carbon materials from tannin comprises a two-step process: the first step is a hydrothermal carbonization at moderate temperatures, 180-200°C, which allows obtaining a hydrochar, richer in carbon, and fixing other heteroatoms. These hydrochars present different morphologies as powder or gel. The second step is a carbonization at higher temperature (900°C), which allows increasing surface area ( $S_{\text{BET}}$ ), porosity as well as improving conductivity. The preparation of a porous carbon presenting mesopores perfectly defined in size and in their organization was realized by associating tannin, as carbon precursor, with a surfactant for porosity templating, the copolymer Pluronic F127. These new carbon materials were tested as electrodes of supercapacitor.